Design and operation of degenerate quantum dot systems for topological quantum computing

Sebastian Miles

DESIGN AND OPERATION OF DEGENERATE QUANTUM DOT SYSTEMS FOR TOPOLOGICAL QUANTUM COMPUTING

DESIGN AND OPERATION OF DEGENERATE QUANTUM DOT SYSTEMS FOR TOPOLOGICAL QUANTUM COMPUTING

Dissertation

for the purpose of obtaining the degree of doctor
at Delft University of Technology
by the authority of the Rector Magnificus prof. dr. ir. H. Bijl,
chair of the Board for Doctorates,
to be defended publicly on
Tuesday 3 March 2026 at 17:30 o'clock

by

Sebastian MILES

Master of Science in Physics,
Rheinisch-Westfälische Technische Hochschule, Aachen, Germany
born in Soltau, Germany.

This dissertation has been approved by

promotor: Prof. Dr. M. T. Wimmer,
promotor: Dr. A. R. Akhmerov.

Composition of the doctoral committee:

Rector Magnificus,	chairperson
Prof. Dr. M. T. Wimmer	Delft University of Technology, promotor
Dr. A. R. Akhmerov	Delft University of Technology, promotor
Independent members:	
Prof. Dr. ir. L. P. Kouwenhoven	Delft University of Technology
Prof. Dr. F. Hassler	RWTH Aachen University
Dr. D. Schuricht	Universiteit Utrecht
Prof. Dr. Y. M. Blanter	Delft University of Technology
Dr. A. Chatterjee	Delft University of Technology, reserve member

This work was supported by funding from the Dutch Organization for Scientific Research (NWO) through OCENW.GROOT.2019.004.

Printed by: Ridderprint

Front & Back: Licht und Materie I, II by Bettina Momma

ISBN (e-print): 978-94-6518-250-6
ISBN (book): 978-94-6384-908-1

An electronic version of this dissertation is available at
http://repository.tudelft.nl/.

CONTENTS

SUMMARY

Topological quantum computation is a paradigm of quantum computation anticipated to be resilient to a wide variety of noise sources. In it information is encoded in distributed, exponentially topologically protected degrees of freedom. These would only be deteriorated by significant perturbations of the system.

At the heart of this paradigm lies the Majorana zero mode It is an effective particle excitation akin to a fractionalized electron. Such Majorana zero modes are non-Abelian meaning their exchange changes the quantum state of the system. This can allow to perform operations in a protected and noise resilient way. Isolating and controlling Majorana zero modes is therefore the first step on the way to topological quantum computation.

The past decade has seen significant efforts to isolate such Majorana zero modes. Especially semiconductor superconductor hybrid systems in the form of proximitized ballistic one dimensional channels have garnered great attention. With time however, it became apparent that ballisticity puts significant constraints on material and fabrication quality.

As alternative, recent work suggests that the relevant physics can similarly be realized in arrays of quantum dots. The idea is to design quantum dot based arrays to implement the desired physics in their low energy degrees of freedom. By having a number of dots be proximitzed through adjacent superconductors, one can implement the relevant couplings for Majorana zero modes. Tuning the individual quantum dots then allows to control the localization and coupling to possibly allow for probes of their non-Abelianess in the near future.

The quantum dot platform largely avoids the challenges associated with material and fabrication dependent disorder. Rather, the system constituents can be controlled individually offering detailed control over the physics. In contrast to previous approaches, protection of the involved zero modes is not exponential. Instead, protection is generally proportional to a polynomial depending on the number of sites of the array.

In this thesis we will discuss designs of systems that can realize Majorana zero modes and how these can be operated to demonstrate the non-Abelian exchange statistics.

We begin in Ch. 1 with an exposé of topological quantum computation. The chapter introduces concepts such as Anyons, non-Abelianeess, Majorana zero modes and Parafermions. We review parity as the relevant degree of freedom in which we can encode information and discuss how braiding of Majorana zero modes corresponds to operations altering the encoded information. The second half of the chapter introduces the relevant physics for all subsequent chapters. We introduce the Kitaev chain as an example target Hamiltonian which can be implemented in a quantum dot based platform. The chapter proceeds with a review of proximity superconductivity leading over to Andreev bound states in quantum dots. These will be essential to mediate the couplings necessary to isolate Majorana zero modes. The chapter closes with a review of existing

proposals for minimal Kitaev chains and a brief introduction of quantum transport in the tunneling limit as means to probe the systems we design.

We proceed in Ch. 2 with a discussion of the Pymablock software package. The package serves as a tool to construct near-degenerate perturbation theories automatically. Near-degenerate perturbation theory is a standard tool in determining effective models from large Hamiltonians where the relevant degrees of freedom are separated by an energy gap. While the involved calculations have uniform structure, performing them by hand is laborious and prone to human error. Pymablock fills this gap by automating this process. The algorithm flexibly accommodates both symbolic and numerical calculations. It does so by implementing classes that handle matrix valued power series while deferring calculations to a user adjustable callable.

In Ch. 3 we design a system based on a quantum dot - Andreev bound state array unit cell to realize Majorana zero modes. The insight is to mediate the necessary couplings through the excited states in the Andreev bound states. This eliminates the need for a third site in the unit cell. We discuss the properties of the system and give conditions on parameters where we expect the system to yield Majorana zero modes. In the chapter, we elucidate the effect interactions, spin-orbit interaction, and leaking proximity superconductivity have on these conditions and the stability of the zero modes. We close the chapter with a discussion of the physics of scaling up the system and emergent next-nearest neighbor terms.

In Ch. 4 we return to previously implemented systems and study their properties in the time-reversal symmetric case. We find that, protected by dominating on-site interactions, the system is able to support zero modes despite the presence of the second spin channel. Interestingly, our analysis demonstrates that in the case of infinitely strong interactions, the spectrum is strongly triply degenerate. This allows to describe the emergent zero modes through both, Majorana Kramers pairs, and $\mathbf{Z}_3$ Parafermions. We end the section with a discussion of the behavior of the system when connected to a normal quantum dot, a standard test to asses quality of emergent zero modes.

Finally, in Ch. 5 we propose a protocol involving two minimal Kitaev chains and an auxiliary dot to probe their non-Abelian exchange statistics. We demonstrate for the ideal case how the auxiliary dot can facilitate braiding through virtual Majoranas when arranged in a π-junction with the surrounding chains. We then move to analyze and discuss the experimentally most relevant error sources which would deteriorate a faithful braid. These are Coulomb repulsion between the auxiliary and surrounding quantum dots, quasistatic noise on parameters, and residual couplings. We devise mitigation strategies for each where possible and discuss relevant constraints where not.

SAMENVATTING

Topologisch kwantumcomputing is een variant binnen de kwantumcomputing welke intrinsiek robuust wordt geacht tegen een groot aantal storingsbronnen. De kwantuminformatie is gecodeerd in ruimtelijk verspreide, topologisch gestabiliseerde vrijheidsgraden, die alleen gevoelig zijn voor ingrijpende verstoringen van het systeem.

Centraal in dit paradigma staat de Majorana nultoestand, een effectief quasideeltje dat kan worden opgevat als een gefractioneerd elektron. Majorana zero modes zijn niet-Abelse deeltjes, wat betekent dat het verwisselen ervan leidt tot een niet-triviale transformatie van de toestand van het kwantumsysteem. Hierdoor kunnen logische operaties op een topologisch beschermde wijze worden uitgevoerd, waardoor het realiseren en controleren van deze modi een cruciale stap vormen richting topologische kwantumcomputatie.

In de afgelopen tien jaar is aanzienlijke vooruitgang geboekt in het experimenteel realiseren van Majorana zero modes. Vooral halfgeleider–supergeleider-hybridesystemen uit eendimensionale nanodraden en supergeleiders, zijn uitgebreid onderzocht. Gaandeweg is echter gebleken dat de balisticiteit in dergelijke systemen zeer hoge eisen stelt aan materiaal- en fabricagekwaliteit.

Recent werk heeft aangetoond dat de relevante effecten ook kunnen worden gerealiseerd in arrays van kwantumstippen. Door normale kwantumstippen te koppelen aan kwantumstippen die via het proximiteitseffect supergeleidend zijn, kunnen de benodigde koppelingen voor Majorana zero modes worden geïmplementeerd. Het afstemmen van deze koppelingen maakt controle over de lokalisatie, interactie en uitlezing van Majorana-modi mogelijk, wat uitzicht biedt op een directe experimentele demonstratie van hun niet-Abelse statistiek.

Het kwantumstip-gebaseerde platform vermijdt in belangrijke mate de beperkingen van nanodraad-gebaseerde systemen en biedt een hoge mate van controle over de afzonderlijke componenten. De robuustheid van de Majorana-modi schaalt in dit geval echter polynomiaal met het aantal kwantumstippen, in plaats van exponentieel.

In deze thesis bestuderen wij systemen die Majorana zero modes kunnen realiseren en onderzoeken wij hoe hun niet-Abelheid experimenteel kan worden aangetoond. In hoofdstuk 1 introduceren wij de relevante concepten, waaronder anyons, niet-Abelheid, Majorana zero modes en parafermionen, evenals pariteit als informatiedragende vrijheidsgraad. Daarnaast bespreken wij hoe verwisselingen van Majorana-modi operaties op gecodeerde kwantuminformatie implementeren. De tweede helft van het hoofdstuk behandelt de fysische mechanismen achter Majorana zero modes, met de Kitaev-keten als prototypisch model. Wij bespreken de implementatie van de vereiste koppelingen met kwantumstippen en de rol van Andreev bound states. Het hoofdstuk sluit af met een overzicht van ontwerpen van minimale Kitaev-keten en een korte introductie tot kwantumtransport in de tunnellimiet.

In hoofdstuk 2 presenteren wij het softwarepakket Pymablock, ontwikkeld voor de automatische constructie van bijna-gedegenereerde perturbatietheorie. Deze methode maakt het mogelijk complexe Hamiltonianen te reduceren tot laag-energetische effectieve theorieën. Pymablock automatiseert deze foutgevoelige berekeningen en ondersteunt zowel analytische als numerieke toepassingen.

Hoofdstuk 3 behandelt een systeem bestaande uit een kwantumstip en een Andreev bound state welke Majorana zero modes kan realiseren. Door gebruik te maken van aangeslagen toestanden in de Andreev bound state kunnen de vereiste koppelingen worden gerealiseerd, waardoor een extra kwantumstip overbodig wordt. Wij analyseren de voorwaarden voor het ontstaan van Majorana-modi en bestuderen de invloed van spin-baankoppeling, Coulomb-interacties en weglekkende supergeleiding. Het hoofdstuk sluit af met een bespreking van de schaalbaarheid van dit ontwerp en de bijbehorende langeafstandskoppelingen.

In hoofdstuk 4 onderzoeken wij hetzelfde systeem in afwezigheid van een extern magnetisch veld. Wij tonen aan dat sterke Coulomb-interacties zero modes kunnen stabiliseren, zelfs in aanwezigheid van spinvrijheidsgraden. In de limiet van oneindig sterke interactie vertoont het spectrum een drievoudige degeneratie, die kan worden geïnterpreteerd in termen van Majorana-Kramersparen of $\mathbb{Z}_3$-parafermionen. Het hoofdstuk eindigt met een analyse van de invloed van een extra gekoppelde kwantumpstip op de kwaliteit van de zero modes.

In hoofdstuk 5 presenteren wij een protocol om de niet-Abelse verwisselingsstatistiek van Majorana-modi te onderzoeken. Het ontwerp bestaat uit twee minimale Kitaev-ketens die via een normaal kwantumstip zijn gekoppeld. Onder ideale omstandigheden maakt deze configuratie de verwisseling van Majorana-modi tussen de ketens mogelijk. Wij bespreken de belangrijkste experimentele storingsbronnen, waaronder Coulomb-interacties, lokale potentiaalfluctuaties en resterende koppelingen. Voor elk van deze effecten formuleren wij strategieën om deze te verminderen en bespreken wij de fundamentele beperkingen.

ZUSAMMENFASSUNG

Topologisches Quantencomputing ist eine Teildisziplin der Quanteninformationstheorie, in der Quanteninformation in Systemen enkodiert wird, die aufgrund topologischer Schutzmechanismen eine hohe Robustheit gegenüber äußeren Störungen aufweisen. Die Information wird dabei in nichtlokalen, topologisch geschützten Freiheitsgraden gespeichert und kann nur durch starke Störungen unbrauchbar werden.

Zentrale Objekte dieses Ansatzes sind Majorana-Nullmoden, effektive Quasiteilchen, die als räumlich getrennte Anteile eines Elektrons interpretiert werden können. Aufgrund ihrer nicht-abelschen Austauschstatistik führt das Vertauschen solcher Moden zu einer nichttrivialen Transformation des Quantenzustands. Dies ermöglicht die Realisierung geschützter Quantenoperationen, deren Implementierung weitgehend unabhängig von lokalen Störungen ist. Die kontrollierte Erzeugung und Manipulation von Majorana-Nullmoden stellt daher einen entscheidenden Schritt hin zum topologischen Quantencomputing dar.

In der vergangenen Dekade wurden erhebliche Fortschritte bei der Realisierung von Majorana-Nullmoden erzielt, insbesondere in hybriden Systemen aus nano Halbleiterdrähten mit aufgebrachten Supraleitern. Dabei hat sich jedoch gezeigt, dass die erforderliche Ballistizität hohe Anforderungen an Materialqualität und Nanofabrikation stellt.

Neuere Arbeiten zeigen hingegen, dass die für Majorana-Nullmoden notwendige Physik auch in Systemen gekoppelter Quantenpunkte realisiert werden kann. Durch gezielte Steuerung solcher Systeme lassen sich die relevanten Niedrigenergie-Freiheitsgrade effektiv erzeugen. Insbesondere erlaubt die Kopplung normaler Quantenpunkte über supraleitende, durch den Proximity-Effekt induzierte Elemente die Implementierung aller notwendigen Kopplungsterme. Die individuelle Ansteuerung der Quantenpunkte ermöglicht zudem eine Kontrolle über Lokalisierung und Paarung der Majorana-Moden, was perspektivisch den experimentellen Nachweis ihrer Nicht-Abelschheit erlaubt.

Auf Quantenpunkten basierende Systeme umgehen dabei viele der Herausforderungen der Nanodrahtsysteme. Anstelle extremer Materialanforderungen rückt die präzise elektrische Steuerbarkeit der Systemparameter in den Vordergrund. Weiterhin skalliert der urpsrünglich topologische Schutz in diesen Systemen nicht mehr exponentiell, sondern skaliert polynomiell mit der Systemgröße.

In dieser Arbeit untersuchen wir Entwürfe solcher Quantenpunktsysteme, analysieren ihre Eigenschaften und entwickeln Protokolle zum Nachweis der nicht-abelschen Vertauschungsstatistik der Majorana-Nullmoden.

Kapitel 1 führt in die Grundlagen des topologischen Quantencomputings ein und behandelt zentrale Konzepte wie Anyonen, Nicht-Abelschheit, Majorana-Nullmoden und Parafermionen. Anschließend diskutieren wir die Kitaev-Kette als prototypisches Modell und zeigen, wie sie in Quantenpunktketten realisiert werden kann. Dabei führen wir durch den Proximity-Effekt induzierte Andreev-Zustände ein, und diskutieren deren

Nutzen zur Erzeugung der notwendigen Kopplungen. Das Kapitel schließt mit einem Überblick über bestehende Entwürfe zur Erzeugung von Majoranas in Systemen basierend auf Quantenpunkten, sowie einer Einführung in die Quantentransporttheorie im Tunnellimit.

Kapitel 2 stellt Pymablock vor, ein Softwarepaket zur automatisierten Berechnung effektiver Modelle mittels Störungstheorie. Der Fokus liegt auf der systematischen Trennung von Freiheitsgraden in verschiedene Sektoren, wobei der Algorithmus sowohl numerische als auch analytische Berechnungen auf Basis matrixwertiger Potenzreihen erlaubt.

In Kapitel 3 analysieren wir ein System aus zwei Quantenpunkten mit elektronischen beziehungsweise Andreev-Zuständen und zeigen, wie sich darin Majorana-Nullmoden realisieren lassen. Die Besonderheit des Systems liegt in der Verwendung des angeregten Andreev Niveaus, um die relevanten Kopplungen zur Erzeugung der Nullmoden zu verwenden. Wir untersuchen die Abhängigkeit der Nullmoden von Spin-Bahn-Kopplung, Coulombwechselwirkung und supraleitender Leckage sowie das Verhalten des Systems bei Skallierung zu längeren Ketten.

Kapitel 4 widmet sich zeitumkehrinvarianten Systemen mit starker Coulombwechselwirkung. Wir zeigen, dass in diesem Regime stabile Nullmoden auftreten, die im Grenzfall unendlicher Wechselwirkung entweder als Majorana-Kramers-Paare oder als $\mathbb{Z}_3$ - Parafermionen interpretiert werden können. Eine Stabilitätsanalyse bei zusätzlicher normaler Kopplung schließt das Kapitel ab.

Abschließend entwickeln wir in Kapitel 5 ein Protokoll zur Vertauschung von Majorana-Nullmoden. Wir nehmen ein System aus zwei minimalen Kitaev-Ketten und einem koppelnden elektronischen Quantenpunkt an. Darin wird die Vertauschung durch virtuelle Majoranamoden im elektronischen Quantenpunkt bei einer Phasendifferenz von π zwischen den Supraleitern der Kitaev-Ketten ermöglicht. Wir analysieren relevante experimentelle Fehlerquellen und diskutieren Strategien zu deren Umgehung oder Minimierung.

1

INTRODUCTION

1.1. PREFACE

The generation of coherent superpositions of quantum states [1, 2] and the ability to perform operations on quantum states [3, 4] were significant developments in the last decade of the last century. These developments can be seen as the advent of the *second quantum revolution* [5], which became perhaps most apparent in the field of quantum computing [6]. The idea is simple: exchange classical bits for quantum bits, qubits, and perform computations by operating on the qubits. The hope is to leverage quantum correlations for potentially faster or more powerful computations which may yield a quantum advantage [7, 8]. Examples of problems in which quantum computers are suspected to offer advantages are optimization problems [9, 10] and quantum chemistry [11–13].

In this thesis we focus on topological quantum computation (TQC) [14], as compared with implementations in other physical systems, e.g., trapped ions [15–17], spins [18–20], photonic systems [21–23], and superconducting circuits [24–26]. While other quantum architectures encode information in local degrees of freedom, TQC uses a nonlocal encoding anyonic quasiparticle excitations [14, 27–30]. These emergent quasiparticles manifest a topological ground-state degeneracy. In such a degeneracy, the information can be stored in e.g., the local fermion parity, a macroscopic degree of freedom [28] of each subsystem. Certain systems [31–33] can host such excitations, specifically Majorana zero modes (MZMs). These are spatially separated, charge-neutral states that pairwise define a nonlocal fermion. By splitting the MZMs in space, errors from their interactions and the environment become exponentially suppressed due to the separation. At the same time, the degenerate ground states are separated by an energy gap from the remaining states. This gap protects the states against global perturbations up to the scale of the gap.

Recent research [34–37] indicates that an implementation of such designs requires disorder-free materials and fabrication-optimized devices. Alternatively, recent studies [38–41] show that MZMs can also be implemented in quantum dot chains. However,

The language and clarity of this section has been improved using AI tools.

1

quantum dot systems are generally well understood and can be fabricated reproducibly, which substitute the problem of disorder for the need for detailed tuning. The ability to tune parameters reliably, therefore, would allow for protected storage of information. Given the typical magnitude of parameter noise in quantum dot systems [42–44], we anticipate sufficiently protected systems based on quantum dot chain well within reach. This might suffice to implement TQC, and it is the motivation of this work. We discuss the design and analysis of systems that can be the building blocks for TQC with MZMs. To this end, we will explore the physics of non-Abelian anyons, semiconductor-superconductor hybrid systems, and low-energy effective modeling.

1.2. TOPOLOGICAL QUANTUM COMPUTING

We begin by reviewing the key concepts of topological quantum computation following the presentation in Refs. [27–29].

1.2.1. ABELIAN AND NON-ABELIAN ANYONS

In Sec. 1.1 we mentioned anyons as information carriers in TQC. Specifically, that these anyons must be non-Abelian. Such non-Abelian anyons can emerge as quasiparticles in two-dimensional systems [27, 29]. As first demonstrated in Ref. [45], particle exchange in two dimensions is not restricted to fermionic or bosonic exchange statistics. Rather, macroscopically degenerate systems, such as those mentioned in Sec. 1.1, can host emergent non-Abelian anyons. Their defining property is that, upon exchange, they change the quantum state of the system. Exchange of non-Abelian anyons in two dimensions corresponds to elements b_i of the braid group B_N [27]. Each exchange, associated with a b_i, corresponds to a unitary transformation U applied to the degenerate states. Let $\{|\psi_i\rangle\}_{i=1,\dots,N}$ be a set of degenerate states. The exchange of two non-Abelian anyons then acts as $U\vec{\psi}$, where $\vec{\psi} = (|\psi_1\rangle,\dots,|\psi_N\rangle)^T$. Crucially, the details of exchange matter, i.e., the final state can differ for different exchanges $U_1U_2\vec{\psi} \neq U_2U_1\vec{\psi}$. We exploit this property for TQC, specifically in Ch. 5 of this thesis. Rather than performing operations by modifying local degrees of freedom, we can perform operations by the exchange of quasiparticles.

The archetypical non-Abelian anyon is the Majorana fermion or Majorana zero mode (MZM) [46]. It is a self-conjugate fermionic excitation that is described by a Hermitian operator γ satisfying,

$$\gamma = \gamma^\dagger \tag{1.1}$$

$$\{\gamma_i, \gamma_j\} = 2\delta_{i,j} \tag{1.2}$$

Two MZMs γ_1, γ_2 can be combined to represent a single electronic degree of freedom described by the creation and annihilation operators $c^\dagger, c$ via

$$c = (\gamma_1 + i\gamma_2)/2 \tag{1.3}$$

$$c^\dagger = (\gamma_1 - i\gamma_2)/2 \tag{1.4}$$

Their electronic number operator $n = c^\dagger c = (1 + i\gamma_1\gamma_2)/2$ distinguishes two degenerate states $|0\rangle, |1\rangle = c^\dagger|0\rangle$ in which quantum information can be encoded. Crucially, because the MZMs can be spatially separated, this fermionic degree of freedom is nonlocal.

With the connection to electronic degrees of freedom, one could be led to believe that individual MZM themself represent a physical state. However, this is not true. To understand the action of the MZMs on states, we need the concept of fermionic parity. The parity operator,

$$\mathcal{P} = \prod_i (2c_i^\dagger c_i - 1), \tag{1.5}$$

informs if a system contains an odd or an even number of electrons c_i. For the previous example of a single electron c described by two MZMs γ_1, γ_2, we recognize the parity in the electronic occupation states. We see that $\langle 0|\mathcal{P}|0\rangle = -1$ and $\langle 1|\mathcal{P}|1\rangle = 1$. The meaning of the MZMs can be understood by inspecting their representation in the fermionic basis. From eqs. (1.3) and (1.4), we can infer

$$\gamma_1 = c^\dagger + c \tag{1.6}$$

$$\gamma_2 = -i(c^\dagger - c). \tag{1.7}$$

Writing the MZMs, γ_1, γ_2, in the fermionic basis $|0\rangle, |1\rangle$, we find their representation

$$\gamma_1 = |1\rangle\langle 0| + |0\rangle\langle 1|, \tag{1.8}$$

$$\gamma_2 = -i\left(|1\rangle\langle 0| - |0\rangle\langle 1|\right). \tag{1.9}$$

We see that, while the MZMs do not represent physical states, they represent changes of the parity of the system. The parity, eq. (1.5), can be equivalently represented by MZM operators as

$$\mathcal{P} = (-1)^{N+1} \prod_i^{2N} \gamma_i, \tag{1.10}$$

where N is the number of MZM pairs. This number is the same as the number of degenerate pairs of states.

Finally, we extend the discussion to parafermions, which we consider in greater detail in Ch. 4. MZMs correspond to the case where the system hosts two-fold degenerate states with opposing parity. Systems can feature higher-order degeneracies, e.g., in interacting systems [47–50]. The emergent modes associated with such higher-order degenerate sets of states involve more than two electrons. This leads to the concept of $\mathbb{Z}_n$ parafermions [48, 51], which are described by operators α satisfying

$$\alpha_i^n = 1, \tag{1.11}$$

$$\alpha_l \alpha_m = e^{i\frac{2\pi}{n}\mathrm{sgn}[m-l]} \alpha_m \alpha_l. \tag{1.12}$$

For $n = 2$ the definition coincides with that of MZMs. For $n \geq 2$, parafermions are associated with an emergent fractional charge connected to an emergent $\mathbb{Z}_n$ parity symmetry [48] that distinguishes states in the degenerate manifold. In contrast to MZMs, $Z_{n\geq 3}$ parafermions cannot be found as a topological zero modes due to the lack of stable $n \geq 3$ particle processes [52]. For that reason, emergent Parafermion modes always depend on fine-tuning of the physical system due to finite coupling between degenerate sets of states [52].

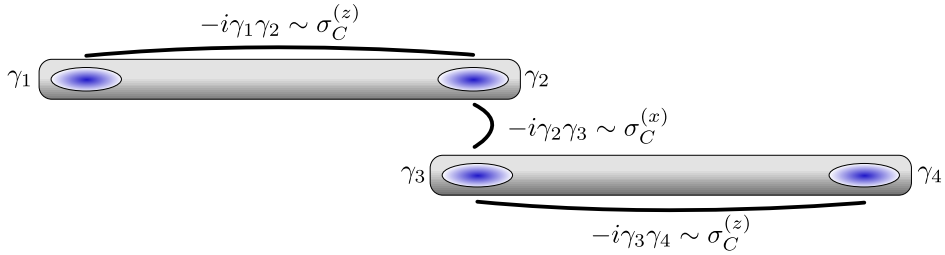

Figure 1.1: Basic set-up for a Majorana-based qubit. Each wire hosts a pair of MZMs, which define a distributed fermion. Two such wires together encode one qubit and allow for both $\sigma^{(z)}$ and $\sigma^{(x)}$ Pauli operations.

1.2.2. QUANTUM COMPUTATION WITH MAJORANA FERMIONS

We have seen how MZMs relate to parity and physical fermions. Next, we use these ingredients to encode information. In particular, we want to use the macroscopic parity of a system to encode qubit states. For a closed system, described by some Hamiltonian H, it holds that

$$[\mathcal{P}, H] = 0. \tag{1.13}$$

To encode a qubit, we need at least four MZMs, i.e., two fermions (see Fig. 1.1). Restricting ourselves to the globally even parity sector, we define our qubit states as

$$|0_C\rangle = |0_{1,2}\rangle \otimes |0_{3,4}\rangle, \tag{1.14}$$
$$|1_C\rangle = |1_{1,2}\rangle \otimes |1_{3,4}\rangle, \tag{1.15}$$

where the index C specifies a computational state and the numeric indices indicate the associated MZM operators. Next, we need to identify single-qubit operations, which we parametrize by the Pauli matrices

$$\sigma^{(0)} = \begin{pmatrix} 1 & 0 \\ 0 & 1 \end{pmatrix} \quad \sigma^{(x)} = \begin{pmatrix} 0 & 1 \\ 1 & 0 \end{pmatrix} \quad \sigma^{(y)} = \begin{pmatrix} 0 & -i \\ i & 0 \end{pmatrix} \quad \sigma^{(z)} = \begin{pmatrix} 1 & 0 \\ 0 & -1 \end{pmatrix}. \tag{1.16}$$

In the previous equation, $\sigma^{(x)}$ corresponds to a bit-flip operation, $\sigma^{(y)}$ implements a phase, and $\sigma^{(z)}$ is a projection in the computational basis. We encode the first occupation index in the computational states by two MZMs γ_1, γ_2, and the second by two MZMs γ_3, γ_4. Their respective state is then encoded in their local parities

$$\mathcal{P}_{1,2} = -i\gamma_1\gamma_2, \tag{1.17}$$
$$\mathcal{P}_{3,4} = -i\gamma_3\gamma_4, \tag{1.18}$$

such that the total parity is even. Pairs of MZMs encode the occupation of a distributed fermionic degree of freedom. We can consider the effect of eq. (1.17) in the computational basis.

$$\langle 0_C|\mathcal{P}_{1,2}|0_C\rangle = \langle 0_{1,2}|\mathcal{P}_{1,2}|0_{1,2}\rangle\langle 0_{3,4}|0_{3,4}\rangle = 1 \tag{1.19}$$
$$\langle 1_C|\mathcal{P}_{1,2}|1_C\rangle = \langle 1_{1,2}|\mathcal{P}_{1,2}|1_{1,2}\rangle\langle 1_{3,4}|1_{3,4}\rangle = -1, \tag{1.20}$$

and similarly for $\mathcal{P}_{3,4}$. Therefore, we can identify eqs. (1.17) and (1.18) as $\sigma^{(z)}$ in the computational basis. In addition, we need access to another Pauli operation in the computational states [6, 53]. Following the same idea as above, we can consider what happens when coupling MZMs between wires. Coupling e.g., γ_2 with γ_3, we recognize a simultaneous parity change across both local parities. This we identify with $\sigma^{(x)}$ in the computational basis, i.e., $\sigma^{(x)} = -i\gamma_2\gamma_3$. As previously discussed, all involved degrees of freedom are, in principle, well separated. This separation makes them resilient against local fluctuations of the system, as long as the global parity of the system is conserved.

To perform the presented operations, we can exchange, or braid, MZMs pairwise. As noted in Sec. 1.2.1, exchange corresponds to a change of the quantum state of the system. To see this, we construct the unitary associated with an exchange, i.e., the time evolution operator of the process. Following an argument presented in [28], exchanging two MZMs γ_1, γ_2 clockwise amounts to a transformation that maps

$$\gamma_1 \to -\gamma_2, \tag{1.21}$$
$$\gamma_2 \to \gamma_1, \tag{1.22}$$

where the minus sign is a consequence of the branch cut [28] that induces the statistical phase. The operator facilitating this exchange is

$$B_{1,2} = \left(1 + \gamma_1\gamma_2\right)/\sqrt{2}. \tag{1.23}$$

In contrast, if we instead exchange both particles in a counterclockwise manner, the unitary associated with the exchange is $\tilde{B}_{1,2} = (1 - \gamma_1\gamma_2)/\sqrt{2}$. Exchanging both MZMs again by applying $B_{1,2}^2 = \gamma_1\gamma_2$, we again arrive at the initial configuration of the system. However, due to the non-Abelian exchange statistics, the states of the system differ by a phase factor

$$\gamma_1\gamma_2|0_{1,2}\rangle = -i|0_{1,2}\rangle \tag{1.24}$$
$$\gamma_1\gamma_2|1_{1,2}\rangle = i|1_{1,2}\rangle. \tag{1.25}$$

In terms of MZMs, this can be seen from the fact that

$$\gamma_i \to (\gamma_1\gamma_2)\gamma_i(\gamma_1\gamma_2)^\dagger = -\gamma_i. \tag{1.26}$$

Comparing eq. (1.26) with our discussion at the beginning of Sec. 1.2.2, we can identify how exchange corresponds to Pauli operations in the computational states:

$$B_{12} = B_{34} = e^{-i\frac{\pi}{4}\sigma^{(z)}}, \tag{1.27}$$
$$B_{23} = e^{-i\frac{\pi}{4}\sigma^{(x)}}. \tag{1.28}$$

Unfortunately, gates implemented via braiding alone do not form a universal set of gates in this encoding. In particular, we need to be able to perform entangling operations between multiple qubits [53, 54]. This is because braiding operations can only implement Clifford gates [55]. For universal quantum computation, we need either a $\pi/8$- or T-gate [6, 53, 56]. Fortunately, previous works have proposed schemes to generate for

entanglement. There are proposals that rely on the geometric properties of the Majorana Hilbert space [57], coupling to an auxiliary Transmon [58], coupling of MZMs via spin degrees of freedom [59], gate-based measurement schemes [60], or larger numbers of MZMs in which the computational states are encoded differently [61, 62].

Going beyond MZMs, it is possible to perform universal quantum computation with parafermionic anyons when only assuming braiding operations [63]. Their higher fractionalized exchange statistics (c.f. eq. (1.12)) enable implementation of entangling gates through multipartite exchange. Alternative proposals [64] propose universal gates for $\mathbb{Z}_{2n}$ parafermions when coupled to a spin degree of freedom.

1.3. DESIGNING TOPOLOGICAL SYSTEMS

We now develop the building blocks to design semiconductor-superconductor hybrid systems that host Majorana zero modes. First, in Sec. 1.3.1, we introduce the Kitaev chain. It is the simplest system to feature MZMs and useful to understand the ingredients we need. In Sec. 1.3.2, we introduce quantum dots in semiconductors. They are the basic building blocks for the systems we design. When reviewing MZMs in Sec. 1.2.1, a crucial ingredient was parity. In practice, we will encounter this in Sec. 1.3.1 in the form of pairing interactions that involve two particles, hence not changing the local parity of a subsystem. The only known interaction that facilitates this is superconductivity. We review its principles in Sec. 1.3.3. Finally, in Sec. 1.3.4, we bring everything together and review the idea of Poor man's Majoranas [39].

1.3.1. KITAEV CHAIN

An important model to understand the ingredients needed for MZMs is the Kitaev chain [65]. The Hamiltonian of this one-dimensional, spinless lattice model reads

$$H = \mu \sum_{n=0}^{N} c_n^\dagger c_n + t \sum_{n=0}^{N} (c_{n+1}^\dagger c_n + h.c.) + \Delta \sum_{n=0}^{N} (c_n c_{n+1} + h.c.), \tag{1.29}$$

where μ is the chemical potential, t is the normal hopping amplitude, and Δ is a p-wave pairing term. We transform the electronic operators into the Majorana basis by using the relations of eqs. (1.6) and (1.7). Per site, we replace

$$\gamma_{n,A} = (c_n^\dagger + c_n) \tag{1.30}$$

$$\gamma_{n,B} = -i(c_n^\dagger - c_n). \tag{1.31}$$

Per site, we obtain two distinct Majorana species A, B.

We now transform eq. (1.29) using eqs. (1.30) and (1.31). Expressing the tunneling and pairing terms in the Majorana basis, we obtain

$$t(c_2^\dagger c_1 + c_1^\dagger c_2) = i\frac{t}{2}\left[\gamma_{B,1}\gamma_{A,2} - \gamma_{A,1}\gamma_{B,2}\right], \tag{1.32}$$

$$\Delta(c_2^\dagger c_1^\dagger + c_1 c_2) = -i\frac{\Delta}{2}\left[\gamma_{B,1}\gamma_{A,2} + \gamma_{A,1}\gamma_{B,2}\right]. \tag{1.33}$$

Similarly, the number operator in the Majorana basis reads

$$\mu c_n^\dagger c_n = \frac{\mu}{2}[2 - i\gamma_{A,n}\gamma_{B,n}]. \tag{1.34}$$

Figure 1.2: Kitaev chain in the Majorana basis. Each electronic site is split into two Majoranas which couple through the chemical potential, μ, on each site. Between sites, coupling is mediated by combinations of normal hopping, t, and p-wave pairing, Δ. At $\mu = 0$ and $|t| = |\Delta|$, the onsite couplings and one diagonal coupling vanish, isolating a single Majorana on the terminating sites.

We collect eqs. (1.32), (1.33), and (1.34) in the picture presented in Fig. 1.2. Intersite coupling depends only on $|t \pm \Delta|$ and couples opposite species. On-site coupling is proportional to μ itself and couples MZMs on one site. Fig. 1.2 implies the topological phase of eq. (1.29). At $\mu = 0$ and $|t| = |\Delta|$, the on-site coupling and one intercell coupling vanish. This leaves two uncoupled MZMs in the terminating sites. At this point, eq. (1.29) can be written as

$$H = -i\Delta \sum_{n=1}^{N-1} \gamma_{n,A}\gamma_{n+1,B}. \tag{1.35}$$

The two uncoupled Majoranas, $\gamma_{1,B}, \gamma_{N,A}$ imply one fermionic degree of freedom with degenerate eigenstates at $E = 0$. They are separated from the rest of the spectrum by an energy gap Δ. The two MZMs imply one fermion distributed between the ends of the system.

Crucially, the zero modes are topologically protected, i.e., perturbing the system will not destroy the MZMs on a scale Δ. For the Kitaev chain this means that the MZMs also remain when one or multiple $\mu_i < \Delta$ are changed. This is guaranteed by the particle-hole symmetry of eq. (1.29). Rewriting eq. (1.29) in the particle-hole basis (or BdG basis, see Sec. 1.3.3) $\vec{c} = (c_1, ...c_N, c_1^\dagger, ..., c_N^\dagger)^T$, we obtain

$$H = \vec{c}^\dagger \frac{1}{2} \sum_{i,j} \left(\mu\tau^{(z)}\delta_{i,j} + t\tau^{(z)}(\delta_{i+1,j} + \delta_{i,j+1}) + i\Delta\tau^{(y)}(\delta_{i+1,j} + \delta_{i,j+1}) \right) \vec{c}, \tag{1.36}$$

where $\delta_{i,j}$ is the Kronecker symbol. Observe that the transformation doubles the degrees of freedom. The matrices $\tau^{(i)}$ are a set of Pauli matrices (c.f. the definition for $\sigma^{(i)}$ in Sec. 1.2.2) that act in particles-hole space. We see that eq. (1.36) satisfies $\Pi H \Pi^{-1} = -H$ with the operator $\Pi = \tau^{(x)}\mathcal{K}$, where $\mathcal{K}$ is complex conjugation. This is the particle-hole symmetry of eq. (1.29), which protects the MZMs [66]. The MZMs are pinned at $E = 0$ and can only couple through the excited states which are at $E = \Delta$.

Looking back, if we want to implement the Kitaev chain, we need three things: 1) an analogue of a lattice site with controllable μ, 2) a tunable tunneling process t, and 3) a tunable p-wave pairing Δ between sites. We address 1) and 2) in Sec. 1.3.2 and discuss 3) in Sec. 1.3.3.

1.3.2. SINGLE LEVEL QUANTUM DOTS

An analogue of a lattice site in condensed matter is the semiconductor quantum dot. This will be our basic building block from Ch. 3 through Ch. 5.

A quantum dot is a small region in space where otherwise free electrons are confined electrostatically and/or by system terminations [67, 68]. To make a quantum dot useful, we need to be able to address levels individually. This means we need the level spacing $\sim \mu/N_{\text{el}}$ to be comparable to the charging energy $\sim e/L_{dot}$ where L_{dot} is a characteristic length of the dot. We can achieve this by either changing the density of electrons $\sim \mu$ in the material, or the geometry $\sim L$ of the dot. The most flexible compromise between both is offered by semiconducting materials due to their controllable electronic density [67, 68].

The Hamiltonian for a single level, spinful quantum dot reads

$$H_{QD} = (\mu + E_Z)c_\uparrow^\dagger c_\uparrow + (\mu - E_Z)c_\downarrow^\dagger c_\downarrow + Uc_\uparrow^\dagger c_\uparrow c_\downarrow^\dagger c_\downarrow \tag{1.37}$$

where μ is the chemical potential, $E_Z = \mu_B g B/2$ is the Zeeman energy induced by a magnetic field B, and U is the onsite charging energy (Coulomb repulsion). The g-factor g is a material- and confinement-dependent parameter that can in principle depend on the direction of the magnetic field [69].

To implement a site in the Kitaev chain, we want exactly one level on the quantum dot. This can be achieved by applying sufficiently a large magnetic field. The remaining, spin polarized level can then be considered as either occupied or unoccupied. In principle, quantum dots can be coupled to each other via quantum point contacts or barrier gates. This would however not suffice to implement Kitaev chains as this would only satisfy 2) from the previous list in Sec. 1.3.1.

1.3.3. ANDREEV BOUND STATES IN PROXIMITZED QUANTUM DOTS

To implement the p-wave pairing required in eq. (1.29), we need to review superconductivity. Conventional superconductors are described by the Bardeen-Cooper-Schrieffer (BCS) [70, 71] theory of superconductivity. In metallic systems, lattice phonons induce an effective, attractive coupling between the electrons [72]. This leads to an instability of the Fermi surface where electrons bind pairwise into Cooper pairs [73]. The instability is characterized by an order parameter $\Delta_0 = |\Delta_0|e^{i\phi}$. $|\Delta_0|$ is the excitation gap of Cooper pairs, and ϕ is the superconducting phase. For the subgap ($E < |\Delta_0|$) phenomena of interest, we can write the BCS Hamiltonian in the same particle-hole basis as the Kitaev chain in Sec. 1.3.1

$$H_{BCS} = \vec{c}^\dagger \frac{1}{2}\begin{pmatrix} H & \Delta_0 \\ -\Delta_0^* & -H^* \end{pmatrix}\vec{c} \tag{1.38}$$

where the asterisk means complex conjugation. Similar to eq. (1.36), eq. (1.38) has a particle hole symmetry $\Pi = \tau^{(x)}\mathcal{K}$ such that $\Pi H_{BCS}\Pi^{-1} = -H_{BCS}$.

Eq. (1.38) can be solved by expressing it in a new set of operators. This is called Bogoliubov transformation [74, 75]. For spinful Hamiltonians, it reads

$$b_\uparrow = uc_\uparrow + vc_\downarrow^\dagger \tag{1.39}$$

$$b_\downarrow = -uc_\downarrow + vc_\uparrow^\dagger, \tag{1.40}$$

where the coefficients $|u|^2 + |v|^2 = 1$.

For Hamiltonians, H, with energy ε, chemical potential μ, and without applied fields or spin-orbit interaction, the dispersion of the Bogoliubov quasiparticles reads

$$E_\pm = \pm\sqrt{\xi^2 + |\Delta_0|^2}. \tag{1.41}$$

where we define $\xi = \epsilon - \mu$. Eq. (1.41) clearly shows the excitation gap of the Cooper pairs. In this case, the previously mentioned coefficients u, v (c.f. eq. (1.39)) take the form $u^2 = 1 - v^2 = 1/2 + \xi/\left(2\sqrt{\xi^2 + |\Delta_0|^2}\right)$

Cooper pairs bind together and correlate on the scale of the coherence length

$$\ell_0 = \frac{\hbar v_F}{\pi \Delta_0}, \tag{1.42}$$

where v_F is the Fermi velocity. On the same scale we can implant the superconducting correlations from the metallic superconductor into the semiconductor hosting the quantum dots. This effect is known as proximity effect [71, 76, 77]. The proximity (or induced) gap is rescaled by the coupling as $\Delta \sim \Delta_0\Gamma/(\Delta_0 + \Gamma)$ [35, 78], where Γ is the coupling between the electrons in superconductor and semiconductor. Given finite pairing, we can modify eq. (1.37) by adding an s-wave pairing term

$$H_{SC} = \Delta(c_\uparrow^\dagger c_\downarrow^\dagger + c_\downarrow c_\uparrow). \tag{1.43}$$

The states in confined, proximitized regions are commonly referred to as Andreev bound states (ABSs) [79]. In the single particle regime, the dispersion is given by eq. (1.41). An example dispersion (offset by a constant factor $-0.75|\Delta|$) is shown in Fig.1.4 a) as a function of ξ. The ABS allows tuning of the electron-hole content by changes of the chemical potential. This we indicate in Fig. 1.4 a) with the line-color. Being able to tune the charge content of the ABS will be crucial when discussing the effective couplings for Kitaev chains (Sec. 1.3.4).

1.3.4. POOR MAN'S MAJORANAS AND THE MINIMAL KITAEV CHAIN

Finally, we can consider a system of two quantum dots (eq. (1.37)) coupled via a superconducting degree of freedom. This type of setup is commonly referred to as Cooper pair splitter (CPS) and has previously been suggested to distribute entanglement [80, 81]. The initial proposal for PMMs [38, 39] utilizes bulk superconductors where $\ell_0 > L_{SC}$ (cf. eq. (1.42)). These are rather constrained in their tunability, which limits scalability. A more recent proposal suggests replacing the bulk superconductor by an ABS in e.g. a quantum dot in proximity to a superconductor [82]. In this setup, the ABSs can be tuned by back gates which offers more detailed tunability in turn allowing more flexible scaling. We show a schematic of this second setup in Fig. 1.3.

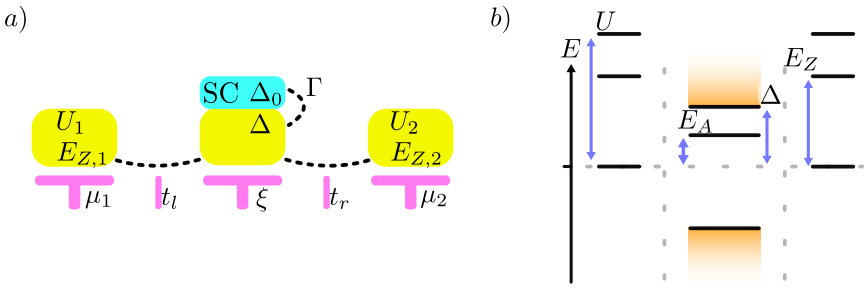

Figure 1.3: Relevant energy scales and schematic of a minimal Kitaev chain. a) A minimal Kitaev chain consists of three quantum dots. The central dot is proximitized by a superconductor. The chemical potential on each dot is tunable by a back gate. The pairwise tunneling between them is controlled by a tunnel gate. The electronic dots each feature an on-site interaction U_i and are spin-polarized by a Zeeman energy $E_{Z,i}$. Both are renormalized by the proximity effect in the central dot. b) Schematic illustration of energy scales. The Zeeman energy splits different spins leading to the singly occupied regime required in eq. (1.29). On-site interactions U additionally push away double occupied states and suppress local Andreev reflection. We assume a single ABS with energy $E_A < \Delta$ in the enrgy gap of the superconductor.

We achieve the single occupation required by eq. (1.29) by spin polarizing the quantum dots. This is achieved by applying a magnetic field, which yields a Zeeman splitting of E_z (cf. eq. (1.37)) between the two spin species. We then consider the effective, virtual tunneling processes across the ABS. As illustrated in Fig. 1.4 b), there are three types of processes possible: 1) ECT, or electron co-tunneling; 2) CAR, or crossed Andreev reflection; 3) LAR, or local Andreev reflection. ECT describes a process in which one electron tunnels through the superconductor onto the other dot. We refer to ECT as Γ_{ECT}. CAR, Γ_{CAR}, is a joint deposition of electrons on the dots by the splitting of a Cooper pair. The latter is a process which requires an excitation of an ABS into the continuum. Crucially, the SC is of s-wave type. Hence, we need an ingredient that mixes spin species. In semiconductors, this happens through spin-orbit interaction (SOI) [83]. This, in some materials [84], is suggested to be tunable. Lastly, LAR corresponds to a virtual process through the ABS that locally couples the $|0\rangle$ and $|\uparrow\downarrow\rangle$ states on a quantum dot. This process scales as $\sim 1/(E_z+U)$ due to the energy difference between the involved states. Due to the spin polarizing magnetic field and the usually large Coulomb repulsion (cf. Ch. 4 and [41]), LAR is strongly suppressed and can hence be omitted in the low-energy theory.

Collecting everything, we arrive at the effective low-energy model in the particle-hole basis $\vec{c} = (c_1, c_2, c_1^\dagger, c_2^\dagger)$

$$H = \begin{pmatrix} \mu_1 & \Gamma_{ECT} \\ \Gamma_{ECT} & \mu_2 \end{pmatrix} \tau^{(z)} + i \begin{pmatrix} 0 & \Gamma_{CAR} \\ \Gamma_{CAR} & 0 \end{pmatrix} \tau^{(y)} \tag{1.44}$$

where we introduced the dot chemical potentials μ_i, and τ are Pauli matrices that act in particle-hole space (c.f. Sec. 1.3.1). Eq. (1.44) is analogous to eq. (1.36) for a system of two sites. This system is commonly referred to as 'Poor man's Majorana' (PMM) [39].

The dependencies of the quantum dot coupling via the ABS, $\Gamma_{ECT}, \Gamma_{CAR}$, can be determined via Schrieffer-Wolff perturbation theory [85–87], which we discuss in Ch. 2. For

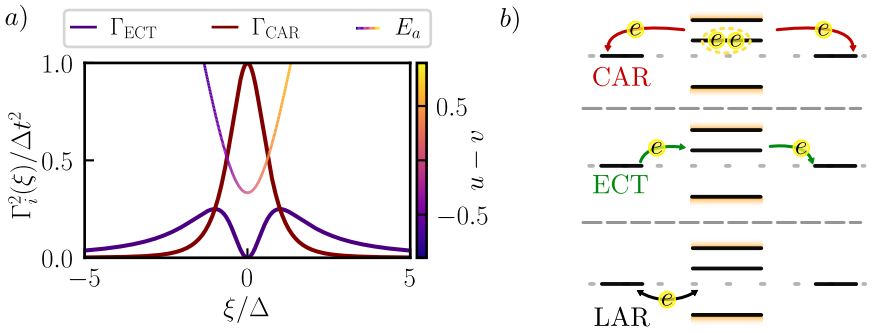

Figure 1.4: Amplitudes of CAR, ECT, and the Bogoliubov coefficients (c.f. eq. (1.39)) of the ABS depending on its chemical potential for $\theta = 0$ and processes in a minimal Kitaev chain. a) Tuning the chemical potential ξ allows to tune the electronic content of the ABS as indicated by the parabola (shifted by -0.75Δ). That tuning allows to change the magnitude of CAR and ECT processes leading to a crossing at $\xi = \Delta$. b) Effective processes that determine the dynamics of and between quantum dots. Crossed Andreev reflection (CAR) deposits electrons on each quantum dot by splitting a Cooper pair. Electron co-tunneling (ECT) describes a single electron tunneling through the ABS. Local Andreev reflection (LAR) corresponds to local pairing on a quantum dot induced by virtual processes through the ABS.

a single ABS in the proximitized dot given in the presence of spin-orbit interaction, these read [88]

$$\Gamma_{ECT} = -t^2 \frac{\xi \cos(\theta)}{E_A^2} \tag{1.45}$$

$$\Gamma_{CAR} = -t^2 \frac{\Delta \sin(\theta)}{E_A^2}, \tag{1.46}$$

where t is the hopping amplitude from either dot to the ABS, $E_A = \sqrt{\xi^2 + |\Delta|^2}$ is the energy of the ABS (cf. Sec. 1.3.3), and θ is the spin-orbit angle. Crucially, the magnitude of both can be controlled by tuning the chemical potential ξ. At $\xi = \Delta \tan(\theta)$, $|\Gamma_{CAR}| = |\Gamma_{ECT}|$ as required for a topological phase for eq. (1.29). Fixing ξ to this value and setting the dot chemical potentials to zero, $\mu_i = 0$, we can identify two MZMs with energy $E_1 = E_2 = 0$ acting in the degenerate manifold

$$\vec{\psi}_1 = (1,0,1,0)/\sqrt{2} \tag{1.47}$$

$$\vec{\psi}_2 = i(0,1,0,-1)/\sqrt{2}. \tag{1.48}$$

The difference between this system and the existing expectations on MZMs lies in their protection. Calculating the energy splitting in $\delta\mu_i$ at the point where $\Gamma = |\Gamma_{ECT}| = |\Gamma_{CAR}|$, a point we will re-encounter as 'sweet spot', one finds [39]

$$E_{1,2} = \pm \frac{\delta\mu_1 \delta\mu_2}{2\Gamma} \left[1 + \mathcal{O}\left((\delta\mu_i/\Gamma)^2\right)\right]. \tag{1.49}$$

While it is still true that the MZMs persist given a local perturbation $\delta\mu_i$ satisfying $|\delta\mu_i| < |\Gamma_i|$, the same cannot be said about a global shift $\delta\mu_i = \delta\mu$. The degeneracy breaks

quadratically in $\delta\mu$ when tuned away from the sweet spot. Additionally, deviations in either coupling $\Gamma_i = \Gamma + \delta\Gamma$ split the degeneracy linearly as $E_{1,2} = \pm\delta\Gamma$. Despite the apparent shortcomings of reduced protection of the MZMs, we were able to shift the problem from material disorder [35, 89] to detailed tuning of external parameters. Furthermore, given the prediction to converge to the topologically protected Kitaev chain when scaled up [38], there is reason to expect that potential noise on parameters only plays a secondary role. Recently, it was possible to realize minimal Kitaev chains in Refs. [40] and [41] and extended Kitaev chains in Ref. [90] and [91].

1.3.5. PREDICTING CURRENT IN THE TUNNELING LIMIT

Finally, we want to be able to make predictions of experimentally relevant observables when studying our systems.

A standard technique to do so is quantum transport in the tunneling limit [92–94]. We consider the Hamiltonian $H = H_S + \sum_i (H_{B_i} + H_{SB_i})$, where H_S is the closed system Hamiltonian, and each $H_{B_i} + H_{SB_i}$ corresponds to a bath and its coupling to H_S. We assume we have access to the spectrum of $H_S = \sum_i \varepsilon_i |i\rangle\langle i|$, where $|i\rangle$ is the i-th eigenstate belonging to the eigenvalue ε_i. In this basis, we write the system-bath coupling as

$$H_{SB_i} = g_i \left(\langle j|c_i^\dagger|j'\rangle b_i + b_i^\dagger \langle j|c_i|j'\rangle \right) \tag{1.50}$$

$$= g_i \left(T^+_{i;j,j'} b_i + b_i^\dagger T^-_{i;j,j'} \right) \tag{1.51}$$

where g_i is the coupling strength to the i-th bath, and c_i, b_i are electronic operators on system and bath respectively. Via Fermi's golden rule we can determine the transition rates as

$$\Gamma^{(-)}_{i;j,j'} = \frac{2\pi}{\hbar} \nu_i |g_i|^2 |T^-_{i,j,j'}|^2 [1 - n_F(\epsilon_{j'} - \epsilon_j - \mu_i)] \tag{1.52}$$

$$\Gamma^{(+)}_{i;j,j'} = \frac{2\pi}{\hbar} \nu_i |g_i|^2 |T^+_{i,j,j'}|^2 n_F(\epsilon_j - \epsilon_{j'} - \mu_i) \tag{1.53}$$

where n_F is the Fermi-Dirac distribution and ν_i is the density of states of lead i which we assume to be constant. We find the master equation governing the occupation probabilities of each state, p_j, as

$$\frac{dp_j}{dt} = \sum_i \sum_{j'} \left[\Gamma^{(+)}_{i;j,j'} + \Gamma^{(-)}_{i;j,j'} \right] p_{j'} - \sum_i \sum_j \left[\Gamma^{(+)}_{i;j',j} + \Gamma^{(-)}_{i;j',j} \right] p_j, \tag{1.54}$$

where the first (second) term corresponds to inflow (outflow) into (from) level j due to the transitions introduced by a given H_{SB_i} respectively. The probabilities in eq. (1.54) are additionally normalized to satisfy $\sum_i p_i = 1$. With the occupation probabilities we can then obtain the current induced by lead i via

$$I_i = -e \sum_{j,j'} \left[\Gamma^{(+)}_{i;j',j} - \Gamma^{(-)}_{i;j',j} \right] p_j. \tag{1.55}$$

We note that this approach is valid only in the limit $g_i \ll k_b T$ as it neglects higher-order processes. Throughout the remainder of this work we will repeatedly make use of transport as signature of zero modes. In particular we make use of an implementation that was collected in Ref. [94].

1.4. THIS THESIS

In this thesis, we explore various designs for systems that can implement MZMs and other non-Abelian modes. We furthermore discuss a proposal to demonstrate their non-Abelian nature, and a tool useful for the design of the involved systems.

We begin in Ch. 2 with a discussion of a computational tool that automates the construction of near-degenerate perturbation theories. This method, more commonly referred to as Schrieffer-Wolff perturbation theory [86, 95], is a standard tool in the study of low-energy subspaces. In experimental studies usually only a few low-energy degrees of freedom of the system are relevant. These are captured by an effective Hamiltonian. To design such effective Hamiltonians one usually begins with large Hilbert spaces. When the low-energy spectrum is separated by an energy gap from the remainder of the spectrum we can apply perturbation theory. For the case of separating the low energy subspace from the rest of the Hilbert space, one applies Schrieffer-Wolff perturbation theory. While tedious and prone to human error by hand, the involved calculations are mathematically uniform. This makes it possible to automate them, the task Pymablock, the developed tool, facilitates.

In Sec. 1.3.4 we discussed how to implement the interactions of a Kitaev chain in chains of quantum dots. Initial designs [40, 41, 82] use one quantum dot specifically to mediate these interactions. In Ch. 3, we use the developed methods to design a system that implements MZMs in only two quantum dots, avoiding the need for a third dot to facilitate the required couplings. Instead of using a auxiliary dot with an ABS to mediate the couplings, we implement them via an excited ABS instead. We discuss the sweet spot conditions for emergent MZMs, their behavior with respect to parameter changes, and challenges in scaling the system.

In Ch. 4 we return our focus to the systems presented in [40, 41]. It has been shown [41] that these systems appear to feature signatures indicative of emergent MZMs also in the absence of strong spin splitting. In this time-reversal invariant regime, we find that the demonstrated signatures are explained well by strong on-site interactions on the quantum dots. We find that at tunings where time-reversal and an emergent Z_3 parity symmetry coexist, the spectrum becomes strongly degenerate. This property allows for descriptions of the zero modes in terms of both Majorana Kramers pairs and $\mathbb{Z}_3$-parafermions.

Finally, in Ch. 5 we discuss operations on the studied zero modes. The zero modes studied in preceding chapters 3 and 4 and related literature [40–42, 90, 91] behave consistently with descriptions through MZMs. To conclusively demonstrate this, one needs to probe the non-Abelian exchange statistics directly. This is possible by either probing their fusion rules [96] or by braiding (cf. 1.2.1). This chapter discusses a proposal for the latter. By fine-tuning parameters, it is possible to probe the exchange statistics in a quasi one-dimensional system consisting of two minimal Kitaev chains coupled via an auxiliary dot. The exchange realized by the protocol is measurable by performing parity measurements [97–99] on the minimal chains.

REFERENCES

[1] Monroe, C. et al. “A “Schrödinger Cat” Superposition State of an Atom”. In: *Science* 272.5265 (1996). DOI: 10.1126/science.272.5265.1131.

[2] Hagley, E. et al. “Generation of Einstein-Podolsky-Rosen Pairs of Atoms”. In: *Phys. Rev. Lett.* 79.1 (1997). DOI: 10.1103/PhysRevLett.79.1.

[3] Monroe, C. “Demonstration of a Fundamental Quantum Logic Gate”. In: *Phys. Rev. Lett.* 75.25 (1995). DOI: 10.1103/PhysRevLett.75.4714.

[4] Rauschenbeutel, A. “Coherent Operation of a Tunable Quantum Phase Gate in Cavity QED”. In: *Phys. Rev. Lett.* 83.24 (1999). DOI: 10.1103/PhysRevLett.83.5166.

[5] MacFarlane, A. G. J., Dowling, J. P., and Milburn, G. J. “Quantum technology: the second quantum revolution”. In: *Philosophical Transactions of the Royal Society of London. Series A: Mathematical, Physical and Engineering Sciences* 361.1809 (2003). DOI: 10.1098/rsta.2003.1227.

[6] Nielsen, M. A. and Chuang, I. L. *Quantum Computation and Quantum Information: 10th Anniversary Edition*. en. Cambridge University Press, 2010. ISBN: 978-1-139-49548-6.

[7] Bravyi, S., Gosset, D., and König, R. “Quantum advantage with shallow circuits”. In: *Science* 362.6412 (2018). DOI: 10.1126/science.aar3106.

[8] Daley, A. J. et al. “Practical quantum advantage in quantum simulation”. en. In: *Nature* 607.7920 (2022). DOI: 10.1038/s41586-022-04940-6.

[9] Abbas, A. et al. “Challenges and opportunities in quantum optimization”. en. In: *Nat Rev Phys* 6.12 (2024). DOI: 10.1038/s42254-024-00770-9.

[10] Ajagekar, A., Humble, T., and You, F. “Quantum computing based hybrid solution strategies for large-scale discrete-continuous optimization problems”. In: *Computers & Chemical Engineering* 132 (2020). DOI: 10.1016/j.compchemeng.2019.106630.

[11] Google AI Quantum and Collaborators et al. “Hartree-Fock on a superconducting qubit quantum computer”. In: *Science* 369.6507 (2020). DOI: 10.1126/science.abb9811.

[12] Cao, Y. et al. “Quantum Chemistry in the Age of Quantum Computing”. In: *Chem. Rev.* 119.19 (2019). DOI: 10.1021/acs.chemrev.8b00803.

[13] McArdle, S. “Quantum computational chemistry”. In: *Rev. Mod. Phys.* 92.1 (2020). DOI: 10.1103/RevModPhys.92.015003.

[14] Kitaev, A. “Fault-tolerant quantum computation by anyons”. In: *Annals of Physics* 303.1 (2003). DOI: https://doi.org/10.1016/S0003-4916(02)00018-0.

[15] Bruzewicz, C. D. et al. “Trapped-ion quantum computing: Progress and challenges”. In: *Appl. Phys. Rev.* 6.2 (2019). DOI: 10.1063/1.5088164.

[16] Cirac, J. I. “Quantum Computations with Cold Trapped Ions”. In: *Phys. Rev. Lett.* 74.20 (1995). DOI: 10.1103/PhysRevLett.74.4091.

[17] Brown, K. R. et al. “Materials challenges for trapped-ion quantum computers”. en. In: *Nat Rev Mater* 6.10 (2021). DOI: 10.1038/s41578-021-00292-1.

[18] Loss, D. and DiVincenzo, D. P. “Quantum computation with quantum dots”. In: *Phys. Rev. A* 57.1 (1998). DOI: 10.1103/PhysRevA.57.120.

[19] Scappucci, G. et al. “The germanium quantum information route”. en. In: *Nat Rev Mater* 6.10 (2021). DOI: 10.1038/s41578-020-00262-z.

[20] Chatterjee, A. et al. “Semiconductor qubits in practice”. en. In: *Nat Rev Phys* 3.3 (2021). DOI: 10.1038/s42254-021-00283-9.

[21] Peruzzo, A. et al. “A variational eigenvalue solver on a photonic quantum processor”. en. In: *Nat Commun* 5.1 (2014). DOI: 10.1038/ncomms5213.

[22] Alexander, K. et al. “A manufacturable platform for photonic quantum computing”. en. In: *Nature* 641.8064 (2025). DOI: 10.1038/s41586-025-08820-7.

[23] Bao, J. et al. “Very-large-scale integrated quantum graph photonics”. en. In: *Nat. Photon.* 17.7 (2023). DOI: 10.1038/s41566-023-01187-z.

[24] Koch, J. et al. “Charge-insensitive qubit design derived from the Cooper pair box”. In: *Phys. Rev. A* 76.4 (2007). DOI: 10.1103/PhysRevA.76.042319.

[25] Schreier, J. A. et al. “Suppressing charge noise decoherence in superconducting charge qubits”. In: *Phys. Rev. B* 77.18 (2008). DOI: 10.1103/PhysRevB.77.180502.

[26] Manucharyan, V. E. et al. “Fluxonium: Single Cooper-Pair Circuit Free of Charge Offsets”. In: *Science* 326.5949 (2009). DOI: 10.1126/science.1175552.

[27] Nayak, C. et al. “Non-Abelian anyons and topological quantum computation”. en. In: *Rev. Mod. Phys.* 80.3 (2008). DOI: 10.1103/RevModPhys.80.1083.

[28] Leijnse, M. and Flensberg, K. “Introduction to topological superconductivity and Majorana fermions”. en. In: *Semicond. Sci. Technol.* 27.12 (2012). DOI: 10.1088/0268-1242/27/12/124003.

[29] Sarma, S. D., Freedman, M., and Nayak, C. “Majorana zero modes and topological quantum computation”. In: *Npj Quantum Information* 1 (2015).

[30] Wilczek, F. *Fractional Statistics and Anyon Superconductivity*. en. World Scientific, 1990. ISBN: 978-981-02-0049-7.

[31] Lutchyn, R. M. “Majorana Fermions and a Topological Phase Transition in Semiconductor-Superconductor Heterostructures”. In: *Phys. Rev. Lett.* 105.7 (2010). DOI: 10.1103/PhysRevLett.105.077001.

[32] Sau, J. D. “Generic New Platform for Topological Quantum Computation Using Semiconductor Heterostructures”. In: *Phys. Rev. Lett.* 104.4 (2010). DOI: 10.1103/PhysRevLett.104.040502.

[33] Oreg, Y. “Helical Liquids and Majorana Bound States in Quantum Wires”. In: *Phys. Rev. Lett.* 105.17 (2010). DOI: 10.1103/PhysRevLett.105.177002.

[34] Kouwenhoven, L. “Perspective on Majorana bound-states in hybrid superconductor-semiconductor nanowires”. In: *Mod. Phys. Lett. B* 39.03 (2025). DOI: 10.1142/S0217984925400020.

[35] Aghaee, M. et al. “InAs-Al hybrid devices passing the topological gap protocol”. en. In: *Phys. Rev. B* 107.24 (2023). DOI: 10.1103/PhysRevB.107.245423.

[36] Das Sarma, S. "Disorder-induced zero-bias peaks in Majorana nanowires". In: *Phys. Rev. B* 103.19 (2021). DOI: 10.1103/PhysRevB.103.195158.

[37] Beenakker, C. W. J. "Search for Majorana Fermions in Superconductors". en. In: *Annual Review of Condensed Matter Physics* 4.Volume 4, 2013 (2013). DOI: 10.1146/annurev-conmatphys-030212-184337.

[38] Sau, J. D. and Sarma, S. D. "Realizing a robust practical Majorana chain in a quantum-dot-superconductor linear array". en. In: *Nat Commun* 3.1 (2012). DOI: 10.1038/ncomms1966.

[39] Leijnse, M. "Parity qubits and poor man's Majorana bound states in double quantum dots". In: *Phys. Rev. B* 86.13 (2012). DOI: 10.1103/PhysRevB.86.134528.

[40] Dvir, T. et al. "Realization of a minimal Kitaev chain in coupled quantum dots". en. In: *Nature* 614.7948 (2023). DOI: 10.1038/s41586-022-05585-1.

[41] ten Haaf, S. L. D. et al. "A two-site Kitaev chain in a two-dimensional electron gas". en. In: *Nature* 630.8016 (2024). DOI: 10.1038/s41586-024-07434-9.

[42] Zatelli, F. et al. "Robust poor man's Majorana zero modes using Yu-Shiba-Rusinov states". en. In: *Nat Commun* 15.1 (2024). DOI: 10.1038/s41467-024-52066-2.

[43] Petersson, K. D. "Quantum Coherence in a One-Electron Semiconductor Charge Qubit". In: *Phys. Rev. Lett.* 105.24 (2010). DOI: 10.1103/PhysRevLett.105.246804.

[44] Alase, A. et al. *Decoherence of Majorana qubits by 1/f noise*. 2025. DOI: 10.48550/arXiv.2506.22394.

[45] Leinaas, J. M. and Myrheim, J. "On the theory of identical particles". en. In: *Nuovo Cim B* 37.1 (1977). DOI: 10.1007/BF02727953.

[46] Majorana, E. "Teoria simmetrica dell'elettrone e del positrone". it. In: *Nuovo Cim* 14.4 (1937). DOI: 10.1007/BF02961314.

[47] Klinovaja, J. "Parafermions in an Interacting Nanowire Bundle". In: *Phys. Rev. Lett.* 112.24 (2014). DOI: 10.1103/PhysRevLett.112.246403.

[48] Fendley, P. "Parafermionic edge zero modes in Zn-invariant spin chains". en. In: *J. Stat. Mech.* 2012.11 (2012). DOI: 10.1088/1742-5468/2012/11/P11020.

[49] Fendley, P. "Free parafermions". en. In: *J. Phys. A: Math. Theor.* 47.7 (2014). DOI: 10.1088/1751-8113/47/7/075001.

[50] Mong, R. S. K. et al. "Parafermionic conformal field theory on the lattice". en. In: *J. Phys. A: Math. Theor.* 47.45 (2014). DOI: 10.1088/1751-8113/47/45/452001.

[51] Zamolodchikov, A. B. and Fateev, V. A. "Nonlocal (parafermion) currents in two-dimensional conformal quantum field theory and self-dual critical points in Z/sub N/-symmetric statistical systems". English. In: *Sov. Phys. - JETP (Engl. Transl.); (United States)* 62:2 (1985).

[52] Jermyn, A. S. "Stability of zero modes in parafermion chains". In: *Phys. Rev. B* 90.16 (2014). DOI: 10.1103/PhysRevB.90.165106.

[53] Bravyi, S. "Universal quantum computation with ideal Clifford gates and noisy ancillas". In: *Phys. Rev. A* 71.2 (2005). DOI: 10.1103/PhysRevA.71.022316.

[54] Freedman, M. et al. "Topological quantum computation". en. In: *Bull. Amer. Math. Soc.* 40.1 (2003). DOI: 10.1090/S0273-0979-02-00964-3.

[55] Ahlbrecht, A. "Implementation of Clifford gates in the Ising-anyon topological quantum computer". In: *Phys. Rev. A* 79.3 (2009). DOI: 10.1103/PhysRevA.79.032311.

[56] Gottesman, D. *Stabilizer Codes and Quantum Error Correction*. 1997. DOI: 10.48550/arXiv.quant-ph/9705052.

[57] Karzig, T. "Robust Majorana magic gates via measurements". In: *Phys. Rev. B* 99.14 (2019). DOI: 10.1103/PhysRevB.99.144521.

[58] Hassler, F., Akhmerov, A. R., and Beenakker, C. W. J. "The top-transmon: a hybrid superconducting qubit for parity-protected quantum computation". en. In: *New J. Phys.* 13.9 (2011). DOI: 10.1088/1367-2630/13/9/095004.

[59] Hoffman, S. "Universal quantum computation with hybrid spin-Majorana qubits". In: *Phys. Rev. B* 94.4 (2016). DOI: 10.1103/PhysRevB.94.045316.

[60] Plugge, S. et al. "Majorana box qubits". en. In: *New J. Phys.* 19.1 (2017). DOI: 10.1088/1367-2630/aa54e1.

[61] Georgiev, L. S. "Topologically protected gates for quantum computation with non-Abelian anyons in the Pfaffian quantum Hall state". In: *Phys. Rev. B* 74.23 (2006). DOI: 10.1103/PhysRevB.74.235112.

[62] Karzig, T. et al. "Scalable designs for quasiparticle-poisoning-protected topological quantum computation with Majorana zero modes". In: *Phys. Rev. B* 95 (23 2017). DOI: 10.1103/PhysRevB.95.235305.

[63] Hutter, A. "Quantum computing with parafermions". In: *Phys. Rev. B* 93.12 (2016). DOI: 10.1103/PhysRevB.93.125105.

[64] Kurlov, D. V. "Quantum computation with hybrid parafermion-spin qubits". In: *Phys. Rev. Res.* 7.3 (2025). DOI: 10.1103/7cd9-c7yc.

[65] Kitaev, A. Y. "Unpaired Majorana fermions in quantum wires". en. In: *Phys.-Usp.* 44.10S (2001). DOI: 10.1070/1063-7869/44/10S/S29.

[66] Altland, A. "Nonstandard symmetry classes in mesoscopic normal-superconducting hybrid structures". In: *Phys. Rev. B* 55.2 (1997). DOI: 10.1103/PhysRevB.55.1142.

[67] Kouwenhoven, L. P., Austing, D. G., and Tarucha, S. "Few-electron quantum dots". en. In: *Rep. Prog. Phys.* 64.6 (2001). DOI: 10.1088/0034-4885/64/6/201.

[68] Kouwenhoven, L. and Marcus, C. "Quantum dots". en. In: *Phys. World* 11.6 (1998). DOI: 10.1088/2058-7058/11/6/26.

[69] Froning, F. N. M. et al. "Strong spin-orbit interaction and g-factor renormalization of hole spins in Ge/Si nanowire quantum dots". In: *Phys. Rev. Res.* 3.1 (2021). DOI: 10.1103/PhysRevResearch.3.013081.

[70] Bardeen, J., Cooper, L. N., and Schrieffer, J. R. "Microscopic Theory of Superconductivity". In: *Phys. Rev.* 106.1 (1957). DOI: 10.1103/PhysRev.106.162.

[71] Tinkham, M. *Introduction to Superconductivity*. en. Courier Corporation, 2004. ISBN: 978-0-486-13472-7.

[72] Bardeen, J. "Electron-Phonon Interaction in Metals". In: *Phys. Rev.* 99.4 (1955). DOI: 10.1103/PhysRev.99.1140.

[73] Cooper, L. N. "Bound Electron Pairs in a Degenerate Fermi Gas". In: *Phys. Rev.* 104.4 (1956). DOI: 10.1103/PhysRev.104.1189.

[74] Bogoljubov, N. N. "On a new method in the theory of superconductivity". en. In: *Nuovo Cim* 7.6 (1958). DOI: 10.1007/BF02745585.

[75] Valatin, J. G. "Comments on the theory of superconductivity". en. In: *Nuovo Cim* 7.6 (1958). DOI: 10.1007/BF02745589.

[76] Meissner, H. "Superconductivity of Contacts with Interposed Barriers". In: *Phys. Rev.* 117.3 (1960). DOI: 10.1103/PhysRev.117.672.

[77] Holm, R. and Meissner, W. "Messungen mit Hilfe von flüssigem Helium. XIII". de. In: *Z. Physik* 74.11 (1932). DOI: 10.1007/BF01340420.

[78] Stanescu, T. D. and Tewari, S. *Fermion parity and quantum capacitance oscillation with partially separated Majorana and quasi-Majorana modes*. 2025. DOI: 10.48550/arXiv.2505.23741.

[79] Andreev, A. et al. "Thermal conductivity of the intermediate state of superconductors II". In: *Sov. Phys. JETP* 20 (1965).

[80] Recher, P. "Andreev tunneling, Coulomb blockade, and resonant transport of nonlocal spin-entangled electrons". In: *Phys. Rev. B* 63.16 (2001). DOI: 10.1103/PhysRevB.63.165314.

[81] Recher, P. "Superconductor coupled to two Luttinger liquids as an entangler for electron spins". In: *Phys. Rev. B* 65.16 (2002). DOI: 10.1103/PhysRevB.65.165327.

[82] Liu, C.-X. "Tunable Superconducting Coupling of Quantum Dots via Andreev Bound States in Semiconductor-Superconductor Nanowires". In: *Phys. Rev. Lett.* 129.26 (2022). DOI: 10.1103/PhysRevLett.129.267701.

[83] Roland, W. "Spin-orbit coupling effects in two-dimensional electron and hole systems". In: *Springer Tracts in Modern Physiscs: Springer, Berlin, Heidelberg* 191 (2003). DOI: 10.1007/b13586.

[84] Kloeffel, C. "Strong spin-orbit interaction and helical hole states in Ge/Si nanowires". In: *Phys. Rev. B* 84.19 (2011). DOI: 10.1103/PhysRevB.84.195314.

[85] Schrieffer, J. R. "Relation between the Anderson and Kondo Hamiltonians". In: *Phys. Rev.* 149.2 (1966). DOI: 10.1103/PhysRev.149.491.

[86] Bravyi, S., DiVincenzo, D. P., and Loss, D. "Schrieffer–Wolff transformation for quantum many-body systems". In: *Annals of Physics* 326.10 (2011). DOI: 10.1016/j.aop.2011.06.004.

[87] Araya Day, I. et al. "Pymablock: An algorithm and a package for quasi-degenerate perturbation theory". In: *SciPost Phys. Codebases* (2025). DOI: 10.21468/SciPostPhysCodeb.50.

[88] Torres Luna, J. D. et al. *Pareto-optimality of Majoranas in hybrid platforms*. 2025. DOI: 10.48550/arXiv.2510.07406.

[89] Aasen, D. et al. *Roadmap to fault tolerant quantum computation using topological qubit arrays*. 2025. DOI: 10.48550/arXiv.2502.12252.

[90] ten Haaf, S. L. D. et al. "Observation of edge and bulk states in a three-site Kitaev chain". en. In: *Nature* 641.8064 (2025). DOI: 10.1038/s41586-025-08892-5.

[91] Bordin, A. et al. "Enhanced Majorana stability in a three-site Kitaev chain". en. In: *Nat. Nanotechnol.* 20.6 (2025). DOI: 10.1038/s41565-025-01894-4.

[92] Tsintzis, A., Souto, R. S., and Leijnse, M. "Creating and Detecting Poor Man's Majorana Bound States in Interacting Quantum Dots". In: *Phys. Rev. B* 106.20 (2022). DOI: 10.1103/PhysRevB.106.L201404.

[93] Kiršanskas, G. et al. "QmeQ 1.0: An open-source Python package for calculations of transport through quantum dot devices". In: *Computer Physics Communications* 221 (2017). DOI: 10.1016/j.cpc.2017.07.024.

[94] *Quantum Tinkerer / qrate · GitLab*. en. 2025.

[95] Schrieffer, J. R. and Wolff, P. A. "Relation between the Anderson and Kondo Hamiltonians". In: *Phys. Rev.* 149 (2 1966). DOI: 10.1103/PhysRev.149.491.

[96] Liu, C.-X. "Fusion protocol for Majorana modes in coupled quantum dots". In: *Phys. Rev. B* 108.8 (2023). DOI: 10.1103/PhysRevB.108.085437.

[97] Loo, N. v. et al. *Single-shot parity readout of a minimal Kitaev chain*. 2025. DOI: 10.48550/arXiv.2507.01606.

[98] Aghaee, M. et al. "Interferometric single-shot parity measurement in InAs–Al hybrid devices". en. In: *Nature* 638.8051 (2025). DOI: 10.1038/s41586-024-08445-2.

[99] Aghaee, M. et al. *Distinct Lifetimes for X and Z Loop Measurements in a Majorana Tetron Device*. 2025. DOI: 10.48550/arXiv.2507.08795.

2

PYMABLOCK: AN ALGORITHM AND A PACKAGE FOR QUASI-DEGENERATE PERTURBATION THEORY

Isidora Araya Day, **Sebastian Miles**, Hugo K. Kerstens, Daniel Varjas, and Anton R. Akhmerov

A common technique in the study of complex quantum-mechanical systems is to reduce the number of degrees of freedom in the Hamiltonian by using quasi-degenerate perturbation theory. While the Schrieffer–Wolff transformation achieves this and constructs an effective Hamiltonian, its scaling is suboptimal, it is limited to two subspaces, and implementing it efficiently is both challenging and error-prone. We introduce an algorithm for constructing an equivalent effective Hamiltonian as well as a Python package, Pymablock, that implements it. Our algorithm combines an optimal asymptotic scaling and the ability to handle any number of subspaces with a range of other improvements. The package supports numerical and analytical calculations of any order and it is designed to be interoperable with any other packages for specifying the Hamiltonian. We demonstrate how the package handles constructing a k.p model, analyses a superconducting qubit, and computes the low-energy spectrum of a large tight-binding model. We also compare its performance with reference calculations and demonstrate its efficiency.

Own contribution to work: Co-developed the algorithm and implementation of the package, consulted on writing the paper.

This chapter has been published as SciPost Phys. Codebases 50 (2025).

2.1. INTRODUCTION

Effective models enable the study of complex quantum systems by reducing the dimensionality of the Hilbert space. Their construction separates the low and high-energy subspaces by block-diagonalizing a perturbed Hamiltonian

$$\mathcal{H} = \begin{pmatrix} H_0^{AA} & 0 \\ 0 & H_0^{BB} \end{pmatrix} + \mathcal{H}', \tag{2.1}$$

where H_0^{AA} and H_0^{BB} are separated by an energy gap, and $\mathcal{H}'$ is a series in a perturbative parameter. This procedure requires finding a series of the basis transformation $\mathcal{U}$ that is unitary and that also cancels the off-diagonal block of the transformed Hamiltonian order by order, as shown in Fig. 2.1. The low-energy effective Hamiltonian $\tilde{\mathcal{H}}^{AA}$ is then a series in the perturbative parameter, whose eigenvalues and eigenvectors are approximate solutions of the complete Hamiltonian. As a consequence, the effective model is sufficient to describe the low-energy properties of the original system while also being simpler and easier to handle.

A common approach to constructing an effective Hamiltonian is the Schrieffer–Wolff transformation [1, 2], also known as Löwdin partitioning [3], or quasi-degenerate perturbation theory. This method parameterizes the unitary transformation $\mathcal{U} = e^{-\mathcal{S}}$ and finds the series $\mathcal{S}$ that decouples the A and B subspaces of $\tilde{\mathcal{H}} = e^{\mathcal{S}}\mathcal{H}e^{-\mathcal{S}}$. This idea enabled advances in multiple fields of quantum physics. As an example, all the k.p models are a result of treating crystalline momentum as a perturbation that only weakly mixes atomic orbitals separated in energy [4–7]. More broadly, this method serves as a go-to tool in the study of superconducting circuits and quantum dots, where couplings between circuit elements and drives are treated as perturbations to reproduce the dynamics of the system [8, 9]. Applied to time-dependent Hamiltonians, the Schrieffer–Wolff transformation is an essential tool for the design of quantum gates [10, 11].

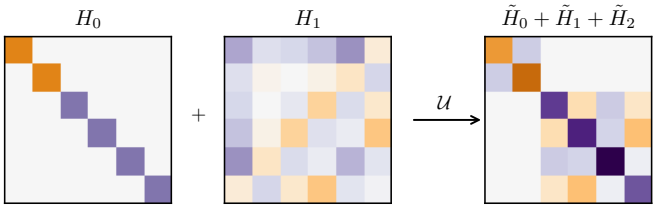

Figure 2.1: Block-diagonalization of a Hamiltonian with a first order perturbation.

Constructing effective Hamiltonians is, however, both algorithmically complex and computationally expensive. This is a consequence of the recursive equations that define the unitary transformation, which require an exponentially growing number of matrix products in each order. In particular, already a 4-th order perturbative expansion that is necessary for many applications may require hundreds of terms. While the computational complexity is only a nuisance when analysing model systems, it becomes a bottleneck whenever the Hilbert space is high-dimensional. Several other approaches improve the performance of the Schrieffer–Wolff algorithm by either using different parametrizations of the unitary transformation [3, 12–15], adjusting the problem setting to density

matrix perturbation theory [16, 17], or a finding a similarity transform instead of a unitary [18]. An alternative formulation of the perturbative diagonalization uses Wegner's flow equation [19, 20] to construct a continuous unitary transformation (CUT) that depends on a fictitious flow parameter, which at infinity eliminates the undesired terms from the Hamiltonian [21, 22]. CUT is common in the study of many-body systems [23], and it relies on solving a set of differential equations to obtain the effective Hamiltonian. A more recent line of research even applies the ideas of Schrieffer–Wolff transformation to quantum algorithms for the study of many-body systems [24, 25]. Despite these advances, neither of the approaches combines an optimal scaling with the ability to construct effective Hamiltonians.

Another limitation of the Schrieffer–Wolff transformation is that it only decouples two subspaces at a time. While a straightforward generalization of the Schrieffer–Wolff transformation to multiple subspaces is to decouple one block at a time, this approach is suboptimal and depends on the order in which the blocks are decoupled. The literature on multi-block diagonalization is scarce and considers two approaches: the least action or the block-diagonality of the generator [26]. The former constructs a unitary transformation that is as close as possible to the identity, and the latter constructs a block off-diagonal unitary similar to the Schrieffer–Wolff generator. These approaches are useful to design gates for superconducting qubits [27] and to characterize nonlocal interactions in multi-qubit systems [28], both of which require the decoupling of qubit subspaces from different sets of higher energy states. Reference [26], however, showed that the two generalizations of the Schrieffer–Wolff transformation yield different effective Hamiltonians when applied to more than two subspaces. While the perturbative CUT method naturally decouples multiple subspaces [29], in general solving the differential equations inherent to the method may become a computational bottleneck. To our knowledge, there is no general algorithm that constructs effective Hamiltonians for multiple subspaces directly from the least action principle, and how to do so is an open question.

We introduce an algorithm to construct effective models with optimal scaling, thus making it possible to find high order corrections for systems with millions of degrees of freedom. This algorithm exploits the efficiency of recursive evaluations of series satisfying polynomial constraints and obtains the same effective Hamiltonian as the Schrieffer–Wolff transformation in the case of two subspaces. Our algorithm, however, deals with any number of subspaces, providing a generalization of the Schrieffer–Wolff transformation for multi-block diagonalization and selective decoupling between any two states. We make the algorithm available via the open source package Pymablock [1] (PYthon MAtrix BLOCK-diagonalization), a versatile tool for the study of numerical and symbolic models.

2.2. CONSTRUCTING AN EFFECTIVE MODEL

We illustrate the construction of effective models by considering several representative examples. The simplest application of effective models is the reduction of finite symbolic Hamiltonians, which appear in the derivation of low-energy dispersions of materials.

[1] The documentation and tutorials are available in `https://pymablock.readthedocs.io/`

Starting from a tight-binding model, one performs Taylor expansions of the Hamiltonian near a k-point, and then eliminates several high-energy states [4, 6]. In the study of superconducting qubits, for example, the Hamiltonian contains several bosonic operators, so its Hilbert space is infinite-dimensional, and the coupling between bosons makes the Hamiltonian impossible to diagonalize. The effective qubit model describes the analytical dependence of qubit frequencies and couplings on the circuit parameters [8, 30–34]. This allows to design circuits that realize a desired qubit Hamiltonian, as well as ways to understand and predict qubit dynamics, for which computational tools are being actively developed [35–37]. Finally, mesoscopic quantum devices are described by a single particle tight-binding model with short range hoppings. This produces a numerical Hamiltonian that is both big and sparse, which allows to compute a few of its states but not the full spectrum [38]. Because only the low-energy states contribute to observable properties, deriving how they couple enables a more efficient simulation of the system's behavior.

Pymablock treats all the problems, including the ones above, using a unified approach that only requires three steps:

- Define a Hamiltonian
- Call `pymablock.block_diagonalize`
- Request the desired order of the effective Hamiltonian

The following code snippet shows how to use Pymablock to compute the fourth order correction to an effective Hamiltonian $\tilde{\mathcal{H}}$:

```
# Define perturbation theory
H_tilde, *_ = block_diagonalize([H_0, H_1],
↪  subspace_eigenvectors=[vecs_A, vecs_B])

# Request 4th order correction to the effective Hamiltonian
H_AA_4 = H_tilde[0, 0, 4]
```

The function `block_diagonalize` interprets the Hamiltonian $H_0 + H_1$ as a series with two terms, zeroth and first order and calls the block diagonalization routine. The subspaces to decouple are spanned by the eigenvectors `vecs_A` and `vecs_B` of H_0. This is the main function of Pymablock, and it is the only one that the user ever needs to call. Its first output is a multivariate series whose terms are different blocks and orders of the transformed Hamiltonian. Calling `block_diagonalize` only defines the computational problem, whereas querying the elements of `H_tilde` does the actual calculation of the desired order. This interface treats arbitrary formats of Hamiltonians and system descriptions on the same footing and supports both numerical and symbolic computations.

2.2.1. K.P MODEL OF BILAYER GRAPHENE

To illustrate how to use Pymablock with analytic models, we consider two layers of graphene stacked on top of each other, as shown in Fig. 2.2. Our goal is to find the low-energy model near the **K** point [6]. To do this, we first construct the tight-binding model Hamiltonian of bilayer graphene. The main features of the model are its 4-atom unit cell

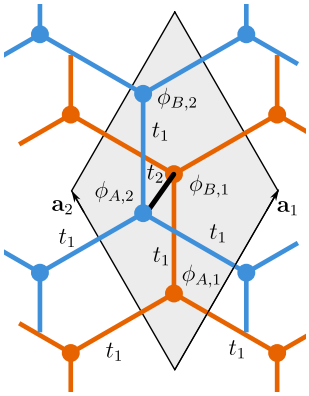

Figure 2.2: Crystal structure and hoppings of AB-stacked bilayer graphene.

spanned by vectors $\mathbf{a}_1 = (1/2, \sqrt{3}/2)$ and $\mathbf{a}_2 = (-1/2, \sqrt{3}/2)$, and with wave functions $\phi_{A,1}, \phi_{B,1}, \phi_{A,2}, \phi_{B,2}$, where A and B indices are the two sublattices, and $1, 2$ are the layers. The model has hoppings t_1 and t_2 within and between the layers, respectively, as shown in Fig. 2.2. We also include a layer-dependent onsite potential $\pm m$.

We define the Bloch Hamiltonian using the Sympy package for symbolic Python [39].

```
t_1, t_2, m = sympy.symbols("t_1 t_2 m", real=True)
alpha = sympy.symbols(r"\alpha")

H = Matrix([
    [m, t_1 * alpha, 0, 0],
    [t_1 * alpha.conjugate(), m, t_2, 0],
    [0, t_2, -m, t_1 * alpha],
    [0, 0, t_1 * alpha.conjugate(), -m]]
)
```

$$H = \begin{pmatrix} m & t_1\alpha & 0 & 0 \\ t_1\alpha^* & m & t_2 & 0 \\ 0 & t_2 & -m & t_1\alpha \\ 0 & 0 & t_1\alpha^* & -m \end{pmatrix}$$

where $\alpha(\mathbf{k}) = 1 + e^{i\mathbf{k}\cdot\mathbf{a}_1} + e^{\mathbf{k}\cdot\mathbf{a}_2}$, with k the wave vector. We consider $\mathbf{K} = (4\pi/3, 0)$ the reference point point in $\mathbf{k}$-space: $\mathbf{k} = (4\pi/3 + k_x, k_y)$ because $\alpha(\mathbf{K}) = 0$, making k_x and k_y small perturbations. Additionally, we consider $m \ll t_2$ a perturbative parameter.

To call `block_diagonalize`, we need to define the subspaces for the block diagonalization, so we compute the eigenvectors of the unperturbed Hamiltonian at the $\mathbf{K}$ point, $H(\alpha(\mathbf{K}) = m = 0)$. Then, we substitute $\alpha(\mathbf{k})$ into the Hamiltonian, and call the block diagonalization routine using that k_x, k_y, and m are perturbative parameters via the `symbols` argument.

```
vecs = H.subs({alpha: 0, m: 0}).diagonalize(normalize=True)[0]
```

```
H_tilde, U, U_adjoint = block_diagonalize(
    H.subs({alpha: alpha_k}),
    symbols=(k_x, k_y, m),
    subspace_eigenvectors=[vecs[:, :2], vecs[:, 2:]] # AA, BB
)
```

The order of the variables in the perturbative series will be that of `symbols`. For example, requesting the term $\propto k_x^i k_y^j m^l$ from the effective Hamiltonian is done by calling `H_tilde[0, 0, i, j, l]`, where the first two indices are the block indices (AA). The series of the unitary transformation U and $U^\dagger$ are also defined, and we may use them to transform other operators.

We collect corrections up to third order in momentum to compute the standard quadratic dispersion of bilayer graphene and trigonal warping. We query these terms from `H_tilde` and those proportional to mass to obtain the effective Hamiltonian (shown as produced by the code)[2]:

$$\tilde{H}_{\text{eff}} = \begin{bmatrix} m & \frac{3t_1^2}{4t_2}(-k_x^2 - 2ik_xk_y + k_y^2) \\ \frac{3t_1^2}{4t_2}(-k_x^2 + 2ik_xk_y + k_y^2) & -m \end{bmatrix} + \begin{bmatrix} \frac{3mt_1^2}{2t_2^2}(-k_x^2 - k_y^2) & \frac{\sqrt{3}t_1^2}{8t_2}(k_x^3 - 5ik_x^2k_y + 9k_xk_y^2 + 3ik_y^3) \\ \frac{\sqrt{3}t_1^2}{8t_2}(k_x^3 + 5ik_x^2k_y + 9k_xk_y^2 - 3ik_y^3) & \frac{3mt_1^2}{2t_2^2}(k_x^2 + k_y^2) \end{bmatrix}$$

The first term is the standard quadratic dispersion of gapped bilayer graphene. The second term contains trigonal warping and the coupling between the gap and momentum. All the terms take less than two seconds in a personal computer to compute.

2.2.2. DISPERSIVE SHIFT OF A TRANSMON QUBIT COUPLED TO A RESONATOR

The need for analytical effective Hamiltonians often arises in circuit quantum electrodynamics (cQED) problems, which we illustrate by studying a transmon qubit coupled to a resonator [8]. Specifically, we choose the standard problem of finding the frequency shift of the resonator due to its coupling to the qubit, a phenomenon used to measure the qubit's state [30]. The Hamiltonian of the system is given by

$$\mathcal{H} = -\omega_t(a_t^\dagger a_t - \frac{1}{2}) + \frac{\alpha}{2}a_t^\dagger a_t^\dagger a_t a_t + \omega_r(a_r^\dagger a_r + \frac{1}{2}) - g(a_t^\dagger - a_t)(a_r^\dagger - a_r), \tag{2.2}$$

where a_t and a_r are bosonic annihilation operators of the transmon and resonator, respectively, and ω_t and ω_r are their frequencies. The transmon has an anharmonicity α, so that its energy levels are not equally spaced. In presence of both the coupling g between the transmon and the resonator and the anharmonicity, this Hamiltonian admits no analytical solution. We therefore treat g as a perturbative parameter.

To deal with the infinite dimensional Hilbert space, we observe that the perturbation only changes the occupation numbers of the transmon and the resonator by ± 1. Therefore computing n-th order corrections to the n_0-th state allows to disregard states

[2] The full code is available at https://pymablock.readthedocs.io/en/latest/tutorial/bilayer_graphene.html.

with any occupation numbers larger than $n_0 + n/2$. We want to compute the second order correction to the levels with occupation numbers of either the transmon or the resonator being 0 and 1. We accordingly truncate the Hilbert space to the lowest 3 levels of the transmon and the resonator. The resulting Hamiltonian is a 9×9 matrix that we construct using Sympy [39].

Finally, to compute the energy corrections of the lowest levels, we call `block_diagonalize` for each state separately, replicating a regular perturbation theory calculation for single wavefunctions. To do this, we observe that H_0 is diagonal, and use `subspace_indices` to assign the elements of its eigenbasis to the 4 subspaces of interest and the rest. This corresponds to a multi-block diagonalization problem with 5 blocks. For example, to find the qubit-dependent frequency shift of the resonator, χ, we start by computing the second order correction to $|0_t 0_r\rangle$:

```
indices = [0, 1, 2, 3, 4, 4, 4, 4, 4] # 00 is the first state in the
 ↪  basis
H_tilde, *_ = block_diagonalize(H, subspace_indices=indices,
 ↪  symbols=[g])
H_tilde[0, 0, 2][0, 0] # 2nd order correction to 00
```

$$E_{00}^{(2)} = \frac{g^2}{-\omega_r + \omega_t}. \tag{2.3}$$

Repeating this process for the states $|1_t 0_r\rangle$, $|0_t 1_r\rangle$, and $|1_t 1_r\rangle$ requires requesting the terms `H_tilde[1, 1, 2][0, 0]`, `H_tilde[2, 2, 2][0, 0]`, and `H_tilde[3, 3, 2][0, 0]`, and yields the desired resonator frequency shift:

$$\begin{aligned}\chi &= (E_{11}^{(2)} - E_{10}^{(2)}) - (E_{01}^{(2)} - E_{00}^{(2)}) \\ &= -\frac{2g^2}{\alpha + \omega_r - \omega_t} + \frac{2g^2}{-\alpha + \omega_r + \omega_t} - \frac{2g^2}{\omega_r + \omega_t} + \frac{2g^2}{\omega_r - \omega_t} \\ &= -\frac{4\alpha g^2 \left(\alpha\omega_t - \omega_r^2 - \omega_t^2\right)}{(\omega_r - \omega_t)(\omega_r + \omega_t)(-\alpha + \omega_r + \omega_t)(\alpha + \omega_r - \omega_t)}.\end{aligned} \tag{2.4}$$

In this example, we have not used the rotating wave approximation, including the frequently omitted counter-rotating terms $\sim a_r a_t$ to illustrate the extensibility of Pymablock. Computing higher order corrections to the qubit frequency only requires increasing the size of the truncated Hilbert space and requesting `H_tilde[0, 0, n]` to any order n.

2.2.3. INDUCED GAP IN A DOUBLE QUANTUM DOT

Large systems pose an additional challenge due to the cubic scaling of linear algebra routines with matrix size. To overcome this, Pymablock is equipped with an implicit method, which utilizes the sparsity of the input and avoids the construction of the full transformed Hamiltonian. We illustrate the efficiency of this method by applying it to a system of two quantum dots coupled to a superconductor between them, shown in Fig. 2.3, and described by the Bogoliubov-de Gennes Hamiltonian:

$$H_{BdG} = \begin{cases} (\mathbf{k}^2/2m - \mu_{sc})\sigma_z + \Delta\sigma_x & \text{for } L/3 \le x \le 2L/3, \\ (\mathbf{k}^2/2m - \mu_n)\sigma_z & \text{otherwise,} \end{cases} \tag{2.5}$$

where the Pauli matrices σ_z and σ_x act in the electron-hole space, $\mathbf{k}$ is the 2D wave vector, m is the effective mass, and Δ the superconducting gap.

We use the Kwant package [40] to build the Hamiltonian of the system [3], which we define over a square lattice of $L \times W = 200 \times 40$ sites. On top of this, we consider two perturbations: the barrier strength between the quantum dots and the superconductor, t_b, and an asymmetry of the dots' potentials, $\delta\mu$.

The system is large: it is a sparse array of size 63042×63042, with 333680 non-zero elements, so even storing all the eigenvectors would take 60 GB of memory. The perturbations are also sparse, with 632, and 126084 non-zero elements for the barrier strength and the potential asymmetry, respectively. The sparsity structure of the Hamiltonian and the perturbations is shown in the left panel of Fig. 2.3, where we use a smaller system of $L \times W = 8 \times 2$ for visualization. Therefore, we use sparse diagonalization [41] and compute only four eigenvectors of the unperturbed Hamiltonian closest to zero energy, which are the Andreev states of the quantum dots.

```
vals, vecs = scipy.sparse.linalg.eigsh(h_0, k=4, sigma=0)
vecs, _ = scipy.linalg.qr(vecs, mode="economic")  # orthogonalize the
↪  vectors
```

We now call the block diagonalization routine and provide the computed eigenvectors.

```
H_tilde, *_ = block_diagonalize([h_0, barrier, dmu],
↪  subspace_eigenvectors=[vecs])
```

Because we only provide the low-energy subspace, Pymablock uses the implicit method. Calling `block_diagonalize` is now the most time-consuming step because it requires pre-computing several decompositions of the full Hamiltonian. It is, however, manageable and it only produces a constant overhead of less than three seconds.

To compute the spectrum, we collect the lowest three orders in each parameter in an appropriately sized tensor.

```
h_tilde = np.array(np.ma.filled(H_tilde[0, 0, :3, :3],
↪  fill_value).tolist())
```

This takes two more seconds to run, and we can now compute the low-energy spectrum after rescaling the perturbative corrections by the magnitude of each perturbation.

```
def effective_energies(h_tilde, barrier, dmu):
    barrier_powers = barrier ** np.arange(3).reshape(-1, 1, 1, 1)
    dmu_powers = dmu ** np.arange(3).reshape(1, -1, 1, 1)
    return scipy.linalg.eigvalsh(
        np.sum(h_tilde * barrier_powers * dmu_powers, axis=(0, 1))
    )
```

Finally, we plot the spectrum of the 2 Andreev states in Fig. 2.3. As expected, the crossing at $E = 0$ due to the dot asymmetry is lifted when the dots are coupled to the superconductor. In addition, we observe how the proximity gap of the dots increases with the coupling strength.

[3] The full code is available at https://pymablock.readthedocs.io/en/latest/tutorial/induced_gap.html.

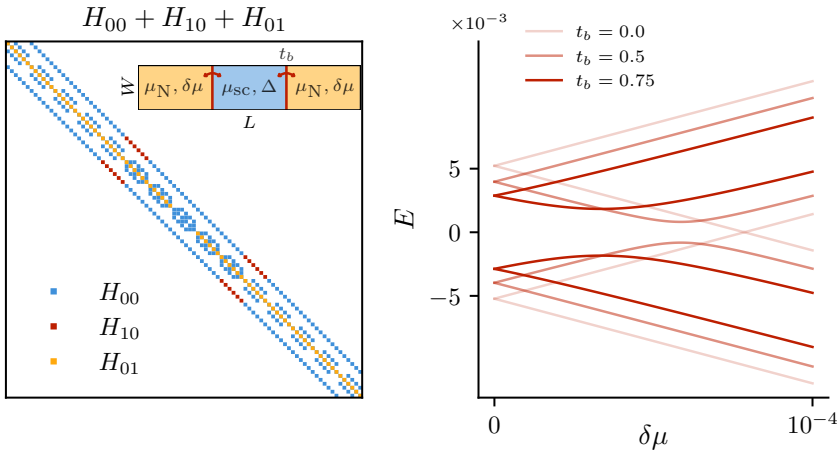

Figure 2.3: Hamiltonian (left) and Andreev levels (right) of two quantum dots coupled to a superconductor (inset). The barrier t_b between the dots and the superconductor, H_{10}, and the asymmetry $\delta\mu$ between the dots' potential, H_{01}, are perturbations.

Computing the spectrum of the system for 3 points in parameter space would require the same time as the total runtime of Pymablock in this example. This demonstrates the speed of the implicit method and the efficiency of Pymablock's algorithm.

2.2.4. SELECTIVE DIAGONALIZATION

Lastly, we demonstrate the generality of Pymablock's algorithm by applying it to decouple arbitrary states in a generic Hamiltonian. This is an alternative to separating a Hamiltonian into blocks, and it requires that the states to decouple are different in energy. To illustrate this, we consider a 16×16 Hamiltonian $\mathcal{H} = H_0 + H_1$ with H_0 a diagonal matrix and H_1 a random Hermitian perturbation. Our goal is to construct an effective Hamiltonian whose only matrix elements are those in a binary mask, which, without loss of generality, we choose to be a smiley face.

We apply the mask to the Hamiltonian by providing it as the `fully_diagonalize` argument to `block_diagonalize`[4].

```
H_tilde, *_ = block_diagonalize([H_0, H_1], fully_diagonalize={0:
↪ mask})
```

The argument `fully_diagonalize` is a dictionary where the keys label the blocks of the Hamiltonian, and the values are the masks that select the terms to keep in that block. We only used one block in this example: the entire Hamiltonian. Finally, the effective Hamiltonian only contains the terms in the mask, as shown in Fig. 2.4.

[4]The full code is available at https://pymablock.readthedocs.io/en/latest/tutorial/getting_started.html#selective-diagonalization.

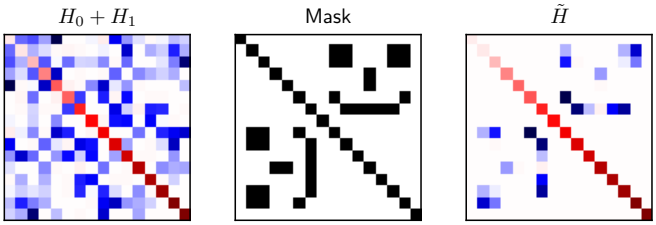

Figure 2.4: Selective diagonalization of a Hamiltonian with a random perturbation.

2.3. PERTURBATIVE BLOCK-DIAGONALIZATION ALGORITHM

2.3.1. PROBLEM STATEMENT

Pymablock finds a series of the unitary transformation $\mathcal{U}$ (we use calligraphic letters to denote series) that eliminates the off-diagonal components of the Hamiltonian

$$\mathcal{H} = H_0 + \mathcal{H}', \tag{2.6}$$

with $\mathcal{H}' = \mathcal{H}'_S + \mathcal{H}'_R$ containing an arbitrary number and orders of perturbations with block-diagonal and block-offdiagonal components, respectively. Here and later we use the subscript S to denote the selected part and R to denote remaining components of a series, with the goal of the perturbation theory to obtain a Hamiltonian with only the selected part. In other words, we aim to find a unitary transformation $\mathcal{U}$ that cancels the remaining part of the Hamiltonian. In different settings, selected and remaining parts may mean different things. In quasi-degenerate perturbation theory, the Hilbert space is subdivided into A and B subspaces, which makes H_0 a block-diagonal matrix

$$H_0 = \begin{pmatrix} {H_0}^{AA} & 0 \\ 0 & {H_0}^{BB} \end{pmatrix}, \tag{2.7}$$

and the goal of the perturbation theory is to eliminate the offdiagonal AB and BA blocks of $\mathcal{H}$. In this case the selected part is the block-diagonal part, and the remaining part is the block-offdiagonal part. Differently, in the context of Rayleigh-Schrödinger perturbation theory, H_0 is a diagonal matrix so that the selected part is the diagonal, and the remaining part of an operator are all its matrix elements that are not on the diagonal.

To consider the problem in the most general setting, we only require the selected and remaining parts of an operator to satisfy the following constraints:

1. The selected and remaining parts of an operator add to identity: $\mathcal{A} = \mathcal{A}_S + \mathcal{A}_R$.
2. Taking either part of an operator is idempotent: $(\mathcal{A}_S)_S = \mathcal{A}_S$.
3. Taking either part commutes with Hermitian conjugation: $(\mathcal{A}_S)^\dagger = (\mathcal{A}^\dagger)_S$.
4. The remaining part of any operator has no matrix elements within eigensubspaces of H_0. This is required to ensure that the perturbation theory is well-defined.

The separation of an operator into selected and remaining parts is a generalization of taking block-diagonal and block-offdiagonal parts. In particular, the separation allows to choose any subset of the offdiagonal matrix elements as remaining, as long as none of the matrix elements belong to an eigensubspace of H_0. That none of the matrix elements belong to a same eigensubspace of H_0 becomes evident in the textbook quasi-degenerate perturbation theory, where the corrections to energies and wavefunctions contain differences between energy of the states from different subspaces. The main difference between our generalization and the standard separation into block-diagonal and block-offdiagonal is that the product of a selected part and remaining part of two operators may have a non-zero selected part: $(\mathcal{A}_S\mathcal{B}_R)_S \neq 0$, while $(\mathcal{A}^{AA}\mathcal{B}^{AB})^{AA} = 0$. The generality of the selected and remaining parts allows to consider all perturbation theory methods with the same algorithm, including multi-block diagonalization, selective diagonalization, and the Schrieffer–Wolff transformation. Several expressions simplify if the selected part corresponds to a block-diagonal operator and simplify further if there are only two subspaces. We keep track of these simplifications.

All the series we consider may be multivariate, and they represent sums of the form

$$\mathcal{A} = \sum_{n_1=0}^{\infty}\sum_{n_2=0}^{\infty}\cdots\sum_{n_k=0}^{\infty}\lambda_1^{n_1}\lambda_2^{n_2}\cdots\lambda_k^{n_k}A_{n_1,n_2,\ldots,n_k}, \tag{2.8}$$

where λ_i are the perturbation parameters and $A_{n_1,n_2,\ldots,n_k}$ are linear operators. The problem statement, therefore, is finding $\mathcal{U}$ and $\tilde{\mathcal{H}}$ such that

$$\tilde{\mathcal{H}} = \mathcal{U}^\dagger\mathcal{H}\mathcal{U}, \quad \tilde{\mathcal{H}}_R = 0, \quad \mathcal{U}^\dagger\mathcal{U} = 1, \tag{2.9}$$

which is schematically shown in Fig. 2.1 for the case of two subspaces, where the selected parts are AA and BB, and the remaining parts are AB and BA. Series multiply according to the Cauchy product:

$$\mathcal{C} = \mathcal{A}\mathcal{B} \Leftrightarrow C_{\mathbf{n}} = \sum_{\mathbf{m}+\mathbf{p}=\mathbf{n}} A_{\mathbf{m}}B_{\mathbf{p}}.$$

The Cauchy product is the most expensive operation in perturbation theory, because it involves a large number of multiplications between potentially large matrices. For example, evaluating $\mathbf{n}$-th order of $\mathcal{C}$ requires $\sim \prod_i n_i \equiv N$ multiplications of the series elements.[5] A direct computation of all the possible index combinations in a product between three series $\mathcal{A}\mathcal{B}\mathcal{C}$ would have a higher cost $\sim N^2$, however, if we use associativity of the product and compute this as $(\mathcal{A}\mathcal{B})\mathcal{C}$, then the scaling of the cost stays $\sim N$.

There are many ways to solve the problem (2.9) that give identical expressions for $\mathcal{U}$ and $\tilde{\mathcal{H}}$. We are searching for a procedure that satisfies two additional constraints:

- It has the same complexity scaling as a Cauchy product, and therefore $\sim N$ multiplications per additional order.
- It does not require multiplications by H_0.

[5] If both $\mathcal{A}$ and $\mathcal{B}$ are known in advance, fast Fourier transform-based algorithms can reduce this cost to $\sim N\log N$. In our problem, however, the series are constructed recursively and therefore this optimization is impossible.

- It requires only one Cauchy product by $\mathcal{H}_S$, the selected part of $\mathcal{H}$.

The first requirement is that the algorithm scaling is optimal: the desired expression at least contains a Cauchy product of $\mathcal{U}$ and $\mathcal{H}$. Therefore the complexity scaling of the complete algorithm may not become lower than the complexity of a Cauchy product and we aim to reach this lower bound. The second requirement is because in perturbation theory, n-th order corrections to $\tilde{\mathcal{H}}$ carry n energy denominators $1/(E_i - E_j)$, where E_i and E_j are the eigenvalues of H_0 belonging to different subspaces. Therefore, any additional multiplications by H_0 must cancel with additional energy denominators. Multiplying by H_0 is therefore unnecessary work, and it gives longer intermediate expressions. The third requirement we impose by considering a case in which $\mathcal{H}_R = 0$, where $\mathcal{H}_S$ must at least enter $\tilde{\mathcal{H}}$ as an added term, without any products. Moreover, because $\mathcal{U}$ depends on the entire Hamiltonian, there must be at least one Cauchy product by $\mathcal{H}'_S$. The goal of our algorithm is thus to be efficient and to produce compact results that do not require further simplifications.

2.3.2. EXISTING SOLUTIONS

A common approach to constructing effective Hamiltonians in the 2×2 block case is to use the Schrieffer–Wolff transformation [1]:

$$\begin{aligned} \tilde{\mathcal{H}} &= e^{\mathcal{S}} \mathcal{H} e^{-\mathcal{S}}, \\ e^{\mathcal{S}} &= 1 + \mathcal{S} + \frac{1}{2!}\mathcal{S}\mathcal{S} + \frac{1}{3!}\mathcal{S}\mathcal{S}\mathcal{S} + \cdots, \end{aligned} \tag{2.10}$$

where $\mathcal{S} = \sum_n S_n$ is an antihermitian polynomial series in the perturbative parameter, making $e^{\mathcal{S}}$ a unitary transformation. Requiring that $\tilde{\mathcal{H}}^{AB} = 0$ gives a recursive equation for S_n, whose terms are nested commutators between the series of $\mathcal{S}$ and $\mathcal{H}$. Similarly, the transformed Hamiltonian is given by a series of nested commutators

$$\tilde{\mathcal{H}} = \sum_{j=0}^{\infty} \frac{1}{j!} \Big[\mathcal{H}, \sum_{n=0}^{\infty} S_n \Big]^{(j)}, \tag{2.11}$$

where the superscript (j) denotes the j-th nested commutator $[A,B]^{(j)} = [[A,B]^{(j-1)}, B]$, with $[A,B]^{(0)} = A$ and $[A,B]^{(1)} = AB - BA$. Regardless of the specific implementation, this expression does not meet either of our two requirements:

- The direct computation of the series elements requires $\sim \exp N$ multiplications, and even an optimized one has a $\sim N^2$ scaling.
- Evaluating Eq. (2.11) contains multiplications by H_0.

Additionally, while in the 2×2 block case the Schrieffer–Wolff transformation produces a minimal unitary transformation, i.e. as close to identity as possible, this is not the case in the multi-block case [26]. The generalization of this approach to multiple subspaces is an open question [26].

Alternative parametrizations of the unitary transformation $\mathcal{U}$ require solving unitarity and block diagonalization conditions too, but give rise to a different recursive proce-

dure for the series elements. For example, using hyperbolic functions

$$\mathcal{U} = \cosh\mathcal{G} + \sinh\mathcal{G}, \quad \mathcal{G} = \sum_{i=0}^{\infty} G_i, \tag{2.12}$$

leads to different recursive expressions for G_i [13], but does not change the algorithm's complexity. On the other hand, using a polynomial series directly

$$\mathcal{U} = \sum_{i=0}^{\infty} U_i, \tag{2.13}$$

gives rise to another recursive equation for U_i [3, 12, 14, 15]. Still, this choice results in an expression for $\tilde{\mathcal{H}}$ whose terms include products by H_0, and therefore requires additional simplifications.

Another approach uses Wegner's flow equation [19, 20] to construct a continuous unitary transformation (CUT) that depends smoothly on a fictitious parameter l, $\mathcal{U}(l)$. The goal is to define a generator $\eta(l)$ such that $\mathcal{H}(l) = \mathcal{U}^\dagger(l)\mathcal{H}(0)\mathcal{U}(l)$ flows towards the desired effective Hamiltonian:

$$\frac{d\mathcal{H}(l)}{dl} = [\eta(l), \mathcal{H}(l)], \tag{2.14}$$

where $\mathcal{U}(l)$, $\mathcal{H}(l)$, and $\eta(l)$ are once again series in the perturbative parameters. At $l = \infty$, the transformed Hamiltonian does not contain the undesired terms, $\mathcal{H}(\infty) = \tilde{\mathcal{H}}$. Finding the unitary amounts to solving a set of differential equations

$$\frac{d\mathcal{U}(l)}{dl} = \eta(l)\mathcal{U}(l). \tag{2.15}$$

Together with the Eq. (2.14) and an appropriate choice of η, this gives a set of coupled differential equations, that become linear if solved order by order. The convergence and stability of flow equations depends on the parameterization of the flow generator η, and multiple strategies for this choice are known [23, 42]. The CUT method is common in the study of many-body systems, where one needs to either decompose the Hamiltonian into sets of quasiparticle creation and annihilation operators, or choose a different operator basis together with a set of commutation rules. Despite the numerical complication of solving differential equations, CUT extends beyond the perturbative regime [20, 22, 23].

The following three algorithms satisfy both of our requirements while solving a related problem. First, density matrix perturbation theory [16, 17, 43] constructs the density matrix ρ of a perturbed system as a power series with respect to a perturbative parameter:

$$\rho = \sum_{i=0}^{\infty} \rho_i. \tag{2.16}$$

The elements of the series are found by solving two recursive conditions, $\rho^2 = \rho$ and $[\mathcal{H}, \rho] = 0$, which avoid multiplications by H_0 and require a single Cauchy product each. This approach, however, deals with the entire Hilbert space, rather than the low-energy

subspace, and does not provide an effective Hamiltonian. Second, the perturbative similarity transform by C. Bloch [2, 18] constructs the effective Hamiltonian in a non-orthogonal basis, which preserves the Hamiltonian spectrum while breaking its hermiticity. Third, the recursive Schrieffer–Wolff algorithm [37] applies the Schrieffer–Wolff transformation to the output of lower-order iterations, and calculates the effective Hamiltonian at a fixed perturbation strength, rather than as a series. Finally, none of these linear scaling algorithms above handles more than two subspaces. We thus identify the following open question: can we construct an effective Hamiltonian with a linear scaling algorithm that produces compact expressions?

2.3.3. PYMABLOCK'S ALGORITHM

The first idea that Pymablock exploits is the recursive evaluation of the operator series, which we illustrate by considering the unitarity condition. Let us separate the transformation $\mathcal{U}$ into an identity and $\mathcal{U}' = \mathcal{W} + \mathcal{V}$:

$$\mathcal{U} = 1 + \mathcal{U}' = 1 + \mathcal{W} + \mathcal{V}, \quad \mathcal{W}^\dagger = \mathcal{W}, \quad \mathcal{V}^\dagger = -\mathcal{V}. \tag{2.17}$$

We use the unitarity condition $\mathcal{U}^\dagger\mathcal{U} = 1$ by substituting $\mathcal{U}'$ into it:

$$1 = (1 + \mathcal{U}'^\dagger)(1 + \mathcal{U}') = 1 + \mathcal{U}'^\dagger + \mathcal{U}' + \mathcal{U}'^\dagger\mathcal{U}'. \tag{2.18}$$

This immediately yields

$$\mathcal{W} = \frac{1}{2}(\mathcal{U}'^\dagger + \mathcal{U}') = -\frac{1}{2}\mathcal{U}'^\dagger\mathcal{U}'. \tag{2.19}$$

Because $\mathcal{U}'$ has no 0-th order term, $(\mathcal{U}'^\dagger\mathcal{U}')_{\mathbf{n}}$ does not depend on the $\mathbf{n}$-th order of $\mathcal{U}'$ nor $\mathcal{W}$, and therefore Eq. (2.19) allows to compute $\mathcal{W}$ using the already available lower orders of $\mathcal{U}'$. Alternatively, using Eq. (2.17) we could define $\mathcal{W}$ as a Taylor series in $\mathcal{V}$:

$$\mathcal{W} = \sqrt{1 + \mathcal{V}^2} - 1 \equiv f(\mathcal{V}) \equiv \sum_n a_n \mathcal{V}^{2n}.$$

A direct computation of all possible products of terms in this expression requires $\sim \exp N$ multiplications. A more efficient approach for evaluating this expression introduces each term in the sum as a new series $\mathcal{A}^{n+1} = \mathcal{A}\mathcal{A}^n$ and reuses the previously computed results. This optimization brings the exponential cost down to $\sim N^2$. However, we see that the Taylor expansion approach is both more complicated and more computationally expensive than the recurrent definition in Eq. (2.19). Therefore, we use Eq. (2.19) to efficiently compute $\mathcal{W}$. More generally, a Cauchy product $\mathcal{A}\mathcal{B}$ where $\mathcal{A}$ and $\mathcal{B}$ have no 0-th order terms depends on $\mathcal{A}_1, \ldots, \mathcal{A}_{n-1}$ and $\mathcal{B}_1, \ldots, \mathcal{B}_{n-1}$. This makes it possible to use $\mathcal{A}\mathcal{B}$ in a recurrence relation, a property that we exploit throughout the algorithm.

To compute $\mathcal{U}'$ we also need to find $\mathcal{V}$, which is defined by the requirement $\tilde{\mathcal{H}}_R = 0$. Additionally, we constrain $\mathcal{V}$ to have no selected part: $\mathcal{V}_S = 0$, a choice we make to minimize the norm of $\mathcal{U}'$, and satisfy the least action principle [44]. That $\mathcal{V}_S = 0$ minimizes the norm of $\mathcal{U}'$ follows from the following statements:

1. The norm of a series is minimal, when each of the subsequent terms is chosen to be minimal order by order.

2. The Hermitian part of $\mathcal{U}'$, $W_{\mathbf{n}}$, is determined by the unitarity condition (2.19) at each order from lower orders of $\mathcal{U}'$.

3. The norm of $W_{\mathbf{n}} + V_{\mathbf{n}}$ is minimal, when the norm of $V_{\mathbf{n}}$ is minimal because of Hermiticity properties of $\mathcal{W}$ and $\mathcal{V}$.

4. Finally, because $\mathcal{V}_R$ is fixed by the requirement $\tilde{\mathcal{H}}_R = 0$, $\mathcal{V}_S = 0$ provides the minimal norm of $\mathcal{U}'$.

In the 2×2 block case, this choice makes $\mathcal{W}$ block-diagonal and ensures that the resulting unitary transformation is equivalent to the Schrieffer–Wolff transformation (see section 2.3.4). In general, however, $\mathcal{W}_R \neq 0$.

The remaining condition for finding a recurrent relation for $\mathcal{U}'$ is that the transformed Hamiltonian

$$\tilde{\mathcal{H}} = \mathcal{U}^\dagger \mathcal{H} \mathcal{U} = \mathcal{H}_S + \mathcal{U}'^\dagger \mathcal{H}_S + \mathcal{H}_S \mathcal{U}' + \mathcal{U}'^\dagger \mathcal{H}_S \mathcal{U}' + \mathcal{U}^\dagger \mathcal{H}'_R \mathcal{U}, \tag{2.20}$$

has only the selected part $\tilde{\mathcal{H}}_R = 0$, a condition that determines $\mathcal{V}$. Here we used $\mathcal{U} = 1 + \mathcal{U}'$ and $\mathcal{H} = \mathcal{H}_S + \mathcal{H}'_R$, since H_0 is has no remaining part by definition. Because we want to avoid products by $\mathcal{H}_S$, we need to get rid of the terms that contain it by replacing them with an alternative expression. Our strategy is to define an auxiliary operator $\mathcal{X}$ that we can compute without ever multiplying by $\mathcal{H}_S$. Like $\mathcal{U}'$, $\mathcal{X}$ needs to be defined via a recurrence relation, which we determine later. Because Eq. (2.20) contains $\mathcal{H}_S$ multiplied by $\mathcal{U}'$ from the left and from the right, eliminating $\mathcal{H}_S$ requires moving it to the same side. To achieve this, we choose $\mathcal{X} = \mathcal{Y} + \mathcal{Z}$ to be the commutator between $\mathcal{U}'$ and $\mathcal{H}_S$:

$$\mathcal{X} \equiv [\mathcal{U}', \mathcal{H}_S] = \mathcal{Y} + \mathcal{Z}, \quad \mathcal{Y} \equiv [\mathcal{V}, \mathcal{H}_S] = \mathcal{Y}^\dagger, \quad \mathcal{Z} \equiv [\mathcal{W}, \mathcal{H}_S] = -\mathcal{Z}^\dagger. \tag{2.21}$$

If the selected part $\mathcal{A}_S$ corresponds to a block-diagonal operator, $\mathcal{Y}$ is block off-diagonal. Additionally, in the 2×2 block case $\mathcal{Z}$ is block-diagonal. We use $\mathcal{H}_S\mathcal{U}' = \mathcal{U}'\mathcal{H}_S - \mathcal{X}$ to move $\mathcal{H}_S$ through to the right and find

$$\begin{aligned}
\tilde{\mathcal{H}} &= \mathcal{H}_S + \mathcal{U}'^\dagger \mathcal{H}_S + (\mathcal{H}_S \mathcal{U}') + \mathcal{U}'^\dagger \mathcal{H}_S \mathcal{U}' + \mathcal{U}^\dagger (\mathcal{H}'_R \mathcal{U}) \\
&= \mathcal{H}_S + \mathcal{U}'^\dagger \mathcal{H}_S + \mathcal{U}' \mathcal{H}_S - \mathcal{X} + \mathcal{U}'^\dagger (\mathcal{U}' \mathcal{H}_S - \mathcal{X}) + \mathcal{U}^\dagger \mathcal{H}'_R \mathcal{U} \\
&= \mathcal{H}_S + (\mathcal{U}'^\dagger + \mathcal{U}' + \mathcal{U}'^\dagger \mathcal{U}') \mathcal{H}_S - \mathcal{X} - \mathcal{U}'^\dagger \mathcal{X} + \mathcal{U}^\dagger \mathcal{H}'_R \mathcal{U} \\
&= \mathcal{H}_S - \mathcal{X} - \mathcal{U}'^\dagger \mathcal{X} + \mathcal{U}^\dagger \mathcal{H}'_R \mathcal{U},
\end{aligned} \tag{2.22}$$

where the terms multiplied by $\mathcal{H}_S$ cancel according to Eq. (2.18). The transformed Hamiltonian does not contain multiplications by $\mathcal{H}_S$ anymore, but it does depend on $\mathcal{X}$, an auxiliary operator whose recurrent definition we do not know yet. To find it, we first focus on its anti-Hermitian part, $\mathcal{Z}$. Since recurrence relations are expressions whose right-hand side contains Cauchy products between series, we need to find a way to make a product appear. We do so by using the unitarity condition $\mathcal{U}'^\dagger + \mathcal{U}' = -\mathcal{U}'^\dagger \mathcal{U}'$ to obtain

the recursive definition of $\mathcal{Z}$:

$$\begin{aligned}\mathcal{Z} &= \frac{1}{2}(\mathcal{X} - \mathcal{X}^\dagger)\\ &= \frac{1}{2}\Big[(\mathcal{U}' + \mathcal{U}'^\dagger)\mathcal{H}_S - \mathcal{H}_S(\mathcal{U}' + \mathcal{U}'^\dagger)\Big]\\ &= \frac{1}{2}\Big[-\mathcal{U}'^\dagger(\mathcal{U}'\mathcal{H}_S - \mathcal{H}_S\mathcal{U}') + (\mathcal{U}'\mathcal{H}_S - \mathcal{H}_S\mathcal{U}')^\dagger\mathcal{U}'\Big]\\ &= \frac{1}{2}(-\mathcal{U}'^\dagger\mathcal{X} + \mathcal{X}^\dagger\mathcal{U}').\end{aligned} \tag{2.23}$$

Similar to computing $W_{\mathbf{n}}$, computing $Z_{\mathbf{n}}$ requires lower-orders of $\mathcal{X}$ and $\mathcal{U}'$. Then, we compute the Hermitian part of $\mathcal{X}$ by requiring that $\tilde{\mathcal{H}}_R = 0$ in the Eq. (2.22) and find

$$\mathcal{Y}_R = (\mathcal{U}^\dagger\mathcal{H}'_R\mathcal{U} - \mathcal{U}'^\dagger\mathcal{X} - \mathcal{Z})_R. \tag{2.24}$$

Once again, despite $\mathcal{X}$ enters the right hand side, because all the terms lack 0^{th} order, this defines a recursive relation $\mathcal{Y}$. To fix $\mathcal{Y}_S$, we use its definition (2.21), which gives

$$[\mathcal{V}, H_0] = \mathcal{Y} - [\mathcal{V}, \mathcal{H}'_S], \tag{2.25}$$

which is a continuous-time Lyapunov equation for $\mathcal{V}$. In order for this equation to be satisfiable, the selected part of the right hand side must vanish, since the left hand side has no selected part. Therefore we find:

$$\mathcal{Y}_S = [\mathcal{V}, \mathcal{H}'_S]_S, \tag{2.26}$$

and it vanishes if the selected part corresponds to a block-diagonal matrix.

The final part is straightforward. Finding $\mathcal{V}$ from $\mathcal{Y}$ amounts to solving a Sylvester's equation, Eq. 2.26, which we only need to solve once for every new order. This is the only step in the algorithm that requires a direct multiplication by $\mathcal{H}'_S$. In the eigenbasis of H_0, the solution of Sylvester's equation is $V_{\mathbf{n},ij} = (\mathcal{Y}_R - [\mathcal{V}, \mathcal{H}'_S]_R)_{\mathbf{n},ij}/(E_i - E_j)$, where E_i are the eigenvalues of H_0. However, even if the eigenbasis of H_0 is not available, there are efficient numerical algorithms to solve Sylvester's equation (see Sec. 2.4.2). An alternative is to decompose the Hamiltonian into its eigenoperator basis. This approach avoids specifying the eigenbasis of H_0, and therefore it is better suited for second-quantized Hamiltonians [45, 46].

We now have the complete algorithm:

1. Define series $\mathcal{U}'$ and $\mathcal{X}$ and make use of their block structure and Hermiticity.
2. To define the hermitian part of $\mathcal{U}'$, use $\mathcal{W} = -\mathcal{U}'^\dagger\mathcal{U}'/2$.
3. To find the antihermitian part of $\mathcal{U}'$, solve Sylvester's equation $[\mathcal{V}, H_0] = (\mathcal{Y} - [\mathcal{V}, \mathcal{H}'_S])_R$. This requires $\mathcal{X}$.
4. To find the antihermitian part of $\mathcal{X}$, define $\mathcal{Z} = (-\mathcal{U}'^\dagger\mathcal{X} + \mathcal{X}^\dagger\mathcal{U}')/2$.
5. For the Hermitian part of $\mathcal{X}$, use $\mathcal{Y} = (-\mathcal{U}'^\dagger\mathcal{X} + \mathcal{U}^\dagger\mathcal{H}'\mathcal{U})_R + [\mathcal{V}, \mathcal{H}'_S]_S$.
6. Compute the effective Hamiltonian as $\tilde{\mathcal{H}} \equiv \tilde{\mathcal{H}}_S = \mathcal{H}_S - \mathcal{X} - \mathcal{U}'^\dagger\mathcal{X} + \mathcal{U}^\dagger\mathcal{H}'_R\mathcal{U}$.

2.3.4. EQUIVALENCE TO SCHRIEFFER–WOLFF TRANSFORMATION

Pymablock's algorithm applied to 2×2 block-diagonalization and the Schrieffer–Wolff transformation both find a unitary transformation $\mathcal{U}$ such that $\tilde{\mathcal{H}}_R = \tilde{\mathcal{H}}^{AB} = 0$. They are therefore equivalent up to a gauge choice in each subspace, A and B. We establish the equivalence between the two by demonstrating that this gauge choice is the same for both algorithms. The Schrieffer–Wolff transformation uses $\mathcal{U} = \exp \mathcal{S}$, where $\mathcal{S} = -\mathcal{S}^\dagger$ and $\mathcal{S}^{AA} = \mathcal{S}^{BB} = 0$, this restriction makes the result unique [2]. On the other hand, our algorithm produces the unique block-diagonalizing transformation with a block structure $\mathcal{U}^{AA} = \mathcal{U}^{AA\dagger}$, $\mathcal{U}^{BB} = \mathcal{U}^{BB\dagger}$ and $\mathcal{U}^{AB} = -\mathcal{U}^\dagger_{BA}$. The uniqueness is a consequence of the construction of the algorithm, where calculating every order gives a unique solution satisfying these conditions. To see that the two solutions are identical, we expand $\exp \mathcal{S}$ into Taylor series. In the resulting series every term containing a product of an even number of terms of $\mathcal{S}$ is a Hermitian, block-diagonal matrix, while every term containing a product of an odd number of terms of $\mathcal{S}$ is an anti-Hermitian block off-diagonal matrix. Therefore $\exp \mathcal{S}$ has the same structure as $\mathcal{U}$ above. Because both series are fixed by the hermiticity constraints on their block structure, we conclude that $\exp \mathcal{S}$ from conventional Schrieffer–Wolff transformation is identical to $\mathcal{U}$ found by our algorithm.

2.3.5. EXTRA OPTIMIZATION: COMMON SUBEXPRESSION ELIMINATION

While the algorithm of Sec. 2.3.3 satisfies our requirements, we improve it further by reusing products that are needed in several places, such that the total number of matrix multiplications is reduced. Firstly, we rewrite the expressions for $\mathcal{Z}$ in Eq. (2.23) and $\tilde{\mathcal{H}}$ in Eq. (2.22) by utilizing the Hermitian conjugate of $\mathcal{U}'^\dagger \mathcal{X}$ without recomputing it:

$$\mathcal{Z} = \frac{1}{2}\Big[(-\mathcal{U}'^\dagger \mathcal{X}) - \text{h.c.}\Big],$$
$$\tilde{\mathcal{H}} = \mathcal{H}_S + \mathcal{U}^\dagger \mathcal{H}'_R \mathcal{U} - (\mathcal{U}'^\dagger \mathcal{X} + \text{h.c.})/2 - \mathcal{Y}_S,$$

where h.c. is the Hermitian conjugate, and $\mathcal{Z}$ drops out from $\tilde{\mathcal{H}}$ because it is antihermitian. Additionally, we reuse the repeated $\mathcal{A} \equiv \mathcal{H}'_R \mathcal{U}'$ in

$$\mathcal{U}^\dagger \mathcal{H}'_R \mathcal{U} = \mathcal{H}'_R + \mathcal{A} + \mathcal{A}^\dagger + \mathcal{U}'^\dagger \mathcal{A}. \tag{2.27}$$

Next, we observe that some products from the $\mathcal{U}^\dagger \mathcal{H}_R \mathcal{U}$ term appear both in $\mathcal{X}$ in Eq. (2.24) and in $\tilde{\mathcal{H}}$ (2.22). To avoid recomputing these products, we introduce $\mathcal{B} = \mathcal{X} - \mathcal{H}'_R - \mathcal{A}$ and define the recursive algorithm using $\mathcal{B}$ instead of $\mathcal{X}$. With this definition, we compute the remaining part of $\mathcal{B}$ as:

$$\begin{aligned}
\mathcal{B}_R &= [\mathcal{Y} + \mathcal{Z} - \mathcal{H}'_R - \mathcal{A}]_R \\
&= \left[\mathcal{A}^\dagger + \mathcal{U}'^\dagger \mathcal{A} - \mathcal{U}'^\dagger \mathcal{X}\right]_R \\
&= \left[\mathcal{U}'^\dagger \mathcal{H}'_R + \mathcal{U}'^\dagger \mathcal{A} - \mathcal{U}'^\dagger \mathcal{X}\right]_R \\
&= -(\mathcal{U}'^\dagger \mathcal{B})_R,
\end{aligned} \tag{2.28}$$

where we also used Eq. (2.24) and the definition of $\mathcal{A}$. The selected part of $\mathcal{B}$, on the other hand, is given by

$$\begin{aligned}\mathcal{B}_S &= [\mathcal{X} - \mathcal{H}'_R - \mathcal{A}]_S \\ &= \left[\frac{1}{2}[(-\mathcal{U}'^\dagger \mathcal{X}) - \text{h.c.}] + \mathcal{Y} - \mathcal{A}\right]_S \\ &= \left[\frac{1}{2}[(-\mathcal{U}'^\dagger [\mathcal{X} - \mathcal{H}'_R - \mathcal{A}]) - \text{h.c.}] + \mathcal{Y} - \frac{1}{2}[\mathcal{A}^\dagger + \mathcal{A}] + \frac{1}{2}[(-\mathcal{U}'^\dagger \mathcal{A}) - \text{h.c.}]\right]_S, \\ &= \left[\frac{1}{2}[(-\mathcal{U}'^\dagger \mathcal{B}) - \text{h.c.}] + [\mathcal{V}\mathcal{H}'_S + \text{h.c}] - \frac{1}{2}[\mathcal{A}^\dagger + \text{h.c.}]\right]_S,\end{aligned} \tag{2.29}$$

where we used Eq. (2.23) and that $\mathcal{U}'^\dagger \mathcal{A}$ is Hermitian. Using $\mathcal{B}$ changes the relation for $\mathcal{V}$ in Eq. (2.26) to

$$[\mathcal{V}, H_0] = \left(\mathcal{B} - \mathcal{H}' - \mathcal{A} - [\mathcal{V}, \mathcal{H}'_S]\right)_R. \tag{2.30}$$

Finally, we combine Eq. (2.22), Eq. (2.27), Eq. (2.29) and Eq. (2.28) to obtain the final expression for the effective Hamiltonian:

$$\tilde{\mathcal{H}}_S = \mathcal{H}_S + \frac{1}{2}\left[\mathcal{A} - \mathcal{U}'^\dagger \mathcal{B} + 2\mathcal{V}\mathcal{H}'_S + \text{h.c.}\right]_S. \tag{2.31}$$

Together with the series $\mathcal{U}'$ in Eqs. (2.19,2.30), $\mathcal{A} = \mathcal{H}'_R \mathcal{U}'$, and $\mathcal{B}$ in Eqs. (2.29,2.28), this equation defines the optimized algorithm.

2.4. IMPLEMENTATION

2.4.1. THE DATA STRUCTURE FOR BLOCK OPERATOR SERIES

The optimized algorithm from the previous section requires constructing 14 operator series, whose elements are computed using a collection of recurrence relations. This warrants defining a specialized data structure suitable for this task that represents a multidimensional series of operators. Because the recurrent relations are block-wise, the data structure needs to keep track of separate blocks. In order to support varied use cases, the actual representation of the operators needs to be flexible: the block may be dense arrays, sparse matrices, symbolic expressions, or more generally any object that defines addition and multiplication. Finally, the series needs to be queryable by order and block, so that it supports a block-wise multivariate Cauchy product—the main operation in the algorithm.

The most straightforward way to implement a perturbation theory calculation is to write a function that has the desired order as an argument, computes the series up to that order, and returns the result. This makes it hard to reuse already computed terms for a new computation, and becomes complicated to implement in the multidimensional case when different orders in different perturbations are needed. We find that a recursive approach addresses these issues: within this paradigm, each series needs to define how its entries depend on lower-order terms.

To address these requirements, we define a `BlockSeries` Python class and use it to represent the series of $\mathcal{U}$, $\mathcal{H}$, and $\tilde{\mathcal{H}}$, as well as the intermediate series used to define the

algorithm. The objects of this class are equipped with a function to compute their elements and it stores the already computed results in a dictionary. Storing the results for reuse is necessary to optimize the evaluation of higher order terms and it allows to request additional orders without restarting the computation. For example, the definition of the `BlockSeries` for $\tilde{\mathcal{H}}$ has the following form:


```
H_tilde = BlockSeries(
    shape=(2, 2),  # 2x2 block matrix
    n_infinite=n,  # number of perturbative parameters
    eval=compute_H_tilde,  # function to compute the elements
    name="H_tilde",
    dimension_names=("lambda", ...),  # parameter names
)
```

Here `compute_H_tilde` is a function implementing Eq. (2.31) by querying other series objects. Calling `H_tilde[0, 0, 2]`, the second order perturbation $\sim \lambda^2$ of the AA block, then does the following:

1. Evaluates `compute_H_tilde(0, 0, 2)` if it is not already computed.
2. Stores the evaluation result in a dictionary.
3. Returns the result.

To conveniently access multiple orders at once, we implement NumPy array indexing so that `H_tilde[0, 0, :3]` returns a NumPy masked array array with the orders $\sim \lambda^0$, $\sim \lambda^1$, and $\sim \lambda^2$ of the AA block. The masking allows to support a common use case where some orders of a series are zero, so that they are omitted from the computations. We expect that the `BlockSeries` data structure is suitable to represent a broad class of perturbative calculations, and we plan to extend it to support more advanced features in the future.

We utilize `BlockSeries` to implement multiple other optimizations. For example, we exploit Hermiticity when computing the Cauchy product of $U'^{\dagger}U'$ in Eq. (2.19), by only evaluating half of the matrix products, and then complex conjugate the result to obtain the rest. Similarly, for Hermitian and anti-Hermitian series, like the off-diagonal blocks of $\mathcal{U}'$, we only compute the AB blocks, and use the conjugate transpose to obtain the BA blocks. This approach should also allow us to implement efficient handling of symmetry-constrained Hamiltonians, where some blocks either vanish or are equal to other blocks due to a symmetry. Moreover, using `BlockSeries` with custom objects yields additional information about the algorithm and accommodates its further development. Specifically, we have used a custom object with a counter to measure the algorithm complexity (see also Sec. 2.5) and to determine which results are only used once so that they can be immediately discarded from storage.

2.4.2. THE IMPLICIT METHOD FOR LARGE SPARSE HAMILTONIANS

A distinguishing feature of Pymablock is its ability to handle large sparse Hamiltonians, that are too costly to diagonalize, as illustrated in Sec. 2.2.3. Specifically, we consider the situations when the size N_E of the subspace of interest—explicit subspace—is

small compared to the entire Hilbert space, so that obtaining the basis Ψ_E of the explicit subspace is feasible using sparse diagonalization. The projector on this subspace $P_E = \Psi_E^\dagger \Psi_E$ is then a low-rank matrix, a property that we exploit to avoid constructing the matrix representation of operators in the other, implicit, subspace.

The key tool to solve this problem is the projector approach introduced in Ref. [47], which introduces an equivalent extended Hamiltonian using the projector $P_I = 1 - P_A$ onto the implicit subspace:

$$\tilde{\mathcal{H}} = \begin{pmatrix} \Psi_E^\dagger \mathcal{H} \Psi_E & \Psi_E^\dagger \mathcal{H} P_I \\ P_I \mathcal{H} \Psi_E & P_I \mathcal{H} P_I \end{pmatrix}. \tag{2.32}$$

In other words, the explicit subspace is written in the basis of Ψ_E, while the basis of the implicit subspace is the same as the original complete basis of $\mathcal{H}$ to preserve its sparsity. The extended Hamiltonian projects out the E-degrees of freedom from the implicit subspace to avoid duplicate solutions in $\tilde{\mathcal{H}}$, which introduces N_E eigenvectors with zero eigenvalues. Introducing $\tilde{\mathcal{H}}$ allows to multiply by operators of a form $P_I H_{\mathbf{n}} P_I$ efficiently by using the low-rank structure of P_E. In the code we represent the operators of the implicit subspace as `LinearOperator` objects from the SciPy package [41], enabled by the ability of the `BlockSeries` to store arbitrary objects. Storing the remaining blocks of $\tilde{\mathcal{H}}$ as dense matrices—efficient because these are small and dense—finishes the implementation of the Hamiltonian.

To solve the Sylvester's equation we write it for every row of $V_{\mathbf{n}}^{EI}$ separately:

$$V_{\mathbf{n},ij}^{EI}(E_i - H_0) = Y_{\mathbf{n},j}^{EI} \tag{2.33}$$

This equation has a solution despite $E_i - H_0$ not being invertible because $Y_{\mathbf{n}}^{EI} P_A = 0$. We solve this equation using the MUMPS sparse solver [48, 49], which prepares an efficient sparse LU-decomposition of $E_i - H_0$, or the KPM approximation of the Green's function [50]. Both methods work on sparse Hamiltonians with millions of degrees of freedom.

2.4.3. CODE GENERATION

An efficient computation of a perturbative block-diagonalization requires a significant amount of repeated optimizations. These include keeping track of the Hermiticity of involved series, applying the simplifications due to block-diagonalization and the presence of only two blocks, or deletion of series terms that are only used once. To separate the conceptual definition of the algorithm from these optimizations, we designed the code generation system that accepts a high-level description of the algorithm written in a domain-specific language and outputs the optimized Python code using the Python parser and the manipulation of the Python abstract syntax tree. For example, the definition of the series $\mathcal{B}$ from Eqs. (2.29,2.28) is written as:

```
with "B":
    start = 0
    if diagonal:
        ("U'† @ B" - "U'† @ B".adj + "H'_offdiag @ U'" + "H'_offdiag @
        ↪  U'".adj) / -2
```

```
    if diagonal:
        zero if commuting_blocks[index[0]] else "V @ H'_diag" + "V @
         ↪ H'_diag".adj
    if offdiagonal:
        -"U'† @ B"
```


The corresponding compiled function for evaluating the terms of $\mathcal{B}$ begins with

```
def series_eval(*index):
    which = linear_operator_series if use_linear_operator[index[:2]]
     ↪ else series
    result = zero
    if index[0] == index[1]:
        result = _zero_sum(
            result,
            diag(
                _safe_divide(
                    _zero_sum(
                        which["U'† @ B"][index], -Dagger(which["U'† @
                         ↪ B"][index]),
                        which["H'_offdiag @ U'"][index],
                        Dagger(which["H'_offdiag @ U'"][index]),
                    ), -2,
                ), index,
            ),
        )
    ...
```

Here we only show the beginning of the generated function to illustrate the correspondence between the high-level description and the generated code.

The code generation system has accommodated multiple rewrites of the algorithm during the development. We anticipate that it will enable treating different types of perturbative computations or other related algorithms, such as the derivative removal by adiabatic gate (DRAG) algorithm [51, 52]. Contrary to the perturbation theory setting, DRAG requires that the time-dependent Hamiltonian is block-diagonal in the rotating frame, and it achieves this goal by adding a series of corrections to the original Hamiltonian. Its overall setting, however, is similar to time-dependent perturbation theory in that it amounts to solving a system of recurrent algebraic equations. Our preliminary research already demonstrates that our code generation framework allows for a generalization of our work to the time-dependent perturbation theory, and we are confident that it applies to the DRAG algorithm as well.

2.5. BENCHMARK

To the best of our knowledge, there are no other packages implementing arbitrary order quasi-degenerate perturbation theory. Literature references provide explicit expressions for the 2×2 effective Hamiltonian up to fourth order, together with the procedure for obtaining higher order expressions [5]. Because the full reference expressions are lengthy[6],

[6] The full expression takes almost a page of text.

we do not provide them, but for example at 4-th order the effective Hamiltonian is a sum of several expressions of the form:

$$\sum_{m''m'''l} \frac{H'_{mm''}H'_{m''m'''}H'_{m'''l}H'_{lm'}}{(E_{m''}-E_l)(E_{m'''}-E_l)(E_m-E_l)}, \tag{2.34}$$

where the m-indices label states from the A-subspace and l-indices label the states from the B-subspace. More generally, at n-th order each term is a product of n matrix elements of the Hamiltonian and $n-1$ energy denominators. Directly carrying out the summation over all the states requires $\mathcal{O}(N_A^2 N_B^{n-1})$ operations, where N_A and N_B are the number of states in the two subspaces. In other words, the direct computation scales worse than a matrix product with the problem size. Formulating Eq. (2.34) as $n-1$ matrix products combined with $n-1$ solutions of Sylvester's equation, brings this complexity down to $\mathcal{O}((n-1)\times N_A N_B^2)$. This optimization, together with the hermiticity of the sum, allows us to evaluate the reference expressions for the effective Hamiltonian for 2-nd, 3-rd, and 4-th order using 1, 4, and 27 matrix products, respectively. Pymablock's algorithm yields the following expressions for the first four orders of the effective Hamiltonian:[7]

$$\begin{aligned}
Y_{1,AB} &= H_{1,AB},\\
\tilde{H}_{2,AA} &= H_{1,AB}V_1^\dagger/2 + \text{h.c.},\\
Y_{2,AB} &= V_1 H_{1,BB} - H_{1,AA}^\dagger V_1,\\
\tilde{H}_{3,AA} &= H_{1,AB}V_2^\dagger + \text{h.c.},\\
Y_{3,AB} &= -\frac{V_1 V_1^\dagger H_{1,BA}^\dagger}{2} + V_2 H_{1,BB} - \frac{\left(H_{1,AB}V_1^\dagger + V_1 H_{1,AB}^\dagger\right)V_1}{2} - H_{1,AA}^\dagger V_2,\\
\tilde{H}_{4,AA} &= \frac{H_{1,AB}V_3^\dagger}{2} + \frac{V_1 V_1^\dagger\left(H_{1,AB}V_1^\dagger + V_1 H_{1,AB}^\dagger\right)}{8} + \text{h.c.},
\end{aligned} \tag{2.35}$$

where V_n are the solutions of Sylvester's equation with $Y_{n,AB}$ as the right-hand side. These expressions utilize 1, 3, and 11, matrix products to obtain the same orders of the effective Hamiltonian. The advantage of the Pymablock algorithm becomes even more pronounced at higher orders or with multiple perturbative parameters due to the exponential growth of the number of terms in the reference expressions. While finding the optimized implementation from the reference expressions is possible for the 3-rd order, we expect it to be extremely challenging for the 4-th order, and essentially impossible to do manually for higher orders. Moreover, because the `BlockSeries` class tracks absent terms, in practice the number of matrix products depends on the sparsity of the block structure of the perturbation, as shown in Fig. 2.5.

The efficiency of Pymablock becomes especially apparent when applied to sparse numerical problems, similar to Sec. 2.2.3. We demonstrate the performance of the implicit method by using it to compute the low-energy spectrum of a large tight-binding

[7] The output is generated by the algorithm, with manual modifications only done for formatting.

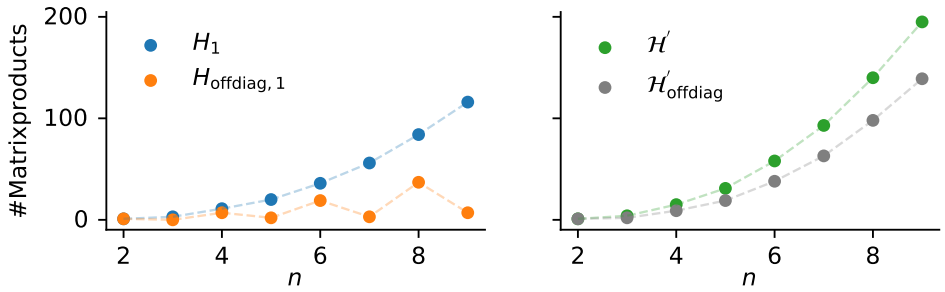

Figure 2.5: Matrix products required to compute $\tilde{H}_n^{AA}$ for a dense and block off-diagonal first-order perturbation (left) and a dense and block off-diagonal perturbative series with terms of all orders present (right).

model, and comparing Pymablock's time cost to that of sparse diagonalization. We define a 2D square lattice of 52×52 sites with nearest-neighbor hopping and a random on-site potential $\mu(\mathbf{r})$. The perturbation $\delta\mu(\mathbf{r})$ interpolates between two different disorder realizations. For the sake of an illustration, we choose the system's parameters such that the dispersion of the lowest few levels with $\delta\mu$ features avoided crossings and an overall nonlinear shape, whose details are not relevant. Similar to Sec. 2.2.3, constructing the effective Hamiltonian involves three steps. First, we compute the 10 lowest states of the unperturbed Hamiltonian using sparse diagonalization. Second, `block_diagonalize` computes a sparse LU decomposition of the Hamiltonian at each of the 10 eigenenergies. Third, we compute corrections $\tilde{H}_1$, $\tilde{H}_2$, and $\tilde{H}_3$ to the effective Hamiltonian, each being a 10×10 matrix. Each of these steps is a one-time cost, see Fig. 2.6. Finally, to compare the perturbative calculation to sparse diagonalization, we construct the effective Hamiltonian $\tilde{H} = H_0 + \delta\mu\tilde{H}_1 + \delta\mu^2\tilde{H}_2 + \delta\mu^3\tilde{H}_3$ and diagonalize it to obtain the low-energy spectrum for a range of $\delta\mu$. This has a negligible cost compared to constructing the series. The comparison is shown in Fig. 2.6. We observe that while the second order results are already very close to the exact spectrum, the third order corrections fully reproduce the sparse diagonalization. At the same time, the entire cost of computing the perturbative band structure for a range of $\delta\mu$ is lower than computing a single additional sparse diagonalization.

2.6. CONCLUSION

We developed an algorithm for constructing an effective Hamiltonian that combines advantages of different perturbative expansions. The main building block of our approach is a set of recurrence relations that define several series that depend on each other and combine into the effective Hamiltonian. Our algorithm constructs the same effective Hamiltonians as the Schrieffer–Wolff transformation [1] in the case of 2 subspaces, while keeping the linear scaling per extra order similar to the density matrix perturbation theory [16, 17] or the non-orthogonal perturbation theory [18]. Its expressions minimize the number of matrix multiplications per order, making it appealing both for symbolic and numerical computations. Pymablock's algorithm performs multi-block diagonalization and selective diagonalization with a single optimized algorithm.

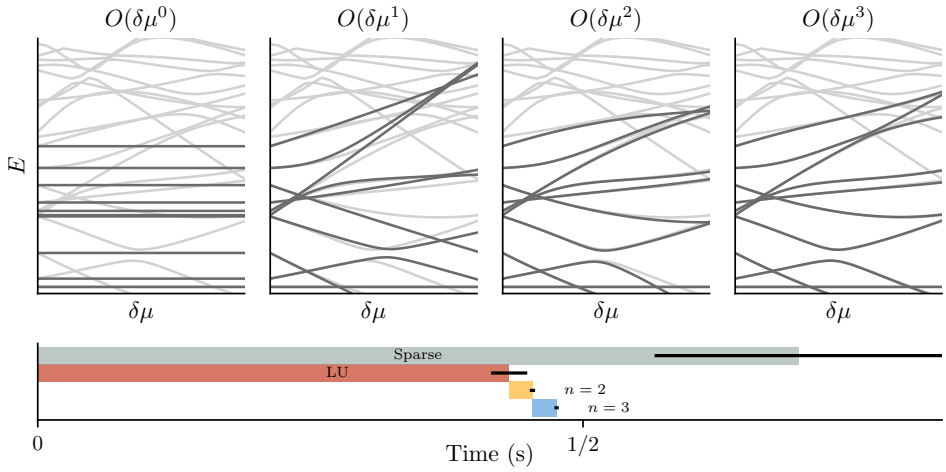

Figure 2.6: Top panels: band structure of the perturbative effective Hamiltonian (black) of a tight-binding model compared to exact sparse diagonalization (gray). Bottom panel: a comparison of the Pymablock's time cost with sparse diagonalization. Most of the time is spent in the LU decomposition of the Hamiltonian (red). The entire cost of the implicit method is lower than a single sparse diagonalization (gray). The operations of negligible cost are not shown. The bars length corresponds to the average time cost over 40 runs, and the error bars show the standard deviation.

We provide a Python implementation of the algorithm in the Pymablock package [53]. The package is thoroughly tested (95% test coverage as of version 2.1), becoming a reliable tool for constructing effective Hamiltonians that combine multiple perturbations to high orders. The core of the Pymablock interface is the `BlockSeries` class that handles arbitrary objects as long as they support algebraic operations. This enables Pymablock's construction of effective models for large tight-binding models using its implicit method as well as for second quantized Hamiltonians. As of version 2.1, applying Pymablock to second quantized Hamiltonians requires the user to provide a custom solver of the Lyapunov equation, which we plan to streamline in future versions. It also allows Pymablock to solve both symbolic and numerical problems in diverse physical settings, and potentially to incorporate it into existing packages, such as scqubits [35], QuTiP [54, 55], or dft2kp [56].

Beyond the Schrieffer–Wolff transformation, the Pymablock package provides a foundation for defining other perturbative expansions. We anticipate extending it to time-dependent problems, where the different regimes of the time-dependent drive modify the recurrence relations that need to be solved [10, 57]. Applying the same framework to problems with weak position dependence would allow to construct a nonlinear response theory of quantum materials. These two extensions are active areas of research [7, 46, 51, 52, 58, 59]. Finally, we expect that in the many-particle context the same framework supports implementing different flavors of diagrammatic expansions.

ACKNOWLEDGEMENTS

We thank Valla Fatemi and Antonio Manesco for feedback on the manuscript. We also thank David P. DiVincenzo for motivating and helpful discussions regarding the multi-block diagonalization algorithm.

DATA AVAILABILITY

The code used to produce the reported results is available on Zenodo [53].

FUNDING INFORMATION

This research was supported by the Netherlands Organization for Scientific Research (NWO/OCW) as part of the Frontiers of Nanoscience program, a NWO VIDI grant 016.Vidi.189.180, and OCENW.GROOT.2019.004. D.V. acknowledges funding from the Deutsche Forschungsgemeinschaft (DFG, German Research Foundation) under Germany's Excellence Strategy through the Würzburg-Dresden Cluster of Excellence on Complexity and Topology in Quantum Matter – ct.qmat (EXC 2147, project-ids 390858490 and 392019).

REFERENCES

[1] Schrieffer, J. R. and Wolff, P. A. "Relation between the Anderson and Kondo Hamiltonians". In: *Phys. Rev.* 149 (2 1966). DOI: 10.1103/PhysRev.149.491.

[2] Bravyi, S., DiVincenzo, D. P., and Loss, D. "Schrieffer–Wolff transformation for quantum many-body systems". In: *Annals of Physics* 326.10 (2011). DOI: 10.1016/j.aop.2011.06.004.

[3] Löwdin, P.-O. "Studies in Perturbation Theory. IV. Solution of Eigenvalue Problem by Projection Operator Formalism". In: *Journal of Mathematical Physics* 3.5 (1962). DOI: 10.1063/1.1724312.

[4] Luttinger, J. M. and Kohn, W. "Motion of Electrons and Holes in Perturbed Periodic Fields". In: *Phys. Rev.* 97 (4 1955). DOI: 10.1103/PhysRev.97.869.

[5] Roland, W. "Spin-orbit coupling effects in two-dimensional electron and hole systems". In: *Springer Tracts in Modern Physiscs: Springer, Berlin, Heidelberg* 191 (2003). DOI: 10.1007/b13586.

[6] McCann, E. and Koshino, M. "The electronic properties of bilayer graphene". In: *Reports on Progress in Physics* 76.5 (2013). DOI: 10.1088/0034-4885/76/5/056503.

[7] Bernevig, B. A. et al. "Twisted bilayer graphene. I. Matrix elements, approximations, perturbation theory, and a $k \cdot p$ two-band model". In: *Phys. Rev. B* 103 (20 2021). DOI: 10.1103/PhysRevB.103.205411.

[8] Krantz, P. et al. "A quantum engineer's guide to superconducting qubits". In: *Applied physics reviews* 6.2 (2019). DOI: 10.1063/1.5089550.

[9] Romhányi, J., Burkard, G., and Pályi, A. "Subharmonic transitions and Bloch–Siegert shift in electrically driven spin resonance". In: *Phys. Rev. B* 92 (5 2015). DOI: 10.1103/PhysRevB.92.054422.

[10] Malekakhlagh, M., Magesan, E., and McKay, D. C. "First-principles analysis of cross-resonance gate operation". In: *Physical Review A* 102.4 (2020). DOI: 10.1103/physreva.102.042605.

[11] Petrescu, A. et al. "Accurate Methods for the Analysis of Strong-Drive Effects in Parametric Gates". In: *Physical Review Applied* 19.4 (2023). DOI: 10.1103/physrevapplied.19.044003.

[12] Van Vleck, J. H. "On σ-Type Doubling and Electron Spin in the Spectra of Diatomic Molecules". In: *Phys. Rev.* 33 (4 1929). DOI: 10.1103/PhysRev.33.467.

[13] Shavitt, I. and Redmon, L. T. "Quasidegenerate perturbation theories. A canonical van Vleck formalism and its relationship to other approaches". In: *The Journal of Chemical Physics* 73.11 (1980). DOI: 10.1063/1.440050.

[14] Klein, D. J. "Degenerate perturbation theory". In: *The Journal of Chemical Physics* 61.3 (1974). DOI: 10.1063/1.1682018.

[15] Suzuki, K. and Okamoto, R. "Degenerate Perturbation Theory in Quantum Mechanics". In: *Progress of Theoretical Physics* 70.2 (1983). DOI: 10.1143/PTP.70.439.

[16] McWeeny, R. "Perturbation Theory for the Fock–Dirac Density Matrix". In: *Phys. Rev.* 126 (3 1962). DOI: 10.1103/PhysRev.126.1028.

[17] Truflandier, L. A., Dianzinga, R. M., and Bowler, D. R. "Notes on density matrix perturbation theory". In: *The Journal of Chemical Physics* 153.16 (2020). DOI: 10.1063/5.0022244.

[18] Bloch, C. "Sur la théorie des perturbations des états liés". In: *Nuclear Physics* 6 (1958). DOI: 10.1016/0029-5582(58)90116-0.

[19] Wegner, F. "Flow-equations for Hamiltonians". In: *Annalen der physik* 506.2 (1994).

[20] Kehrein, S. *The flow equation approach to many-particle systems*. Vol. 217. Springer, 2007. ISBN: 978-3-540-34067-6.

[21] Knetter, C. and Uhrig, G. S. "Perturbation theory by flow equations: dimerized and frustrated S=1/2 chain". In: *The European Physical Journal B-Condensed Matter and Complex Systems* 13 (2000). DOI: 10.1007/s100510050026.

[22] Oitmaa, J., Hamer, C., and Zheng, W. *Series expansion methods for strongly interacting lattice models*. Cambridge University Press, 2006. ISBN: 9780511584398.

[23] Krull, H., Drescher, N. A., and Uhrig, G. S. "Enhanced perturbative continuous unitary transformations". In: *Phys. Rev. B* 86 (12 2012). DOI: 10.1103/PhysRevB.86.125113.

[24] Wurtz, J., Claeys, P. W., and Polkovnikov, A. "Variational Schrieffer–Wolff transformations for quantum many-body dynamics". In: *Phys. Rev. B* 101 (1 2020). DOI: 10.1103/PhysRevB.101.014302.

[25] Zhang, Z. et al. "Quantum algorithms for Schrieffer–Wolff transformation". In: *Phys. Rev. Res.* 4 (4 2022). DOI: 10.1103/PhysRevResearch.4.043023.

[26] Mankodi, I. N. H. and DiVincenzo, D. P. *Perturbative power series for block diagonalisation of Hermitian matrices*. 2024. DOI: 10.48550/arXiv.2408.14637. arXiv: 2408.14637 [quant-ph].

[27] Magesan, E. and Gambetta, J. M. "Effective Hamiltonian models of the cross-resonance gate". In: *Phys. Rev. A* 101 (5 2020). DOI: 10.1103/PhysRevA.101.052308.

[28] Xu, X. et al. *Lattice Hamiltonians and Stray Interactions Within Quantum Processors*. 2024. DOI: 10.48550/arXiv.2402.09145. arXiv: 2402.09145 [quant-ph].

[29] Knetter, C., Schmidt, K. P., and Uhrig, G. S. "The structure of operators in effective particle-conserving models". In: *Journal of Physics A: Mathematical and General* 36.29 (2003). DOI: 10.1088/0305-4470/36/29/302.

[30] Blais, A. et al. "Cavity quantum electrodynamics for superconducting electrical circuits: An architecture for quantum computation". In: *Phys. Rev. A* 69 (6 2004). DOI: 10.1103/PhysRevA.69.062320.

[31] Zhu, G. et al. "Circuit QED with fluxonium qubits: Theory of the dispersive regime". In: *Phys. Rev. B* 87 (2 2013). DOI: 10.1103/PhysRevB.87.024510.

[32] Li, X. et al. "Tunable Coupler for Realizing a Controlled-Phase Gate with Dynamically Decoupled Regime in a Superconducting Circuit". In: *Phys. Rev. Appl.* 14 (2 2020). DOI: 10.1103/PhysRevApplied.14.024070.

[33] Blais, A. et al. "Circuit quantum electrodynamics". In: *Rev. Mod. Phys.* 93 (2 2021). DOI: 10.1103/RevModPhys.93.025005.

[34] Sete, E. A. et al. "Floating Tunable Coupler for Scalable Quantum Computing Architectures". In: *Phys. Rev. Appl.* 15 (6 2021). DOI: 10.1103/PhysRevApplied.15.064063.

[35] Groszkowski, P. and Koch, J. "Scqubits: a Python package for superconducting qubits". In: *Quantum* 5 (2021). DOI: 10.22331/q-2021-11-17-583.

[36] Chitta, S. P. et al. "Computer-aided quantization and numerical analysis of superconducting circuits". In: *New Journal of Physics* 24.10 (2022). DOI: 10.1088/1367-2630/ac94f2.

[37] Li, B., Calarco, T., and Motzoi, F. "Nonperturbative Analytical Diagonalization of Hamiltonians with Application to Circuit QED". In: *PRX Quantum* 3 (3 2022). DOI: 10.1103/PRXQuantum.3.030313.

[38] Melo, A., Tanev, T., and Akhmerov, A. R. "Greedy optimization of the geometry of Majorana Josephson junctions". In: *SciPost Phys.* 14 (2023). DOI: 10.21468/SciPostPhys.14.3.047.

[39] Meurer, A. et al. "SymPy: symbolic computing in Python". In: *PeerJ Computer Science* 3 (2017). DOI: 10.7717/peerj-cs.103.

[40] Groth, C. W. et al. "Kwant: a software package for quantum transport". In: *New Journal of Physics* 16.6 (2014). DOI: 10.1088/1367-2630/16/6/063065.

[41] Virtanen, P. et al. "SciPy 1.0: fundamental algorithms for scientific computing in Python". In: *Nature methods* 17.3 (2020). DOI: 10.1038/s41592-019-0686-2.

[42] Savitz, S. and Refael, G. “Stable unitary integrators for the numerical implementation of continuous unitary transformations”. In: *Phys. Rev. B* 96 (11 2017). DOI: 10.1103/PhysRevB.96.115129.

[43] McWeeny, R. “Self-consistent perturbation thèory”. In: *Chemical Physics Letters* 1.12 (1968). DOI: 10.1016/0009-2614(68)85047-X.

[44] Cederbaum, L. S., Schirmer, J., and Meyer, H. .-. “Block diagonalisation of Hermitian matrices”. In: *J. Phys. A* 22.13 (1989). DOI: 10.1088/0305-4470/22/13/035.

[45] Landi, G. T. *Eigenoperator approach to Schrieffer–Wolff perturbation theory and dispersive interactions*. 2024. DOI: 10.48550/arXiv.2409.10656. arXiv: 2409.10656 [quant-ph].

[46] Reascos, L., Diotallevi, G. F., and Benito, M. *Universal solution to the Schrieffer–Wolff Transformation Generator*. 2024. DOI: 10.48550/arXiv.2411.11535. arXiv: 2411.11535 [quant-ph].

[47] Irfan, M. et al. *Hybrid kernel polynomial method*. 2019. DOI: 10.48550/arXiv.1909.09649.

[48] Amestoy, P. R. et al. “A Fully Asynchronous Multifrontal Solver Using Distributed Dynamic Scheduling”. In: *SIAM Journal on Matrix Analysis and Applications* 23.1 (2001). DOI: 10.1137/S0895479899358194.

[49] Amestoy, P. R. et al. “Hybrid scheduling for the parallel solution of linear systems”. In: *Parallel Computing* 32.2 (2006). DOI: 10.1016/j.parco.2005.07.004.

[50] Weiße, A. et al. “The kernel polynomial method”. In: *Rev. Mod. Phys.* 78 (1 2006). DOI: 10.1103/RevModPhys.78.275.

[51] Motzoi, F. et al. “Simple Pulses for Elimination of Leakage in Weakly Nonlinear Qubits”. In: *Phys. Rev. Lett.* 103 (11 2009). DOI: 10.1103/PhysRevLett.103.110501.

[52] Theis, L. S. et al. “Counteracting systems of diabaticities using DRAG controls: The status after 10 years”. In: *Europhys. Lett.* 123.6 (2018). DOI: 10.1209/0295-5075/123/60001.

[53] Araya Day, I. et al. *Pymablock*. Version 2.0. 2024. DOI: 10.5281/zenodo.14188554.

[54] Johansson, J., Nation, P., and Nori, F. “QuTiP: An open-source Python framework for the dynamics of open quantum systems”. In: *Computer Physics Communications* 183.8 (2012). DOI: 10.1016/j.cpc.2012.02.021.

[55] Johansson, J., Nation, P., and Nori, F. “QuTiP 2: A Python framework for the dynamics of open quantum systems”. In: *Computer Physics Communications* 184.4 (2013). DOI: 10.1016/j.cpc.2012.11.019.

[56] Cassiano, J. V. V. et al. “DFT2kp: Effective kp models from ab-initio data”. In: *SciPost Phys. Codebases* (2024). DOI: 10.21468/SciPostPhysCodeb.25.

[57] Rodriguez-Vega, M., Lentz, M., and Seradjeh, B. “Floquet perturbation theory: formalism and application to low-frequency limit”. In: *New Journal of Physics* 20.9 (2018). DOI: 10.1088/1367-2630/aade37.

[58] Venkatraman, J. et al. “Static Effective Hamiltonian of a Rapidly Driven Nonlinear System”. In: *Phys. Rev. Lett.* 129 (10 2022). DOI: 10.1103/PhysRevLett.129.100601.

[59] Xu, Y. and Guo, L. *Perturbative Framework for Engineering Arbitrary Floquet Hamiltonian*. 2024. DOI: 10.48550/arXiv.2410.10467. arXiv: 2410.10467 [quant-ph].

3

KITAEV CHAIN IN AN ALTERNATING QUANTUM DOT-ANDREEV BOUND STATE ARRAY

Sebastian Miles, David van Driel, Michael Wimmer, and Chun-Xiao Liu

We propose to implement a Kitaev chain based on an array of alternating normal and superconductor hybrid quantum dots embedded in semiconductors. In particular, the orbitals in the dot and the Andreev bound states in the hybrid are now on equal footing and both emerge as low-energy degrees of freedom in the Kitaev chain, with the couplings being induced by direct tunneling. Due to the electron and hole components in the Andreev bound state, this coupling is simultaneously of the normal and Andreev types, with their ratio being tunable by varying one or several of the experimentally accessible physical parameters, e.g., strength and direction of the Zeeman field, as well as changing proximity effect on the normal quantum dots. As such, it becomes feasible to realize a two-site Kitaev chain in a simple setup with only one normal quantum dot and one hybrid segment. Interestingly, when scaling up the system to a three-site Kitaev chain, next-nearest-neighbor couplings emerge as a result of high-order tunneling, lifting the Majorana zero energy at the sweet spot. This energy splitting is mitigated in a longer chain, approaching topological protection. Our proposal has two immediate advantages: obtaining a larger energy gap from direct tunneling and creating a Kitaev chain using a reduced number of quantum dots and hybrid segments.

Own contribution to work: Performed the analytical and numerical calculations, produced the plots, contributed to the writing of the manuscript.

This chapter has been published as Phys. Rev. **B** 110, 024520.. The formatting has been adapted for this thesis.

3.1. INTRODUCTION

The Kitaev chain is a toy model comprised of an array of spinless fermions with both normal and Andreev tunnelings between neighboring sites [1]. As a one-dimensional p-wave superconductor, the Kitaev chain in its topological phase will host a pair of Majorana zero modes localized at the endpoints of the chain [2–13]. These exotic quasiparticles are non-Abelian anyons, i.e., exchanging or braiding two Majoranas will transform between distinct ground-state wavefunctions in the degenerate manifold [14]. Moreover, since two Majorana modes are spatially separated, quantum information encoded in such a Majorana pair will be more robust against local perturbation and decoherence. With all these intriguing physical properties, Majorana zero modes are regarded as a promising candidate for implementing error-resilient topological quantum computing [15–18].

In solid-state physics, one-dimensional topological superconductivity can be realized in several different types of hybrid materials, e.g., semiconductor-superconductor nanowires [11, 19–23], normal channels between planar Josephson junctions [24–26], ferromagnetic atomic chains on top of a superconductor [27, 28]. Despite much experimental progress, a hybrid nanowire is inevitably subject to inhomogeneity and disorder, which can give rise to topologically trivial subgap states [29–35], hindering an unambiguous detection of a topological superconductor. Within this context, a very appealing solid-state platform for implementing a Kitaev chain is based on an array of semiconducting quantum dots [36], which is much more immune to the effect of disorder owing to the large level spacing of dot orbitals relative to the disorder fluctuations. In particular, under a sufficiently strong magnetic field, the spin-polarized dot orbitals serve as spinless fermions, coupling with neighboring ones through both, normal and Andreev couplings originating from elastic cotunneling (ECT), and crossed Andreev reflection (CAR) mediated by a superconductor. Interestingly, even in a setup of only two quantum dots, a two-site Kitaev chain can be realized and host a pair of poor man's Majorana zero modes at a fine-tuned sweet spot [37].

Very recently, significant experimental progress has been made to transform the above-mentioned theoretical proposals and ideas into a physical realization. In a minimal Kitaev chain device of double quantum dots, the conductance spectrocopies measured at the sweet spot are consistent with the signatures of Majorana zero modes [38]. Here, the key physical insight is to mediate the effective couplings between dot orbitals using Andreev bound states (ABS) in a semiconductor-superconductor hybrid [39] instead of the continuum states of superconductivity [36, 37]. Coupling through an ABS allows that the ratio of CAR and ECT amplitudes can be controlled by varying the chemical potential in the hybrid segment via electrostatic gating [39–42]. This effect was shown to be robust to Coulumb interactions in the dots as well as strong coupling [43]. In spite of progress, current Kitaev chain devices are still suffering from several shortcomings which may limit its application in quantum technology in the future. First, the excitation energy gap is relatively small ($\sim 25\ \mu$eV), owing to the fact that CAR and ECT couplings, which are induced by second-order tunneling processes, scale with the tunneling amplitude as $\sim t_0^2/\Delta_0$, with t_0 the characteristic dot-hybrid tunneling strength and Δ_0 the induced gap of ABS. Second, when scaling up the system into an N-site Kitaev chain, one needs to have N quantum dots and $N-1$ pieces of hybrid segments, which makes

the device fabrication process increasingly challenging for a longer chain.

Alternatively to using normal quantum dots, Ref. [44] proposed to use Andreev bound states in proximitized quantum dots directly as spinless fermions in a Kitaev chain. There, control over the proximity effect in each quantum dot was required, e.g. by using a quantum point contact to couple to the superconductor.

In the current work, we propose a new method to create Kitaev chain combining the advantages of previous proposals. Our implementation is based on an array of alternating quantum dot and semiconductor-superconductor hybrid (see Fig. 3.1). In particular, the orbitals in the quantum dots and the ABS in the hybrids are now on equal footing as the spinless fermions in the Kitaev chain, with the effective couplings being induced by direct tunneling. Due to the electron and hole nature of the ABS, this coupling is simultaneously of the normal and Andreev type, with their ratio being tunable by varying one or several of the experimentally accessible physical parameters, such as strength and direction of the Zeeman field, as well as the changing the tunnel coupling between normal and hybrid quantum dots. As such, it becomes possible to implement a two-site Kitaev chain in a simple setup with only one quantum dot and one hybrid segment, and in general an N-site Kitaev chain requires only N pieces of basic elements of either dot or hybrid instead of $2N-1$ as proposed in Ref. [36]. At the same time, our proposal does not require control of proximity effect in individual dots as in Ref. [44], and can be realized in the same type of devices as previous experiments [39–42]. Moreover, the energy gap of the proposed Kitaev chain will be readily enhanced $\sim t_0$ owing to the direct tunneling between dot and hybrid. Interestingly, when scaling up the system to a three-site Kitaev chain, next-nearest neighbor couplings emerge as a result of high-order tunneling, lifting the Majorana zero energy at the sweet spot. Nevertheless, this energy splitting is mitigated in a longer chain, giving robust zero mode within a larger parameter space, as topological protection is approached.

While our approach is based on alternating normal and hybrid quantum dots, a parallel work considers the case of two superconducting quantum dots showing that a phase difference alone can be used to tune to a sweet spot [45].

The remainder of the work is structured as follows: Section 3.2 focuses on the study of minimal Kitaev chain based on a single pair of quantum dot and ABS. We introduce the model Hamiltonian in Sec. 3.2.1 and derive its low-energy effective theory in Sec. 3.2.2. In particular, in Sec. 3.2.3-3.2.5 we show how one can systematically fine-tune the sweet spot using experimentally accessible physical parameters, e.g., strength and direction of the Zeeman field, as well as induced pairing gap on the quantum dots. In Sec. 3.3, we consider scaling up of the dot-ABS chain, highlighting the emergence of next-nearest couplings and the effects on the Majorana properties at the sweet spot. Section 3.4 is devoted to discussions before we summarize our work in Sec. 3.5.

3.2. MINIMAL KITAEV CHAIN IN A DOT-ABS PAIR

We first consider a minimal setup comprised of one quantum dot in the normal part and one ABS in the hybrid section. In particular, we derive the effective normal and Andreev couplings between them and the dependence of their ratio on experimentally accessible parameters. Importantly, such a simple setup is sufficient for realizing a two-site Kitaev chain and can host poor man's Majorana zero modes at a fine-tuned sweet spot.

3.2.1. MODEL HAMILTONIAN

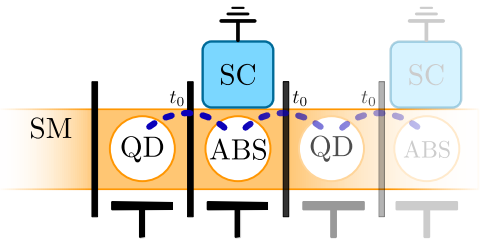

Figure 3.1: Schematic of a Kitaev chain device from alternating quantum dots and Andreev bound states created in semiconductor-superconductor hybrids. Quantum dots are formed by confinement potentials induced by tunnel gates (vertical black lines), while ABS emerge in the quantum dot hosted in the hybrid segment where the semiconductor is proximitized by superconductivity. The tunneling strength (purple dashed lines) between dot and ABS can be tuned by varying the voltage of the tunnel gates, and the chemical potentials of the dot and ABS can be adjusted by changing the plunger gate voltages (black T-elements).

The model Hamiltonian for a quantum dot-ABS pair is

$$\begin{aligned} H_{DA} &= H_D + H_A + H_T, \\ H_D &= (\varepsilon_D + E_{ZD}) n_{D\uparrow} + (\varepsilon_D - E_{ZD}) n_{D\downarrow} + U_D n_{D\uparrow} n_{D\downarrow}, \\ H_A &= (E_A + E_{ZA}) \gamma_{A\uparrow}^\dagger \gamma_{A\uparrow} + (E_A - E_{ZA}) \gamma_{A\downarrow}^\dagger \gamma_{A\downarrow}, \\ H_T &= t_0 \sum_{\sigma,\eta=\uparrow,\downarrow} c_\sigma^\dagger (U_{so})_{\sigma\eta} d_\eta + h.c.. \end{aligned} \tag{3.1}$$

Here H_D is the Hamiltonian for a quantum dot with a single spinful orbital, which is a valid approximation when the dot level spacing is large. $n_{D\sigma} = d_\sigma^\dagger d_\sigma$ is the occupancy number of the dot orbital with spin σ, ε_D is the orbital energy, E_{ZD} is the strength of the induced Zeeman spin splitting, and U_D is the Coulomb energy. H_A is the Hamiltonian of the semiconductor-superconductor hybrid. We assume that the low-energy physics of the hybrid is well described by a pair of subgap ABS, with all the above-gap continuum states being neglected. $\gamma_{A\sigma} = \sigma u c_\sigma + v c_{\bar{\sigma}}^\dagger$ is the Bogoliubov operator of the ABS with $\sigma = \pm 1$ for spin $\uparrow\downarrow$, and $u^2 = 1 - v^2 = 1/2 + \varepsilon_A/2E_A$ are the BCS coherence factors. $E_A = \sqrt{\varepsilon_A^2 + \Delta_0^2}$ is the excitation energy, ε_A is the normal-state energy, Δ_0 is the induced pairing gap, and E_{ZA} is the strength of the induced Zeeman spin splitting. Here the Zeeman energy for both quantum dot and ABS are induced by the same globally applied magnetic field, and thereby the spin polarization axis of them coincide. However, owing to the g factor renormalization at the semiconductor-superconductor interface [46–48], E_{ZA} can be much weaker than E_{ZD}. In our numerical simulations, we set $E_{ZA} = E_{ZD}/2$ without loss of generality. H_T is the tunnel Hamiltonian between dot and ABS, with t_0 being the tunneling amplitude which can be controlled by varying the tunnel gate voltage. U_{so} is a unitary matrix

$$\begin{aligned} U_{so} &= e^{-i\alpha\sigma_\theta} \\ &= \begin{pmatrix} \cos\alpha - i\sin\alpha\sin\theta & -\sin\alpha\cos\theta \\ \sin\alpha\cos\theta & \cos\alpha + i\sin\alpha\sin\theta \end{pmatrix}, \end{aligned} \tag{3.2}$$

with the diagonal and off-diagonal elements denoting the spin-conserving and spin-flipping processes, respectively. Here α is the amount of spin precession accumulated in the tunnel region due to spin-orbit interaction. $\sigma_\theta = \cos\theta\sigma_y + \sin\theta\sigma_z$ is the spin-orbit field, which is perpendicular to the quantum dot chain axis. Without loss of generality, here we have chosen a frame where the magnetic field direction and thus the dot spin polarization axis are fixed, and a rotation of the magnetic field is now equivalently described by rotating the spin-orbit field. In particular, θ is the angle between the magnetic field and the dot chain axis, with $\theta = 0$ ($\theta = \pi/2$) corresponding to being perpendicular (parallel) to the applied magnetic field.

3.2.2. LOW-ENERGY EFFECTIVE THEORY AND SWEET SPOT CONDITIONS

We now derive the low-energy effective theory of the dot-ABS pair introduced in Eq. (3.1). In the strong Zeeman field regime, the spin-down ABS state gets closer to the Fermi energy while the spin-up ABS becomes higher in energy and can be projected away in the leading-order approximation. For the quantum dot, either of the spin-polarized orbitals can be closer to the Fermi energy than the other, depending on the value of the dot chemical potential. Here, without loss of generality we restrict our discussions to the spin-down states as the low-energy degrees of freedom in both segments, leaving the discussions of other spin configurations in the supplemental material. Therefore, in the weak tunneling, i.e., $t_0 \ll E_{ZD}, E_{ZA}$, the effective Hamiltonian of a dot-ABS pair is

$$\begin{aligned} H_{DA}^{\text{eff}} \equiv PH_{\text{DA}}P = (\varepsilon_D - E_{ZD})d_\downarrow^\dagger d_\downarrow + (E_A - E_{ZA})\gamma_{A\downarrow}^\dagger \gamma_{A\downarrow} \\ - tu\gamma_{A\downarrow}^\dagger d_\downarrow - t_{so} v\gamma_{A\downarrow} d_\downarrow + h.c., \end{aligned} \tag{3.3}$$

where P projects the original Hamiltonian onto the spin-down states, t and t_{so} are the tunnel amplitudes for the spin-conserving and spin-flipping processes, respectively, which are defined as

$$\begin{aligned} t &= (U_{so})_{\downarrow\downarrow} = t_0(\cos\alpha + i\sin\alpha\sin\theta), \\ t_{so} &= (U_{so})_{\downarrow\uparrow} = t_0\sin\alpha\cos\theta, \end{aligned} \tag{3.4}$$

according to Eq. (3.2). Crucially, because an ABS is a coherent superposition of both electron (u) and hole (v) components, single electron tunneling from the quantum dot to the hybrid will simultaneously create and annihilate an ABS Bogoliubov excitation, giving both normal and Andreev-like effective couplings

$$t_{\text{eff}} = -tu, \quad \Delta_{\text{eff}} = -t_{so} v \tag{3.5}$$

between dot and ABS, as shown in Eq. (3.3). On the other hand, the Hamiltonian for a two-site Kitaev chain is

$$H_{K2} = \varepsilon_1 f_1^\dagger f_1 + \varepsilon_2 f_2^\dagger f_2 + t_{12} f_2^\dagger f_1 + \Delta_{12} f_2 f_1 + h.c., \tag{3.6}$$

where f_i is the annihilation operator of a spinless fermion on site-i, ε_i is the on-site energy, t_{12} and Δ_{12} are the normal and Andreev-like tunneling between adjacent sites. By comparing Eq. (3.3) with Eq. (3.6), we obtain the first main finding in the current work

that the low-energy physics of a dot-ABS pair in the strong Zeeman regime is a two-site Kitaev chain. In particular, the correspondence between the two is as below

$$\begin{aligned} f_1 &\to d_\downarrow, \\ f_2 &\to \gamma_{A\downarrow}, \\ \varepsilon_1 &\to \varepsilon_D - E_{ZD}, \\ \varepsilon_2 &\to E_A - E_{ZA}, \\ t_{12} &\to t_{\text{eff}} = -tu, \\ \Delta_{12} &\to \Delta_{\text{eff}} = -t_{so}v. \end{aligned} \tag{3.7}$$

Furthermore, the sweet spot of a two-site Kitaev chain is defined as $\varepsilon_1 = \varepsilon_2 = 0$ and $|t_{12}| = |\Delta_{12}|$. That is, both the dot orbital energy

$$\varepsilon_D - E_{ZD} = 0, \tag{3.8}$$

and the ABS energy

$$\sqrt{\varepsilon_A^2 + \Delta_0^2} - E_{ZA} = 0, \tag{3.9}$$

need to be adjusted to be on resonance. In addition, the magnitudes of normal and Andreev-like couplings need to be in perfect balance

$$|tu| = |t_{so}v|. \tag{3.10}$$

Once the sweet spot conditions indicated by Eqs. (3.8)- (3.10) are all satisfied, a pair of poor man's Majorana zero modes will emerge and localize themselves on the dot and hybrid segments, respectively, see also Fig. 3.2 (d).

3.2.3. TUNING ZEEMAN FIELD STRENGTH

We now consider how to reach the sweet spot in a dot-ABS pair by varying experimentally accessible parameters. The most crucial step is the capability of tuning the relative amplitude of t_{eff} and Δ_{eff}. In this subsection, we focus on using the Zeeman field strength as the tuning knob, which means one only varies the strength of the applied magnetic field, with its direction being fixed to be perpendicular to the Rashba spin-orbit field. Setting $\theta = \pi/2$, we thereby have $t = t_0 \cos\alpha$ and $t_{so} = t_0 \sin\alpha$ in Eq. (3.4). Among the three sweet spot conditions, the zero-energy dot orbital defined in Eq. (3.8) can be readily satisfied by merely varying the dot chemical potential. By contrast, the other two defined in Eqs. (3.9) and (3.10) are more subtle and mutually constrained. Specifically, under a sufficiently large Zeeman field ($E_{ZA} > \Delta_0$), a zero-energy ABS is obtained only when the normal-state energy is pinned at

$$\varepsilon_A^* \equiv -\sqrt{E_{ZA}^2 - \Delta_0^2} < 0. \tag{3.11}$$

Note that here we particularly choose the negative ε_A solution, corresponding to a hole-dominant ABS ($u < v$) such that a balance between t_{eff} and Δ_{eff} indicated in Eq. (3.10) can be obtained in the weak spin-orbit interaction regime $t_{so} < t$ (a complete overview of all

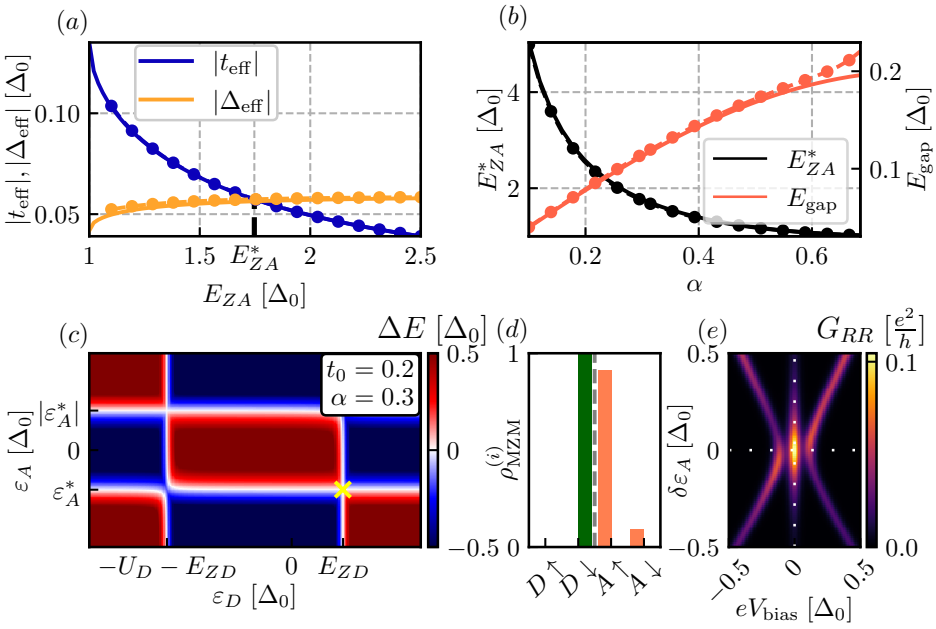

Figure 3.2: (a) strength of the effective couplings $t_{\rm eff}$ and $\Delta_{\rm eff}$ as a function of E_{ZA} in a dot-ABS configuration. Analytic (numerical) results are presented with solid lines (dots). In the numerical calculations, the normal dot Zeeman energy is chosen to be $E_{ZD} = 2E_{ZA}$. At $E_{ZA} = E^*_{ZA}$, we find $|t_{\rm eff}| = |\Delta_{\rm eff}|$. (b) Sweet spot Zeeman energy E^*_{ZA} and excitation gap $E_{\rm gap}$ as a function of α due to spin-orbit interaction. (c) Charge stability diagram at $E_{ZA} = E^*_{ZA}$. Here $\Delta E = E_{\rm odd,\,gs} - E_{\rm even,\,gs}$ is the energy difference between the ground states in opposite fermion parity subspaces. The sweet spot is indicated by a yellow cross. (d) Majorana wavefunctions $\rho^{(i)}_{\rm MZM}$ at the sweet spot in (c). (e) Local conductance G_{RR} as a function of bias voltage $V_{\rm bias}$ and ABS detuning $\delta\varepsilon_A$.

possible sweet-spot conditions is given in the Appendix). As a result, the dependence of the magnitudes of the effective couplings on the Zeeman field strength is as below

$$|t_{\rm eff}(E_{ZA})| = \frac{t_0\cos\alpha}{\sqrt{2}}\sqrt{1-\sqrt{1-\Delta_0^2/E_{ZA}^2}},$$
$$|\Delta_{\rm eff}(E_{ZA})| = \frac{t_0\sin\alpha}{\sqrt{2}}\sqrt{1+\sqrt{1-\Delta_0^2/E_{ZA}^2}}. \tag{3.12}$$

Equations (3.11) and (3.12) show that increasing the Zeeman field strength, is changing the electron and hole components of the zero-energy ABS, i.e., increasing v from $1/\sqrt{2}$ to close to 1, while decreasing u from $1/\sqrt{2}$ to nearly zero. Therefore, with E_{ZA} increasing from Δ_0, the Andreev coupling $|\Delta_{\rm eff}|$ is enhanced from $t_0\sin\alpha/\sqrt{2}$ to $\sim t_0\sin\alpha$ while the normal coupling $|t_{\rm eff}|$ is suppressed from $t_0\cos\alpha/\sqrt{2}$ to zero in the large Zeeman limit [see Fig. 3.2(a)]. As a result, in the weak spin-orbit interaction regime ($\alpha < \pi/4$), which is experimentally relevant for InAs and InSb hybrid nanowires [38, 40–42], the two coupling

strengths will become equal at

$$E^*_{ZA} = \frac{\Delta_0}{\sin(2\alpha)}, \tag{3.13}$$

as indicated by the black dashed line in Fig. 3.2(a). Furthermore, the excitation gap at this fine-tuned point is

$$E_{\text{gap}} = 2|t_{\text{eff}}(E^*_{ZA})| = t_0 \sin(2\alpha), \tag{3.14}$$

which is defined as twice the effective coupling strength. As shown in Fig. 3.2(b), E^*_{ZA} is a decreasing as a function of the spin-orbit interaction strength α, while E_{gap} is increasing. In general, a larger E^*_{ZA} is preferable in order to allow for a wider detuning range of the ABS energy $\delta\varepsilon_A \sim \sqrt{E^{*2}_{ZA} - \Delta_0^2}$. Therefore, in choosing the optimal value of spin-orbit interaction α for the dot-ABS pair, there exists a tradeoff between a sizeable gap E_{gap} and a large range of allowed $\delta\varepsilon_A$ for the effective Kitaev model.

To corroborate the analytic results obtained from the low-energy theory, we perform numerical simulations of the dot-ABS pair based on the full many-body Hamiltonian introduced in Eq. (3.1). In particular, we choose $\Delta_0 = 1$ to be the natural unit, $U_D = 5$, $t_0 = 0.2$ and $\alpha = 0.3$, putting the system into the weak tunneling and weak spin-orbit interaction regime. As shown in Fig. 3.2(a), the numerically calculated $|t_{\text{eff}}|$ and $|\Delta_{\text{eff}}|$ as a function of E_{ZA} are in excellent agreement with the analytic results shown in Eq. (3.12). In Fig. 3.2(b), the calculated E^*_{ZA} and E_{gap} also match very well with the analytical predictions in Eqs. (3.13) and (3.14). Figures 3.2(c) shows the charge stability diagram in the $(\varepsilon_D, \varepsilon_A)$ plane. A sweet spot, which is defined as the degeneracy point between even- and odd-parity ground states along with balanced normal and Andreev coupling strengths, appears in the right-bottom corner when $E_{ZA} \approx 1.75\,\Delta_0$, consistent with the analytically predicted value of $E^*_{ZA} = 1.77\,\Delta_0$. Here, the right-bottom corner corresponds to a spin-down dot orbital and a hole-dominant ABS, which is the focus of this section. Furthermore, the calculated wavefunctions in Fig. 3.2(d) show that indeed, a pair of Majorana zero modes emerge at the sweet spot [yellow cross in Fig. 3.2(c)], localized at the quantum dot and hybrid, respectively. In Fig. 3.2(e), the calculated tunnel conductance spectroscopy in the $(V_{\text{bias}}, \delta\varepsilon_A)$ plane shows a stable zero-bias peak and a parabola-shaped gap peak, consistent with the conductance features of poor man's Majorana zero modes.

3.2.4. TUNING ZEEMAN FIELD DIRECTION

We now consider rotating the applied magnetic field in order to find the sweet spot, with the field strength being fixed. Inside the rotation plane, the field direction can be either parallel or perpendicular to the spin-orbit field [49, 50]. In our consideration, this field rotation is equivalently described by rotating the spin-orbit field while fixing the Zeeman field and spin polarization axis, as explained after Eq. (3.2). While increasing field strength changes u and v of the zero-energy ABS, the effect of field rotation is to change the ratio of the spin-conserving t and spin-flipping amplitudes t_{so}, as indicated in Eq. (3.4). Plugging Eq. (3.4) into Eq. (3.5), we thus obtain

$$\begin{aligned} |t_{\text{eff}}(\theta)| &= t_0 \sqrt{1 - \sin^2\alpha\cos^2\theta} \cdot u(E_{ZA}), \\ |\Delta_{\text{eff}}(\theta)| &= t_0 \sin\alpha\cos\theta \cdot v(E_{ZA}), \end{aligned} \tag{3.15}$$

where u and v do not depend on angle θ. Here we only focus on $0 \le \theta \le \pi/2$, since the strength of the effective couplings are π-periodic and symmetric about $\theta = 0$. As shown in Fig. 3.3(a), $|t_{\rm eff}|$ ($|\Delta_{\rm eff}|$) is an increasing (decreasing) function of the field angle θ. In particular, when the magnetic field aligns with the spin-orbit field ($\theta = \pi/2$), $|\Delta_{\rm eff}|$, which is of triplet nature, is suppressed completely due to spin conservation. In order to obtain a sweet spot in the angle sweep, one thereby needs to start with a sufficiently strong Zeeman field ($E_{ZA} > E^*_{ZA}$), giving $|\Delta_{\rm eff}| > |t_{\rm eff}|$ at $\theta = 0$, and then rotate the magnetic field to reach the balance between $|\Delta_{\rm eff}|$ and $|t_{\rm eff}|$. Thus, in general a larger excitation gap would appear in the vicinity of $\theta = 0$, where the spin-flipping processes are maximized.

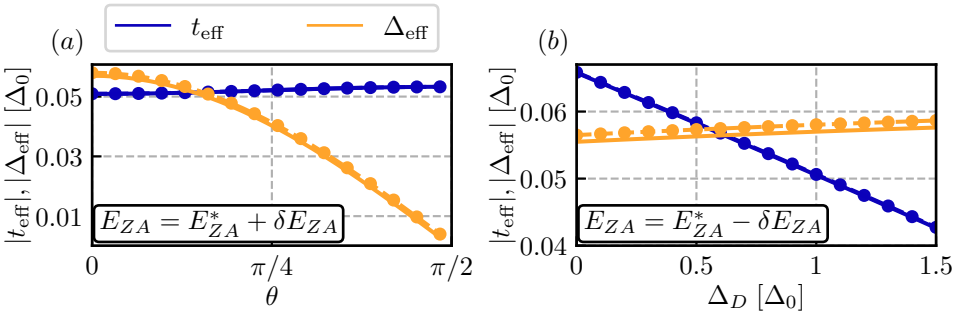

Figure 3.3: (a) Strength of the effective couplings $|t_{\rm eff}|$ and $|\Delta_{\rm eff}|$ as a function of the field angle θ at $E_{ZA} = E^*_{ZA} + \delta E_{ZA}$ ($\delta E_{ZA} = 0.2$). Here θ is the angle between the magnetic field and the dot chain axis, and in particular, $\theta = 0$ corresponds to the magnetic field being perpendicular to the spin-orbit field. (b) $|t_{\rm eff}|$ and $|\Delta_{\rm eff}|$ as a function of induced gap Δ_D at $E_{ZA} = E^*_{ZA} - \delta E_{ZA}$. In both scenarios, a perfect balance between $|t_{\rm eff}|$ and $|\Delta_{\rm eff}|$ can be obtained.

3.2.5. TUNING INDUCED PAIRING GAP IN THE QUANTUM DOT

The third tuning knob we consider in the current work is the superconducting pairing gap in the normal quantum dot, which can be induced from the adjacent hybrid by proximity effect. Microscopically, this proximity effect can originate from either the ABS or the continuum states, with the forms being

$$\begin{aligned} \Delta_{\rm ABS} &= (t^2 + t_{so}^2)\frac{uv}{E_A + E_{ZA}}, \\ \Delta_{\rm cont} &= (t^2 + t_{so}^2)\frac{\chi}{\Delta_0}, \end{aligned} \tag{3.16}$$

up to the leading order. Here $\Delta_{\rm ABS}$ comes from the high-energy spin-up ABS, while $\Delta_{\rm cont}$ is obtained assuming a zero-band-width model for the continuum states, with χ characterizing the continuum density of states which can be quite different from the ABS. Since both $\Delta_{\rm ABS}$ and $\Delta_{\rm cont}$ increase with the tunnel amplitude t_0, their strength can be experimentally enhanced by lowering the tunnel barrier between dot and hybrid. In the following calculations, we do not distinguish between the microscopic origins of the proximity effect, instead we consider their combined effect in a phenomenological way (examples of a microscopic model to change the induced superconductivity by tuning t_0

are given in the Appendix). Now the dot Hamiltonian becomes

$$H'_D = H_D + H_{\text{ind}},$$
$$H_{\text{ind}} = \Delta_D d_\uparrow^\dagger d_\downarrow^\dagger + h.c., \tag{3.17}$$

where H_D is the bare dot Hamiltonian defined in Eq. (3.1), and Δ_D is the total induced gap on the dot. As a result, the dot orbital in the quantum dot is now proximitized into an Yu-Shiba-Rusinov state [51–54], with the electron and hole components being

$$u_D = \sqrt{\frac{1}{2} + \frac{\xi_D}{2(U_D/2 + E_{ZD})}} \approx 1 - \frac{1}{8}\left(\frac{\Delta_D}{U_D/2 + E_{ZD}}\right)^2,$$
$$v_D = \sqrt{\frac{1}{2} - \frac{\xi_D}{2(U_D/2 + E_{ZD})}} \approx \frac{1}{2}\left(\frac{\Delta_D}{U_D/2 + E_{ZD}}\right), \tag{3.18}$$

where

$$\xi_D \equiv \varepsilon_D + U_D/2 = \sqrt{\left(\frac{U_D}{2} + E_{ZD}\right)^2 - \Delta_D^2} \tag{3.19}$$

is determined by the zero-energy condition for the bound state. Note that the approximations in Eq. (3.18) are made in the weak proximity effect regime ($\Delta_D \ll U_D$), and thereby, up to the leading order of Δ_D/U_D, $u_D = 1$ becomes a constant and only $v_D \propto \Delta_D$ grows linearly with Δ_D. As a result, the effective couplings between dot and ABS become

$$t_{\text{eff}} = t(u_A u_D - v_A v_D) \approx t(u_A - v_A v_D),$$
$$\Delta_{\text{eff}} = t_{so}(v_A u_D + u_A v_D) \approx t_{so}(v_A + u_A v_D). \tag{3.20}$$

That is, t_{eff} decreases with the magnitude of the induced pairing, while Δ_{eff} increases with it. In Fig. 3.3(b), the solid lines show the analytic curves of $|t_{\text{eff}}|$ and $|\Delta_{\text{eff}}|$ as a function of Δ_D derived in Eq. (3.20), which agree with the numerical results obtained from the full many-body Hamiltonian (dots and dashed lines). Note that here the Zeeman field is perpendicular to the spin-orbit field, and its strength is chosen to be $E_{ZA} < E^*_{ZA}$ such that $|t_{\text{eff}}| > |\Delta_{\text{eff}}|$ at zero proximity effect, and a balance between them is reached at a sufficiently strong Δ_D.

3.3. SCALING UP THE KITAEV CHAIN

We now go beyond the minimal setup of a dot-ABS pair and scale up the system into a longer chain. Without loss of generality, we consider tuning up the sweet spot and Majorana modes by varying the Zeeman field strength, with its direction being fixed to be perpendicular to the spin-orbit field and no superconducting proximity effect on normal quantum dots. Moreover, we assume homogeneity in the long-chain system, i.e., all the physical parameters for the dots/ABS/tunneling are identical.

3.3.1. THREE-SITE KITAEV CHAIN: DOT-ABS-DOT

As a first example of the three-site Kitaev chain, we consider a dot-ABS-dot chain, focusing on its physical properties around the sweet spot. The Hamiltonian is given by

$$H_{\text{DAD}} = H_{DL} + H_A + H_{DR} + H_{TLA} + H_{TRA}, \tag{3.21}$$

where H_{DL}, H_A and H_{DR} are the Hamiltonians for the left dot, the middle ABS, and the right dot, respectively. H_{TLA} (H_{TRA}) is tunnel Hamiltonian between the ABS and the left (right) dot. The specific forms of these individual Hamiltonian terms are the same as those introduced in Eq. (3.1). Under the assumption of homogeneity, one can simultaneously tune both dot-ABS pairs into their own sweet spot by applying a global Zeeman field $E_{ZA} = E^*_{ZA}$ and setting $\varepsilon_{DL} = \varepsilon_{DR} = \varepsilon^*_D$ and $\varepsilon_A = \varepsilon^*_A$ as indicated in Fig. 3.2(c), such that the whole system is automatically entering the sweet spot regime. Indeed, as shown in Fig. 3.4(a), two unpaired Majorana modes are completely localized on the outermost quantum dots, precisely as expected for the sweet spot of a three-site Kitaev chain [1]. However, a surprising fact is that the energy of the two Majoranas are split into $E_{MZM} \approx 0.01$ which is approximately one-tenth of the excitation gap, [see Fig. 3.4(b) at $\delta\varepsilon = 0$], even though there is no wavefunction overlap between them at all [see Fig. 3.4(a)]. Furthermore, as shown in Fig. 3.4(b), the energy spectrum of the whole system as a function of the detuning energy deviates from the cubic scaling behavior $E \propto (\delta\varepsilon)^3$ of an idealized three-site Kitaev chain. Here the detuning energy is defined as $\delta\varepsilon = \varepsilon_{DL} - \varepsilon^*_D = \varepsilon_{DR} - \varepsilon^*_D = \varepsilon_A - \varepsilon^*_A$.

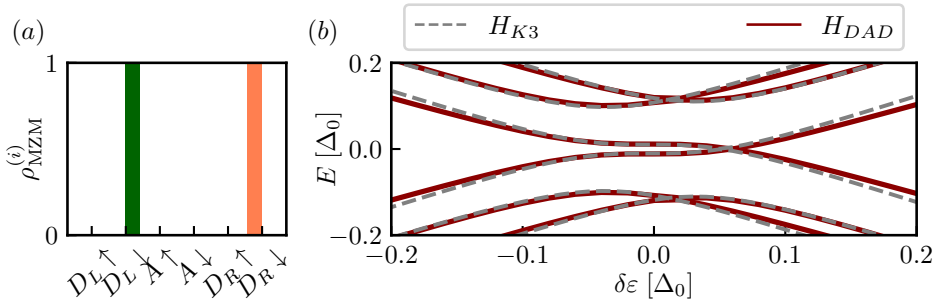

Figure 3.4: (a) Majorana wavefunctions at the sweet spot of a dot-ABS-dot chain. (b) Energy spectrum of the system as a function of detuning energy $\delta\varepsilon$. The solid lines are calculated for the full many-body Hamiltonian, while the grey dashed lines are based on the low-energy effective theory. The energy splitting at $\delta\varepsilon = 0$ is due to effective next-nearest-neighbor coupling between the two outer dots.

To understand the physical mechanism underlying this intriguing energy splitting, we develop a low-energy effective theory for the dot-ABS-dot chain, including both the first- and second-order contributions,

$$H_{\mathrm{DAD,eff}} = H^{(1)}_{\mathrm{DAD,eff}} + H^{(2)}_{\mathrm{DAD,eff}}. \tag{3.22}$$

Here $H^{(1)}_{\mathrm{DAD,eff}}$ includes only the low-energy states and direct tunneling terms, which is a straightforward generalization of the dot-ABS pair, giving

$$\begin{aligned} H^{(1)}_{\mathrm{DAD,eff}} &= PH_{\mathrm{DAD}}P \\ &= (\varepsilon_{DL} - E_{ZD}) d^\dagger_{L\downarrow} d_{L\downarrow} + (E_A - E_{ZA}) \gamma^\dagger_{A\downarrow} \gamma_{A\downarrow} \\ &+ (\varepsilon_{DR} - E_{ZD}) d^\dagger_{R\downarrow} d_{R\downarrow} + t_{\mathrm{eff}LA} \gamma^\dagger_{A\downarrow} d_{L\downarrow} + \Delta_{\mathrm{eff}LA} \gamma_{A\downarrow} d_{L\downarrow} \\ &+ t_{\mathrm{eff}RA} \gamma^\dagger_{A\downarrow} d_{R\downarrow} + \Delta_{\mathrm{eff}RA} \gamma_{A\downarrow} d_{R\downarrow} + h.c.. \end{aligned} \tag{3.23}$$

Indeed, the first-order effective Hamiltonian $H^{(1)}_{\mathrm{DAD,eff}}$ is a three-site Kitaev chain. In particular, the sweet spot is reached when all the onsite energies are zero and $E_{ZA} = E^*_{ZA}$ giving $t_{\mathrm{eff}LA} = t_{\mathrm{eff}RA} = \Delta_{\mathrm{eff}LA} = \Delta_{\mathrm{eff}RA}$. In addition, unlike the dot-ABS pair, we now also include the second-order perturbation terms into the effective Hamiltonian as below

$$\begin{aligned} H^{(2)}_{\mathrm{DAD,eff}} &= PH_T \frac{1-P}{H_A} H_T P \\ &= t_{DD} d^\dagger_{L\downarrow} d_{R\downarrow} + \Delta_{DD} d_{L\downarrow} d_{R\downarrow} + h.c., \end{aligned} \tag{3.24}$$

where $H_T = H_{TLA} + H_{TRA}$. Equation (3.24) indicates that effective next-nearest-neighbor couplings between the outer dots can be mediated by the high-energy ABS in the hybrid via second-order tunnelings (see Fig. 3.5). Specifically, these couplings have the following form

$$\begin{aligned} t_{DD} &= \frac{t^2 v^2 + t_{so}^2 u^2}{2E_{ZA}} \approx \frac{t^2 v^2}{2E_{ZA}}, \\ \Delta_{DD} &= \frac{2 t t_{so} u v}{2E_{ZA}} \ll t_{DD}, \end{aligned} \tag{3.25}$$

where we assume the weak spin-orbit limit $t_{so} \ll t$ and $u \ll v$ holds in the vicinity of the sweet spot. Therefore, up to the second order in t_0, the low-energy physics of a dot-ABS-dot chain is well described by a generalized three-site Kitaev chain

$$\begin{aligned} H_{K3} = &\sum_{i=1}^{3} \varepsilon_i f_i^\dagger f_i + \sum_{i=1}^{2} (t f^\dagger_{i+1} f_i + \Delta f_{i+1} f_i) \\ &+ t_{31} f_3^\dagger f_1 + \Delta_{31} f_3 f_1 + h.c., \end{aligned} \tag{3.26}$$

where f_i is the spinless fermion on the i-th site, ε_i is the on-site energy, t and Δ are the normal and Andreev tunnelings between adjacent sites, and t_{31} and Δ_{31} are the next-nearest-neighbor tunnelings. Indeed, as shown in Fig. 3.4(b), the energy spectrum of the full many-body Hamiltonian in Eq. (3.21) is in excellent agreement with that of the effective model in Eq. (3.26), supporting our perturbation theory analysis. In the calculation of the generalized Kitaev model, the Hamiltonian parameters are chosen as $t = \Delta = t_{\mathrm{eff}}(E^*_{ZA}), t_{31} = t_{DD}, \Delta_{31} = 0$ and $\varepsilon_i = \delta\varepsilon$. Therefore our new finding here is that even though the two Majorana modes have no wavefunction overlap in space at the sweet spot [see Fig. 3.4(a)], they are still coupled to each other via next-nearest-neighbor couplings, giving a finite energy splitting [see Fig. 3.4(b)]. In App. 3.10 we expand our discussion to the case of inhomogeneities of g-factors and spin-orbit mixing between the constituing dots of the array.

3.3.2. THREE-SITE KITAEV CHAIN: ABS-DOT-ABS

We briefly discuss the physics of an ABS-dot-ABS chain which is somewhat dual to a dot-ABS-dot chain. The Hamiltonian is given by

$$H_{\mathrm{ADA}} = H_{AL} + H_D + H_{AR} + H_{TLD} + H_{TRD}, \tag{3.27}$$

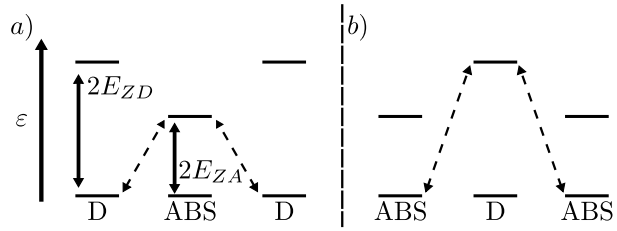

Figure 3.5: Schematic of the second-order tunneling processes that are responsible for the next-nearest-neighbor couplings in a dot-ABS-dot or ABS-dot-ABS chain.

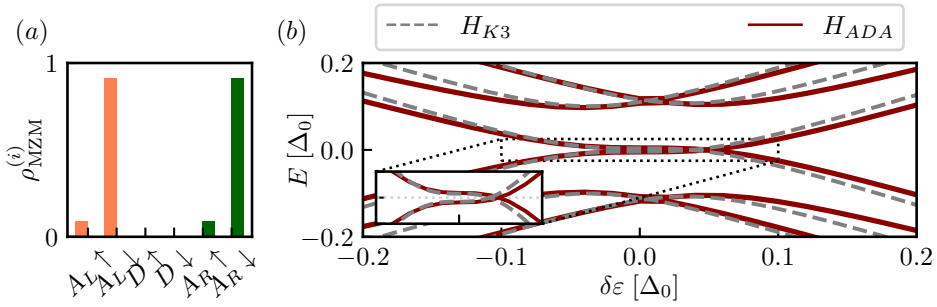

Figure 3.6: (a) Majorana wavefunctions at the sweet spot of an ABS-dot-ABS chain. (b) Energy spectrum of the system as a function of detuning energy $\delta\varepsilon$. The solid lines are calculated for the full many-body Hamiltonian, while the grey dashed lines are based on the low-energy effective theory. The energy splitting at $\delta\varepsilon = 0$ is due to effective next-nearest-neighbor coupling between the two outer ABS.

which has two outer ABS connected by a quantum dot in the middle. Similar to the analysis performed in the previous subsection, the low-energy physics of the system is

$$H_{\text{ADA,eff}} = H^{(1)}_{\text{ADA,eff}} + H^{(2)}_{\text{ADA,eff}}, \tag{3.28}$$

where the first-order term is

$$\begin{aligned} H^{(1)}_{\text{ADA,eff}} &= (E_{AL} - E_{ZA})\gamma^\dagger_{L\downarrow}\gamma_{L\downarrow} + (\varepsilon_D - E_{ZD})d^\dagger_\downarrow d_\downarrow \\ &+ (E_{AR} - E_{ZA})\gamma^\dagger_{R\downarrow}\gamma_{R\downarrow} + t_{\text{eff}LD}\, d^\dagger_\downarrow \gamma_{L\downarrow} + \Delta_{\text{eff}LD}\, d_\downarrow \gamma_{L\downarrow} \\ &+ t_{\text{eff}RD}\, d^\dagger_\downarrow \gamma_{R\downarrow} + \Delta_{\text{eff}RD}\, d_\downarrow \gamma_{R\downarrow} + h.c., \end{aligned} \tag{3.29}$$

and the second-order term is

$$H^{(2)}_{\text{ADA,eff}} = t_{AA}\gamma^\dagger_{L\downarrow}\gamma_{R\downarrow} + \Delta_{AA}\gamma_{L\downarrow}\gamma_{R\downarrow} + h.c., \tag{3.30}$$

with

$$\begin{aligned} t_{AA} &= \frac{t^2 v^2 + t_{so}^2 u^2}{2E_{ZD}} \approx \frac{t^2 v^2}{2E_{ZD}}, \\ \Delta_{AA} &= \frac{2 t t_{so} u v}{2E_{ZD}} \ll t_{AA}. \end{aligned} \tag{3.31}$$

We thus see that the low-energy physics of a ABS-dot-ABS chain is also a generalized three-site Kitaev chain, with only the roles of quantum dots and ABS being interchanged. Actually the sweet spot of the system is also reached at $E_{ZA} = E^*_{ZA}$, giving an excitation energy gap of similar size with its dual system. The only difference is a more suppressed Majorana energy splitting [see Fig. 3.6(b)] because a larger Zeeman spin splitting in the quantum dot suppresses the second-order tunnelings, as indicated in Eq. (3.31). As for the dot - ABS - dot setup, in App. 3.10 we expand the discussion to situations where the dots have inhomogeneities in either g-factors or spin-orbit mixing. In particular we find that the ABS - dot - ABS system yields more resillient sweet spots due to the larger separation of levels on the central normal dot.

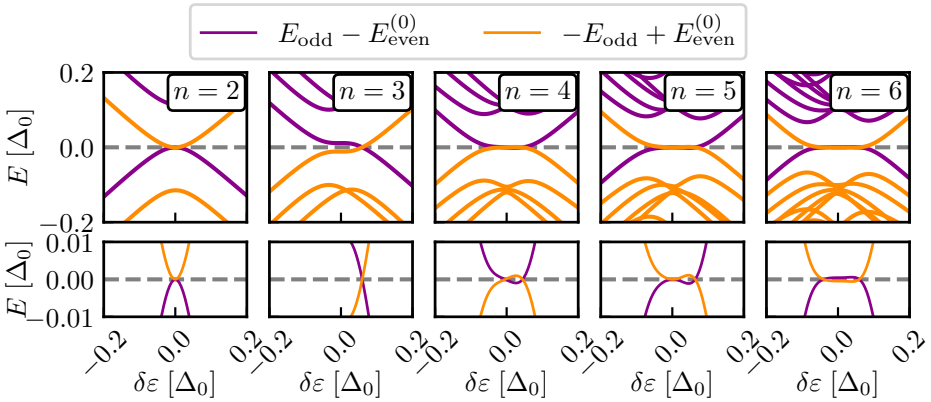

Figure 3.7: Energy spectra of N-site alternating quantum dot-ABS chains around the sweet spot. For intermediate length chains (e.g., $N = 3$), the next-nearest-neighbor coupling has an appreciable effect on the Majorana energy splitting at the sweet spot. As the chain is further scaled up ($N \geq 4$), this Majorana energy splitting is quickly suppressed due to the short-range nature of this effective coupling as shown in Eq. (3.33).

3.3.3. LONGER KITAEV CHAIN

For a general Kitaev chain with N alternating quantum dots and ABS in total, its low-energy physics can be well described by an effective Hamiltonian up to the $N-1$-th order, i.e.,

$$H_{N,\text{eff}} = \sum_{k=1}^{N-1} H^{(k)}_{N,\text{eff}}. \tag{3.32}$$

In particular, the strength of the effective couplings between two arbitrary sites in such an N-site chain has the following scaling behavior

$$\Gamma_k \sim \frac{t_0^k}{(2E_Z)^{k-1}} \sim t_0 \exp\{-(k-1)\log(2E_Z/t_0)\}, \tag{3.33}$$

for $1 \leq k \leq N-1$. Here Γ_k denotes the effective normal or Andreev coupling between any two sites separated by a distance of k (e.g., Γ_1 for the nearest-neighbor coupling), and

E_Z is the Zeeman spin splitting of either dot or ABS located between the two sites considered. Physically, Γ_k originates from virtual tunnelings that include k times of single-electron tunneling events via $k-1$ different high-energy states that are gapped from the Fermi energy due to Zeeman spin splitting. From Eq. (3.33), we see that Γ_k decays exponentially with the distance between the coupled two sites, with the decay length being approximately

$$\xi_\Gamma^{-1} \sim \log(2E_Z/t_0). \tag{3.34}$$

The range of the effective couplings thus decreases with an increase of Zeeman energy in the dot-ABS chain, and as a result, the low-energy physics of the dot-ABS chain will asymptotically approach the idealized spinless Kitaev chain only in the large Zeeman energy limit ($E_Z \gg t_0$). Another crucial feature of Γ_k is being short-ranged in nature, making it possible to reach topological protection in the long-chain limit. Indeed, the numerical simulations based on the full many-body Hamiltonian for N-site dot-ABS chain (see Fig. 3.7) show that the finite Majorana energy splitting become strongly suppressed to nearly zero once there are as many as four or five sites. Moreover, for N as large as six, the range of $\delta\varepsilon$ for hosting zero-energy excitation extends asymptotically to the long-wire limit $-t_{\rm eff}(E^*_{ZA}) \lesssim \delta\varepsilon \lesssim t_{\rm eff}(E^*_{ZA})$ and signatures of gap closing and reopening begin to appear near $|\delta\varepsilon| \sim t_{\rm eff}$, indicating the emergence of topological phase transition.

3.4. DISCUSSION

In the current work, we proposed a new way of implementing a Kitaev chain in an alternating quantum dot-Andreev bound state array. Although the configuration of the proposed hybrid devices resembles those considered in Refs. [36, 37, 39, 43], a fundamental difference is the role of ABS. In Refs. [39, 43], the ABSs are *gapped* and only serve as a virtual coupler to mediate the effective couplings between quantum dots. By contrast, here the spin-polarized ABS is taken close to the Fermi energy and are on equal footing with the dot orbitals as the spinless fermions. Consequently, an immediate advantage of our proposal is to emulate a Kitaev chain using a reduced number of quantum dots and hybrid segments in a device. In particular, it becomes possible to implement a two-site Kitaev chain and poor man's Majoranas using only one quantum dot and one hybrid segment. Furthermore, the existing two-site Kitaev chain device comprised of a double quantum dot linked by a hybrid [38] is now suitable for realizing a three-site Kitaev chain exhibiting the physics of bulk-edge correspondence in the vicinity of its sweet spot. On the other hand, our proposal differs from the ABS chain proposed in Ref. [44] in that we require only half the number of superconducting leads and that we do not need to control the quantum point contact between the semiconductor wire and the superconductor leads, making our theoretical proposal more experimentally accessible. Another advantage of our proposal is the ability of getting a relatively large excitation gap, because now the effective couplings originate from direct couplings of the dot-ABS pair, i. e., $E_{\rm gap} \sim t_0$ in stark contrast with the second-order tunneling processes $E_{\rm gap} \sim t_0^2/\Delta_0$ in the previous works [39]

Throughout the work, we have assumed perfect homogeneity when considering a long Kitaev chain device ($N \geq 3$), but this has to be relaxed in a realistic device. That is, the quantum dots can have different values of charging energy U_D, g factor E_{ZD}, while

E_{ZA} and induced gap Δ_0 of the ABS may vary from piece to piece. Therefore, it would be rather unlikely to drive the whole long chain into the sweet spot by merely controlling a global magnetic field, and as a result, the tuning knob of induced gap on quantum dots become particularly crucial, because it will allow for fine-tuning the couplings in each individual dot-ABS pair into perfect balance.

Another new finding of our work is the presence of couplings beyond the nearest neighbors, which originate from high-order tunneling processes. Its effect will be most prominent in a three-site device (e.g., dot-ABS-dot chain), where the Majorana energy at the sweet spot becomes split even though their wavefunctions are completely separated on the outermost dots. This raises a new open question of whether it is possible to define such a sweet spot which simultaneously satisfies three conditions: 1. complete spatial separation of the Majoranas, 2. robustness against onsite-energy detuning, and 3. minimizing the Majorana energy to nearly zero. In order to obtain an idealized Kitaev chain model, as shown in Eqs. (3.25) and (3.31), the couplings between two distant sites would be suppressed in the strong Zeeman limit, similar to the findings in the Majorana nanowire scenarios [55]. In addition, in the tunneling regime $t_0 \ll E_Z$, such couplings are short-ranged in nature, and therefore the effect will be mitigated as the number of sites is scaled up. As we show, when the number of sites is as large as six, the whole chain becomes very close to a topological Kitaev chain with robust zero energy and signatures of gap closing and reopening near the quantum phase transition.

3.5. SUMMARY

To summarize, we have proposed a new route to simulating Kitaev chain in an alternating quantum dot-Andreev bound state array. In particular, both the dot orbitals and the ABS are now on equal footing as spinless fermions, and the relative amplitude of normal and Andreev couplings between adjacent sites are highly tunable by the strength and direction of the magnetic field, as well as the magnitude of the induced pairing gap on quantum dots. As the quantum dot-ABS chain is scaled up, couplings beyond the nearest neighbors emerge, affecting the Majorana energy at the sweet spot. Nonetheless, due to short-range nature of these couplings, topological protection of Majorana zero modes will recover in the long chain limit. Our proposal will allow for a more efficient simulation of artificial Kitaev chain using a reduced number of quantum dot or hybrid segment and will at the same time obtain a larger excitation gap above the Majorana zero modes. In recent experiments [40, 56], it has been demonstrated possible to isolate a single ABS in a short hybrid region, making our proposal particularly appealing and relevant to the ongoing studies. Finally, we have been made aware of [45] by its authors. In contrast to [45], we consider the the limit of both quantum dots being maximally asymmetric in their proximity coupling to the superconductor.

ACKNOWLEDGEMENTS

We are particularly grateful to S. L. D. ten Haaf, and B. Roovers for sharing and discussing experimental data with us, motivating this work. We further thank A. M. Bozkurt, J. D. Torres Luna, and K. Vilkelis for useful theory discussions. We are grateful to the authors of [45] for making us aware of their work prior to publication. This work was sup-

ported by a subsidy for top consortia for knowledge and innovation (TKI toeslag), by the Dutch Organization for Scientific Research (NWO). S.M. acknowledges funding of NWO through OCENW.GROOT.2019.004.

DATA AVAILABILITY.

All codes related to the results of the present manuscript can be found in the accompanying Zenodo repository [57].

3.6. DETAILS OF THE NUMERICAL CALCULATIONS

The numerical results in this work are obtained by exact diagonalization of the full many-body Hamiltonian, e.g., Eq. (3.1), in Fock space. The dimension of the total Hamiltonian is 2^{2N} where N is the number of quantum dots plus ABS in the chain. Due to fermion parity conservation, we can decompose the Hamiltonian into even- and odd-parity subspace of dimension 2^{2N-1}. As a result, the excitation energy E, as depicted in Figs. 3.4, 3.6, and 3.7, has been obtained through

$$E_\lambda = E^{(\lambda)}_{\text{odd}} - E^{(0)}_{\text{even}} \tag{3.35}$$

for $\lambda = 0, 1, 2, ..., 2^{2N-1} - 1$. In a similar fashion, ΔE in the charge stability diagrams, as depicted in Fig. 3.2(c), is obtained by restricting λ in Eq. (3.35) to $\lambda = 0$. To obtain t_{eff} and Δ_{eff} we make use of the following relation

$$\begin{aligned} \Delta_{\text{eff}} &= (E_1 + E_0)/2, \\ t_{\text{eff}} &= (E_1 - E_0)/2, \end{aligned} \tag{3.36}$$

where E_0, E_1 are defined in Eq. (3.35).

Here t_{eff} is related to the cost of exciting an unpaired electron while Δ_{eff} is related to splitting the lowest Cooper pair into two unpaired electrons. The gap energy, depicted in e.g. Fig. 3.2(b), is obtained directly through

$$E_{\text{gap}} \equiv E_1. \tag{3.37}$$

In addition, the spectrum plots also contain the energy of the MZM itself in the lowest laying line following

$$E_{\text{MZM}} \equiv E_0. \tag{3.38}$$

The Zeeman energies characterising the sweet spot depicted in Fig. 3.2 b) have been determined by using the properties of the CSD [see Fig.3.2 (c)]. As Fig. 3.3 shows, if E_{ZA} is slightly below the sweet spot E^*_{ZA}, the degeneracy crossing vanishes in favor of an t_{eff} dominated ($\Delta E > 0$) anti-crossing. For $E_{ZA} > E^*_{ZA}$ the same anti-crossing is caused by a dominating Δ_{eff} process ($\Delta E < 0$). Therefore, the sweet spot is characterised by the root $\Delta E(E^*_{ZA}) = 0$ at the point where the charge degeneracy lines have their smallest distance in the $(\varepsilon_D, \varepsilon_A)$ plane. To determine the point of minimal distance, we perform a transformation of the chemical potentials into polar coordinates

$$(\varepsilon_D, \varepsilon_A) \to (r_\varepsilon \cos(\varphi_\varepsilon), r_\varepsilon \sin(\varphi_\varepsilon)) \quad r_\varepsilon = \sqrt{\varepsilon_D^2 + \varepsilon_A^2},\ \tan(\varphi_\varepsilon) = \varepsilon_A/\varepsilon_D. \tag{3.39}$$

In polar coordinates, the point with minimal distance between the degeneracy lines is found to satisfy

$$(r_\varepsilon, \varphi_\varepsilon) \in \{r_\varepsilon, \varphi_\varepsilon : \min[\Delta E(r_\varepsilon, \varphi_\varepsilon)] \wedge \max[\Delta E(r_\varepsilon, \varphi_\varepsilon)]\}. \tag{3.40}$$

The bottom right corner we discuss has the further constraint that $\varphi_\varepsilon \in [-\pi/2, 0]$. To obtain the MZM wavefunctions, $\rho^{(i)}_{\mathrm{MZM}}$, depicted in Figs. 3.2, 3.4, and 3.6 we define the spin dependent on-site MZM operators

$$w_\sigma = (d_\sigma + d^\dagger_\sigma) \tag{3.41}$$
$$z_\sigma = i(d_\sigma - d^\dagger_\sigma). \tag{3.42}$$

The MZM on the ABS are defined analogously with the corresponding creation and annihilation operators. From Eq. (3.41) we find the MZM wavefunctions through

$$\rho^{(w)}_{\mathrm{MZM}} = |\langle \psi^{(0)}_{\mathrm{odd}} | w_\sigma + w_{\overline{\sigma}} | \psi^{(0)}_{\mathrm{even}} \rangle|^2 \tag{3.43}$$
$$\rho^{(z)}_{\mathrm{MZM}} = |\langle \psi^{(0)}_{\mathrm{odd}} | z_\sigma + z_{\overline{\sigma}} | \psi^{(0)}_{\mathrm{even}} \rangle|^2 \tag{3.44}$$

where $|\psi^{(\lambda)}\rangle$ denotes an eigenstate of the many-body Hamiltonian, cf. Eq. (3.1). The conductance plot in Fig. 3.2 e) has been obtained by implementing the rate equations listed in the supplementary material of [43]. The energies of the Kitaev model [1] in Figs. 3.4, and 3.6 have been obtained by exact diagonalization and replacing the parameters by their corresponding partners from perturbation theory, cf. Eq. (3.7). Lastly, the perturbative analysis has in parts been performed by using Pymablock [58]. All codes related to the results presented in the manuscript can be found in the accompanying Zenodo repository [57]

3.7. SYMMETRIES OF THE CHARGE STABILITY DIAGRAM

The CSD depicted in Fig. 3.2 shows six distinct regions with alternating groundstate properties. If the low-energy subspace is described by the Hamiltonian given in Eq. (3.3), then varying the chemical potentials ε_i on the two sites changes the charge state of the dots. The possible charge states on each site depending on the chemical potential are

$$|\downarrow\uparrow\rangle, \qquad \varepsilon_D < -U_D - E_{ZD} \tag{3.45}$$
$$|\downarrow\rangle, \qquad -U_D - E_{ZD} < \varepsilon_D < E_{ZD} \tag{3.46}$$
$$|0\rangle, \qquad \varepsilon_D > E_{ZD} \tag{3.47}$$

on the normal dot, and

$$u|0\rangle + v|\uparrow\downarrow\rangle, \qquad \varepsilon_A < -\sqrt{E^2_{ZA} - \Delta^2_0} \tag{3.48}$$
$$|\downarrow\rangle, \qquad -\sqrt{E^2_{ZA} - \Delta^2_0} < \varepsilon_A < \sqrt{E^2_{ZA} - \Delta^2_0} \tag{3.49}$$
$$u|0\rangle + v|\uparrow\downarrow\rangle, \qquad \varepsilon_A > \sqrt{E^2_{ZA} - \Delta^2_0}, \tag{3.50}$$

on the proximitized dot, where $u > v$ in Eq. (3.48), and $v > u$ in Eq. (3.50). The precise choice of the corner in the CSD depends on 1) the choice of the degeneracy on the normal dot, and 2) the choice of the ABS, i.e. $\varepsilon_A = \pm\sqrt{E_{ZA}^2 - \Delta_0^2}$. The choice of the normal dot degeneracy yields different low energy Hamiltonians due to the different spin orientations that are relevant for the transition. For the right two corners, the normal dot orbital is spin-down, so we have

$$\begin{aligned} H_T &\approx -t_{so} c_\uparrow^\dagger d_\downarrow + t c_\downarrow^\dagger d_\downarrow + h.c. \\ &\approx -t_{so} v \gamma_\downarrow d_\downarrow - t u \gamma_\downarrow^\dagger d_\downarrow + h.c., \end{aligned} \tag{3.51}$$

where we have used the Bogoliubov transformation

$$c_\uparrow^\dagger = u\gamma_\uparrow^\dagger + v\gamma_\downarrow, \quad c_\downarrow^\dagger = -u\gamma_\downarrow^\dagger + v\gamma_\uparrow. \tag{3.52}$$

So we have

$$t_{\text{eff}} = -tu, \quad \Delta_{\text{eff}} = -t_{so} v \tag{3.53}$$

for both bottom-right and top-right corners. On the other hand, for the left two corners, the dot orbitals are spin-up states, giving

$$\begin{aligned} H_T &\approx t^* c_\uparrow^\dagger d_\uparrow + t_{so} c_\downarrow^\dagger d_\uparrow + h.c. \\ &\approx t^* v \gamma_\downarrow d_\uparrow - t_{so} u \gamma_\downarrow^\dagger d_\uparrow. \end{aligned} \tag{3.54}$$

Thus

$$t_{\text{eff}} = -t_{so} u, \quad \Delta_{\text{eff}} = t^* v. \tag{3.55}$$

The choice top- or bottom-corner depends on the choice of the ABS. In Fig. 3.8 we have depicted the different options in the parameter regimes relevant for the problem. Choosing the negative energy ABS ($\varepsilon_A = -\sqrt{E_{ZA}^2 - \Delta_0^2}$) yields $v > u$ while it is the opposite ($u > v$) for the positive energy ABS. Finally, the availability of a corner to host a sweet spot depends on the relation between t and t_{so}. The main text discusses the behavior at the bottom-right sweet spot when $t > t_{so}$, a condition that needs to be satisfied for the bottom-right corner to be a viable sweet spot. The choice of corner is then determined by the ABS, i.e. for the bottom-right corner that is $\varepsilon_A = -\sqrt{E_{ZA}^2 - \Delta_0^2}$ which yields $v > u$. This is necessary to enable $|t_{\text{eff}}| = |\Delta_{\text{eff}}|$, see Eq. (3.53). Choosing the opposite ABS, i.e. $\varepsilon_A = \sqrt{E_{ZA}^2 - \Delta_0^2}$, one switches from the bottom right to the top right corner. This corner can however not host any sweet spot when $t > t_{\text{so}}$ since

$$u = \sqrt{\frac{1}{2}\left(1 + \sqrt{1 - \Delta_0^2/E_{ZA}^2}\right)} \overset{\frac{\Delta_0}{E_{ZA}} \nearrow 1}{\approx} \frac{\sqrt{2}}{2} + \frac{\sqrt{1 - \Delta_0^2/E_{ZA}^2}}{2} + \frac{\sqrt{2}}{8}\left(\frac{\Delta_0^2}{E_{ZA}^2} - 1\right) \tag{3.56}$$

$$v = \sqrt{\frac{1}{2}\left(1 - \sqrt{1 - \Delta_0^2/E_{ZA}^2}\right)} \overset{\frac{\Delta_0}{E_{ZA}} \nearrow 1}{\approx} \frac{\sqrt{2}}{2} - \frac{\sqrt{1 - \Delta_0^2/E_{ZA}^2}}{2} + \frac{\sqrt{2}}{8}\left(\frac{\Delta_0^2}{E_{ZA}^2} - 1\right) \tag{3.57}$$

showing that $u > v$ for $E_{ZA} > \Delta_0$ (see also Fig. 3.8). If however $t_{so} > t$, the constraint on u, v is inverted and the availability of the two corners flips. For clarity, we introduce the precise definitions by which we refer to the corners of the CSD in table 3.1. There, we list the participating, i.e. degenerate states, on the normal dot (dot D) and the proximitized dot (dot A). Furthermore, we give the conditions relevant for the existence of the sweet spot, e.g. that a bottom right sweet spot becomes viable if both $v > u$ and $t > t_{so}$ are met.

	Left Dot D: $\|\downarrow\uparrow\rangle$; $\|\downarrow\rangle$	**Right** Dot D: $\|\downarrow\rangle$; $\|0\rangle$
Top Dot A: $u\|0\rangle + v\|\uparrow\downarrow\rangle$; $\|\downarrow\rangle$	$t > t_{so}$ $u > v$	$t < t_{so}$ $u > v$
Bottom Dot A: $\|\downarrow\rangle$; $u\|0\rangle + v\|\uparrow\downarrow\rangle$	$t < t_{so}$ $u < v$	$t > t_{so}$ $u < v$
H_{DA}^{eff} terms	$t_{\text{eff}} = -t_{so}\, u\,; \Delta_{\text{eff}} = t^\dagger v$	$t_{\text{eff}} = -t\, u\,; \Delta_{\text{eff}} = -t_{so}\, v$

Table 3.1: Definition of the corners visible in the charge stability diagram, Fig. 3.2. The given constraints on u, v and t, t_{so} determine the whether the corresponding corner in the charge stability diagram is a viable sweet spot.

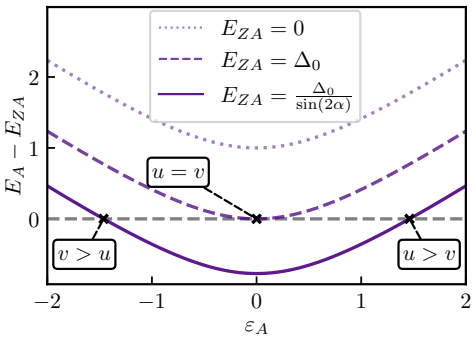

Figure 3.8: ABS energy depending on the on-site chemical potential of the ABS dot for varying Zeeman energies E_{ZA}. Depending on the Zeeman energy, at most two ABS solutions will become available to potentially host sweet spots of the system.

3.8. Finite charging energy U_{ABS} in the Andreev bound state

The main text discusses a configuration without charging energy on the ABS dot. Removing this constraint, we obtain the Hamiltonian on the ABS dot as

$$H_A = (\varepsilon - E_{ZA}) c_\downarrow^\dagger c_\downarrow + (\varepsilon + E_{ZA}) c_\uparrow^\dagger c_\uparrow + \Delta_0 c_\uparrow^\dagger c^\dagger \downarrow + U_{\text{ABS}} c_\uparrow^\dagger c_\downarrow^\dagger c \downarrow c \uparrow + \text{h.c} \tag{3.58}$$

in the electronic basis. U_{ABS} is the charging energy on the ABS and the remaining symbols are defined in Sec. 3.2.1. In the many-body basis, $\{|0\rangle, |\downarrow\uparrow\rangle, |\downarrow\rangle, |\uparrow\rangle\}$, we can write the

Hamiltonian

$$H_A = \begin{pmatrix} 0 & \Delta & 0 & 0 \\ \Delta & 2\varepsilon + U_{\mathrm{ABS}} & 0 & 0 \\ 0 & 0 & \varepsilon - E_{ZA} & 0 \\ 0 & 0 & 0 & \varepsilon + E_{ZA} \end{pmatrix}. \tag{3.59}$$

We substitute $\xi = 2\varepsilon + U_{\mathrm{ABS}}$ and define $E_\xi = \sqrt{\xi^2 + \Delta^2}$. With these replacements we can write the groundstate of the even and odd parity subspaces as

$$E_{\mathrm{GS}}^{(even)} = \xi - \sqrt{\xi^2 + \Delta^2}; \qquad |\mathrm{GS}_{odd}\rangle = \sqrt{\frac{E_\xi + \xi}{2E_\xi}}|0\rangle + \sqrt{\frac{E_\xi - \xi}{2E_\xi}}|\uparrow\downarrow\rangle \tag{3.60}$$

$$E_{\mathrm{GS}}^{(odd)} = \varepsilon - E_{ZA}; \qquad |\mathrm{GS}_{even}\rangle = |\downarrow\rangle \tag{3.61}$$

To induce MZMs on the dots, the two groundstates need to be degenerate. They are connected through a quasiparticle excitation $|\mathrm{GS}_{even}\rangle = (uc_\downarrow^\dagger - vc_\uparrow^\dagger)|\mathrm{GS}_{odd}\rangle$ with u, v to be determined. We obtain the condition

$$u\sqrt{\frac{E_\xi + \xi}{2E_\xi}} + v\sqrt{\frac{E_\xi - \xi}{2E_\xi}} = 1 \tag{3.62}$$

which is solved by $u(U_{\mathrm{ABS}}) = \sqrt{\frac{E_\xi+\xi}{2E_\xi}}$, $v(U_{\mathrm{ABS}}) = \sqrt{\frac{E_\xi-\xi}{2E_x i}}$ since $u(U_{\mathrm{ABS}})^2 + v(U_{\mathrm{ABS}})^2 = 1$. The degeneracy condition requires

$$E_{\mathrm{GS}}^{(even)} = E_{\mathrm{GS}}^{(odd)} \tag{3.63}$$

leading to ξ being constrained to

$$\xi^2 = \left(\frac{U_{\mathrm{ABS}}}{2} + E_{ZA}\right)^2 - \Delta^2. \tag{3.64}$$

To satisfy $v(U_{\mathrm{ABS}}) > u(U_{\mathrm{ABS}})$ (see App. 3.7) we choose the negative root solution for ξ. Gathering all findings into $u(U_{\mathrm{ABS}})$ and $v(U_{\mathrm{ABS}})$ we can write

$$u(U_{\mathrm{ABS}}) = \sqrt{\frac{E_\xi + \xi}{2E_\xi}} \overset{U_{\mathrm{ABS}}\to 0}{\approx} u - \frac{u}{4}\frac{\Delta^2}{\xi_0 E_{ZA}(E_{ZA} - \xi_0)}U_{\mathrm{ABS}} \tag{3.65}$$

$$v(U_{\mathrm{ABS}}) = \sqrt{\frac{E_\xi - \xi}{2E_\xi}} \overset{U_{\mathrm{ABS}}\to 0}{\approx} v + \frac{v}{4}\frac{\Delta^2}{\xi_0 E_{ZA}(E_{ZA} - \xi_0)}U_{\mathrm{ABS}} \tag{3.66}$$

where we used $\xi_0 = \sqrt{E_{ZA}^2 - \Delta^2}$, and u, v as defined in Sec. 3.2.1. We recognize that u decreases while v increases. It is therefore to be expected that the Zeeman energy at which the sweet spot is observed reduces. Indeed we find E_{ZA}^* for $\theta = 0$ at the sweet spot as

$$E_{ZA}^* = \frac{\Delta_0}{\sin(2\alpha)} - \frac{U_{\mathrm{ABS}}}{2}. \tag{3.67}$$

Since two corners of the charge stability diagram are roughly separated by $\simeq 2E_{\mathrm{ZA}}+U_{\mathrm{ABS}}$, a finite U_{ABS} can serve to help make the sweet spot more resilient towards single parameter perturbations. Furthermore, Eq. (3.67) shows that large enough U_{ABS} can push the sweet spot Zeeman energy below Δ_0. Hence, sweet spots can emerge even if $E_{\mathrm{ZA}}<\Delta_0$ as a result of the separation of the ABS states in ε_A and Eq. (3.67). This final property might be particularly useful when the platform inherent g-factor might be limited through other constraints.

3.9. CONTROLLING THE EFFECTIVE PAIRING THROUGH t_0

In Sec. 3.2.5 we used a phenomenological pairing parameter Δ_D on the initially normal dot to demonstrate how a change on the pairing on the dot can recover a sweet spot. This section appends to Sec. 3.2.5, demonstrating explicitly on the many-body system how the induced pairing from the ABS is controlled through the bare hopping t_0. In particular,, when the ABS dot is tuned slightly off the sweet spot in E_{ZA}, we can adjust t_0 to recover a sweet spot. Fig. 3.9 demonstrates sweet spot recovery along two examples: a) and b) show how large t_0 recover a sweet spot when starting with an initially small $t_0(=0.2)$ and $E_{\mathrm{ZA}}=E^*_{\mathrm{ZA}}-\delta E_{\mathrm{ZA}}$; c) and d) demonstrate recovery for small t_0 when beginning with $t_0=1.5$, i.e. strong coupling of the dots, at $E_{\mathrm{ZA}}=E^*_{\mathrm{ZA}}+\delta E_{\mathrm{ZA}}$.

3.10. INHOMOGENEITY IN THE DOT-ABS ARRAY

In this section, we consider the effect of Hamiltonian parameter inhomogeneity in a dot-ABS array. This captures the realistic situation of an experimental device. To demonstrate the main physical effect, we focus on the three-site Kitaev chain with four different scenarios: DAD and ADA with inhomogeneous spin-orbit interaction, and DAD and ADA with inhomogeneous g factor. Here we choose the level of inhomogeneity to be 10% to generate the results in Figs. 3.10and 3.11 and we emphasize that our results are robust even for larger values. We find that the physical findings and main conclusions presented in the main text are still valid, e.g., the presence of long-range coupling between Majoranas with negligible wavefunction overlap, and energy spectra against chemical potential detuning. In our simulation here, we need to first figure out the sweet spots in each two-site DA pair by varying the tunnel strength t_0. After that, the sweet spot of a three-site one is obtained by putting them together. It is likely that the middle site (either dot or ABS) may reach different values of chemical potential for the left and right pairs respectively, and we choose to take the average of them. In addition, to capture the proximity effect from the continuum states, we add a pairing term $\Delta_{D,induced}\approx t_0^2\delta\Delta$ on normal quantum dots, with $\delta\Delta=0.5\Delta_0$. We note that the induced gap is proportional to t_0^2 owing to second-order process of local Andreev reflection, and that $\delta\Delta$ is a phenomonological parameter which is proportional to the superconductor density of states. We have checked that our simulation results do not depend on the precise value of $\delta\Delta$. To summarize, we have shown that even in the presence of parameter inhomogeneity, the sweet spot of an extended Kitaev chain can still be found by varying the tunnel strength between dot and ABS. Furthermore, the main findings presented in the main text are still valid.

3.10.1. INHOMOGENEOUS SPIN-ORBIT MIXING

We first consider inhomogeneous spin-orbit mixing in both ADA and DAD set-ups. We assume that α_L and α_R, i.e. the spin-orbit mixing angles of the two pairs. The results of this analysis are depicted in Fig. 3.10. We recognize that, for both set-ups, we can well recover the spectral behavior discussed in Sec. 3.3. Furthermore, we see that the Majorana wavefunctions shown in Fig. 3.10 a) and c) are still well separated.

3.10.2. INHOMOGENEOUS g-FACTOR

Lastly, we consider inhonmogenuous g-factors between the dots. The different g-factors of the outer dots between the two set-ups makes them differently susceptible to inhomogeneities of the g-factor. We choose $g_L = 2, g_R = 1.8$ for the DAD and $g_L = 1, g_R = 0.9$ for the ADA set-up. This choice yields reasonably different sweet spots of the two pairs of 2-site chains that still allow to be connected by barrier tuning of the second pair, i.e. varying t_0. The results of this analysis are depicted in Fig. 3.11 For both situations we find that the behavior of the spectrum suggested in the main text can still be reasonably well reproduced and that the Majoranas that the systems yield are still well separated.

REFERENCES

[1] Kitaev, A. Y. "Unpaired Majorana fermions in quantum wires". en. In: *Phys.-Usp.* 44.10S (2001). DOI: 10.1070/1063-7869/44/10S/S29.

[2] Alicea, J. "New directions in the pursuit of Majorana fermions in solid state systems". en. In: *Rep. Prog. Phys.* 75.7 (2012). DOI: 10.1088/0034-4885/75/7/076501.

[3] Leijnse, M. and Flensberg, K. "Introduction to topological superconductivity and Majorana fermions". en. In: *Semicond. Sci. Technol.* 27.12 (2012). DOI: 10.1088/0268-1242/27/12/124003.

[4] Beenakker, C. "Search for Majorana Fermions in Superconductors". In: *Annu. Rev. Condens. Matter Phys.* 4.1 (2013). DOI: 10.1146/annurev-conmatphys-030212-184337.

[5] Stanescu, T. D. and Tewari, S. "Majorana fermions in semiconductor nanowires: fundamentals, modeling, and experiment". In: *J. Phys.: Condens. Matter* 25.23 (2013).

[6] Jiang, J.-H. and Wu, S. "Non-Abelian topological superconductors from topological semimetals and related systems under the superconducting proximity effect". In: *J. Phys.: Condens. Matter* 25.5 (2013).

[7] Elliott, S. R. and Franz, M. "Colloquium: Majorana fermions in nuclear, particle, and solid-state physics". In: *Rev. Mod. Phys.* 87 (1 2015). DOI: 10.1103/RevModPhys.87.137.

[8] Sato, M. and Fujimoto, S. "Majorana Fermions and Topology in Superconductors". In: *J. Phys. Soc. Jpn.* 85.7 (2016). DOI: 10.7566/JPSJ.85.072001.

[9] Sato, M. and Ando, Y. "Topological superconductors: a review". In: *Rep. Prog. Phys.* 80.7 (2017).

[10] Aguado, R. “Majorana quasiparticles in condensed matter”. In: *La Rivista del Nuovo Cimento* 40.11 (2017). DOI: 10.1393/ncr/i2017-10141-9.

[11] Lutchyn, R. M. et al. “Majorana zero modes in superconductor–semiconductor heterostructures”. In: *Nat. Rev. Mater.* 3.5 (2018). DOI: 10.1038/s41578-018-0003-1.

[12] Zhang, H. et al. “Next steps of quantum transport in Majorana nanowire devices”. In: *Nat. Commun.* 10.1 (2019). DOI: 10.1038/s41467-019-13133-1.

[13] Frolov, S. M., Manfra, M. J., and Sau, J. D. “Topological superconductivity in hybrid devices”. In: *Nature Physics* 16.7 (2020). DOI: 10.1038/s41567-020-0925-6.

[14] Ivanov, D. A. “Non-Abelian Statistics of Half-Quantum Vortices in *p*-Wave Superconductors”. In: *Phys. Rev. Lett.* 86 (2 2001). DOI: 10.1103/PhysRevLett.86.268.

[15] Nayak, C. et al. “Non-Abelian anyons and topological quantum computation”. In: *Rev. Mod. Phys.* 80 (3 2008). DOI: 10.1103/RevModPhys.80.1083.

[16] Sarma, S. D., Freedman, M., and Nayak, C. “Majorana zero modes and topological quantum computation”. en. In: *npj Quantum Inf* 1.1 (2015). DOI: 10.1038/npjqi.2015.1.

[17] Plugge, S. et al. “Majorana box qubits”. en. In: *New J. Phys.* 19.1 (2017). DOI: 10.1088/1367-2630/aa54e1.

[18] Karzig, T. et al. “Scalable designs for quasiparticle-poisoning-protected topological quantum computation with Majorana zero modes”. In: *Phys. Rev. B* 95 (23 2017). DOI: 10.1103/PhysRevB.95.235305.

[19] Sau, J. D. et al. “Generic New Platform for Topological Quantum Computation Using Semiconductor Heterostructures”. In: *Phys. Rev. Lett.* 104 (4 2010). DOI: 10.1103/PhysRevLett.104.040502.

[20] Lutchyn, R. M., Sau, J. D., and Das Sarma, S. “Majorana Fermions and a Topological Phase Transition in Semiconductor-Superconductor Heterostructures”. In: *Phys. Rev. Lett.* 105 (7 2010). DOI: 10.1103/PhysRevLett.105.077001.

[21] Oreg, Y., Refael, G., and Oppen, F. von. “Helical Liquids and Majorana Bound States in Quantum Wires”. In: *Phys. Rev. Lett.* 105 (17 2010). DOI: 10.1103/PhysRevLett.105.177002.

[22] Mourik, V. et al. “Signatures of Majorana Fermions in Hybrid Superconductor-Semiconductor Nanowire Devices”. In: *Science* 336.6084 (2012). DOI: 10.1126/science.1222360.

[23] Deng, M. T. et al. “Majorana bound state in a coupled quantum-dot hybrid-nanowire system”. In: *Science* 354.6319 (2016). DOI: 10.1126/science.aaf3961.

[24] Pientka, F. et al. “Topological Superconductivity in a Planar Josephson Junction”. In: *Phys. Rev. X* 7 (2 2017). DOI: 10.1103/PhysRevX.7.021032.

[25] Hell, M., Leijnse, M., and Flensberg, K. “Two-Dimensional Platform for Networks of Majorana Bound States”. In: *Phys. Rev. Lett.* 118 (10 2017). DOI: 10.1103/PhysRevLett.118.107701.

[26] Fornieri, A. et al. “Evidence of topological superconductivity in planar Josephson junctions”. In: *Nature* 569.7754 (2019). DOI: 10.1038/s41586-019-1068-8.

[27] Brydon, P. M. R. et al. “Topological Yu-Shiba-Rusinov chain from spin-orbit coupling”. In: *Phys. Rev. B* 91 (6 2015). DOI: 10.1103/PhysRevB.91.064505.

[28] Nadj-Perge, S. et al. “Observation of Majorana fermions in ferromagnetic atomic chains on a superconductor”. In: *Science* 346 (2014). DOI: 10.1126/science.1259327. eprint: 1410.0682.

[29] Kells, G., Meidan, D., and Brouwer, P. W. “Near-zero-energy end states in topologically trivial spin-orbit coupled superconducting nanowires with a smooth confinement”. In: *Phys. Rev. B* 86 (10 2012). DOI: 10.1103/PhysRevB.86.100503.

[30] Prada, E., San-Jose, P., and Aguado, R. “Transport spectroscopy of NS nanowire junctions with Majorana fermions”. In: *Phys. Rev. B* 86 (18 2012). DOI: 10.1103/PhysRevB.86.180503.

[31] Liu, C.-X. et al. “Andreev bound states versus Majorana bound states in quantum dot-nanowire-superconductor hybrid structures: Trivial versus topological zero-bias conductance peaks”. In: *Phys. Rev. B* 96 (7 2017). DOI: 10.1103/PhysRevB.96.075161.

[32] Moore, C., Stanescu, T. D., and Tewari, S. “Two-terminal charge tunneling: Disentangling Majorana zero modes from partially separated Andreev bound states in semiconductor-superconductor heterostructures”. In: *Phys. Rev. B* 97 (16 2018). DOI: 10.1103/PhysRevB.97.165302.

[33] Reeg, C. et al. “Zero-energy Andreev bound states from quantum dots in proximitized Rashba nanowires”. In: *Phys. Rev. B* 98 (24 2018). DOI: 10.1103/PhysRevB.98.245407.

[34] Vuik, A. et al. “Reproducing topological properties with quasi-Majorana states”. In: *SciPost Phys.* 7 (5 2019). DOI: 10.21468/SciPostPhys.7.5.061.

[35] Pan, H. and Das Sarma, S. “Physical mechanisms for zero-bias conductance peaks in Majorana nanowires”. In: *Phys. Rev. Res.* 2 (1 2020). DOI: 10.1103/PhysRevResearch.2.013377.

[36] Sau, J. D. and Sarma, S. D. “Realizing a robust practical Majorana chain in a quantum-dot-superconductor linear array”. In: *Nat. Commun.* 3.1 (2012). DOI: 10.1038/ncomms1966.

[37] Leijnse, M. and Flensberg, K. “Parity qubits and poor man’s Majorana bound states in double quantum dots”. In: *Phys. Rev. B* 86 (13 2012). DOI: 10.1103/PhysRevB.86.134528.

[38] Dvir, T. et al. “Realization of a minimal Kitaev chain in coupled quantum dots”. In: *Nature* 614.7948 (2023). DOI: 10.1038/s41586-022-05585-1.

[39] Liu, C.-X. et al. “Tunable Superconducting Coupling of Quantum Dots via Andreev Bound States in Semiconductor-Superconductor Nanowires”. In: *Phys. Rev. Lett.* 129 (26 2022). DOI: 10.1103/PhysRevLett.129.267701.

[40] Bordin, A. et al. “Tunable Crossed Andreev Reflection and Elastic Cotunneling in Hybrid Nanowires”. In: *Phys. Rev. X* 13 (3 2023). DOI: 10.1103/PhysRevX.13.031031.

[41] Wang, G. et al. “Singlet and triplet Cooper pair splitting in hybrid superconducting nanowires”. In: *Nature* 612.7940 (2022). DOI: 10.1038/s41586-022-05352-2.

[42] Wang, Q. et al. “Triplet correlations in Cooper pair splitters realized in a two-dimensional electron gas”. In: *Nat. Commun.* 14.1 (2023). DOI: 10.1038/s41467-023-40551-z.

[43] Tsintzis, A., Souto, R. S., and Leijnse, M. “Creating and detecting poor man’s Majorana bound states in interacting quantum dots”. In: *Phys. Rev. B* 106 (20 2022). DOI: 10.1103/PhysRevB.106.L201404.

[44] Fulga, I. C. et al. “Adaptive tuning of Majorana fermions in a quantum dot chain”. In: *New J. Phys.* 15.4 (2013). DOI: 10.1088/1367-2630/15/4/045020.

[45] Samuelson, W., Svensson, V., and Leijnse, M. *Minimal quantum dot based Kitaev chain with only local superconducting proximity effect*. 2024. DOI: 10.1103/PhysRevB.109.035415.

[46] Stanescu, T. D. et al. “Proximity effect at the superconductor-topological insulator interface”. In: *Phys. Rev. B* 81 (24 2010). DOI: 10.1103/PhysRevB.81.241310.

[47] Reeg, C., Loss, D., and Klinovaja, J. “Metallization of a Rashba wire by a superconducting layer in the strong-proximity regime”. In: *Phys. Rev. B* 97 (16 2018). DOI: 10.1103/PhysRevB.97.165425.

[48] Antipov, A. E. et al. “Effects of Gate-Induced Electric Fields on Semiconductor Majorana Nanowires”. In: *Phys. Rev. X* 8 (3 2018). DOI: 10.1103/PhysRevX.8.031041.

[49] Bommer, J. D. S. et al. “Spin-Orbit Protection of Induced Superconductivity in Majorana Nanowires”. In: *Phys. Rev. Lett.* 122 (18 2019). DOI: 10.1103/PhysRevLett.122.187702.

[50] Liu, C.-X. et al. “Conductance smearing and anisotropic suppression of induced superconductivity in a Majorana nanowire”. In: *Phys. Rev. B* 99 (2 2019). DOI: 10.1103/PhysRevB.99.024510.

[51] Luh, Y. “Bound state in superconductors with paramagnetic impurities”. In: *Acta Physica Sinica* 21.1 (1965).

[52] Shiba, H. “Classical Spins in Superconductors”. In: *Progress of Theoretical Physics* 40.3 (1968). DOI: 10.1143/PTP.40.435.

[53] Rusinov, A. “Theory of gapless superconductivity in alloys containing paramagnetic impurities”. In: *Sov. Phys. JETP* 29.6 (1969).

[54] Grove-Rasmussen, K. et al. “Yu–Shiba–Rusinov screening of spins in double quantum dots”. In: *Nat. Commun.* 9.1 (2018). DOI: 10.1038/s41467-018-04683-x.

[55] Pan, H. and Das Sarma, S. “Majorana nanowires, Kitaev chains, and spin models”. In: *Phys. Rev. B* 107 (3 2023). DOI: 10.1103/PhysRevB.107.035440.

[56] Zatelli, F. et al. “Robust poor man’s Majorana zero modes using Yu-Shiba-Rusinov states”. In: *arXiv:2311.03193* (2023).

[57] Miles, S., Wimmer, M., and Liu, C.-X. *Kitaev chain in an alternating quantum dot-Andreev bound state array*. 2023. DOI: 10.5281/zenodo.8378440.

[58] Day, I. A. et al. “Pymablock: An algorithm and a package for quasi-degenerate perturbation theory”. In: *SciPost Phys. Codebases* (2025). DOI: 10.21468/SciPostPhysCodeb.50.

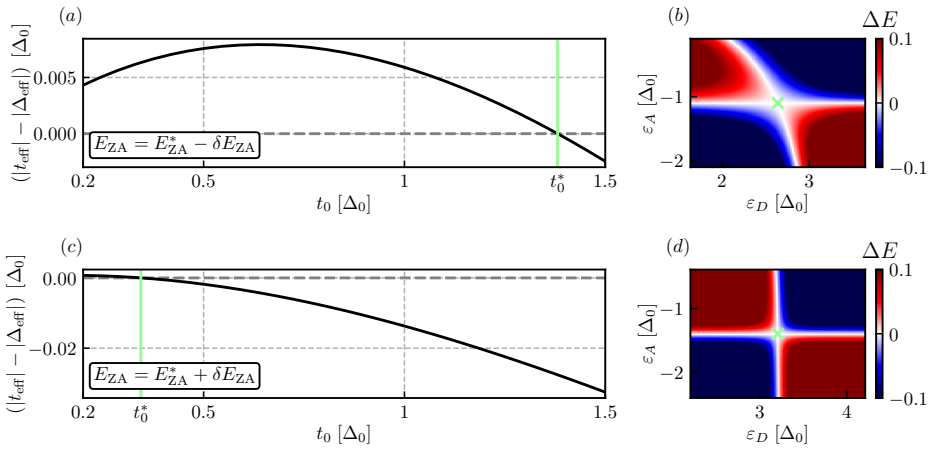

Figure 3.9: sweet spot recovery through adjustment of t_0. a) and b) show how, when starting with $t_0 = 0.2$ but $E_{ZA} = E^*_{ZA} - \delta E_{ZA}$, a sweet spot can be recovered by increasing t_0. Particularly b) demonstrates how the corresponding $t_0 > \Delta_0$, strongly coupling the two dots. We lastly want to highlight that, despite the slope of $|t_{eff}| - |\Delta_{eff}|$ being negative towards smaller t_0 in a), it is impossible to recover a sweet spot by decreasing the hopping further. c) and d) demonstrates sweet spot recovery when $t_0 = 1.5$ initially and $E_{ZA} = E^*_{ZA} + \delta E_{ZA}$.

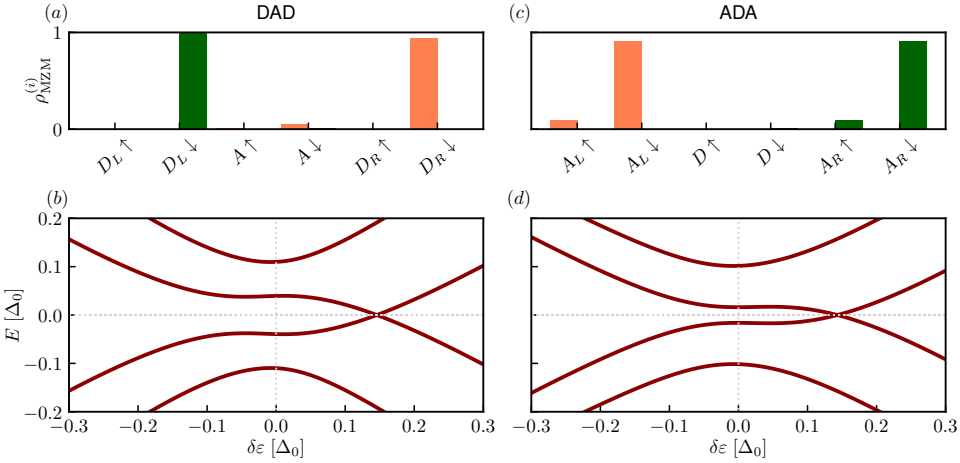

Figure 3.10: Inhomogenuous spin-orbit mixing between the two pairs. We allow for a deviation of 10% between the different α_i ($\alpha_L = 0.3, \alpha_R = 0.27$). We see that the ADA set-up reproduces the behavior suggested in the main text (d)) despite the inhomogeneity and yields well separated Majoranas (c)). This is explained by the better protection against next-nearest neighbor hopping from the larger g-factor in the central, normal dot. The DAD set-up however is more sensitive to changes of the chemical potential of the middle dot. The smaller g-factor in the ABS dot generally leads to poorer protection against next-nearest neighbor hopping. Yet, we obtain still well separated Majoranas despite the sweet spot only being meta stable against global changes of the chemical potential.

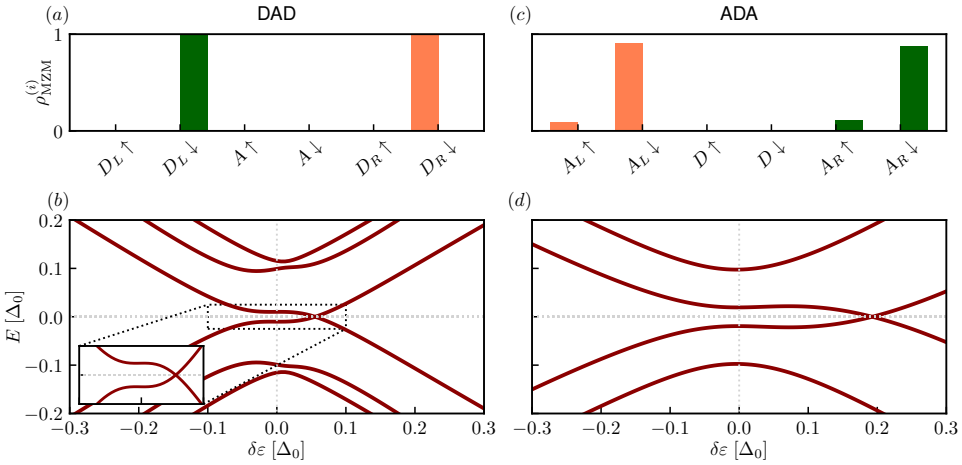

Figure 3.11: Inhomogenuous g-factors between the dots. For the DAD set-up, a) and b), we let the inhomogeneity be as large as 10% ($g_L = 2, g_R = 1.8$). We find that, despite the stark difference, the spectrum reproduces the findings of the main text well and the Majoranas yielded by the system are well separated from each other. This resillience is due to the larger level separation of the levels on the normal dots. For the ADA set-up we allow for an inhomogeneity of 10% ($g_L = 1, g_R = 0.9$). In both cases we recover spectral lines akin to those demonstrated in the main text despite the presence of inhomogeneities. Consequently, also the Majorana wavefunctions remian well separated between the dots.

4

INTERACTION-INDUCED STRONG ZERO MODES IN SHORT QUANTUM DOT CHAINS WITH TIME-REVERSAL SYMMETRY

A. Mert Bozkurt, **Sebastian Miles**, Sebastiaan L.D. ten Haaf, Chun-Xiao Liu, Fabian Hassler, and Michael Wimmer

We theoretically explore the emergence of strong zero modes in a two-site chain consisting of two quantum dots coupled due to a central dot that mediates electron hopping and singlet superconducting pairing. In the presence of time-reversal symmetry, the on-site Coulomb interaction leads to a three-fold ground-state degeneracy when tuning the system to a sweet spot as a function of the inter-dot couplings. This degeneracy is protected against changes of the dot energies in the same way as "poor man's" Majorana bound states in short Kitaev chains. In the limit of strong interactions, this protection is maximal and the entire spectrum becomes triply degenerate, indicating the emergence of a "poor man's" version of a strong zero mode. We explain the degeneracy and protection by constructing corresponding Majorana Kramers-pair operators and $\mathbb{Z}_3$-parafermion operators. The strong zero modes share many properties of Majorana bound states in short Kitaev chains, including the stability of zero-bias peaks in the conductance and the behavior upon coupling to an additional quantum dot. However, they can be distinguished through finite-bias spectroscopy and the exhibit a different behavior when scaling to longer chains.

Own contribution to work: Contributed to defining the project scope, performing the calculations, preparing the figures, and writing the manuscript.

This chapter has been published as SciPost Phys. 18, 206 (2025).

4.1. INTRODUCTION

Arrays of quantum dots offer a platform for quantum simulation of strongly-correlated and topological phases [1–4]. With a superconducting coupling in the form of crossed Andreev reflections, quantum dots have been proposed to implement the Kitaev chain which can be tuned into a topological phase [5]. Recently, it has been shown that both crossed-Andreev reflection (CAR) and elastic co-tunneling (ECT) between two quantum dots can be effectively tuned by an additional proximitized quantum dot between two normal quantum dots [6]. This has allowed to implement high-performance Cooper pair splitters [7–9] and to explore Majorana physics in a minimal Kitaev chain of two sites [10–12] and three sites [13]. When the quantum dots are in the spin-polarized regime and the amplitudes of these two processes are equal, a condition referred to as the *sweet spot*, a double quantum dot system connected by an ABS can feature Majorana bound states localized on the outer dots [6, 14–16], so-called poor man's Majoranas (PMMs).

In these quantum dot systems, the charging energy U is typically the largest energy scale. In current experiments, U is of order several meV, whereas the inter-dot coupling is of order $30-80\mu$eV [10–12]. This two-orders-of-magnitude difference in energy scales evokes the question of the role of interactions in these systems. The presence of strong charging energy makes the quantum dot platform fundamentally different from the original Majorana proposal in nanowires [17, 18], and insights from those systems may not directly apply here. For instance, can interactions lead to false positives in the search for Majorana bound states in quantum dot systems? On the other hand, can interactions be used to engineer new types of states in these systems? The exploration of these two questions is the main goal of this study.

The importance of these questions is highlighted by a recent experimental work [11] implementing an artificial Kitaev chain with two sites in a proximitized two-dimensional electron gas. This experiment revealed stable zero-bias peaks for finite magnetic field, interpreted as PMMs. However, measurements also revealed a stable zero-bias peak in the *absence* of a magnetic field. In fact, the zero-bias conductance features were remarkably similar regardless of the value of magnetic field, despite PMMs only being expected at sufficiently large Zeeman splitting. This raises the question whether signatures of PMMs can be mimicked by trivial mechanisms in quantum dot systems. At the same time, a setup similar to the experiment was predicted theoretically to exhibit Majorana zero modes induced by Coulomb interaction in the presence of only a small Zeeman splitting [19]. Hence, it equally seems possible to induce precursors of topological states in quantum dot systems by interactions. Overall, this underlines the need for a systematic understanding of the zero-field case.

In this manuscript, we investigate strongly interacting double quantum dot system coupled by normal hopping and singlet superconducting inter-dot coupling via an additional proximitized quantum dot in the presence of time-reversal symmetry. We find that any finite charging energy on the quantum dots allows for a sweet spot characterized by a triply degenerate ground state. This ground state degeneracy is protected quadratically against changes of the on-site potential of either dot, akin to the two-site spinless Kitaev chain case. In the limit of large Coulomb interaction, the triple ground state degeneracy becomes completely protected against local changes of the on-site energies. We show that the system in this limit exhibits a poor man's version of strong zero modes, and

construct corresponding Majorana Kramers-pair operators as well as $\mathbb{Z}_3$-parafermion operators explaining the protection against local perturbations. Moreover, just as in the spinless two-site Kitaev chain case [20], the ground state degeneracy is not lifted by coupling a third normal dot to the system via normal hopping. However, we can distinguish the zero-field, interaction-induced strong zero modes from PMMs through finite-bias spectroscopy and the absence of scaling to longer chains.

4.2. CHARGE STABILITY DIAGRAM AND TRANSPORT PROPERTIES OF A DOUBLE-QUANTUM DOT SYSTEM

We consider a double-quantum dot system coupled by ECT and CAR processes, as sketched in Fig. 4.1(a). The Hamiltonian of this system is given by [19, 21]

$$H = \sum_{i,\sigma} \epsilon_i n_{i\sigma} + \sum_i U_i n_{i\uparrow} n_{i\downarrow} + t \sum_\sigma c^\dagger_{L\sigma} c_{R\sigma} + \Delta \sum_\sigma \eta_\sigma c^\dagger_{L\sigma} c^\dagger_{R\bar{\sigma}} + \text{H.c.}, \tag{4.1}$$

where $i = L, R$ denotes the site index, $n_{i\sigma} = c^\dagger_{i\sigma} c_{i\sigma}$ is the number operator on site i with spin σ, ϵ_i is the on-site energy, U_i is the Coulomb energy of dot i, t is the normal hopping and Δ is the singlet type of superconducting pairing between left and right dot.[1] The term $\eta_\sigma = (-1)^\sigma$ encodes the singlet pairing and $\bar{\sigma} = -\sigma$ denotes the opposite spin $\sigma = \uparrow, \downarrow$. We note that as we consider a system with time-reversal symmetry, we can gauge-away the spin-orbit coupling by redefining the spin quantization axis on each dot, as detailed in Appendix 4.11. Consequently, the presence of spin-orbit coupling, and consequently triplet superconducting pairing, is not necessary for our investigation. Tuning the relative strength of t and Δ can for example be achieved through changing the energy of an ABS in a hybrid segment or proximitized quantum dot [6], as indicated in lighter color in Fig. 4.1(a). In the main text, we will exclusively use the effective model (4.1). However, using a model that includes the ABS gives comparable results, as shown in App. 4.7.

The charge stability diagram (CSD) of Eq. (4.1) of a double-quantum dot system coupled by ECT and CAR processes in the absence of a magnetic field has been studied in [21]. We show a sketch of the charge stability diagram in the absence of inter-dot interactions in Fig. 4.1(b), focusing on the energy range where each dot can be either empty or singly-occupied. Due to time-reversal symmetry, all states in the odd parity sector are doubly degenerate (blue parts of the CSD). When both dots are occupied by one electron, there are four degenerate states when the dots are decoupled: one singlet and three triplet states. However, in the presence of any finite t or Δ, it was shown [21] that the triplet states are higher in energy. Hence, for our purposes it is sufficient to only consider the singlet state and thus the even parity sector generally is singly degenerate. Ref. [21] further showed that for finite inter-dot coupling, either the odd or the even parity sectors merge, as we confirm in Figs. 4.1(d) and (f) by varying Δ/t. This is due to either the ground state energy being lowered differently depending on the relative strength of t and Δ. However, since the CSD connectivity can be completely changed, *it is always possible* to find a relative strength of Δ/t such that there is a crossing, which we refer to as a sweet-spot, as shown in Fig. 4.1(e).

[1] Here, we choose a gauge such that $t, \Delta \in \mathbb{R}$.

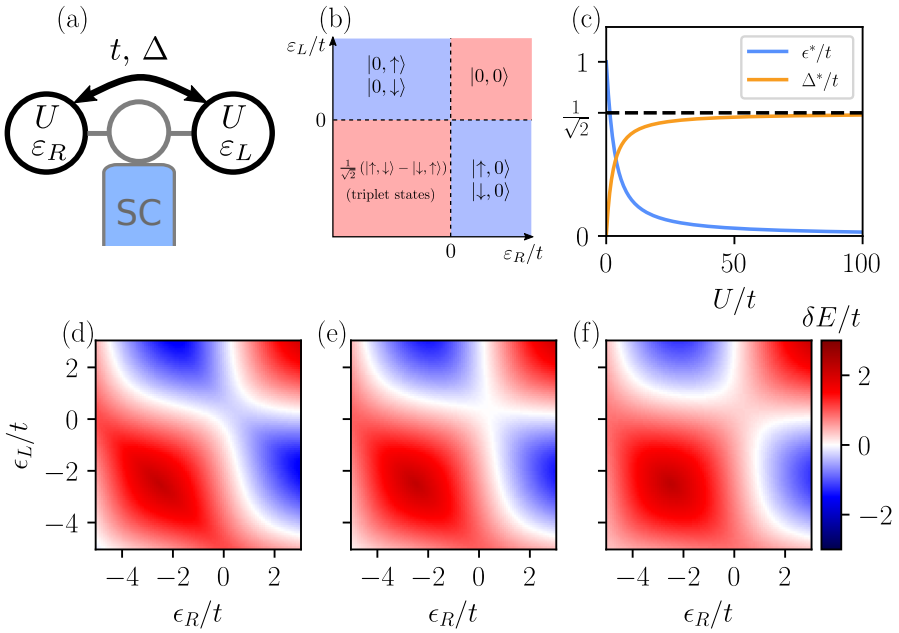

Figure 4.1: (a) Schematics of a two-site chain consisting of three quantum dots. The superconductor (blue) proximitizes the middle dot and facilitates normal hopping and superconducting pairing between the left and right quantum dots, each characterized by their respective on-site energies ϵ_i and charging energy U. (b) Sketch of the charge stability diagram, excluding the doubly-occupied states. The blue regions denote the odd fermion parity ground state, while the red regions represent the even fermion-parity ground state. (c) The parameters for the sweet spot, Δ^* and ϵ^*, are depicted as a function of U. The evolution of the charge stability diagram for (d) $\Delta^* > \Delta = 0.293t$, (e) $\Delta = \Delta^* = 0.493t$, and (f) $\Delta^* < \Delta = 0.693t$. Here, we use $U = 5t$.

Fig. 4.1(d)–(f) shows the charge stability diagram in the form of $\delta E = E_{\text{gs}}^{\text{odd}} - E_{\text{gs}}^{\text{even}}$ being the energy difference of the ground states with opposite fermion parity. At the sweet-spot, and in general for the white lines in the CSD, the energies of the even and odd-parity ground states are equal, and the ground state triply degenerate. Moreover, the crossing corresponding to a sweet-spot represents a saddle point in δE. Hence, for small deviations around the sweet-spot, the three-fold ground state degeneracy is protected quadratically. This quadratic protection of ground state degeneracy is—up to the multiplicity of the degeneracy—identical to the spinless Kitaev chain case [14]. This is not surprising, as our arguments show that it is due to the intrinsic "topology" of the sweet spot, i.e. the fact the sweet spot must be a saddle point for δE. Hence we generally expect this quadratic protection when the connectivity of the CSD switches.

Note that this quadratic protection is seemingly in contradiction to Ref. [22] which claimed that the degeneracy in this system is changing linearly with changing the on-site energies $\epsilon_{R,L}$. This contradiction can be resolved by observing that Ref. [22] only considered degeneracies for $\epsilon_R = \epsilon_L = 0$. The sweet spot however is generally shifted away from zero on-site energy as shown in Fig. 4.1(c).

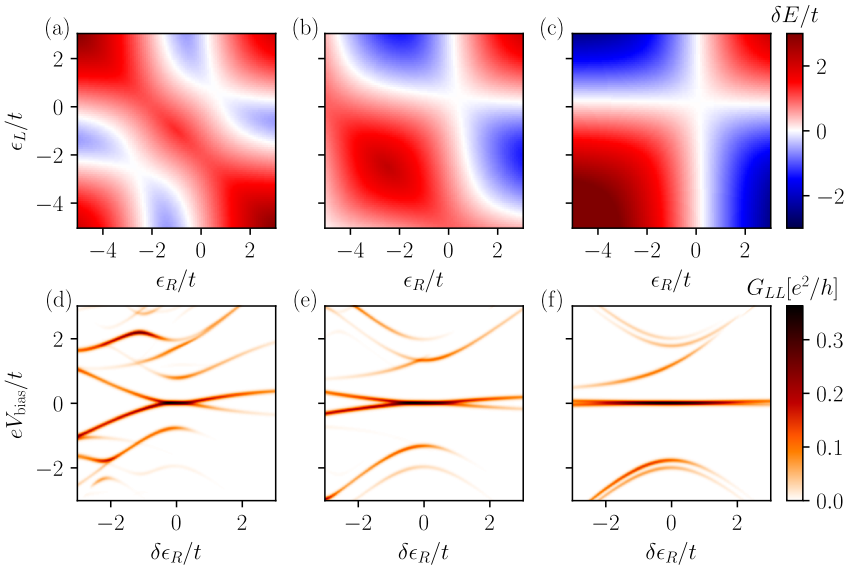

Figure 4.2: The charge stability diagram and local finite bias conductance as a function of the charging energy. Top panels: The charge stability diagram of the two-site spinful interacting chain for (a) $U = 2t$, (b) $U = 5t$, and (c) $U = 15t$, featuring a sweet spot. The crossing of the degeneracy lines at the sweet spot becomes straighter as U increases. Additionally, as U increases, the quadrants of the charge stability diagram move further away from each other. Bottom panels: The local finite bias conductance G_{LL} for (d) $U = 2t$, (e) $U = 5t$, and (f) $U = 15t$, as a function of voltage bias V_{bias} and the variation of the on-site energy on site R away from the sweet spot, $\delta\epsilon_R$. The zero-bias peak persists for a wider range of detuning, $\delta\epsilon_R$, for larger local charging energy. Additionally, the local conductance feature visible in (f) for $\delta\epsilon_R < 0$ and $V_{\text{bias}} > 0$ describes the transport process via coupling of the ground state to the triplet states. For even larger voltage bias values, the conductance features exhibit splitting, which diminishes as U increases.For transport simulations, we use dot-lead coupling $\Gamma = 0.0125t$ and reservoir temperature $T = 0.025t$.

A hallmark of spinless PMMs is the persistence of the ground state degeneracy when changing only a single site on-site energy [14]. In general this does not apply to the degeneracies for the time-reversal symmetric Hamiltonian (4.1). In Fig. 4.2 we show the charge stability diagrams (a)–(c) and the corresponding conductances, calculated using a rate-equation approach [15], for a normal probe on the left site (d)–(f) for different values of the Coulomb interaction U. The separation between the lower left quadrant of the charge stability diagram, comprised of states with double occupancy, from the upper right quadrant, comprised of empty dots, increases with Coulomb energy U. As a consequence, the degeneracy lines of the sweet spot crossing are initially tilted and become increasingly straighter with increasing U, Figs. 4.2(a)–(c). Hence, the ground state degeneracy becomes increasingly better protected against *local* potential changes, i.e. only changing $\epsilon_{R(L)}$ while keeping $\epsilon_{L(R)}$ at the sweet spot value. This can be directly observed in the behavior of the conductance that probes the excitation spectrum of the system. In particular, a ground state degeneracy gives rise to a zero-bias peak, whereas any splitting gives rise to a conductance only at finite bias.

As U increases, the ground state degeneracy becomes more and more protected

against the changes in one of the local on-site energies. This protection is reflected as a robust zero-bias peak in the local conductance spectroscopy on the left dot, as shown in Fig. 4.2(d)–(f). In fact, for large values of U, the zero-bias conductance of the two-site spinful interacting chain described by Eq. (4.1) becomes indistinguishable from the zero-bias conductance of a two-site spinless Kitaev chain hosting PMMs. Hence, these interaction-induced zero-energy states could be mistaken for PMMs. However, they can be distinguished by additional features at finite-bias, in particular the feature at positive bias voltage that approaches zero as the on-site energy of one site is decreased. It originates from the triplet states, and allows to distinguish this system from the spinless Kitaev chain, as discussed in detail in Appendix 4.6.

4.3. STRONG ZERO MODES IN THE $U \to \infty$ LIMIT

4.3.1. EIGENSTATES AND EIGENSPECTRUM IN THE $U \to \infty$ LIMIT

While it is possible to find a sweet spot where the ground state is triply degenerate for any finite charging energy U, the protection of the ground state degeneracy with respect to local changes is only truly possible in the limit of $U \to \infty$.[2] In this limit, double occupancy of a quantum dot is forbidden. This constraint can be implemented in Eq. (4.1) by replacing all fermionic operators by constrained fermions [23]. The constrained fermions are defined by the Hubbard operators $\bar{c}_{i\sigma} = (1 - n_{i\bar{\sigma}})\, c_{i\sigma}$. The Hamiltonian then takes the form

$$H = \sum_i \epsilon_i \bar{n}_i + t \sum_\sigma \bar{c}^\dagger_{L\sigma} \bar{c}_{R\sigma} + \Delta \sum_\sigma \eta_\sigma \bar{c}^\dagger_{L\sigma} \bar{c}^\dagger_{R\bar{\sigma}} + \text{H.c.}\,, \tag{4.2}$$

where $\bar{n}_i = \sum_\sigma \bar{c}^\dagger_{i\sigma} \bar{c}_{i\sigma}$.

In this limit, the many-body energy levels for the odd parity sector are $\frac{1}{2}(\epsilon_L + \epsilon_R) \pm \left[t^2 + \frac{1}{4}(\epsilon_L - \epsilon_R)^2\right]^{1/2}$ with a multiplicity of 2 due to Kramers' degeneracy. For the even parity sector, the energy levels consist of $(\epsilon_L + \epsilon_R)$ with a multiplicity of 3, describing triplet states, and $\frac{1}{2}(\epsilon_L + \epsilon_R) \pm \left[2\Delta^2 + \frac{1}{4}(\epsilon_L + \epsilon_R)^2\right]^{1/2}$, describing singlet states. Therefore, when $t = \sqrt{2}\Delta$ and $\epsilon_L = \epsilon_R = 0$, the ground state becomes triply degenerate with an energy of $E_g = -t$ [19]. The many-body eigenstates of the ground state manifold are

$$|n = 0, \downarrow\rangle = \frac{1}{\sqrt{2}}\left(|0\downarrow\rangle - |\downarrow 0\rangle\right), \tag{4.3a}$$

$$|n = 0, \uparrow\rangle = \frac{1}{\sqrt{2}}\left(|\uparrow 0\rangle - |0\uparrow\rangle\right), \tag{4.3b}$$

$$|n = 0, S\rangle = -\frac{1}{\sqrt{2}}|00\rangle + \frac{1}{2}\left(|\uparrow\downarrow\rangle - |\downarrow\uparrow\rangle\right), \tag{4.3c}$$

where $n = 0$ denotes the ground state manifold (the states $n = 1, 2$ are given in Appendix 4.8), we label odd-parity states with their spins $|\uparrow(\downarrow)\rangle$ and the even-parity ground

[2] In current experimental implementations, U exceeds all other energy scales in the system [10–12]. In this case, coupling to doubly occupied states is strongly suppressed and corrections through these states would only enter perturbatively and become visible through splittings in the excited states (see Fig. 4.2).

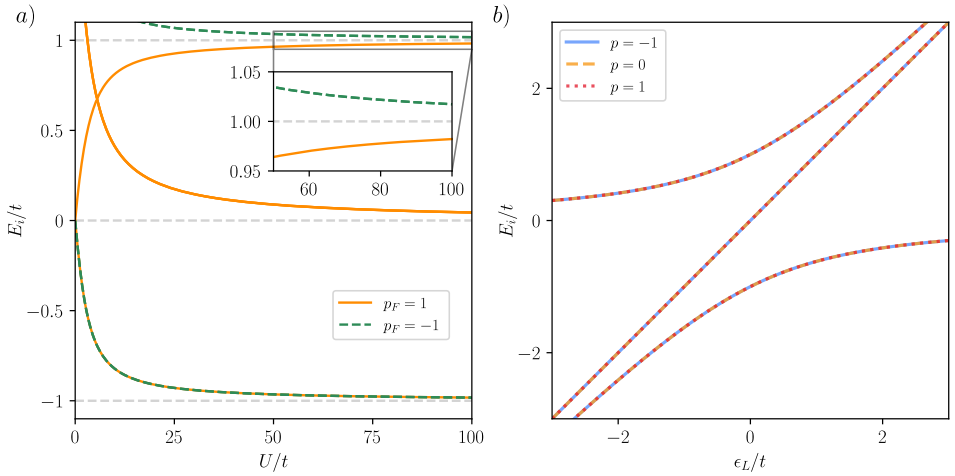

Figure 4.3: Many-body energy spectrum of the double-quantum dot system. In panel a), we demonstrate the many-body energy spectrum at the sweet spot as a function of U. The different colors indicate the different total fermion parity eigenvalues $p_F = \langle\psi|\sum_i(1-2n_i)|\psi\rangle$ of the corresponding eigenstate. The second excited state manifold becomes three-fold degenerate as $U \to \infty$. In addition, the states forming the first excited state manifold for $U \to \infty$ are three-fold degenerate for all U. Hence, the full many-body spectrum is three-fold degenerate for $U \to \infty$. Panel b) shows the many-body spectrum for $U \to \infty$ and protection of the three-fold degenerate structure in the many-body spectrum with respect to changes in ϵ_L. The states with distinct generalized $\mathbb{Z}_3$ parity eigenvalues p are differentiated by their colors and line styles.

state is a superposition of vacuum state and a singlet state $|S\rangle$. These eigenstates are reminiscent of the eigenstates of a two-site spinless Kitaev chain [14], except that the component with both dots occupied has a singlet character. As we show below, this leads to non-local correlations.

However, the three-fold degeneracy extends beyond the ground state manifold in this system. In fact, the many-body spectrum of the system consists of three different manifolds with three-fold degeneracy. As the entire many-body spectrum exhibits the three-fold degenerate structure, the zero energy excitations associated with this system are strong zero modes [24]. In Fig. 4.3(b), we show the many-body spectrum of the two-site chain as we vary one of the on-site energies ϵ_i. The three-fold degeneracy of each three manifold is maintained upon varying one local on-site energy, demonstrating the protection of strong zero modes to this perturbation. Within these three manifolds, both the ground state ($n = 0$) and second excited state ($n = 2$) manifolds each feature two odd and one even parity states. In contrast, the first excited state ($n = 1$) manifold comprises three triplet states with eigenvalues $E = 0$. We want to stress that the strong zero modes in our system only exist in the limit of $U \to \infty$. For any finite U, the entire many-body spectrum does not feature three-fold degenerate manifolds, as shown in Fig. 4.3 a), and hence, the resulting zero modes are weak zero modes.

4.3.2. MAJORANA KRAMERS-PAIR OPERATORS

Given the shared parity structure of the ground state and the second excited state manifolds, featuring two odd and one even fermion parity states, we introduce Majorana operators that allow switching between different parity states across the spectrum. Importantly, we exclude the first excited state manifold, as it does not permit any parity-switching zero-energy excitations and the triplet states do not couple to any of the other states by any term in the Hamiltonian. The modes described by these operators are deemed strong Majorana zero modes due to the consistent degeneracy throughout the spectrum [25, 26]. Additionally, recognizing that the odd states within each manifold are Kramers partners, we also associate Majorana operators with their Kramers partners. Based on these restrictions, Majorana Kramers-pair operators satisfy the conditions

$$\gamma_\sigma = \gamma_\sigma^\dagger, \tag{4.4a}$$

$$\gamma_\sigma |n, S\rangle = e^{i\phi} |n, \sigma\rangle, \tag{4.4b}$$

$$\gamma_\sigma |n, \sigma\rangle = e^{-i\phi} |n, S\rangle, \tag{4.4c}$$

where ϕ is a phase.

We then use the eigenstates of the many-body Hamiltonian and construct the Majorana Kramers-pair operators that satisfy Eq. (4.4) for a given spin projection.[3] We find these Majorana Kramers-pair operators as

$$\gamma_{R\sigma} = \eta_\sigma (1 - \bar{n}_L)\, \bar{c}_{R\sigma} - \frac{1}{\sqrt{2}} \left(\bar{n}_{L\sigma}\, \bar{c}_{R\bar{\sigma}} - \bar{c}^\dagger_{L\sigma}\, \bar{c}_{L\bar{\sigma}}\, \bar{c}_{R\sigma} \right) + \text{H.c.}, \tag{4.5a}$$

$$\gamma_{L\sigma} = i\eta_\sigma (1 - \bar{n}_R)\, \bar{c}_{L\sigma} + \frac{i}{\sqrt{2}} \left(\bar{n}_{R\sigma}\, \bar{c}_{L\bar{\sigma}} - \bar{c}^\dagger_{R\sigma}\, \bar{c}_{R\bar{\sigma}}\, \bar{c}_{L\sigma} \right) + \text{H.c.}, \tag{4.5b}$$

where $\eta_\sigma = (-1)^\sigma$ and $\bar{\sigma} = -\sigma$ denotes the opposite spin. The strong correlation in the system is evident from the presence of products of number operators in the definition of Majorana operators, and by products of operators flipping the spin on a dot. The latter are related to the fact that the even ground state involves a spin singlet state.

The Majorana Kramers-pairs operators given in Eq. (4.5) commute with the Hamiltonian at the sweet spot by construction. Furthermore, each Majorana Kramers-pair operator commutes with one of the number operators $\bar{n}_i$, specifically $[\bar{n}_L, \gamma_{R\sigma}] = [\bar{n}_R, \gamma_{L,\sigma}] = 0$. This explains why any perturbation involving only one of the on-site energies ϵ_i will not lift the degeneracies within the $n = 0, 2$ states. We note that in terms of the commutation relations with the number operators on each dot, these Majorana Kramers-pairs operators are local. However, in terms of dot creation and annihilation operators, they clearly are not.

It is worth emphasizing that these Majorana Kramers-pairs, or in other words the corresponding ground state degeneracy, only exist due to interactions: A no-go theorem states that Majorana Kramers-pairs cannot be realized in non-interacting electronic systems with a single conventional superconductor [27]. Hence, the charging energy U is the driving force for obtaining the ground state degeneracy.

[3] We refer the reader to Appendix 4.9 for more details on how to construct the Majorana operators from the eigenstates.

4.3.3. $\mathbb{Z}_3$-PARAFERMION OPERATORS

Majorana Kramers-pairs operators can only be meaningfully defined in terms of the manifolds $n = 0, 2$ containing even and odd parity states. In the following, we will introduce a different, complementary description that takes the full spectrum into account.

Having a many-body spectrum that is three-fold degenerate signals a symmetry of the system. Beyond the fermion-parity conservation, the system has the additional generalized-parity symmetry

$$P_{\mathbb{Z}_3} = \omega^{\sum_j (n_{j\uparrow} + 2n_{j\downarrow})} \tag{4.6}$$

with $\omega = e^{i2\pi/3}$ [28] and $n_{j\sigma} = c^\dagger_{j\sigma} c_{j\sigma}$ the spin-resolved number operator defined on site j. We find that the eigenstates within each degenerate manifold n are uniquely characterized by their corresponding generalized parity eigenvalue $p = 0, 1, 2$

$$P_{\mathbb{Z}_3} |n, p\rangle = \omega^p |n, p\rangle . \tag{4.7}$$

As all the states $|n, p\rangle$ for fixed n, are degenerate, we can construct a parafermion operator χ. These operators switch between eigenstates with different $P_{\mathbb{Z}_3}$-parity eigenvalues p within each degenerate manifold with

$$\chi |n, p\rangle = a_{n,p} |n, p + 1 \ (\mathrm{mod}\ 3)\rangle , \tag{4.8a}$$

$$\chi^3 = \mathbb{1} \tag{4.8b}$$

$$\chi P_{\mathbb{Z}_3} = \omega P_{\mathbb{Z}_3} \chi , \tag{4.8c}$$

where the coefficients $a_{n,p}$ are complex and satisfy $\prod_p a_{n,p} = 1$ for all n, ensuring that $\chi^3 = \mathbb{1}$. Note that the parafermion operators do not obey superselection as they must contain both fermion-parity switching and conserving operators.

To construct the parafermion operators, we use the many-body eigenstates of the system. In addition to satisfying the conditions outlined for parafermion operators in Eq. (4.8), we require that these operators commute with one of the number operators. This requirement helps explain how the many-body spectrum is protected against changes in local on-site energies.[4] We find two parafermion operators χ_L and χ_R expressed in terms of constrained fermion operators as

$$\begin{aligned}\chi_R = {} & (1 - \bar{n}_L)\left(-\bar{c}^\dagger_{R\downarrow} + \bar{c}_{R\uparrow}\right) + \left(\bar{c}^\dagger_{R\downarrow}\bar{c}_{R\uparrow} + \frac{1}{\sqrt{2}}\left(\bar{c}_{R\downarrow} + \bar{c}^\dagger_{R\uparrow}\right)\right)\bar{c}^\dagger_{L\downarrow}\bar{c}_{L\uparrow} \\ & - \frac{1}{\sqrt{2}}\left(\bar{n}_{L\uparrow}\bar{c}^\dagger_{R\downarrow} + \bar{n}_{L\downarrow}\bar{c}_{R\uparrow}\right) - \left(1 - \frac{1+\sqrt{2}}{\sqrt{2}}\bar{n}_L\right)\bar{c}^\dagger_{R\uparrow}\bar{c}_{R\downarrow} - \left(1 - \frac{1+\sqrt{2}}{\sqrt{2}}\bar{n}_R\right)\bar{c}^\dagger_{L\uparrow}\bar{c}_{L\downarrow}, \end{aligned} \tag{4.9a}$$

$$\begin{aligned}\chi_L = {} & (1 - \bar{n}_R)\left(\bar{c}^\dagger_{L\downarrow} + \bar{c}_{L\uparrow}\right) + \left(\bar{c}^\dagger_{L\downarrow}\bar{c}_{L\uparrow} + \frac{1}{\sqrt{2}}\left(\bar{c}^\dagger_{L\uparrow} - \bar{c}_{L\downarrow}\right)\right)\bar{c}^\dagger_{R\downarrow}\bar{c}_{R\uparrow} \\ & - \frac{1}{\sqrt{2}}\left(\bar{n}_{R\uparrow}\bar{c}^\dagger_{L\downarrow} - \bar{n}_{R\downarrow}\bar{c}_{L\uparrow}\right) + \left(1 + \frac{1-\sqrt{2}}{\sqrt{2}}\bar{n}_L\right)\bar{c}^\dagger_{R\uparrow}\bar{c}_{R\downarrow} + \left(1 + \frac{1-\sqrt{2}}{\sqrt{2}}\bar{n}_R\right)\bar{c}^\dagger_{L\uparrow}\bar{c}_{L\downarrow}. \end{aligned} \tag{4.9b}$$

[4] We refer the reader to Appendix 4.10 for the details.

The parafermion operators given in Eq. (4.9) commute with the Hamiltonian at the sweet spot and satisfy $\chi_i^3 = \mathbb{1}$ by construction. Furthermore, each parafermion operator commutes with one of the number operators $\bar{n}_i$, specifically $[\bar{n}_L, \chi_R] = [\bar{n}_R, \chi_L] = 0$. Hence these parafermion operators also explain the protection of the degeneracy in the many-body spectrum against variations in the on-site energies.

The parafermion operators given in Eq. (4.9) do not satisfy $\mathbb{Z}_3$ parastatistics. The reason for this is that we want the parafermion operators to commute with the number operators to explain the robustness with respect to changes in on-site energies. If we remove this restriction, we can find coefficients $a_{n,p}$ such that the resulting parafermion operators obey the $\mathbb{Z}_3$ parastatistics $\chi_L\chi_R = \omega\,\chi_R\chi_L$.[5] As a interesting side-remark, we note that we were able to find parafermion operators that commute with the number operators and satisfy the $\mathbb{Z}_3$ parastatistics *when* projected to the ground state manifold.[6]

4

4.3.4. Low-energy effective Hamiltonian with parafermion operators

Next, we explore the low-energy physics of the three-fold degenerate ground state manifold. To this end, we project the parafermion operators given in Eq. (4.9) to the ground state manifold. These projected operators, denoted as $\tilde{\chi}_R$ and $\tilde{\chi}_L$, still commute with their respective number operators.

Mapping the parafermion operators onto the ground state allows us to derive the low-energy effective Hamiltonian

$$\tilde{H} = -\frac{\left(t+\sqrt{2}\Delta\right)}{2}\mathbb{1} + \frac{\left(t-\sqrt{2}\Delta\right)}{4}\left(\tilde{\chi}_L^\dagger\tilde{\chi}_R + \tilde{\chi}_R^\dagger\tilde{\chi}_L\right). \tag{4.10}$$

Note that the low-energy Hamiltonian is akin to the low-energy Hamiltonian of a two-site $\mathbb{Z}_3$ parafermion chain[24, 29–31]. The first term is an energy offset such that at the sweet spot, with $t = \sqrt{2}\Delta$, the ground state energy is $E_g = -t$.

4.4. Three-site spinful interacting chains

4.4.1. Quantum dot test

Having established the characterization of the two-site spinful interacting chain and its protection due to $P_{\mathbb{Z}_3}$ parity, we now investigate its behavior when the chain length is increased. To this end, we first consider adding a third spinful quantum dot only coupled by a normal hopping t, as show in Fig. 4.4(a). This system is the time-reversal symmetric variant of a quantum dot test originally designed for Majorana bound state detection. This test, aimed at identifying unpaired localized Majorana bound states, has been previously considered in various setups, including proximitized nanowires [32–34] and artificial Kitaev chains [20, 35]. Here, we probe the two-site chain by using a test quantum dot D in the single electron limit, i.e. $U_D \to \infty$, with an on-site energy $\epsilon_D = 0$. Quantum dot D is coupled to site R of the two-site chain with spin-conserving hopping

[5] The choice of coefficients with $a^1_{n,p} = \omega$ and $a^2_{n,p} = \omega^{-p}$ yields two parafermion operators that obey $\mathbb{Z}_3$ parastatistics. In this case, the first parafermion operator still commutes with n_R, however the second parafermion operator does not commute with n_L.

[6] See Appendix 4.10.2 for details.

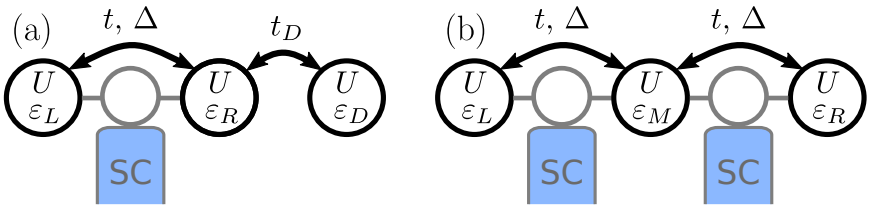

Figure 4.4: (a) Quantum dot test: A two-site spinful interacting chain is coupled to a quantum dot D via a spin-conserving normal hopping. (b) Three-site spinful interacting chain with sites L, M and R, each coupled via normal hopping t and superconducting pairing Δ.

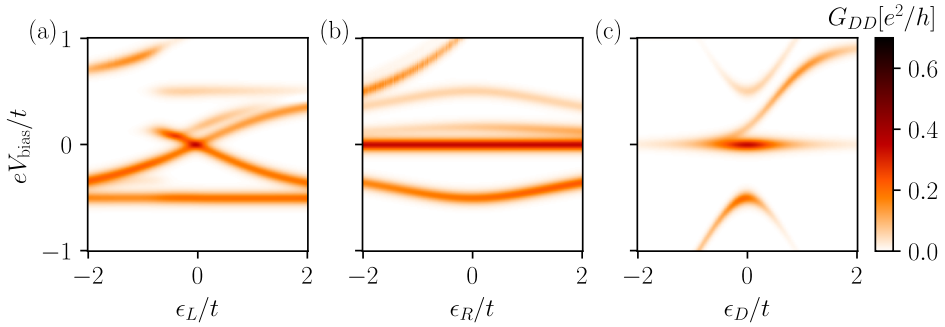

Figure 4.5: Quantum dot test: Another quantum dot D is attached, coupled exclusively to site R through spin-conserving hopping. Variation of (a) on-site energy ϵ_L results in a splitting of the zero-bias peak in the local finite bias conductance measured from quantum dot D. Conversely, changes in (b) on-site energy ϵ_R or (c) the test quantum dot ϵ_D do not induce a splitting of the zero-bias peak. For transport simulations, we use dot-lead coupling $\Gamma = 0.0125t$ and reservoir temperature $T = 0.025t$.

$H_{RD} = t_D \sum_\sigma \bar{c}^\dagger_{R\sigma} \bar{c}_{D\sigma} + \text{H.c.}$, as shown in Fig. 4.4(a). We then measure local finite bias conductance G_{DD} as we vary on-site energies of each of the three sites in the system as shown in Fig. 4.5.

In Fig. 4.5(a), we observe that detuning the on-site energy of site L leads to a splitting in the zero-bias peak in the local differential conductance G_{DD} measured by tunnel coupling a normal lead to quantum dot D. In contrast to varying the on-site energy of site L, varying the on-site energy of site R or the test dot D does not lead a splitting in the zero-bias conductance peak, as shown in Fig 4.5(b)–(c).

The outcome of the quantum dot test closely resembles the quantum dot test for poor man's Majorana zero modes [20]. There the splitting of the zero-bias peak, when the on-site energy of site L is detuned, is attributed to the leakage of the left Majorana wavefunction to the right site. Then, the right site no longer hosts an isolated Majorana wavefunction and the zero-bias peak splits linearly. On the other hand, detuning the on-site energies of site R or the test quantum dot would not lead to any splitting as there would be a single Majorana residing on the site R. Disregarding the interacting nature of our system, the outcomes of the quantum dot test could thus be (mis)interpreted as the presence of an isolated zero-mode in each dot.

To understand the role of the quantum dot test in our spinful interacting system, we construct a low-energy Hamiltonian using the $\mathbb{Z}_3$-parafermion operators that we constructed before to show the stability against changes in local potentials. To that end, we project the spin-conserving coupling term between site R and test quantum dot $H_t = t_D \sum_\sigma \bar{c}^\dagger_{R\sigma} \bar{c}_{D\sigma} + \text{H.c.}$ to the ground state manifold. Then, the projected coupling Hamiltonian takes the form

$$\tilde{H}_t = \frac{t}{\sqrt{6}} \left(A_1 d^\dagger_{D\uparrow} + A_2 d^\dagger_{D\downarrow} + \text{H.c.} \right), \tag{4.11}$$

where operators $A_{1,2}$ act on site L and site R of the original two-site chain and are expressed in terms of parafermion operators

$$A_1 = \frac{1}{2}(\tilde{\chi}_L + \tilde{\chi}_R), \tag{4.12a}$$

$$A_2 = \frac{1}{2}(\tilde{\chi}^\dagger_L + \tilde{\chi}_L \tilde{\chi}_R), \tag{4.12b}$$

and operators

$$d^\dagger_{D,\sigma} = \sqrt{\frac{2}{3}} \left(\frac{1}{\sqrt{2}} \bar{c}^\dagger_{D\sigma} + \bar{c}_{D\bar{\sigma}} \right), \tag{4.13}$$

act on the test quantum dot states.

The form of Eq. (4.11) together with Eq. (4.12) indicate that the fermionic states in the quantum dot D actually couple to both of the parafermions. Therefore, the result of the quantum dot test for our system cannot be interpreted as selectively coupling to a single parafermion, in contrast to Majorana bound states [20, 32, 33].

This leaves the question of why the quantum dot test leaves the ground state degeneracy unchanged. In fact, we find that the entire many-body spectrum of the combined three-dot system is also comprised by degenerate manifolds. The fact that the system still features $P_{\mathbb{Z}_3}$ symmetry, each degenerate manifold has eigenstates with three different generalized parity eigenvalues. This property allows us to construct two parafermion operators χ_1 and χ_2, similar to how we constructed parafermion operators for the two-site chain case given in Eq. (4.9).[7]

Each parafermion operator, in addition to commuting with the Hamiltonian at the sweet spot and $\bar{n}_D$, also commutes with either $\bar{n}_L$ or $\bar{n}_R$, specifically $[\chi_1, \bar{n}_L] = [\chi_2, \bar{n}_R] = 0$. On the other hand, only χ_2 commutes with H_{RD}, the operator that describes spin-conserving hopping between site R and quantum dot D. As a consequence, varying ϵ_L results in the splitting of the degenerate energy levels, whereas varying ϵ_R or ϵ_D does not.

A natural question to ask is whether parafermion operators in three-site and two-site cases are related. Given the strongly-correlated nature of the system, the form of these operators are quite involved, and involve terms mixing operators from all three dots. Nevertheless, we can project the parafermion operators for the three-site system onto a two-site system by tracing out the degrees of freedom related to quantum dot D. In this

[7] See App. 4.10.3 for the construction of the parafermion operators.

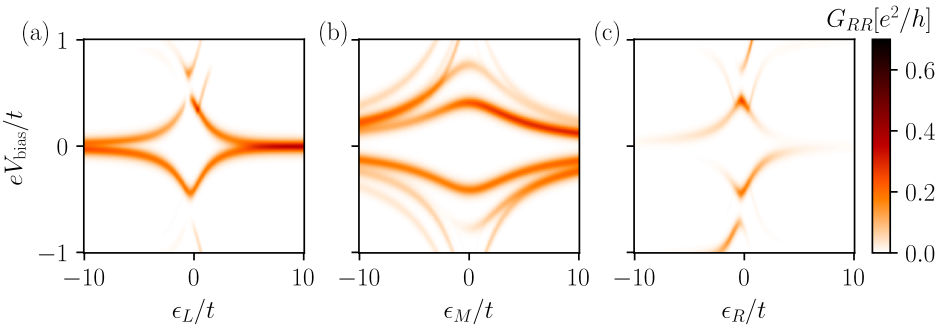

Figure 4.6: The local finite bias conductance for the three site chain shown in Fig. 4.4(b) as we detune (a) ϵ_L, (b) ϵ_M, and (c) ϵ_R on-site energies. At zero-detuning for each case, the system shows a gap, indicating the absence of ground state degeneracy with opposite fermion parity. For transport simulations, we use dot-lead coupling $\Gamma = 0.0125t$ and reservoir temperature $T = 0.025t$.

case, we recover that the projected three-site parafermion operators are identical to the parafermion operators for the two-site case

$$\text{Tr}_D\left[\chi_1\right] = \chi_R, \tag{4.14a}$$

$$\text{Tr}_D\left[\chi_2\right] = \chi_L. \tag{4.14b}$$

This equivalence underlines the protection mechanism for the degeneracies in these two setups as parafermion operators.

4.4.2. ABSENCE OF SCALING

The presence of strong zero modes in a two-site system raises a key question: Can extending the chain to more sites bring about topologically protected zero modes? An example is seen in Majorana zero modes within an N-site Kitaev chain with uniform $t = \Delta$ for all hoppings and $\epsilon = 0$ for all on-site energies. To explore the emergence of such modes in a strongly interacting chain with time-reversal symmetry, we examine a three-site chain, with sites L, M and R as shown in Fig. 4.4(b), with normal hopping and superconducting pairing between adjacent sites induced by proximitized quantum dots. Given our focus on strong zero modes, we assume infinite charging energy in each site and use constrained fermion operators as detailed in Sec. 4.3.

To investigate this, we set the condition $t = \sqrt{2}\Delta$ for all hopping magnitudes and $\epsilon = 0$ for all on-site energies. We find that the many-body ground state no longer maintains the triply degenerate structure with one even- and two odd-parity eigenstates. Instead, the ground state exhibits even fermion parity, accompanied by an excitation gap to the lowest odd fermion parity eigenstates. This aspect becomes apparent in the local finite bias conductance spectroscopy of the three-site chain as illustrated in Fig. 4.6. The absence of a zero-bias peak in Fig. 4.6, which signifies degenerate ground states with opposite fermion parities, is replaced by a gap in the excitation spectrum. As either ϵ_L or ϵ_R is detuned such that the site in question is depleted, the system effectively reduces again to a two-site chain. We observe this feature in local differential conductance shown in

Fig. 4.6(a),(c) as a development of zero bias peak for $\epsilon_i \gg t$.

Hence, despite the zero-bias conductance being identical for a two-site spinless Kitaev chain and a spinful interacting two-site chain and despite the similarity for the quantum dot test in both cases, the spinful interacting three-site chain differs crucially from the spinless three-site Kitaev chain. We believe that this should be testable in current experiments.

4.5. DISCUSSION AND CONCLUSION

In this work, we have studied spinful interacting quantum dots coupled by normal hoppings and singlet-type of superconducting pairings under time-reversal symmetry. The combination of local Coulomb interactions, normal hopping and singlet-type superconducting pairing within a two-site system results in a three-fold degenerate ground state, which is quadratically protected against changes in the on-site energies. This yields experimental features similar to regular Majorana zero modes in a two-site chain, although they can be distinguished through finite bias conductance spectroscopy. Hence, our results show that the presence of a sweet spot alone does not guarantee the existence of localized Majorana bound states.

In the limit of $U \to \infty$, the entire many-body spectrum features three-fold degenerate manifolds, revealing the emergence of strong zero modes. We find two different interpretations for the existence of such strong zero modes, namely Majorana Kramers-pairs and $\mathbb{Z}_3$ parafermions. We explicitly construct corresponding Majorana Kramer-pairs operators and $\mathbb{Z}_3$ parafermion operators. In particular, from the parafermion operators, we can understand the protection of the degeneracy in the entire spectrum with respect to changes in the on-site energies and the coupling strength to the test quantum dot as discussed in Sec. 4.4.1. Projecting the parafermion operators of the two-site spinful interacting chain onto the ground state manifold yields a low-energy Hamiltonian, represented by Eq. (4.10), which resembles a two-site parafermion chain Hamiltonian. Moreover, by selecting appropriate phases for the parafermion operators, the projected operators obey $\mathbb{Z}_3$ parastatistics.

We find that these strong zero modes present in the two-site spinful interacting chain feature the same resilience as regular Majorana zero modes[20, 32, 33] against the quantum dot test. In contrast, however, extending the chain to more sites does not retain its triply-degenerate many-body spectrum. The deviation from the triply degenerate structure in the many-body spectrum for longer chains emphasizes the need for further investigation.

Previous studies [28, 36] have used Fock parafermions proposed in Ref. [37] to embed a parafermionic chain [29] in a fermionic system, resulting in fermionic Hamiltonians with parity breaking terms or three-body interaction terms that are hard to implement in experimental settings. Here, we start from a setup that can be realized experimentally [11] *and* construct parafermion operators for this system. Given that the system has two sites only, we call these modes "poor man's $\mathbb{Z}_3$ parafermions" in analogy to poor man's Majoranas [14]. However, there are several open questions: Can these strong zero modes obtain topological protection once extended to longer chains? Can we use this minimal model to demonstrate braiding or fusion for $\mathbb{Z}_3$ parafermions that could be used for universal quantum computation? Answering these questions may open promis-

ing avenues in strongly-correlated time-reversal invariant systems.

ACKNOWLEDGEMENTS

We acknowledge useful discussions with Martin Leijnse, Michele Burello, Anton Akhmerov, Dirk Schuricht, Natalia Chepiga, Bowy La Rivière, Rubén Seoane Souto, Viktor Svensson, William Samuelson.

DATA AVAILABILITY

The code used to generate the figures is available on Zenodo [38].

4.6. EXPERIMENTAL FEATURES OF SPINLESS KITAEV CHAIN VS. SPINFUL INTERACTING CHAIN

This section compares two-site spinless Kitaev chain to two-site spinful interacting chain, focusing on their charge stability diagrams and the resulting finite bias conductance spectroscopy. The many-body Hamiltonian for spinless two-site Kitaev chain is expressed as

$$H_{\text{Kitaev}} = \sum_{i=L,R} \epsilon_i c_i^\dagger c_i + t c_L^\dagger c_R + \Delta c_L^\dagger c_R^\dagger + \text{H.c.}. \tag{4.15}$$

The sweet spot condition for two-site spinless Kitaev chain requires $\epsilon_i = 0$ and $t = \Delta$, leading to a two-fold degenerate many-body spectrum. This degeneracy becomes apparent in the charge stability diagram illustrated in Fig. 4.7(a), where detuning the on-site energies causes the degeneracies to split. The impact is also reflected in the local finite bias spectroscopy, depicted in Fig. 4.7(b), where the zero-bias peak splits upon detuning both on-site energies by $\epsilon \equiv \epsilon_L = \epsilon_R$. For completeness, in Fig. 4.7(c), we show the nonlocal finite bias conductance G_{LR} as both on-site energies are varied. In comparison with the poor man's Majorana zero modes, we illustrate the charge stability diagram and finite bias conductance spectroscopy for two-site spinful interacting chain in Fig. 4.7(d-f). Although the charge stability diagrams for each system is almost identical, we observe that the finite bias conductance spectroscopy can distinguish between two cases. Specifically, in Fig. 4.7(b) and (e), we show the local finite bias conductance spectroscopy for the spinless Kitaev chain and spinful interacting chain, respectively. Detuning both on-site energies, we observe that the local conductance for the spinful interacting chain, as shown in Fig. 4.7(e), features an additional trace of enhanced conductance at finite energy that moves down with decreasing ϵ. The high charging energy of the dots prevents double occupation, allowing the ground state to only connect with triplet states by adding a single particle. This restriction on the transport process via triplet states explains the conductance asymmetry observed in Fig. 4.7(e) for the two-site spinful interacting chain with respect to bias voltage. The additional feature arises from the triplet states of the spinful interacting chain and is absent in the local conductance spectroscopy of the two-site spinless Kitaev chain. Finally, in Fig. 4.7(c) and (f), we examine the nonlocal differential conductance spectroscopy of both systems and observe that, similar to the local conductance signal, the transport processes via the triplet states in the spinful interacting chain can help distinguish between the two cases.

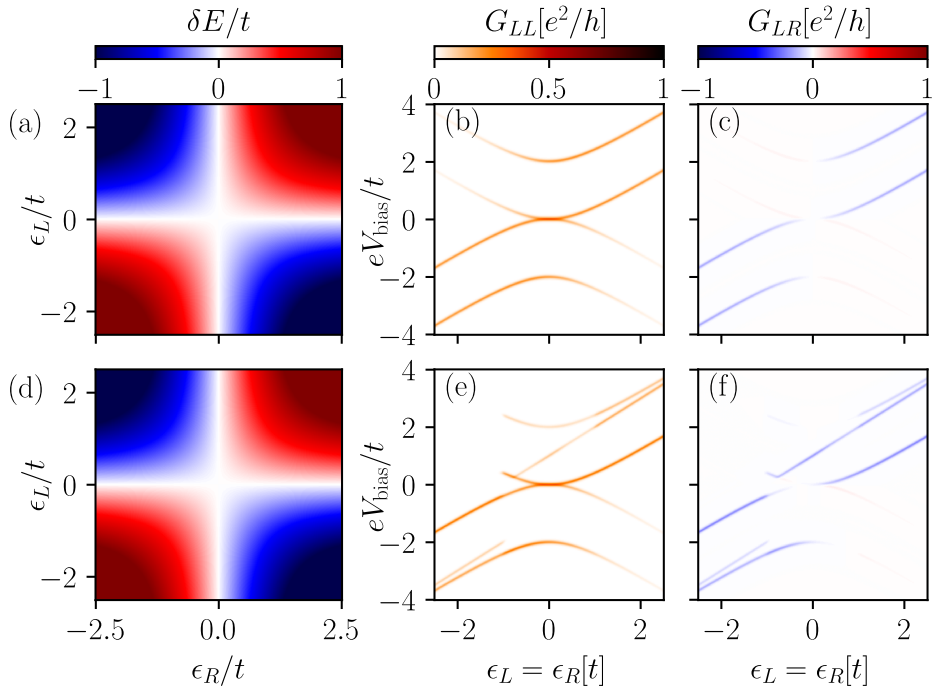

Figure 4.7: Comparison between a two-site spinless Kitaev chain and a two-site spinful interacting chain. Top panels: (a) depicts the charge stability diagram of the two-site Kitaev chain at the sweet spot. (b) illustrates the local and (c) nonlocal differential conductance of the two-site Kitaev chain at the sweet spot, plotted as a function of the voltage bias and simultaneous detuning of both on-site energies. Bottom panels: (d) depicts the charge stability diagram of the two-site spinful interacting chain in the limit $U \to \infty$. (e) shows the local and (f) nonlocal differential conductance of the two-site spinful interacting chain, plotted as a function the voltage bias and simultaneous detuning of both on-site energies. For transport simulations, we use dot-lead coupling $\Gamma = 0.0125t$ and reservoir temperature $T = 0.025t$.

For completeness, we present all of the conductance matrix elements as we detune the left on-site energy ϵ_L in Fig. 4.8. Similar to Fig. 4.7(b,e), the local conductance elements G_{LL} and G_{RR} of the spinful interacting chain, shown in Fig. 4.8(e) and (h), feature an additional enhanced conductance trace compared to the spinless Kitaev chain case, shown in Fig. 4.8(a) and (d). This difference between two cases is also observed for the nonlocal conductance G_{LR}, as shown in Fig. 4.8(b) and (f). On the other hand, the most striking difference between the spinless Kitaev chain and the spinful interacting chain is observed in the nonlocal conductance G_{RL}. While the conductance vanishes entirely for the spinless Kitaev chain, as illustrated in Fig. 4.8(c), it remains finite for the spinful interacting chain. We observe that the transport via triplet states remains visible for the spinful interacting chain.

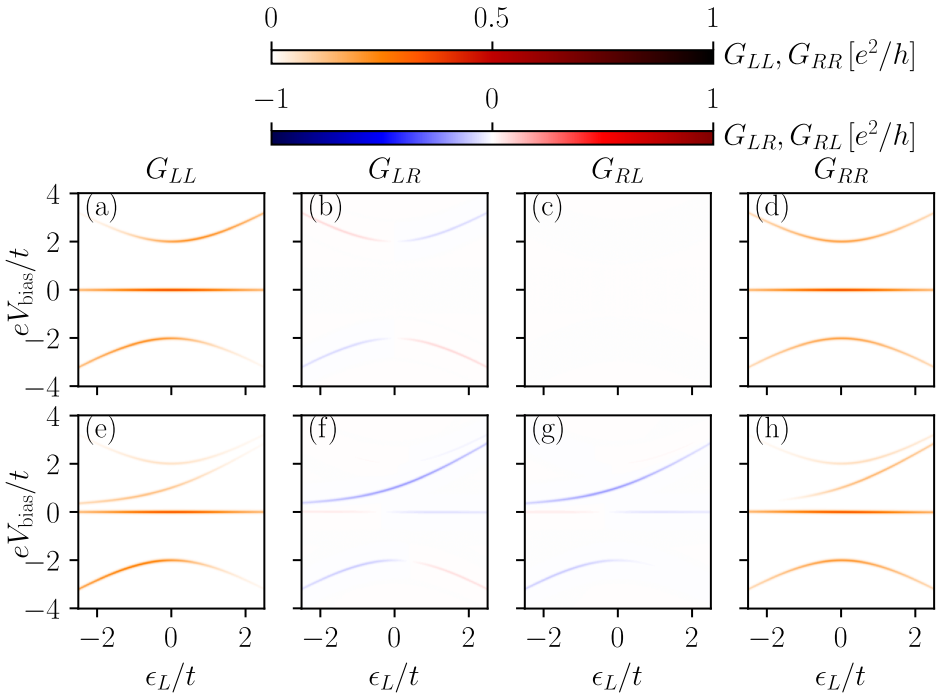

Figure 4.8: Comparison of the finite bias differential conductance between (top panels) a two-site spinless Kitaev chain and (bottom panels) a two-site spinful interacting chain while detuning the left on-site energy ϵ_L. For transport simulations, we use dot-lead coupling $\Gamma = 0.0125t$ for both leads and temperature $T = 0.025t$ for both reservoirs.

4.7. THE MODEL INCLUDING THE ANDREEV BOUND STATE

In this appendix, we show the results obtained with the full model, including the proximitized quantum dot hosts an ABS. Here, ABS in the middle region mediates CAR and ECT between left and right quantum dots. The Hamiltonian for this system is given as [15, 39]

$$H = H_D + H_S + H_T, \tag{4.16a}$$

$$H_D = \sum_{\sigma, i=L,R} \epsilon_i n_{i\sigma} + \sum_{i=L,R} U_i n_{i\uparrow} n_{i\downarrow}, \tag{4.16b}$$

$$H_S = \epsilon_M \sum_{\sigma} n_{M\sigma} + \Delta_0 (c_{M\uparrow} c_{M\downarrow} + c^\dagger_{M\downarrow} c^\dagger_{M\uparrow}), \tag{4.16c}$$

$$H_T = \sum_{\sigma} (t_0 c^\dagger_{M\sigma} c_{L\sigma} + t_0 c^\dagger_{R\sigma} c_{M\sigma}) + \text{H.c.}, \tag{4.16d}$$

where H_D is the Hamiltonian of the quantum dots, $n_{i\sigma} = c^\dagger_{i\sigma} c_{i\sigma}$ is the spin-resolved electron occupation number on dot i, U_i is the charging energy, ϵ_i is the on-site energy. H_T describes the tunnel coupling between the outer dots and ABS in the middle, which fea-

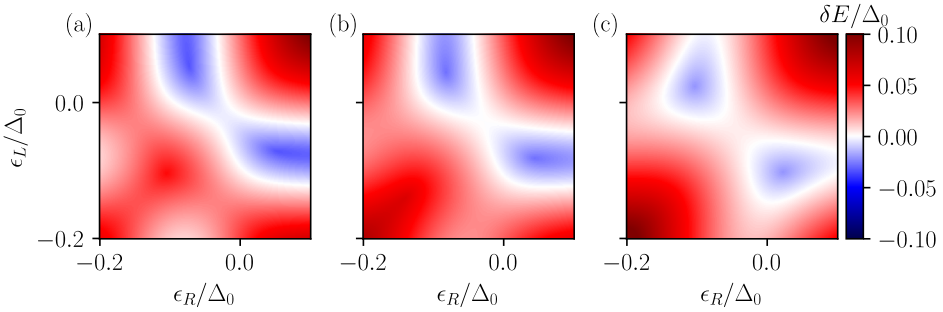

Figure 4.9: The change in connectivity of the charge stability diagram as the energy of the ABS is varied. The ground state switches its fermion-parity from (a) odd, with $\epsilon_M = \epsilon_M^* - 0.5\Delta_0$, to (c) even, with $\epsilon_M = \epsilon_M^* + 0.5\Delta_0$. This ensures that the degeneracy lines cross for a specific value of middle dot on-site energy ϵ_M^*, as shown in panel (b). Here, we have $t_0 = 0.25\Delta_0$, $U = 0.1\Delta_0$, $\epsilon_M^* \approx -0.677\Delta_0$.

4

tures a spin-conserving hopping process with strength t_0. H_S describes the middle dot that hosts an ABS in the low-energy approximation with an induced gap Δ_0.

In Fig. 4.9(a-c), we demonstrate the evolution of the charge stability diagram while changing the energy of the ABS by varying ϵ_M. Changing the ABS energy alters the effective parameters we use in the main text superconducting pairing Δ and normal hopping t. Similarly to the charge stability diagram of the effective model portrayed in Fig. 4.1, the connectivity of the charge stability diagram transitions from an odd ground state, as depicted in Fig. 4.9(a), to an even ground state, as illustrated in Fig. 4.9(c). Consequently, this ensures that a sweet spot condition can be achieved for any given ϵ_M value, as demonstrated in Fig. 4.9(b).

Furthermore, in Fig. 4.10, we depict the evolution of the charge stability diagram and the corresponding local differential conductance at the sweet spot as a function of the charging energy U on the left and right quantum dots. Despite the increased complexity of the full model, qualitative features of the charge stability diagrams and corresponding local conductances exhibit similar behaviors to the effective model results, presented in the main text Fig. 4.2. As in the effective model, increasing the Coulomb interaction U in the quantum dots results in a widening separation between the regions of double occupancy and empty dots in the charge stability diagrams. Consequently, the degeneracy lines of the sweet spot crossing become straighter with increasing U, indicating the increased protection of the ground state degeneracy against local potential changes.

4.8. Energy levels and many-body eigenstates of two-site spinful interacting chain

In this appendix, we list the eigenstate and eigenvalues of the spinful interacting chain in the limit of $U \to \infty$. At the sweet spot, i.e. $t = \sqrt{2}\Delta$ and $\epsilon_{L,R} = 0$, the spectrum exhibits three triply-degenerate manifolds. The many-body eigenstates for the ground state are already given in Eq. (4.3). Here, we show the eigenstates of the excited state manifolds.

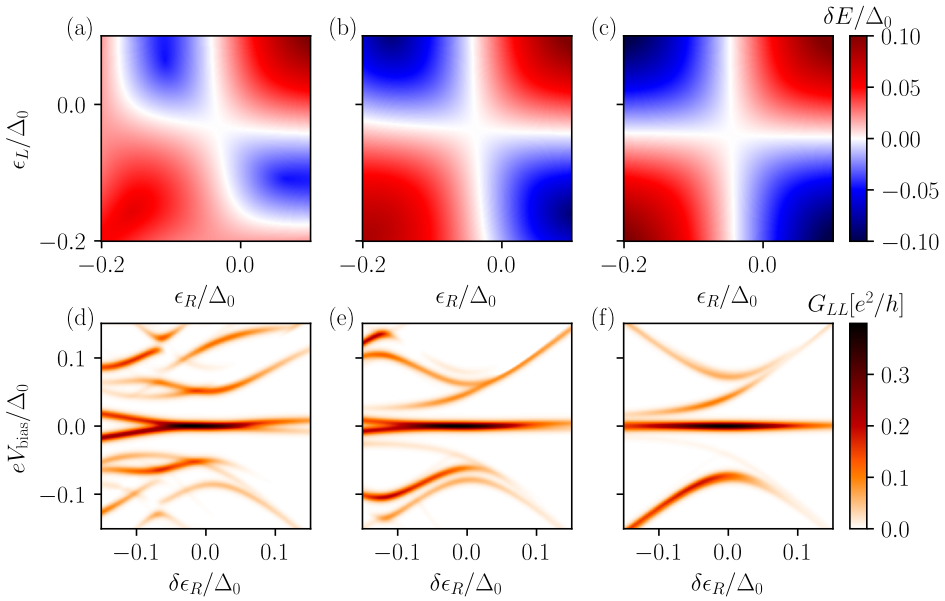

Figure 4.10: The evolution of charge stability diagram and local finite bias conductance G_{LL} at the sweet spot for various charging energies for two-site chain with an ABS in the middle dot. For (a) and (d), we set $U = 0.15\Delta_0$; for (b) and (e), $U = 0.25\Delta_0$; and for (c) and (f), $U = 0.45\Delta_0$. Here, we use $t_0 = 0.25$, $T = 0.0025\Delta_0$, and $\Gamma = 0.00125\Delta_0$.

We start with $n = 1$, namely the triplet manifold

$$|n=1,\downarrow\rangle = -|\downarrow\downarrow\rangle \tag{4.17a}$$

$$|n=1,\downarrow\rangle = +|\uparrow\uparrow\rangle \tag{4.17b}$$

$$|n=1,0\rangle = -\frac{1}{\sqrt{2}}\left(|\downarrow\uparrow\rangle + |\uparrow\downarrow\rangle\right). \tag{4.17c}$$

Finally, the eigenstates of the second excited state manifold, which consists of the bonding version of eigenstates of the ground state manifold

$$|n=2,\downarrow\rangle = -\frac{1}{\sqrt{2}}\left(|\downarrow 0\rangle + |0\downarrow\rangle\right) \tag{4.18a}$$

$$|n=2,\uparrow\rangle = -\frac{1}{\sqrt{2}}\left(|\uparrow 0\rangle + |0\uparrow\rangle\right) \tag{4.18b}$$

$$|n=2,S\rangle = -\frac{1}{\sqrt{2}}|00\rangle - \left(\frac{1}{2}|\uparrow\downarrow\rangle - \frac{1}{2}|\downarrow\uparrow\rangle\right). \tag{4.18c}$$

In the subsequent appendices, we will make use of these many-body eigenstates to construct operators.

4.9. MAJORANA KRAMERS-PAIR OPERATORS

In this appendix, we describe how we obtain the Majorana Kramers-pair operators. As described in the main text, the first excited state manifold is entirely composed of even fermion parity states. Consequently, our analysis of Majorana Kramers-pair operators excludes this manifold. We begin by constructing Majorana operators from the eigenstates of the many-body Hamiltonian. For a given spin projection, we define

$$\gamma_{1\sigma} = \sum_{n=0,2} e^{i\phi_{1,n}} |n,\sigma\rangle\langle n,S| + \text{H.c.}, \tag{4.19a}$$

$$\gamma_{2\sigma} = \sum_{n=0,2} i e^{i\phi_{2,n}} |n,\sigma\rangle\langle n,S| + \text{H.c.}, \tag{4.19b}$$

where $|n,S\rangle$ denotes the even parity state (singlet) and $|n,\sigma\rangle$ denotes the odd parity state with spin σ in the n^{th} manifold, and ϕ_n is an arbitrary phase. We find that for phase configuration

$$\phi_{1,n} = 0, \tag{4.20a}$$

$$\phi_{2,n} = \begin{cases} 0 & \text{if } n = 0, \\ \pi & \text{if } n = 2, \end{cases} \tag{4.20b}$$

$\gamma_{1\sigma}$ commutes with the number operator on the right site n_R, while $\gamma_{2\sigma}$ commutes with the number operator on the left site n_L. Consequently, we relabel $\gamma_{1\sigma}$ and $\gamma_{2\sigma}$ as $\gamma_{L\sigma}$ and $\gamma_{R\sigma}$, respectively. Eq. (4.5) of the main text, we present the decomposition of these operators in terms of constrained fermion operators.

4.10. $\mathbb{Z}_3$ PARITY AND PARAFERMION OPERATORS

The three-fold degenerate structure of the many-body eigenstates of the two site chain presented in Sec. 4.3 and also quantum dot test presented in Sec. 4.4.1 signals a conserved symmetry of the system. As discussed in the main text, this symmetry is the generalized parity $P_{\mathbb{Z}_3} = e^{i\frac{2\pi}{3}\sum_j n_{j\uparrow}+2n_{j\downarrow}}$, where $n_{j\sigma} = c^\dagger_{j\sigma} c_{j\sigma}$ is the spin-resolved number operator defined on dot j. Given the three-fold degenerate manifolds of the system under consideration, we express the parafermion operators as

$$\chi = \sum_{n=0}^{1} \sum_{p=-1}^{1} a_{n,p} \left|n,p\right\rangle\left\langle n,p+1 \bmod 3\right|, \tag{4.21}$$

where n denotes the three-fold degenerate manifolds and p represents the generalized parity eigenvalues of the states

$$P_{\mathbb{Z}_3} \left|n,p\right\rangle = \omega^p \left|n,p\right\rangle. \tag{4.22}$$

In Eq. (4.21), the coefficients $a_{n,p}$ are complex and satisfy $\prod_p a_{n,p} = 1$ for all n, ensuring that $\chi^3 = \mathbb{1}$.

Based on Eq. (4.22), we relabel the eigenstates according to their parity eigenvalues $P_{\mathbb{Z}_3}$. In the ground state manifold, given in Eq. (4.3), and the second excited state manifold, given in Eq. (4.18), we assign $\uparrow \mapsto p = 1$, $\downarrow \mapsto p = -1$ and $S \mapsto p = 0$. Furthermore, in

the first excited state manifold given in Eq. (4.17), the labeling slightly varies due to the state $|n=1,0\rangle$: we assign $\uparrow \mapsto p=1$, $\downarrow \mapsto p=-1$ and $0 \mapsto p=0$.

Our procedure to construct parafermion operators relies on the following steps:

- Obtain the entire many-body spectrum and its eigenstates by exact diagonalization of the Hamiltonian.
- Label the eigenstates based on their energy-manifold n and generalized parity eigenstate p.
- Construct the numerical matrices given in Eq. (4.21) using the eigenstates.
- Find the complex coefficients $a_{n,p}$ such that the corresponding parafermion operators commutes with a corresponding number operator.
- Express the resulting numerical matrix in terms of fermionic creation and annihilation operators.

In the next two subsections, we follow this procedure and construct the parafermion operators.

4.10.1. PARAFERMION OPERATORS FOR TWO-SITE CHAIN

For two-site chain, we have three three-fold degenerate manifolds, as shown in Fig. 4.3 in the main text. Following the method described above, we determine two sets of coefficients, $a_{n,p}$, which yield two parafermion operators. Each parafermion operator either commutes with the left or right number operator. The coefficients for the operator commuting with $\bar{n}_i$, which we name $a^i_{n,p}$, is

$$a^L_{n,p} = \begin{cases} -1 & \text{if } n=0 \text{ and } p \neq -1 \\ -1 & \text{if } n=2 \text{ and } p \neq 0 \\ 1 & \text{else} \end{cases} \tag{4.23}$$

$$a^R_{n,p} = 1. \tag{4.24}$$

We note that the relative minus sign in $a^L_{n,p}$ is crucial for the commutation with the left number operator $\bar{n}_L$. Plugging the coefficients given in Eq. (4.23) into Eq. (4.21), we obtain the parafermion operators defined in Eq. (4.9).

4.10.2. DIFFERENT GAUGE CHOICE FOR PARAFERMION OPERATORS AND PARASTATISTICS

We now use a different gauge choice for χ_L parafermion operator of the two-site spinful interacting chain, while keeping χ_R as the same defined in Eq. (4.10). This amounts to changing the coefficients $a^L_{n,p}$ defined in Eq. (4.23) as follows

$$a^L_{n,p} = \begin{cases} -\omega^{p+1} & \text{if } n=2 \text{ and } p \neq 0 \\ \omega^{p+1} & \text{else} \end{cases}. \tag{4.25}$$

We express the resulting parafermion operator χ'_L in terms of constrained fermion operators as

$$\chi'_L = \left(-\omega(1-\bar{n}_{R\uparrow}) + \left(\frac{1}{\sqrt{2}}+\omega\right)\bar{n}_{R\downarrow}\right)\bar{c}_{L\uparrow} - \left(\frac{\omega}{\sqrt{2}}\bar{c}^\dagger_{L\uparrow} + \frac{1}{\sqrt{2}}\bar{c}_{L\downarrow} + \omega^2\bar{c}^\dagger_{L\downarrow}\bar{c}_{L\uparrow}\right)\bar{c}^\dagger_{R\downarrow}\bar{c}_{R\uparrow}$$
$$+\left(\frac{1}{\sqrt{2}}+\omega^2\right)\left(\bar{n}_{R\uparrow}\bar{c}^\dagger_{L\uparrow}\bar{c}_{L\downarrow} + \bar{n}_{L\uparrow}\bar{c}^\dagger_{R\uparrow}\bar{c}_{R\downarrow}\right) + \left(\frac{\omega^2}{2+\sqrt{2}} - \frac{1}{\sqrt{2}}\right)\left(\bar{n}_{R\downarrow}\bar{c}^\dagger_{L\uparrow}\bar{c}_{L\downarrow} + \bar{n}_{L\downarrow}\bar{c}^\dagger_{R\uparrow}\bar{c}_{R\downarrow}\right)$$
$$+\left(\left(\frac{\omega}{\sqrt{2}}-1\right)\bar{n}_{R\uparrow} + (1-\bar{n}_{R\downarrow})\right)\bar{c}^\dagger_{L\downarrow} - \omega^2\left(\bar{c}^\dagger_{L\uparrow}\bar{c}_{L\downarrow} + \bar{c}^\dagger_{R\uparrow}\bar{c}_{R\downarrow}\right). \tag{4.26}$$

We now explore the low-energy physics of the three-fold degenerate ground state manifold. To that end, we project the parafermion operators, specifically χ_R given in Eq. (4.9) and χ'_L given in Eq. (4.26), to the ground state manifold. These projected operators, denoted as $\tilde{\chi}_R$ and $\tilde{\chi}'_L$, still commute with their respective number operators. Additionally, we observe that the projected parafermion operators satisfy $\mathbb{Z}_3$ parastatistics

$$\tilde{\chi}_R\tilde{\chi}'_L = \omega\tilde{\chi}'_L\tilde{\chi}_R. \tag{4.27}$$

Mapping the parafermion operators on to the ground state and establishing that they obey $\mathbb{Z}_3$-parafermionic statistics allow us to derive the low-energy effective Hamiltonian using parafermion operators

$$\tilde{H} = -\frac{(2t+\sqrt{2}\Delta)}{3}\mathbb{1} + \frac{(t-\sqrt{2}\Delta)}{3}\left(\tilde{\chi}'^\dagger_L\tilde{\chi}_R + \tilde{\chi}^\dagger_R\tilde{\chi}'_L\right) \tag{4.28}$$

We realize that the form of the low-energy Hamiltonian is similar to the low-energy Hamiltonian of a two-site $\mathbb{Z}_3$-parafermion chain. Similar to Eq. (4.10), the first term serves to ensure that at the sweet spot $t = \sqrt{2}\Delta$, the parafermions are decoupled.

4.10.3. PARAFERMION OPERATORS FOR THE QUANTUM DOT TEST

For the quantum dot test, we introduce a third quantum dot, labeled as D, which is attached to the right quantum dot of the two-site spinful interacting chain. In the absence of coupling between the right site and quantum dot D, the system exhibits three nine-fold degenerate manifolds, with each manifold labeled by its $\mathbb{Z}_3$ eigenstates. As the fermion-parity is conserved, we further order every eigenstate in each degenerate manifold according to its fermion-parity eigenvalue.

To ensure that the coupling between the test quantum dot and the two-site spinful interacting chain does not cause a splitting of the ground state degeneracy, we perform a unitary rotation on the ordered basis. This rotation is designed to ensure that the coupling, represented by $H_t = t_D\sum_\sigma \bar{c}^\dagger_{R\sigma}\bar{c}_{D\sigma} + \text{H.c.}$, maintains an identical matrix structure within each $\mathbb{Z}_3$ block. This property guarantees a three-fold degenerate structure in the entire spectrum for any value of t_D. Having established this basis, we proceed with the remaining steps of the procedure described above to determine the coefficients $a^i_{n,p}$. These coefficients ensure that the resulting parafermion operators commute with either $\bar{n}_L$ or $\bar{n}_R$. Furthermore, we confirm that the obtained parafermion operators remain identical to their two-site version once the trace is taken over the test quantum

dot. Details on the steps taken to get these coefficients and the expression of resulting parafermion operators in terms of fermionic creation and annihilation operators can be found in the code repository [38].

4.11. SPIN-ORBIT INSENSITIVITY OF THE DEGENERACIES

This appendix demonstrates how a unitary transformation on the fermion operators in spin-space transforms the Hamiltonian given in Eq. (4.1) to one with spin-orbit interaction (cf. e.g. [40]). We follow the procedure outlined in Ref. [41] and perform a unitary transformation:

$$\begin{pmatrix} c_{L\uparrow} \\ c_{L,\downarrow} \end{pmatrix} = \begin{pmatrix} \tilde{c}_{L\uparrow} \\ \tilde{c}_{L,\downarrow} \end{pmatrix} \quad \text{and} \quad \begin{pmatrix} c_{R\uparrow} \\ c_{R\downarrow} \end{pmatrix} = \begin{pmatrix} \cos\left(\frac{\theta}{2}\right) & -\sin\left(\frac{\theta}{2}\right) \\ \sin\left(\frac{\theta}{2}\right) & \cos\left(\frac{\theta}{2}\right) \end{pmatrix} \begin{pmatrix} \tilde{c}_{R\uparrow} \\ \tilde{c}_{R\downarrow} \end{pmatrix}. \tag{4.29}$$

where θ is the spin-orbit angle relative to the basis of choice. Plugging the above identities into Eq. (4.1) we find the on-site term stays invariant

$$\sum_i \epsilon_i (c^\dagger_{i\uparrow} c_{i\uparrow} + c^\dagger_{i\downarrow} c_{i\downarrow}) = \sum_i \epsilon_i (\tilde{c}^\dagger_{i\uparrow} \tilde{c}_{i\uparrow} + \tilde{c}^\dagger_{i\downarrow} \tilde{c}_{i\downarrow}), \tag{4.30}$$

for the ECT term we have

$$\begin{aligned} t\left(c^\dagger_{L\uparrow} c_{R\uparrow} + c^\dagger_{L\downarrow} c_{R\downarrow} + h.c.\right) &= t\cos\left(\frac{\theta}{2}\right)(\tilde{c}^\dagger_{L\uparrow} \tilde{c}_{R\uparrow} + \tilde{c}^\dagger_{L\downarrow} \tilde{c}_{R\downarrow} + \text{h.c.}) \\ &+ t\sin\left(\frac{\theta}{2}\right)(-\tilde{c}^\dagger_{L\uparrow} \tilde{c}_{R\downarrow} + \tilde{c}^\dagger_{L\downarrow} \tilde{c}_{R\uparrow} + \text{h.c.}), \end{aligned} \tag{4.31}$$

and finally for the CAR term

$$\begin{aligned} \Delta\left(c^\dagger_{L\uparrow} c^\dagger_{R\downarrow} - c^\dagger_{L\downarrow} c^\dagger_{R\uparrow} + \text{h.c.}\right) &= \Delta\cos\left(\frac{\theta}{2}\right)(\tilde{c}^\dagger_{L\uparrow} \tilde{c}^\dagger_{R\downarrow} - \tilde{c}^\dagger_{L\downarrow} \tilde{c}^\dagger_{R\uparrow} + \text{h.c.}) \\ &+ \Delta\sin\left(\frac{\theta}{2}\right)(\tilde{c}^\dagger_{L\uparrow} \tilde{c}^\dagger_{R\uparrow} + \tilde{c}^\dagger_{L\downarrow} \tilde{c}^\dagger_{R\downarrow} + \text{h.c.}). \end{aligned} \tag{4.32}$$

The Coulomb term keeps its form only replacing $c_{i\sigma} \to \tilde{c}_{i\sigma}$. Collecting all terms we find the two-site Hamiltonian with spin-orbit hopping between the dots (cf. [40]).

REFERENCES

[1] Barthelemy, P. and Vandersypen, L. M. K. "Quantum Dot Systems: a versatile platform for quantum simulations". In: *Annalen der Physik* 525.10-11 (2013). DOI: 10.1002/andp.201300124.

[2] Hensgens, T. et al. "Quantum simulation of a Fermi–Hubbard model using a semiconductor quantum dot array". In: *Nature* 548.7665 (2017). DOI: 10.1038/nature23022.

[3] Dehollain, J. P. et al. “Nagaoka ferromagnetism observed in a quantum dot plaquette”. In: *Nature* 579.7800 (2020). DOI: 10.1038/s41586-020-2051-0.

[4] Kiczynski, M. et al. “Engineering topological states in atom-based semiconductor quantum dots”. In: *Nature* 606.7915 (2022). DOI: 10.1038/s41586-022-04706-0.

[5] Sau, J. D. and Sarma, S. D. “Realizing a robust practical Majorana chain in a quantum-dot-superconductor linear array”. In: *Nature Communications* 3.1 (2012). DOI: 10.1038/ncomms1966.

[6] Liu, C.-X. et al. “Tunable Superconducting Coupling of Quantum Dots via Andreev Bound States in Semiconductor-Superconductor Nanowires”. In: *Phys. Rev. Lett.* 129.26 (2022). DOI: 10.1103/PhysRevLett.129.267701.

[7] Wang, G. et al. “Singlet and Triplet Cooper Pair Splitting in Hybrid Superconducting Nanowires”. In: *Nature* 612.7940 (2022). DOI: 10.1038/s41586-022-05352-2.

[8] Wang, Q. et al. “Triplet correlations in Cooper pair splitters realized in a two-dimensional electron gas”. In: *Nature Communications* 14.1 (2023). DOI: 10.1038/s41467-023-40551-z.

[9] Bordin, A. et al. “Tunable Crossed Andreev Reflection and Elastic Cotunneling in Hybrid Nanowires”. In: *Phys. Rev. X* 13.3 (2023). DOI: 10.1103/PhysRevX.13.031031.

[10] Dvir, T. et al. “Realization of a minimal Kitaev chain in coupled quantum dots”. In: *Nature* 614.7948 (2023). DOI: 10.1038/s41586-022-05585-1.

[11] ten Haaf, S. L. D. et al. “A two-site Kitaev chain in a two-dimensional electron gas”. In: *Nature* 630.8016 (2024). DOI: https://doi.org/10.1038/s41586-024-07434-9.

[12] Zatelli, F. et al. “Robust poor man’s Majorana zero modes using Yu-Shiba-Rusinov states”. In: *Nature Communications* 15.1 (2024). DOI: https://doi.org/10.1038/s41467-024-52066-2.

[13] Bordin, A. et al. *Signatures of Majorana protection in a three-site Kitaev chain*. 2024. DOI: 10.48550/arXiv.2402.19382. arXiv: 2402.19382[cond-mat].

[14] Leijnse, M. and Flensberg, K. “Parity Qubits and Poor Man’s Majorana Bound States in Double Quantum Dots”. In: *Phys. Rev. B* 86.13 (2012). DOI: 10.1103/PhysRevB.86.134528.

[15] Tsintzis, A., Souto, R. S., and Leijnse, M. “Creating and Detecting Poor Man’s Majorana Bound States in Interacting Quantum Dots”. In: *Phys. Rev. B* 106.20 (2022). DOI: 10.1103/PhysRevB.106.L201404.

[16] Torres Luna, J. D. et al. “Flux-tunable Kitaev chain in a quantum dot array”. In: *SciPost Phys. Core* 7 (2024). DOI: 10.21468/SciPostPhysCore.7.3.065.

[17] Lutchyn, R. M., Sau, J. D., and Das Sarma, S. “Majorana Fermions and a Topological Phase Transition in Semiconductor-Superconductor Heterostructures”. In: *Phys. Rev. Lett.* 105 (7 2010). DOI: 10.1103/PhysRevLett.105.077001.

[18] Oreg, Y., Refael, G., and Oppen, F. von. "Helical Liquids and Majorana Bound States in Quantum Wires". In: *Phys. Rev. Lett.* 105 (17 2010). DOI: 10.1103/PhysRevLett.105.177002.

[19] Wright, A. R. and Veldhorst, M. "Localized Many-Particle Majorana Modes with Vanishing Time-Reversal Symmetry Breaking in Double Quantum Dots". In: *Phys. Rev. Lett.* 111.9 (2013). DOI: 10.1103/PhysRevLett.111.096801.

[20] Souto, R. S. et al. "Probing Majorana Localization in Minimal Kitaev Chains through a Quantum Dot". In: *Phys. Rev. Res.* 5.4 (2023). DOI: 10.1103/PhysRevResearch.5.043182.

[21] Scherübl, Z., Pályi, A., and Csonka, S. "Transport Signatures of an Andreev Molecule in a Quantum Dot–Superconductor–Quantum Dot Setup". In: *Beilstein J. Nanotechnol.* 10.1 (2019). DOI: 10.3762/bjnano.10.36.

[22] O'Brien, T. E., Wright, A. R., and Veldhorst, M. "Many-Particle Majorana Bound States: Derivation and Signatures in Superconducting Double Quantum Dots". In: *physica status solidi (b)* 252.8 (2015). DOI: 10.1002/pssb.201552019.

[23] Batista, C. D. and Ortiz, G. "Generalized Jordan-Wigner Transformations". In: *Phys. Rev. Lett.* 86.6 (2001). DOI: 10.1103/PhysRevLett.86.1082.

[24] Alicea, J. and Fendley, P. "Topological Phases with Parafermions: Theory and Blueprints". In: *Annu. Rev. Condens. Matter Phys.* 7.1 (2016). DOI: 10.1146/annurev-conmatphys-031115-011336. arXiv: 1504.02476 [cond-mat, physics:quant-ph].

[25] Vasiloiu, L. M., Tiwari, A., and Bardarson, J. H. "Dephasing-Enhanced Majorana Zero Modes in Two-Dimensional and Three-Dimensional Higher-Order Topological Superconductors". In: *Phys. Rev. B* 106.6 (2022). DOI: 10.1103/PhysRevB.106.L060307.

[26] Chepiga, N. and Laflorencie, N. "Topological and Quantum Critical Properties of the Interacting Majorana Chain Model". In: *SciPost Physics* 14.6 (2023). DOI: 10.21468/SciPostPhys.14.6.152.

[27] Haim, A. et al. "No-go theorem for a time-reversal invariant topological phase in noninteracting systems coupled to conventional superconductors". In: *Phys. Rev. B* 94 (16 2016). DOI: 10.1103/PhysRevB.94.161110.

[28] Teixeira, R. L. R. C. and Dias da Silva, L. G. G. V. "Edge $\mathbb{Z}_3$ Parafermions in Fermionic Lattices". In: *Phys. Rev. B* 105.19 (2022). DOI: 10.1103/PhysRevB.105.195121.

[29] Fendley, P. "Parafermionic Edge Zero Modes in Zn-invariant Spin Chains". In: *J. Stat. Mech.* 2012.11 (2012). DOI: 10.1088/1742-5468/2012/11/P11020.

[30] Jermyn, A. S. et al. "Stability of Zero Modes in Parafermion Chains". In: *Phys. Rev. B* 90.16 (2014). DOI: 10.1103/PhysRevB.90.165106.

[31] Zhuang, Y. et al. "Phase diagram of the Z_3 parafermionic chain with chiral interactions". In: *Phys. Rev. B* 92 (3 2015). DOI: 10.1103/PhysRevB.92.035154.

[32] Clarke, D. J. "Experimentally Accessible Topological Quality Factor for Wires with Zero Energy Modes". In: *Phys. Rev. B* 96.20 (2017). DOI: 10.1103/PhysRevB.96.201109.

[33] Prada, E., Aguado, R., and San-Jose, P. "Measuring Majorana Non-Locality and Spin Structure with a Quantum Dot". In: *Phys. Rev. B* 96.8 (2017). DOI: 10.1103/PhysRevB.96.085418. arXiv: 1702.02525 [cond-mat].

[34] Deng, M.-T. et al. "Nonlocality of Majorana modes in hybrid nanowires". In: *Phys. Rev. B* 98 (8 2018). DOI: 10.1103/PhysRevB.98.085125.

[35] Tsintzis, A. et al. "Majorana Qubits and Non-Abelian Physics in Quantum Dot–Based Minimal Kitaev Chains". In: *PRX Quantum* 5 (1 2024). DOI: 10.1103/PRXQuantum.5.010323.

[36] Calzona, A. et al. "$\mathbb{Z}_4$ parafermions in one-dimensional fermionic lattices". In: *Phys. Rev. B* 98 (20 2018). DOI: 10.1103/PhysRevB.98.201110.

[37] Cobanera, E. and Ortiz, G. "Fock Parafermions and Self-Dual Representations of the Braid Group". In: *Phys. Rev. A* 89.1 (2014). DOI: 10.1103/PhysRevA.89.012328.

[38] Bozkurt, A. M. et al. *Interaction-induced strong zero modes in short quantum dot chains with time-reversal symmetry*. Zenodo, 2024. DOI: 10.5281/zenodo.11243862.

[39] Liu, C.-X. et al. "Enhancing the excitation gap of a quantum-dot-based Kitaev chain". en. In: *Commun Phys* 7.1 (2024). DOI: 10.1038/s42005-024-01715-5.

[40] Miles, S. et al. "Kitaev chain in an alternating quantum dot-Andreev bound state array". In: *Phys. Rev. B* 110 (2024). DOI: https://doi.org/10.1103/PhysRevB.110.024520.

[41] Choy, T.-P. et al. "Majorana fermions emerging from magnetic nanoparticles on a superconductor without spin-orbit coupling". In: *Phys. Rev. B* 84 (2011). DOI: https://doi.org/10.1103/PhysRevB.84.195442.

5

BRAIDING MAJORANAS IN A LINEAR QUANTUM DOT-SUPERCONDUCTOR ARRAY: MITIGATING THE ERRORS FROM COULOMB REPULSION AND RESIDUAL TUNNELING

Sebastian Miles, Francesco Zatelli, A. Mert Bozkurt, Michael Wimmer, and Chun-Xiao Liu

Exchanging the positions of two non-Abelian anyons transforms between many-body wavefunctions within a degenerate ground-state manifold. This behavior is fundamentally distinct from fermions, bosons and Abelian anyons. Recently, quantum dot-superconductor arrays have emerged as a promising platform for creating topological Kitaev chains that can host non-Abelian Majorana zero modes. In this work, we propose a minimal braiding setup in a linear array of quantum dots consisting of two minimal Kitaev chains coupled through an ancillary, normal quantum dot. We focus on the physical effects that are peculiar to quantum dot devices, such as interdot Coulomb repulsion and residual single electron tunneling. We find that the errors caused by either of these effects can be efficiently mitigated by optimal control of the ancillary quantum dot that mediates the exchange of the non-Abelian anyons. Moreover, we propose experimentally accessible methods to find this optimal operating regime and predict signatures of a successful Majorana braiding experiment.

Own contribution to work: Contributed to ideation and scoping, performed the analytical and numerical calculations, wrote the manuscript.

This chapter has been published as arXiv:2501.16056. The format has been adapted for this thesis.

5.1. INTRODUCTION

The exchange statistics of identical particles is a central concept in quantum mechanics. It allows for classifying elementary particles (e.g., electrons and photons) into fermions and bosons. In two-dimensional spaces, there exist more exotic particles, e.g., non-Abelian anyons [1, 2]. By exchanging the positions of two such anyons, referred to as a braid operation, the many-body wavefunction transforms into a different one in the degenerate ground-state manifold. Thus, applying the same set of braid operations in a different order results in different unitary evolutions of the system. In addition, non-Abelian anyons are regarded as the building blocks of topological quantum computation, where qubit information is encoded in a pair of anyons, and quantum gates are implemented by anyonic braiding [2, 3]. Ideally, this protocol is intrinsically fault-tolerant, because both storage and processing of the quantum information are immune to local perturbations due to the topological protection. Therefore, demonstrating non-Abelian exchange statistics is of great importance to fundamental physics as well as to topological quantum computation.

Majorana zero modes, which are Ising anyons, are the simplest example of non-Abelian anyons [3–14]. They can appear at the defects of a topological superconductor in the form of a mid-gap quasiparticle excitation [15–18]. In particular, it was proposed that topological Kitaev chains and Majorana zero modes can be engineered in a quantum-dot-superconductor array using a bottom-up approach [19]. An advantage of this proposal is the intrinsic robustness against the effect of disorder that is ubiquitous in mesoscopic systems [20–22]. Moreover, by controlling the relative strengths of normal and superconducting couplings between neighboring quantum dots [23, 24], it is even possible to create Majoranas in the short-chain limit [25], albeit lacking true topological protection in this case. Based on these proposals, significant experimental progress has been achieved recently in realizing short Kitaev chains in two- [26–28] and three-quantum-dot chains [29–31], supported by tunnel spectroscopy evidence of Majorana zero modes at finely tuned sweet spots. This opened up a new research field for Majorana physics and topological superconductivity [23, 32–55]. It also provides a new and promising platform to demonstrate the non-Abelian character of the exchange statistics [56–59], which has been elusive for decades.

In quasi-one-dimensional systems, braid operations can also be implemented by cyclic tuning of the pairwise Majorana couplings in a trijunction [60–63], or by a sequence of measurement on the fermion parity in Majorana pairs [64–66], both of which are mathematically equivalent to physically moving Majoranas in a T-junction [67]. Furthermore, it was shown that the setup of trijunction braiding can be further simplified, where the role of a vertical topological superconductor branch can be replaced by a quantum dot [68–70]. However, it is a critical open question whether a braid protocol proposed for Majorana nanowires remains valid in the quantum dot setups with strong interactions. For example, it has been recently shown that strong interdot Coulomb interaction can prevent the extraction of Majorana quality measures [34], and that Coulomb interaction within a Kitaev chain can be detrimental to the protection of Majorana zero modes or qubits [25, 47, 50].

In the current work, we generalize the minimal braid protocol to engineered Kitaev chains, focusing on the physical effects that are peculiar to quantum dot devices, e.g.,

strong interdot Coulomb repulsion and residual single-electron tunneling. Surprisingly, we find that the detrimental errors caused by both effects can be efficiently mitigated by optimal control of the ancillary quantum dot. Moreover, we propose experimentally accessible methods to find this optimal operating regime and predict signatures of a successful Majorana braiding experiment.

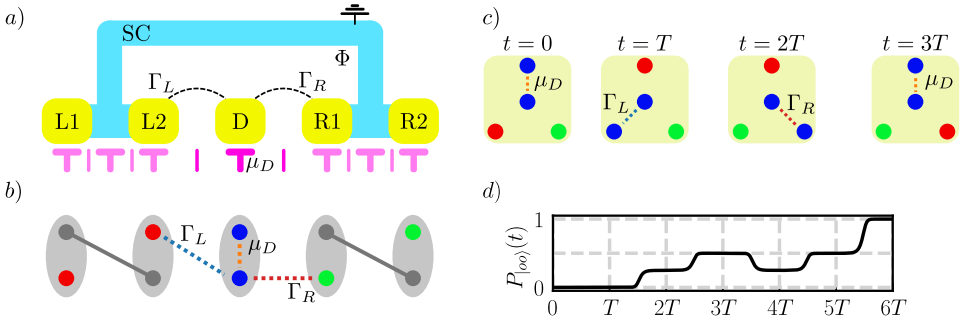

Figure 5.1: (a) Schematic of the minimal setup required for braiding in a linear array of quantum dots. Yellow squares are normal quantum dots, blue regions are superconducting leads mediating normal and Andreev tunneling. Purples lines are electrostatic gates to control the parameters. (b) Majorana representation of the Hamiltonian: The grey ovals with filled circles represent the Majorana operators $\gamma_{a,A/B}$ for dot a, lines represent effective couplings. By tuning its chemical potential, the ancillary dot D supplies two Majoranas forming a virtual trijunction together with dots $L2$ and $R1$. (c) Schematic of the single Majorana exchange protocol. A full braid is implemented by varying μ_D, Γ_L, and Γ_R in sequence twice. μ_D, Γ_L, and Γ_R can be experimentally controlled via three electrostatic gates (dark purple). (d) Occupation probability of the $|oo\rangle$ state depending on t over a full braiding operation. At times $3T$ and $6T$ the protocol implements exchange and full braid of the two Majoranas neighboring the ancillary dot respectively. The line highlights the change in parity the system undergoes during the protocol.

5.2. SETUP AND MODEL HAMILTONIAN

The minimal braiding setup in a linear array of quantum dots consists of two copies of a two-site Kitaev chain connected by an ancillary quantum dot in the middle. A schematic of this setup is shown in Fig. 5.1(a). The model Hamiltonian is

$$\begin{aligned} H &= H_L + H_R + H_D + H_{\text{tunnel}} + H_{\text{Coulomb}}, \\ H_a &= \sum_{i=1,2} \mu_{ai} n_{ai} + t_a c_{a2}^\dagger c_{a1} + \Delta_a c_{a2} c_{a1} + h.c., \\ H_D &= \mu_D n_D, \\ H_{\text{tunnel}} &= \Gamma_L c_D^\dagger c_{L2} + \Gamma_R e^{i\varphi/2} c_D^\dagger c_{R1} + h.c., \\ H_{\text{Coulomb}} &= U_L n_D n_{L2} + U_R n_D n_{R1}. \end{aligned} \tag{5.1}$$

Here H_a with $a = L/R$ are the Kitaev chain Hamiltonians, c_{ai} and $n_{ai} = c_{ai}^\dagger c_{ai}$ are the annihilation and number operators of the dot orbitals, μ_{ai} is the orbital energy, and t_a and Δ_a are the normal and Andreev tunnelings. H_D is the Hamiltonian for the ancillary quantum dot. Here we assume that both the magnetic-field-induced Zeeman energy and the level spacing are large, such that all quantum dots are in the spinless regime.

The effect of onsite Coulomb interaction can thus be safely neglected. H_{tunnel} describes single electron transfer between the end of the Kitaev chain and the ancillary quantum dot, with $\Gamma_{L/R}$ being the tunneling amplitudes. φ is the phase difference between the two superconducting leads, which can be controlled by the magnetic flux Φ through the loop. Here we choose a gauge such that $t_a, \Delta_a > 0$. H_{Coulomb} describes the interdot Coulomb interaction between the inner dots of the Kitaev chains and the ancillary dot. We neglect Coulomb interaction between two dots of the same chain due to the strong screening effect of the grounded superconductor.

5.3. MINIMAL MAJORANA BRAIDING IN A QUANTUM DOT CHAIN

5.3.1. EFFECTIVE TRIJUNCTION IN THE MAJORANA REPRESENTATION

One of the key results of Refs. [68, 69] was that a quantum dot forming a junction between two Majorana bound states behaves as an effective tri-junction at a phase difference of π. Here, we briefly show how this argument applies to the quantum dot chain.

To this end, we rewrite the Hamiltonian (5.1) in the Majorana basis. For each dot, we transform the fermionic operators into Majorana operators as

$$c_a = (\gamma_{aA} + i\gamma_{aB})/2, \quad c_a^\dagger = (\gamma_{aA} - i\gamma_{aB})/2. \tag{5.2}$$

At the sweet spot of the Kitaev chain we have

$$H_L + H_R = i\Delta_L \gamma_{L2A}\gamma_{L1B} + i\Delta_R \gamma_{R2A}\gamma_{R1B}, \tag{5.3}$$

with unpaired Majoranas $\gamma_{L1A}, \gamma_{L2B}, \gamma_{R1A}, \gamma_{R2B}$. On the other hand, the Hamiltonian for the ancillary dot reads

$$H_D = i\frac{\mu_D}{2}\gamma_{DA}\gamma_{DB}. \tag{5.4}$$

The left tunneling Hamiltonian can be rewritten as

$$H_{tunn,L} = i\frac{\Gamma_L}{2}(\gamma_{L2A}\gamma_{DB} - \gamma_{L2B}\gamma_{DA}) \approx -i\frac{\Gamma_L}{2}\gamma_{L2B}\gamma_{DA} \tag{5.5}$$

where the approximation is to project away the coupling to the high-energy Majorana when $\Delta_L \gg \Gamma_L$. For the right tunneling Hamiltonian, at $\varphi = \pi$, we have equally

$$H_{tunn,R} = i\frac{\Gamma_R}{2}(\gamma_{R1A}\gamma_{DA} + \gamma_{R1B}\gamma_{DB}) \approx i\frac{\Gamma_R}{2}\gamma_{R1A}\gamma_{DA}. \tag{5.6}$$

Thus the effective Hamiltonian is

$$H_{\text{eff}} = i\frac{\mu_D}{2}\gamma_{DA}\gamma_{DB} - i\frac{\Gamma_L}{2}\gamma_{L2B}\gamma_{DA} - i\frac{\Gamma_R}{2}\gamma_{R1A}\gamma_{DA}, \tag{5.7}$$

and thus equivalent to a Majorana trijunction [61], and schematically shown in Fig. 5.1(b). Here, the dot energy μ_D plays effectively the role of a Majorana coupling.

5.3.2. BRAIDING IN THE IDEAL CASE

We first consider an ideal scenario for Majorana braiding. Assuming no interdot Coulomb interaction ($U_L = U_R = 0$), two finely tuned Kitaev chains ($\mu_{ai} = 0$ and $t_a = \Delta_a$) can host four zero-energy Majoranas

$$\gamma_1 = \gamma_{L1A}, \gamma_2 = \gamma_{L2B}, \gamma_3 = \gamma_{R1A}, \gamma_4 = \gamma_{R2B}, \tag{5.8}$$

localized on four different quantum dots. They form the degenerate ground-state manifold. As shown above, when the phase condition $\varphi = \pi$ is satisfied, Majoranas γ_2 and γ_3 together with the ancillary quantum dot, form an effective trijunction, with the coupling strengths being Γ_L, Γ_R and μ_D, respectively. Starting from uncoupled Majoranas with $\Gamma_L = \Gamma_R = 0$ and $\mu_D > 0$, we perform a sequence of three operations, adapting the protocol of Ref. [61]:

1. turn off μ_D while turn on Γ_L, $\quad 0 < t \leq T$
2. turn off Γ_L while turn on Γ_R, $\quad T < t \leq 2T$
3. turn off Γ_R while turn on μ_D to its original value, $\quad 2T < t \leq 3T$.

The effect is to exchange the positions of γ_2 and γ_3 as shown in Fig. 5.1(c). The action of the braid protocol is described by the operator

$$B = U(3T) = \exp\left\{\frac{\pi}{4}\gamma_2\gamma_3\right\}. \tag{5.9}$$

Here we assume that all the operations are performed with perfect precision in the adiabatic limit and without any noise from the environment. The effect of the braiding operation becomes apparent when tracking the time evolution of some initial state in the ground-state manifold through the time evolution. Due to fermion parity conservation in Eq. (5.1), we can focus on the subspace with total even parity without losing generality. When $\Gamma_L = \Gamma_R = 0$ and $\mu_D > 0$, the ground states are doubly degenerate with

$$\begin{aligned} |ee\rangle &\equiv \frac{1}{2}(|00\rangle_L - |11\rangle_L) \otimes (|00\rangle_R - |11\rangle_R) \otimes |0\rangle_D, \\ |oo\rangle &\equiv \frac{1}{2}(|10\rangle_L - |01\rangle_L) \otimes (|10\rangle_R - |01\rangle_R) \otimes |0\rangle_D, \end{aligned} \tag{5.10}$$

where the basis states are defined as $|n_{L1}, n_{L2}\rangle \otimes |n_{R1}, n_{R2}\rangle \otimes |n_D\rangle$. If the system is initialized as an even-even state

$$\big|\psi(0)\big\rangle = |ee\rangle, \tag{5.11}$$

it will evolve into

$$\big|\psi(3T)\big\rangle = B\big|\psi(0)\big\rangle = (|ee\rangle - i\,|oo\rangle)/\sqrt{2}, \tag{5.12}$$

after performing the braid operation once. By repeating the same braid operation, although Majoranas γ_2 and γ_3 return to their original positions, the system becomes

$$\big|\psi(6T)\big\rangle = B^2\big|\psi(0)\big\rangle = |oo\rangle, \tag{5.13}$$

which is orthorgonal to the inital state. Equations (5.12) and (5.13) are regarded as the signatures of non-Abelian statistics of Majorana anyons. However, an experimental demonstration of Eq. (5.12) would be challenging. What can be measured are probabilities $P_{|ee\rangle}(3T) = \left|\langle ee|\psi(3T)\rangle\right|^2$ and $P_{|oo\rangle}(3T) = \left|\langle oo|\psi(3T)\rangle\right|^2$, which do not contain the crucial information of the relative phase $(-i)$ between the two basis states. Moreover, even a detection of $P_{|ee\rangle}(3T) = P_{|oo\rangle}(3T) = 1/2$, which is consistent with Eq. (5.12), cannot exclude the possibility of a completely decohered state with an uniform probability distribution. In contrast, measuring the outcome of a double braid operation in Eq. (5.13), which yields $P_{|ee\rangle}(6T) = 0$ and $P_{|oo\rangle}(6T) = 1$, will be transparent to interpret and thus more convincing. Therefore, in the rest of the work, we will focus on the double-braid protocol, which takes six steps of operations and a total time of $6T$, unless stated otherwise. A complete overview of the time-dependence of $P_{|oo\rangle}(t)$ is schematically shown in Fig. 5.1 (d).

5.3.3. BRAIDING IN THE IMPERFECT CASE

A real system will deviate from this ideal case. For example, inter-dot Coulomb repulsion may lead to additional splittings, or some residual couplings between quantum dots may remain. Additionally, the "leg" of the effective trijunction formed by the middle quantum dot is not protected. Hence, noise in μ_D can be expected to have a significant impact. Moreover, the phase-difference may deviate from the ideal value of π.

In the remainder of the paper, we will study the effects of these imperfections, and how to mitigate them. To this end, we will use the full Hamiltonian (5.1) with time-dependent parameters $\Gamma_{L/R}(t)$ and $\mu_D(t)$. We then compute $\psi(6T)$ by solving the time-dependent Schrödinger equation. For details on the simulations, we refer the reader to App. 5.10.

To characterize the faithfulness of the protocol, we calculate the infidelity

$$1 - F \equiv 1 - \left|\langle oo|\psi(6T)\rangle\right|^2 = 1 - P_{|oo\rangle}(6T), \tag{5.14}$$

where $|\psi(6T)\rangle$ is the final state after time evolution through a double braid protocol and $|oo\rangle$ is the analytical target state, respectively. Note that the infidelity can be obtained experimentally from readout measurement on $P_{|ee\rangle}(6T)$ and $P_{|oo\rangle}(6T)$.

In our simulations, unless stated otherwise, we choose the system parameters to be $t_L = \Delta_L = t_R = \Delta_R = \Delta = 5\Gamma_0, \mu_{L1} = \mu_{L2} = \mu_{R1} = \mu_{R2} = 0$ to satisfy the sweet-spot condition, and $\varphi = \pi$ for the phase condition. Here, Γ_0 is the maximal strength of single electron tunneling setting the energy and time scale of the braiding process. We make sure that the time evolution satisfies the adiabatic limit, i.e. $T \gg h/\Gamma_0$, and assume no environmental noise or quasiparticle poisoning.

5.4. INTERDOT COULOMB REPULSION

We now consider the effect of interdot Coulomb repulsion on Majorana braiding. Coulomb interaction is ubiquitous for quantum-dot-based devices, with the strength varying in a wide range of tens of μeV to as large as one meV [71, 72]. As described by H_C in Eq. (5.1), it is present among electrons on dots $L2, D$, and $R1$ due to the long-range nature of Coulomb interaction, while the interaction between dots within a Kitaev chain is

strongly suppressed by the screening effect of the grounded superconductor.

We begin by assuming that Coulomb interaction is present, but that the three time-varying parameters have equal variation magnitude and can be tuned perfectly to zero,

$$0 \le \Gamma_L(t), \Gamma_R(t), \mu_D(t) \le \Gamma_0, \tag{5.15}$$

before relaxing this assumption in later discussions. As shown in Fig. 5.2 (a) ($U_L = U_R$) and (d) ($U_L \neq U_R$), interdot Coulomb energy has a very detrimental effect on braiding, with the infidelity quickly approaching one as $U \gtrsim \Gamma_0$.

To understand the physics behind this behavior, we focus on the first step of the braiding operation ($0 \le t \le T$). Since the right Kitaev chain is decoupled in this process, we can work on a simpler Hamiltonian of $H_{LD} = H_{K,L} + H_{\text{tunn},L} + H_{C,L} + H_D$. Within the subspace of total even parity, it can be written as

$$H_{LD}^{(\text{even})} = \begin{pmatrix} 0 & -\frac{\Gamma_L}{2} & 0 & \frac{\Gamma_L}{2} \\ -\frac{\Gamma_L}{2} & \mu_D + \frac{U_L}{2} & \frac{\Gamma_L}{2} & -\frac{U_L}{2} \\ 0 & \frac{\Gamma_L}{2} & 2\Delta_L & \frac{\Gamma_L}{2} \\ \frac{\Gamma_L}{2} & -\frac{U_L}{2} & \frac{\Gamma_L}{2} & 2\Delta_L + \mu_D + \frac{U_L}{2} \end{pmatrix} \tag{5.16}$$

where the basis is $|e_L, 0_D\rangle, |o_L, 1_D\rangle, |e'_L, 0_D\rangle, |o'_L, 1_D\rangle$ and primes indicate excited states. Here we shift all states by Δ_L for simplicity of discussion, and the prime denotes the excited states in the Kitaev chain. In the tunneling regime of $\Gamma_L \ll \Delta_L$, the low-energy effective Hamiltonian is

$$H_{LD,\text{eff}}^{(\text{even})} = \begin{pmatrix} 0 & -\frac{\Gamma_L}{2}(a+b) \\ -\frac{\Gamma_L}{2}(a+b) & \mu_D + \frac{U_L}{2} + \Delta_L - \lambda \end{pmatrix} \tag{5.17}$$

for arbitrary strength of U_L, and valid up to second order in Γ_L. Here $\lambda = \sqrt{\Delta_L^2 + (U_L/2)^2}$, and a, b are positive numbers with $a^2 = 1 - b^2 = \frac{1}{2} + \frac{\Delta_L}{2\lambda}$. The low-energy basis states are $|\psi_1\rangle = |e_L, 0_D\rangle$, and $|\psi_2\rangle = a|o_L, 1_D\rangle + b|o'_L, 1_D\rangle$. There are two major effects from the interdot Coulomb repulsion. First, the instantaneous ground state of the total system now includes a component of the excited states $|o'_L\rangle$ in $|\psi_2\rangle$, compared to the idealized $|\psi_2\rangle = |o_L, 1_D\rangle$ for the case with $U_L = 0$. Second, as shown in Eq. (5.17), the effective energy of the ancillary quantum dot is shifted: $\mu_D \to \mu_D + \frac{U_L}{2} + \Delta_L - \lambda$, which enhances the energy of $|\psi_2\rangle$. In the strong Coulomb regime, $U \gg 1$, restricting $0 \le \mu_D \le \Gamma_0$ does not effectively take the dot down to resonance. As a result, the state $|\psi(t)\rangle$ would stay close to $|ee\rangle$ without moving any Majoranas, which explains the high infidelity in Fig. 5.2(a). Based on Eq. (5.17), one way to mitigate this detrimental error is to shift the dot energy as below

$$\begin{aligned} &\mu_{D,\min} \le \mu_D(t) \le \mu_{D,\min} + \Gamma_0, \\ &\mu_{D,\min} = \mu_D^* = \sum_{a=L,R} \left(-\frac{U_a}{2} - \Delta_a + \sqrt{\Delta_a^2 + (U_a/2)^2} \right). \end{aligned} \tag{5.18}$$

Note that the dot energy shift now includes contributions from both Kitaev chains because the Coulomb potential is additive and we assume no coupling between the two

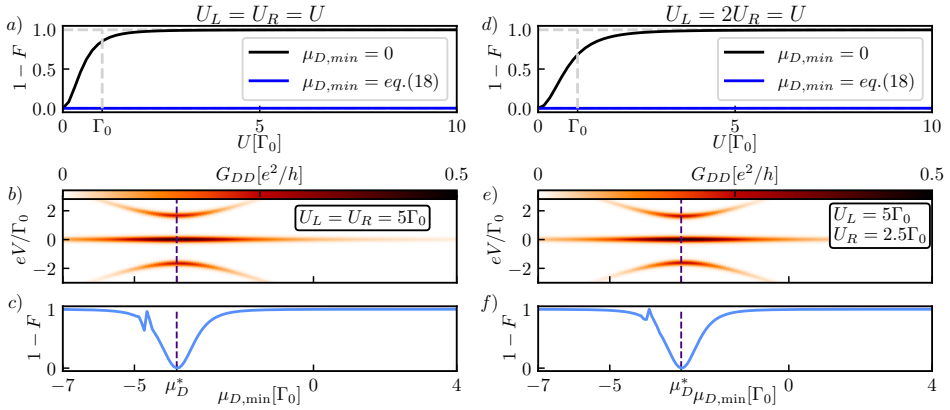

Figure 5.2: Effects of interdot Coulomb interaction between ancillary dot and adjacent Kitaev chain dots. (a) and (d) show the infidelity in dependence of symmetric and asymmetric Coulomb energy respectively. (b) and (e) show local conductance spectroscopy through the ancillary dot. Due to the interaction, the excitation minimum shifts in chemical potential to a lower value corresponding to Eq. (5.18). Retuning $\mu_{D,\min}$ to this value corrects the adverse effect of the Coulomb interaction. This is supported by (c) and (f) showing the infidelity in dependence of $\mu_{D,\min}$. In line with the excitation minimum, the infidelity reduces to zero when $\mu_{D,\min} = \mu^*_D$. The discontinuity at $\mu^*_D - \Gamma_0$ is due to our choice of $\mu_{D,\max} - \mu_{D,\min} = \Gamma_0$ where the occupied state on the dot becomes resonant with the states in the Kitaev chains. Measuring the traces as those presented in c) and f) experimentally can be considered a signature of Majorana braiding.

Kitaev chains directly. Applying Eq. (5.18) to the braid protocol and without changing any other conditions, we obtain the blue curve in Fig. 5.2 (a) for $U_L = U_R$ and (d) for $U_L \neq U_R$. It shows an excellent correction of the errors with $1 - F \lesssim 10^{-3}$, validating our analysis and proposal. Notably, since our treatment of Coulomb repulsion is nonperturbative in the interaction strength, the error mitigation applies to strong Coulomb case ($U > \Delta$) as well, provided the system stays in the tunneling regime $\Gamma_L \ll \Delta_L$. Figure 5.2 (a) and (d) are the first main findings of this work, which positively indicates that it is possible to mitigate the detrimental effect of interdot Coulomb repulsion in Majorana braiding.

To find the value of μ^*_D in an actual device, we propose two experiments. The first one is a local tunnel spectroscopy on the ancillary dot in the (eV, μ_D) plane, as shown in Fig. 5.2(b) and (e). Here a normal lead is coupled to the ancillary dot to obtain G_{DD}. Although the Majorana-induced zero-bias peak stays robust, the subgap peak from the first excited state varies with μ_D, and reaches a minimum along the bias-voltage axis at $\mu_D = \mu^*_D$ [see Fig. 5.2(b) and (e)], thus providing a way to find μ^*_D for the braid protocol. Note that this does not add to the device complexity, when transport measurements are needed to fine-tune the Kitaev chains into their sweet spots. Our second proposal is to measure the infidelity as a function of $\mu_{D,\min}$. As shown in Fig. 5.2(c) and (f), the infidelity drops to nearly zero at the optimal value $\mu_{D,\min} = \mu^*_D$, and then increases to one when $\mu_{D,\min}$ is tuned away by $\sim \Gamma_0$. The numerical simulations are consistent with our analytical results in Eq. (5.17) and (5.18). Moreover, a measurement of Figs. 5.2(c) or 5.2(f) can be regarded as a signature of successful Majorana braiding. We note that

the apparent discontinuity visible in Fig. 5.2 (c) and (f) are a consequence of our initial choice $\max(\mu_D(t)) = \Gamma_0$. When $\mu_{D,\min} \to \mu_D^* - \Gamma_0$ the occupied state of the ancillary dot is on resonance with the states on the Kitaev chain, interfering with the braiding. As this happens only for $\mu_{D,\min} < \mu_D^*$ and can be controlled by changing $\max(\mu_D(t)) > \Gamma_0$, this feature can be disregarded for the effectiveness of the central result at μ_D^*.

5.5. RESIDUAL SINGLE ELECTRON TUNNELING

In semiconducting quantum dot devices, the single electron tunneling strength is controlled by electrostatic gates. Although the strength can be varied deterministically, it is challenging to turn off the coupling completely, causing unwanted errors in qubit control [73, 74]. To study the effect of residual coupling we assume

$$\Gamma_{\min} \leq \Gamma_L(t), \Gamma_R(t) \leq \Gamma_0, \tag{5.19}$$

$$\mu_{D,\min} \leq \quad \mu_D(t) \quad \leq \mu_{D,\min} + \Delta\mu_D, \tag{5.20}$$

where $\Gamma_{\min} > 0$ is the residual tunneling strength, and $\Delta\mu_D = \mu_{D,\max} - \mu_{D,\min}$ is the variation magnitude of the ancillary dot energy. For the analytic considerations we set the interdot Coulomb energy at first to zero, unless stated otherwise (we relax this assumption in Fig. 5.4 (c) and (d)). Figure 5.3(a) shows the numerically calculated infidelities in the $(\Delta\mu_D, \Gamma_{\min})$ plane. The infidelity increases with the residual tunneling strength $\Gamma_{\min}$ while it decreases with the dot variation magnitude $\Delta\mu_D$, see Figs. 5.3(b) and 5.3(c). As it will be shown below, the infidelity is a joint consequence of two distinct error mechanisms, which we call leakage and geometrical leakage error.

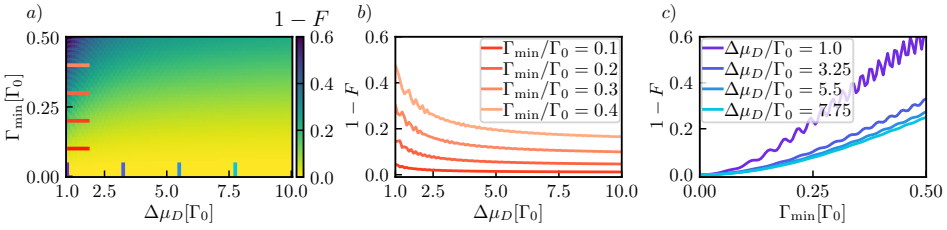

Figure 5.3: (a) Infidelity, $1-F$, in the $(\Delta\mu_D, \Gamma_{\min})$-plane. (b) Infidelity as a function of $\Delta\mu_D$ for different cuts of $\Gamma_{\min}$ in (a). (c) Infidelity as a function of $\Gamma_{\min}$ for different cuts of $\Delta\mu_D$ in (a).

The leakage error, on one hand, can be understood from a heuristic perturbation theory analysis: At the initial time, treating the residual tunnelings $\Gamma_{a,\min}$ as a perturbative effect, the state $|ee\rangle$ can leak into the excited states

$$|oe\rangle = \frac{1}{2}(|10\rangle_L - |01\rangle_L) \otimes (|00\rangle_R - |11\rangle_R) \otimes |1\rangle_D \tag{5.21}$$

$$|eo\rangle = \frac{1}{2}(|00\rangle_L - |11\rangle_L) \otimes (|10\rangle_R - |01\rangle_R) \otimes |1\rangle_D \tag{5.22}$$

with a characteristic amplitude of $\Gamma_{\min}/\Delta\mu_D$. Thus the leakage probability is

$$P_{\text{leak}} \propto \left(\frac{\Gamma_{\min}}{\Delta\mu_D}\right)^2 \tag{5.23}$$

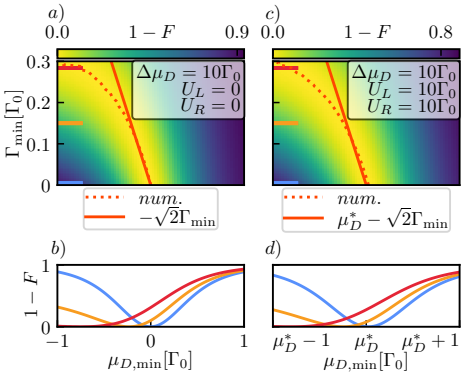

Figure 5.4: (a) and (c) Infidelity, $1-F$, in the $(\mu_{D,\min},\Gamma_{\min})$ plane for $U_a = 0$ and $U_a = 10\Gamma_0$ respectively. For both, we choose $\Delta\mu_D = 10\Gamma_0$. The dotted lines show the numerical minimum of the infidelity, solid lines correspond to the expectation of eqns. (5.30) and (5.18). (b) and (d) Infidelity as a function of $\mu_{D,\min}$ for different cuts in $\Gamma_{\min}$ through (a) and (c) showing that for increasingly negative values of $\mu_{D,\min}$ the infidelity vanishes regardless of residual tunnel coupling.

5

to leading order in residual tunneling strength. The same argument can be made for any specific state expected at an intermediate step of the time evolution. In light of Eq. (5.14), for a perfect double braid besides residual couplings of the Majoranas, it is therefore to expect that $1-F = 1-P_{|oo\rangle} \propto P_{\text{leak}} \times const.$, with a constant proportional to T. Indeed, as shown in Fig. 5.3(c), the numerically calculated infidelity decays with a larger variation magnitude, consistent with Eq. (5.23). As indicated by Eq. (5.23), leakage errors can be mitigated by an increase of the chemical potential variation on the ancillary dot, i.e.

$$\Delta\mu_D \gg \Gamma_0. \tag{5.24}$$

We note that an increase of $\Delta\mu_D$ comes at the expense of diabatic errors due to faster changes of $\mu_D(t)$. We do however expect the existence of a window in protocol time where the leakage error is strongly suppressed before the diabatic error becomes prominent.

The geometrical error, on the other hand, can be understood by calculating the unitary evolution operator, Eq. (5.9), in the presence of residual couplings between the Majoranas. This amounts to calculating the non-Abelian Berry phase of the cyclic variation of the Hamiltonian, which has a geometrical origin. Performing a similar calculation to that of Ref. [61] generalized to asymmetric couplings (see App. 5.12), the unitary operator in Eq. (5.9) becomes

$$U_{\text{res}}(3T) = \exp\left\{\left(\frac{\pi}{4} - \epsilon\right)\gamma_2\gamma_3\right\}, \tag{5.25}$$

where ϵ denotes the deviation from perfect braiding. The corresponding infidelity is

$$1 - F = \sin^2(2\epsilon) \approx 4\epsilon^2 \tag{5.26}$$

when $\epsilon \ll 1$. Calculating ϵ in Eq. (5.25) explicitly, we find for $\Gamma_{L,\max} = \Gamma_{R,\max} = \mu_{D,\max} = \Gamma_0$

$$\epsilon \approx \frac{1}{\sqrt{2}\Gamma_0}\left(\Gamma_{L,\min} + \Gamma_{R,\min} + \mu_{D,\min}\right) \tag{5.27}$$

in leading order of the residual coupling of the Majoranas (see App. 5.12). We note that Eq. (5.27) coincides with the result in Ref. [61] when $\Gamma_{L,\min} = \Gamma_{R,\min} = \mu_{D,\min}$. Assuming no residual coupling of the Majoranas on the ancillary dot, i.e. $\mu_{D,\min} \equiv 0$ in the absence of Coulomb repulsion, we find through Eq. (5.26) that the infidelity scales quadratically with the residual tunnel coupling,

$$1 - F \propto \left(\frac{\Gamma_{\min}}{\Gamma_0}\right)^2. \tag{5.28}$$

We can find an analytical correction to the geometrical error when excluding the presence of leakage errors, that is in the limit $\Gamma_{L,\max} = \Gamma_{R,\max} = \Gamma_0 \ll \mu_{D,\max}$. We then obtain

$$\epsilon \approx \frac{1}{\sqrt{2}\Gamma_0}\left(\Gamma_{L,\min} + \Gamma_{R,\min} + \sqrt{2}\mu_{D,\min}\right), \tag{5.29}$$

to leading order in residual tunnelings and in $\Gamma_0/\mu_{D,\max}$. The key observation now is that, despite $\Gamma_{a,\min}/\Gamma_{a,\max} > 0$ for any applied voltage to the tunnel gates, one can change the sign of $\mu_{D,\min}$ with respect to $\mu_{D,\max}$ by tuning the dot to chemical potentials below the resonance of dot with the Kitaev chains. In particular, the geometrical error vanishes up to the leading (quadratic) order in $\Gamma_{\min}/\Gamma_0$ when one chooses

$$\mu_{D,\min} = -\sqrt{2}\Gamma_{\min} < 0. \tag{5.30}$$

Figure 5.4 (a) shows the infidelity of the double braid protocol in the $(\mu_{D.\min}, \Gamma_{\min})$ plane for $\Delta\mu_D = 10\Gamma_0$. The dotted red line indicates the numerical minimum of the infidelity, $1 - F$, for fixed $\Gamma_{\min}$ in dependence of $\mu_{D,\min}$ while the solid red line shows Eq.(5.30). Indeed, the optimized $\mu_{D,\min}$ take negative values as predicted. Moreover, the analytic result in Eq. (5.30) matches well with the numerical result in the weak residual tunneling regime . We furthermore find that our analysis remains well valid even in the presence of Coulomb repulsion when additionally applying the correction suggested in Sec. 5.4, i.e. $\mu_D \to \mu_D + \mu_D^*$ as visible in Fig. 5.4 (c) and (d).

5.6. SUPERCONDUCTING PHASE DIFFERENCE

Satisfying the phase condition $\varphi = \pi$ is crucial for a successful braiding experiment. The phase is controlled via the magnetic flux through the superconducting loop, i.e. $\varphi = 2\pi e\Phi/h + const.$, see Fig. 5.1(a). Here we propose two experiments to find where $\varphi = \pi$, which are similar in spirit to those discussed in Sec. 5.4. The first one is a transport measurement. Figure 5.5(a) shows the tunnel spectroscopy of G_{DD} in the (eV, φ) plane. The signature of $\varphi = \pi$ is a zero-bias conductance peak, which is induced by the Majorana zero modes formed at the trijunction and splits linearly when the phase

is away from π. Our second proposed experiment is to measure the double-braid infidelity $1-F$ as a function of φ, as shown in Fig. 5.5(b). Interestingly, in addition to $\varphi=\pi$, there are multiple other values of φ also giving zeros of $1-F$. These zeros are due to Rabi oscillations induced by the undesired ground-state degeneracy splitting, similar to the observations in Ref. [68, 75]. However, a fundamental distinction between them is that the outcome of non-Abelian braiding does not depend on the precise control of the protocol time as the dynamical effects such as Rabi oscillations. Therefore, after averaging over different lengths of protocol time T, while keeping the adiabaticity constraint still satisfied, only the infidelity at $\varphi=\pi$ remains zero [see Fig. 5.7(c)], indicating the robustness of a geometrical braid operation.

In addition, we notice that both the conductance spectroscopy and the infidelities in Fig. 5.5 are 2π-periodic in φ, or equivalently $h/2e$-periodic in magnetic flux Φ. However, the tunneling Γ_R in Eq. (5.1) at $\varphi=3\pi$ acquires a minus sign relative to $\varphi=\pi$, giving

$$B_{3\pi}=B_{\pi}^{-1}, \tag{5.31}$$

where B_π is defined in Eq. (5.9). This is a consequence of the 4π Josephson effect due to fractionalized Majorana zero modes. In particular, single braids B_π and $B_{3\pi}$ give $(|ee\rangle \pm i|oo\rangle)/\sqrt{2}$, respectively. However, it is challenging to distinguish the different phases $\pm i$ here from a measurement of $P_{|ee\rangle}$ and $P_{|oo\rangle}$ only. Thus we propose the following three-step experiment.

1. apply B_π on $|ee\rangle$ twice to obtain $|oo\rangle$
2. apply $B_{3\pi}$ on $|ee\rangle$ twice to obtain $|oo\rangle$
3. apply B_π on $|ee\rangle$ once followed by another $B_{3\pi}$ to obtain $|ee\rangle$

Here in each step the system should be initialized at $|ee\rangle$. A successful implementation of the above experiments would manifest 4π-periodicity in a fractional Josephson junction. We demonstrate our proposal in Fig. 5.5 for the system described in Sec. 5.3.3 for $\Delta\mu_D=1$ and without Coulomb repulsion. We see that, if the phase stays constant over the double braid, the Majoranas exchange as expected and the quantum state of the system changes. If, however, the phase is adiabatically changed for the second exchange the state returns to the initial state due to the 4π-Josephson effect.

5.7. DIABATIC AND DEPHASING EFFECTS

We now consider the impact of diabatic and dephasing errors when executing the braid protocol. Figure 5.7 shows the infidelity as a function of the protocol step time T at time $t=6T$ for different values of $\Delta\mu_D$ and U. The infidelity decreases exponentially with the protocol time, consistent with the behavior of diabatic error in holonomy or anyonic braiding [76]. Interestingly, by comparing the blue and orange lines in Fig. 5.7(a), we find that increasing $\Delta\mu_D$ decreases the diabatic error. Physically, although the change of $\mu_D(t)$ becomes faster, the energy gap of the effective trijunction increases, which compensates the former effect as long no Landau-Zener transitions into the excited manifold are induced. This means that we can suppress the leakage in Eq. (5.23) without increasing the diabatic error. Additionally, with finite Coulomb, the infidelity saturates

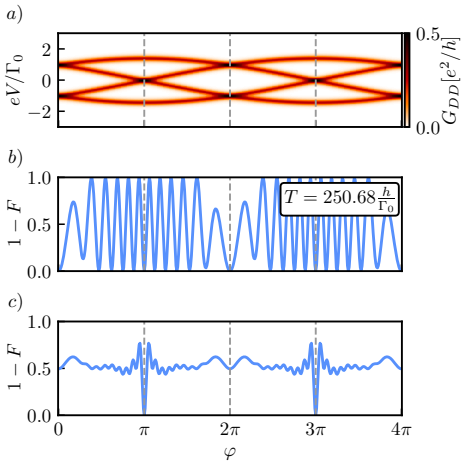

Figure 5.5: (a) Tunnel spectroscopy, G_{DD}, over the ancillary dot in the (V,φ) plane. Only at odd integer multiples of π the conductance indicates the necessary degeneracy at $V = 0$. Additionally, the linear splitting of that degeneracy with phase indicates the lack of protection of the protocol against phase noise. (b) Infidelity, $1-F$, as a function of φ for a single T. The oscillations indicate Rabi oscillations between the states in the ground-state manifold. (c) Infidelity of the double braid protocol averaged over multiple T. Since the outcome of the non-Abelian exchange does not depend on any specific choice of T, the perfect fidelities at odd interger multiples of π persist while the Rabi oscillations present in (b) average away.

5

at $1-F \approx 10^{-3}$ for $T \to \infty$, which is due to the higher-order corrections to μ_D^* from Γ_a that are not included in leading-order result shown in Eq. (5.18).

In semiconducting quantum dot devices, charge noise is the primary source of noise, which can be caused by charge impurities or gate voltage fluctuations [77–84]. Since it is $1/f$ noise, which is dominated by the low-frequency component, we can model the noises using the quasi-static disorder approximation [85, 86]. In particular, we focus on the effect of noise in the ancillary dot that does not exhibit any protection, whereas noisw in the short Kitaev chains could be mitigated by extending the chain length. Moreover, the dephasing effects of noise within the Kitaev chains were studied in previous work in the context of imperfect Majorana polarizations [59].

We assume the noise on the ancillary dot chemical potential can be modeled as

$$\mu_D(t) \to \mu_D(t) + \delta\mu_D,, \tag{5.32}$$

where δ_{μ_D} is a constant shift drawn from a normal distribution with width σ_{μ_D} and centered around zero for each execution of the protocol(see App. 5.10). To quantify the effect of the noise we perform an ensemble average over 100 different noise values. As shown in Fig. 5.7(b), the main effect of μ_D-noise is to deteriorate the fidelity around $\mu_{D,\min} = \mu_D^*$ ($= 0$ when $U_a = 0$). Since the width of the $1-F$ dip is of the order of Γ_0, a necessary condition for observing this signature is a characteristic disorder strength $\mu_{D,\text{dis}} \ll \Gamma_0$ to indicate the success of the braid.

In contrast to chemical potential noise, the modeling of the tunneling noise, Γ, differs due to its distinct dependence on the electrostatic potential. In particular, the quantum

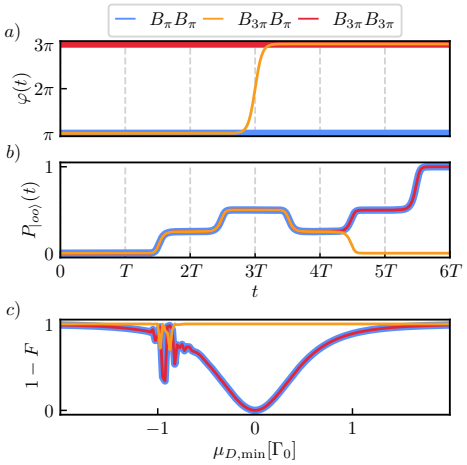

Figure 5.6: Time and dot chemical potential traces demonstrating the 4π-Josephson effect of the system for the system specified in Sec. 5.3.3 up to phase. We choose $\Delta\mu_D = 1$ and neglect interdot Coulomb repulsion. (a) Superconducting phase φ in dependence of time. To implement $B_\pi B_\pi$ and $B_{3\pi} B_{3\pi}$ we keep the phase fixed while for $B_{3\pi} B_\pi$ we adiabatically change the phase from $\pi \to 3\pi$ around $t = 3T$. (b) occupation probability of the $|oo\rangle$ state. Only for $B_{3\pi} B_\pi$, the initialized $|ee\rangle$ state returns into itself over the time evolution. (c) Infidelity, $1 - F$, depdending on $\mu_{D,\min}$. Only the $B_\pi B_\pi$ and $B_{3\pi} B_{3\pi}$ show the transition from $|ee\rangle \to |oo\rangle$ predicted for non-Abelian exchange. For $B_{3\pi} B_\pi$ the initial state returns to itself identically.

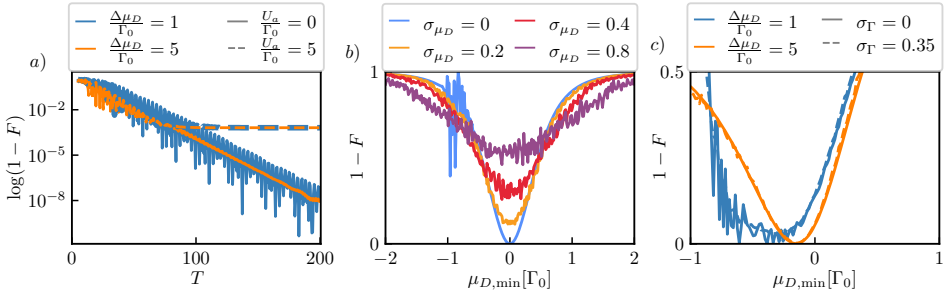

Figure 5.7: (a) Logarithm of the infidelity, $\log 1 - F$, in dependence of protocol step time T showing oscillations due to leakage into excited states. The reduced fidelity at finite U is due to perturbative corrections to $\mu_D^* \Gamma_a$ not taken into account in Eq. (5.18). (b) Ensemble averaged infidelity of the double braid in dependence of $\mu_{D,\min}$ for different variances of quasistatic noise on μ_D averaged over 100 realizations . (c) Ensemble averaged infidelity in dependence of $\mu_{D,\min}$ at fixed residual tunneling $\Gamma_{\min} = 0$ over 100 noise values. Solid and dashed lines correspond to noise with a variance of 0 and $0.35\Gamma_0$ on the tunnel coupling Γ_a respectively.

dot energy has a linear dependence because it is capacitively coupled to the electrostatic potential nearby, while the electron transfer rate has an exponential dependence since it is determined by the transmission probability through a tunnel barrier. Therefore, noise in Γ_a is proportional to Γ_a itself, i.e.

$$\Gamma_a(t) \to (1 + \alpha)\Gamma_a(t), \tag{5.33}$$

Here α is a dimensionless coefficient which we draw from a normal distribution of width σ_Γ and mean zero. We use this simple model of noise on tunneling, as it avoids taking into account details of the tunnel barrier, but we expect it is sufficient to demonstrate the principal effect of noise in the tunnel barriers when ensuring $\sigma_\Gamma \ll 1$. As shown in Fig. 5.7(c), although the $1-F$ dip is again lifted by the noise, its effect is much weaker to the effect of chemical potential noise as shown in Fig. 5.7(b). This feature can be well understood using Eq. (5.33). When the tunneling Γ_a is in the *off*-state, the fluctuation is strongly suppressed due to the small residual tunneling amplitude. On the other hand, the deviation of Γ_a strength in the *on*-state predominantly changes the energy gap of the effective trijunction, without greatly affecting the outcome braiding operation. Thus, tunneling noise is less detrimental than noise on μ_D in this braid setup.

5.8. DISCUSSION

It has been shown that braiding of non-Abelian anyons can take place only in two-dimensional space, which seemingly contradicts with the conclusions of the current work. However, we emphasize that although the quantum dot-superconductor array has a linear structure at the first glance, it is quasi-one-dimensional in nature. In particular, since $\varphi = \pi$ is a crucial requirement for a successful Majorana braid, a superconducting loop [see Fig. 5.1(a)] has to be formed along with a controllable magnetic flux Φ, which extends the setup geometry to the second dimension. Moreover, the proposed braiding setup allows a "minimal braiding" experiment in the sense that the outcome is *not* topologically protected, but depends on fine-tuning of parameters, in particular μ_D and ϕ.

We here discuss several relevant time scales of the braiding protocol. First, the protocol time should be sufficiently long in order to satisfy the adiabatic condition. Although there is no common standard, here we choose a threshold diabatic error to be 10^{-2} for concrete discussions. According to Fig. 5.7(a), the protocol time needs to be larger than $\sim 300\hbar/\Gamma_0$, which correponds to a time scale of ~ 20 ns for a typical single electron tunneling strength of $\Gamma_0 \sim 10$ μeV.

Second, as discussed in Sec. 5.7, the dephasing effect from noises in μ_D and those within Kitaev chains should be sufficiently mitigated. In particular, in order to experimentally observe Fig. 5.2(c) or (f), which is regarded as one of the signatures of a successful Majorana braiding, the amplitude of the μ_D noise must be smaller than the characteristic single electron tunneling strength, i.e.,

$$\mu_{D,\mathrm{dis}} \ll \Gamma_0, \tag{5.34}$$

as shown in Fig. 5.7(b). Additionally, the energy splitting between the instantaneous ground states should also be much weaker than Γ_0 to avoid decoherence. This can be achieved by either enhancing the excitation gap of a Kitaev chain [27, 28, 33] or extending the chain length [30, 31, 40, 43]. By contrast, based on our simulations and arguments, the noises in $\Gamma_{L/R}$ are less detrimental.

The third time scale is the quasiparticle poisoning effect. For example, a random incoming electron from outside the system can flip the total fermion parity, causing leakage errors that cannot be corrected. The poisoning time is reported to be around ~ 1 ms in devices of InSb/InAs semiconductor nanowires proximitized by Al superconductors [87], which has a very similar nanostructure to the Kitaev chain devices [26–31].

As long as the adiabatic condition is satisfied (e.g., ~ 20 ns for diabatic error $< 10^{-2}$) within that time scale, the quasiparticle poisoning effect should not be a major concern in this braid experiment.

5.9. SUMMARY

In summary, we have investigated a minimal Majorana braiding protocol in quantum-dot-based Kitaev chains, focusing on the physical phenomena that are peculiar to quantum dot devices, e.g., interdot Coulomb repulsion and residual single electron tunneling. We find that the detrimental errors from them can be efficiently mitigated by optimal control of the ancillary quantum dot via $\mu_{D,\min}$ and $\mu_{D,\max}$. Furthermore, we propose a series of experiments to find this optimal operating regime and predict signatures of a successful braiding. We also analyze the diabatic errors and dephasing effect from various types of noises.

ACKNOWLEDGEMENTS

We acknowledge useful discussions with Alberto Bordin, Bart Roovers, Florian Bennebroek Evertsz, and Juan Daniel Torres Luna about current experiments and their analysis. This work was supported by a subsidy for top consortia for knowledge and innovation (TKI toeslag), by the Dutch Organization for Scientific Research (NWO) and Microsoft Station Q. S.M. acknowledges funding of NWO through OCENW.GROOT.2019.004.

DATA AVAILABILITY

The code and the data that was generated for the plots are available in the repository of Ref. [88]

5.10. DETAILS OF THE NUMERICAL CALCULATION

In this appendix we expand on the numerical tools used to generate the figures of this work. The associated repository containing all codes used for this work can be found in Ref. [88].

To simulate braiding in the setup described in Sec. 5.2, we use the QUTIP [89] Python package to calculate the time evolution. The perturbation theory results of Sec. 5.4 and App. 5.11 are generated with Pymablock [90].

To model the time dependent coupling between the different Majoranas (cf. Fig. 5.1 c)) we have to specify the profiles for μ_D, Γ_L, and Γ_R. We model each parameter by the time dependent function

$$p(t, p_{min}, p_{max}, \sigma_p) = (p_{max} - p_{min}) \left(\frac{1}{2} + \tanh\left(\frac{\tilde{t} - \frac{T}{2}}{t_{ramp}} \right) - \tanh\left(\frac{\tilde{t} - \frac{3T}{2}}{t_{ramp}} \right) + \tanh\left(\frac{\tilde{t} - \frac{7T}{2}}{t_{ramp}} \right) \right), \tag{5.35}$$

$$\tilde{t} = (t + t_0) \mod 3T. \tag{5.36}$$

Choosing $t_0 = T$ generates the profile of μ_D, $t_0 = 0$ Γ_L, and $t_0 = 2T$ yields Γ_R. The

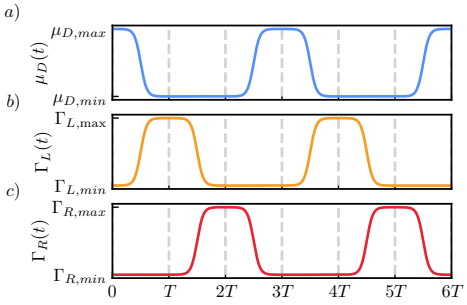

Figure 5.8: Parameters of the double braid protocol depending on time. (a) chemical potential $\mu_D(t)$ of the ancillary dot. (c) and (d), tunnel coupling of the ancillary dot to the left and right Kitaev chain respecitvely.

resulting profiles can be found in Fig. 5.8.

The parameters for the time evolution need to obey the adiabaticity constraint $T \sim h/\Gamma_0$ of the protocol. To find parameters for the time evolution that both, obey the adiabaticity constraint and deliver unit fidelities, we construct the full Hamiltonian as given in Eq. (5.1). We fix all the parameters at their optimal point ($t_L = \Delta_L = t_R = \Delta_R = 5\Gamma_0$, and $\varphi = \pi$). We choose the stepsize of the time discretization to $\Delta t = 0.2h/\Gamma$ corresponding to $\sim 0.1ns$ given typical coupling strengths of $\Gamma_0 \sim 10\mu eV$. We then optimize numerically for T and the ramping time t_{ramp} by demanding that $P_{|oo\rangle}(3T) = 1/2$ and $P_{|oo\rangle}(6T)$=1. This results in $(T_{opt}, t_{ramp,opt}) = (200.54, 21.21)\hbar/\Gamma_0$ which is our default parameter choice unless specified otherwise. When changing T away from the optimized value, we have to adjust the ramping time accordingly. This we do by letting $t_{ramp} \to T\, t_{ramp,opt}/T_{opt}$ such as to coincide with the optimal choice when $T = T_{opt}$.

5.11. EFFECTIVE ODD PARITY HAMILTONIAN AND EXCITATION MINIMUM

5.11.1. EFFECTIVE HAMILTONIAN IN ODD AND EVEN PARITY SECTORS

As discussed in the main text, it suffices to only consider a single PMM coupled to the ancillary dot to understand the physics relevant for the Coulomb repulsion. The Hamiltonian of this system reads

$$
\begin{aligned}
H_{LD} &= H_{K,L} + H_{\text{tunn},L} + H_{C,L} + H_D, \\
H_{K,L} &= \mu_{L1} n_{L1} + \mu_{L2} n_{L2} + t c^\dagger_{L2} c_{L1} + \Delta c_{L2} c_{L1} + h.c., \\
H_D &= \mu_D n_D, \\
H_{\text{tunn,L}} &= \Gamma_L \left(c^\dagger_D c_{L2} + c^\dagger_{L2} c_D \right), \\
H_{C,L} &= U_L n_D n_{L2}.
\end{aligned}
\tag{5.37}
$$

Since the system preserves the total fermionic parity we can separate the Hilbert space into the even and odd total parity subspaces. In the even parity sector consist-

ing of the basis $|e_L,0_D\rangle,|o_L,1_D\rangle,|e'_L,0_D\rangle,|o'_L,1_D\rangle$ we find Eq. (5.16), i.e.

$$H_{LD}^{(even)} = \begin{pmatrix} 0 & \frac{\Gamma_L}{2} & 0 & \frac{\Gamma_L}{2} \\ \frac{\Gamma_L}{2} & \mu_D + \frac{U_L}{2} & \frac{\Gamma_L}{2} & -\frac{U_L}{2} \\ 0 & \frac{\Gamma_L}{2} & 2\Delta_L & \frac{\Gamma_L}{2} \\ \frac{\Gamma_L}{2} & -\frac{U_L}{2} & \frac{\Gamma_L}{2} & 2\Delta_L + \mu_D + \frac{U_L}{2} \end{pmatrix}. \tag{5.38}$$

In the odd parity basis, consisting of $|e_L,1_D\rangle,|o_L,0_D\rangle,|e'_L,1_D\rangle,|o'_L,0_D\rangle$, we find through an analogous calculation the Hamiltonian

$$H_{LD}^{(odd)} = \begin{pmatrix} \frac{U_L}{2} + \mu_D & \frac{\Gamma_L}{2} & \frac{U_L}{2} & -\frac{\Gamma_L}{2} \\ \frac{\Gamma_L}{2} & 0 & -\frac{\Gamma_L}{2} & 0 \\ \frac{U_L}{2} & -\frac{\Gamma_L}{2} & \frac{U_L}{2} + 2\Delta_L + \mu_D & \frac{\Gamma_L}{2} \\ -\frac{\Gamma_L}{2} & 0 & \frac{\Gamma_L}{2} & 2\Delta_L \end{pmatrix}, \tag{5.39}$$

Due to the aforementioned parity conservation the spectrum will be strongly degenerate between parity sectors.

5.11.2. EXCITATION GAP MINIMUM

The excitation gap can be found through Eq. (5.17) from the main text. We find the eigenvalues of the effective Hamiltonian to be

$$\epsilon_\pm = \frac{1}{2}\left(\mu_D + \frac{U_L}{2} + \Delta_L - \lambda\right) \pm \sqrt{\frac{\Gamma_L^2}{4}(a+b)^2 + \frac{1}{4}\left(\mu_D + \frac{U_L}{2} + \Delta_L - \lambda\right)^2}. \tag{5.40}$$

The excitation gap is the difference of these two eigenvalues given as

$$\Delta\epsilon = \sqrt{\Gamma_L^2(a+b)^2 + \left(\mu_D + \frac{U_L}{2} + \Delta_L - \lambda\right)^2} \tag{5.41}$$

Inspecting Eq. (5.41), it becomes apparent that the excitation gap becomes minimal exactly for the predicted value of $\mu_D = \mu_D^*$ as given in Eq. (5.18). We find the value of the excitation gap to be

$$\Delta\epsilon_{\min} = \Gamma_L \frac{\sqrt{\sqrt{4\Delta_L^2 + U_L^2} + 2\Delta_L} + \sqrt{\sqrt{4\Delta_L^2 + U_L^2} - 2\Delta_L}}{\sqrt{2}(4\Delta_L^2 + U_L^2)^{1/4}} \tag{5.42}$$

for a single Kitaev chain attached to the ancillary dot.

5.12. CALCULATION OF THE NON-ABELIAN BERRY PHASE

In this section, we show the details for calculating the non-Abelian Berry's phase in the presence of residual couplings. The calculation is similar in spirit to Ref. [61], but we generalize it to asymmetric couplings. The Hamiltonian is given by

$$H = \sum_{k=1}^{3} \Delta_k i\gamma_0\gamma_k, \tag{5.43}$$

which involves four Majoranas in total. We thus define fermionic operators as below

$$f_1 = (\gamma_1 + i\gamma_2)/2, \quad f_2 = (\gamma_0 + i\gamma_3)/2, \tag{5.44}$$

so that we can further define the four-dimensional Fock space as

$$\begin{aligned} &|00\rangle, \\ &|10\rangle = f_1^\dagger |00\rangle, \\ &|01\rangle = f_2^\dagger |00\rangle, \\ &|11\rangle = f_1^\dagger f_2^\dagger |00\rangle. \end{aligned} \tag{5.45}$$

As such, the Hamiltonian can now be written as

$$H = \begin{pmatrix} |00\rangle \\ |11\rangle \\ |10\rangle \\ |01\rangle \end{pmatrix}^T \begin{pmatrix} -\Delta_3 & i\Delta_1 + \Delta_2 & 0 & 0 \\ -i\Delta_1 + \Delta_2 & \Delta_3 & 0 & 0 \\ 0 & 0 & -\Delta_3 & -i\Delta_1 + \Delta_2 \\ 0 & 0 & i\Delta_1 + \Delta_2 & \Delta_3 \end{pmatrix} \begin{pmatrix} \langle 00| \\ \langle 11| \\ \langle 10| \\ \langle 01| \end{pmatrix}. \tag{5.46}$$

We note that here the even- and odd-parity subspaces are block diagonalized due to fermion parity conservation. The dimension of each subspace is two.

We first focus on the even-parity subspace, where the ground-state energy is

$$E_{e,gs} = -\varepsilon = -\sqrt{\Delta_1^2 + \Delta_2^2 + \Delta_3^2}, \tag{5.47}$$

and the wavefunction is

$$|e\rangle = \sqrt{\frac{\varepsilon - \Delta_3}{2\varepsilon}} \begin{pmatrix} -i\frac{\Delta_3+\varepsilon}{\Delta_1+i\Delta_2} \\ 1 \end{pmatrix}. \tag{5.48}$$

Using sympy, we obtain that

$$A_{e,1} = \langle e|\frac{d}{d\Delta_1}|e\rangle = \frac{\Delta_2}{\Delta_1^2+\Delta_2^2}\frac{i(\varepsilon+\Delta_3)}{2\varepsilon}, \quad A_{e,2} = \langle e|\frac{d}{d\Delta_2}|e\rangle = \frac{-\Delta_1}{\Delta_1^2+\Delta_2^2}\frac{i(\varepsilon+\Delta_3)}{2\varepsilon}, A_{e,3} = 0.$$

Using the same calculation method, we find that

$$E_{o,gs} = -\varepsilon = -\sqrt{\Delta_1^2 + \Delta_2^2 + \Delta_3^2}, \tag{5.49}$$

5

and the wavefunction is

$$|o\rangle = \sqrt{\frac{\varepsilon - \Delta_3}{2\varepsilon}} \begin{pmatrix} i\frac{\Delta_3+\varepsilon}{\Delta_1 - i\Delta_2} \\ 1 \end{pmatrix}. \tag{5.50}$$

Note that the odd-parity wavefunction is different from the even one by $i \to -i$. Thus the signs of the Berry connections are simply reversed, i.e.

$$\vec{A}_o = -\vec{A}_e. \tag{5.51}$$

Due to parity conservation, the matrix elements between even- and odd-parity states are zero.

The unitary evolution for the Majorana braiding is defined as

$$U = \exp\left(-\oint_c \sum_k A_k d\Delta_k\right). \tag{5.52}$$

5

Here the Berry connection shown in Eq. (5.49) is singular when $\Delta_1 = \Delta_2 = 0$ because of the presence of a term $\Delta_1/(\Delta_1^2 + \Delta_2^2)$. To avoid the singular points, we assume that the couplings have some residual amplitudes even when they are "switched off", i.e., $\eta_k \le \Delta_k \le \Gamma$. Here we first assume that the maximal strengths of all Δ_k's are assumed to be the same and equal to Γ to simplify the calculation. In particular, in the three-step braid operation, we assume six contours in the parameter path as below

$$\begin{aligned}
&C1: (\eta_1, \eta_2, \Gamma) \to (\Gamma, \eta_2, \Gamma),\\
&C2: (\Gamma, \eta_2, \Gamma) \to (\Gamma, \eta_2, \eta_3),\\
&C3: (\Gamma, \eta_2, \eta_3) \to (\Gamma, \Gamma, \eta_3),\\
&C4: (\Gamma, \Gamma, \eta_3) \to (\eta_1, \Gamma, \eta_3),\\
&C5: (\eta_1, \Gamma, \eta_3) \to (\eta_1, \Gamma, \Gamma),\\
&C6: (\eta_1, \Gamma, \Gamma) \to (\eta_1, \eta_2, \Gamma),
\end{aligned}$$

where each bracket denotes $(\Delta_1, \Delta_2, \Delta_3)$. We note that only 4 out of the 6 contours contribute to the Berry's phase. We name them as $C1 \to I_1, C4 \to I_2, C3 \to I_3, C6 \to I_4$.

$$-\oint_c \sum_k A_k d\Delta_k = \left(\frac{-i}{2}\right) I = \left(\frac{-i}{2}\right)(I_1 + I_2 + I_3 + I_4), \tag{5.53}$$

In particular

$$I_1 = \int_{\eta_1}^{\Gamma} A_1(\Delta_1, \eta_2, \Gamma) d\Delta_1 = \int_{\eta_1}^{\Gamma} d\Delta_1 \frac{\eta_2}{\Delta_1^2 + \eta_2^2}\left(1 + \frac{\Gamma}{\sqrt{\Delta_1^2 + \Gamma^2}}\right). \tag{5.54}$$

Here the first integral is

$$I_{11} = \int_{\eta_1}^{\Gamma} d\Delta_1 \frac{\eta_2}{\Delta_1^2 + \eta_2^2} = \int_a^b dx \frac{1}{x^2+1} = \arctan(b) - \arctan(a), \tag{5.55}$$

where $b = \Gamma/\eta_2$ and $a = \eta_1/\eta_2$. The second part is

$$I_{12} = \int_{\eta_1}^{\Gamma} d\Delta_1 \frac{\eta_2}{\Delta_1^2 + \eta_2^2} \frac{\Gamma}{\sqrt{\Delta_1^2 + \Gamma^2}} = \int_a^b dx \frac{1}{x^2+1} \frac{b}{\sqrt{x^2+b^2}}. \tag{5.56}$$

We obtain the result for the indefinite integral as given below

$$\int dx \frac{1}{x^2+1} \frac{b}{\sqrt{x^2+b^2}} = \frac{b}{\sqrt{1-b^2}} \tanh^{-1}\left(\frac{\sqrt{1-b^2}}{\sqrt{b^2+x^2}} x\right) \approx \arctan\left(\frac{bx}{\sqrt{b^2+x^2}}\right), \tag{5.57}$$

where we assume $b \gg 1$ and use the relation of $\tanh^{-1}(ib) = i\arctan(b)$. Therefore we have

$$I_{12} = \arctan\left(\frac{b}{\sqrt{2}}\right) - \arctan(a) \approx \frac{\pi}{2} - \frac{\sqrt{2}}{b} - \arctan(a), \tag{5.58}$$

where we consider $a \sim O(1) \ll b$ and use the identity of $\arctan(x) = \pi/2 - \arctan(1/x)$. We thus have

$$I_1 = \arctan\big(\Gamma/\eta_2\big) - 2\arctan\big(\eta_1/\eta_2\big) + \frac{\pi}{2} - \frac{\sqrt{2}\eta_2}{\Gamma}. \tag{5.59}$$

Next, the second integral is

$$\begin{aligned} I_2 &= \int_{\Gamma}^{\eta_1} A_1(\Delta_1, \Gamma, \eta_3) d\Delta_1 = -\int_{\eta_1}^{\Gamma} d\Delta_1 \frac{\Gamma}{\Delta_1^2 + \Gamma^2} \left(1 + \frac{\eta_3}{\sqrt{\Delta_1^2 + \Gamma^2}}\right) \\ &= -\left[\arctan(1) - \arctan\big(\eta_1/\Gamma\big) + \frac{\eta_3}{\sqrt{2}\Gamma}\right]. \end{aligned} \tag{5.60}$$

And the third integral is

$$\begin{aligned} I_3 &= \int_{\eta_2}^{\Gamma} A_2(\Gamma, \Delta_2, \eta_3) d\Delta_2 \\ &= \int_{\eta_2}^{\Gamma} d\Delta_2 \frac{-\Gamma}{\Delta_2^2 + \Gamma^2} \left(1 + \frac{\eta_3}{\sqrt{\Delta_2^2 + \Gamma^2}}\right) \qquad = -\left[\arctan(1) - \arctan\big(\eta_2/\Gamma\big) + \frac{\eta_3}{\sqrt{2}\Gamma}\right]. \end{aligned} \tag{5.61}$$

Lastly, the fourth integral is

$$\begin{aligned} I_4 &= \int_{\Gamma}^{\eta_2} A_2(\eta_1, \Delta_2, \Gamma) d\Delta_2 \\ &= \arctan\big(\Gamma/\eta_1\big) + \frac{\pi}{2} - \frac{\sqrt{2}\eta_1}{\Gamma} - 2\arctan\big(\eta_2/\eta_1\big). \end{aligned} \tag{5.62}$$

5

After summing them up, we obtain

$$I = \sum_{i=1}^{4} I_i = \frac{\pi}{2} - \frac{\sqrt{2}}{\Gamma}(\eta_1 + \eta_2 + \eta_3), \tag{5.63}$$

giving the unitary evolution matrix as below

$$U = \exp\left(\frac{-i}{2} I\sigma_z\right) = \exp\left(-i\left(\frac{\pi}{4} - \epsilon\right)\sigma_z\right), \tag{5.64}$$

where

$$\epsilon = \frac{(\eta_1 + \eta_2 + \eta_3)}{\sqrt{2}\Gamma} + O(\eta_i/\Gamma)^2. \tag{5.65}$$

In the notation for braiding Majoranas in Kitaev chains, it becomes

$$U_{\text{braid}} = \exp\left(-i\left(\frac{\pi}{2} - \epsilon\right)\gamma_2\gamma_3\right), \tag{5.66}$$

where

$$\epsilon = \frac{(\Gamma_{L,min} + \Gamma_{R,min} + \mu_{D,min})}{\sqrt{2}\Gamma} + O(\eta_i/\Gamma)^2 \tag{5.67}$$

A similar calculation can be performed assuming $\Delta_{1,max} = \Delta_{2,max} \ll \Delta_{3,max}$. It yields

$$\epsilon = \frac{1}{\sqrt{2}}\left(\frac{\Gamma_{L,\min}}{\Gamma} + \frac{\Gamma_{R,\min}}{\Gamma} + \frac{\sqrt{2}\mu_{D,\min}}{\Gamma}\right) + O(\eta_i/\Gamma, \Gamma/\mu_{D,max}). \tag{5.68}$$

REFERENCES

[1] Moore, G. and Read, N. "Nonabelions in the fractional quantum hall effect". In: *Nuclear Physics B* 360.2 (1991). DOI: 10.1016/0550-3213(91)90407-O.

[2] Nayak, C. et al. "Non-Abelian anyons and topological quantum computation". In: *Rev. Mod. Phys.* 80 (3 2008). DOI: 10.1103/RevModPhys.80.1083.

[3] Sarma, S. D., Freedman, M., and Nayak, C. "Majorana zero modes and topological quantum computation". en. In: *npj Quantum Inf* 1.1 (2015). DOI: 10.1038/npjqi.2015.1.

[4] Alicea, J. "New directions in the pursuit of Majorana fermions in solid state systems". en. In: *Rep. Prog. Phys.* 75.7 (2012). DOI: 10.1088/0034-4885/75/7/076501.

[5] Leijnse, M. and Flensberg, K. "Introduction to topological superconductivity and Majorana fermions". en. In: *Semicond. Sci. Technol.* 27.12 (2012). DOI: 10.1088/0268-1242/27/12/124003.

[6] Beenakker, C. "Search for Majorana Fermions in Superconductors". In: *Annu. Rev. Condens. Matter Phys.* 4.1 (2013). DOI: 10.1146/annurev-conmatphys-030212-184337.

[7] Stanescu, T. D. and Tewari, S. “Majorana fermions in semiconductor nanowires: fundamentals, modeling, and experiment”. In: *J. Phys.: Condens. Matter* 25.23 (2013).

[8] Jiang, J.-H. and Wu, S. “Non-Abelian topological superconductors from topological semimetals and related systems under the superconducting proximity effect”. en. In: *J. Phys.: Condens. Matter* 25.5 (2013). DOI: 10.1088/0953-8984/25/5/055701.

[9] Elliott, S. R. and Franz, M. “Colloquium: Majorana fermions in nuclear, particle, and solid-state physics”. In: *Rev. Mod. Phys.* 87 (1 2015). DOI: 10.1103/RevModPhys.87.137.

[10] Sato, M. and Ando, Y. “Topological superconductors: a review”. en. In: *Rep. Prog. Phys.* 80.7 (2017). DOI: 10.1088/1361-6633/aa6ac7.

[11] Aguado, R. “Majorana quasiparticles in condensed matter”. In: *La Rivista del Nuovo Cimento* 40.11 (2017). DOI: 10.1393/ncr/i2017-10141-9.

[12] Lutchyn, R. M. et al. “Majorana zero modes in superconductor–semiconductor heterostructures”. In: *Nat. Rev. Mater.* 3.5 (2018). DOI: 10.1038/s41578-018-0003-1.

[13] Zhang, H. et al. “Next steps of quantum transport in Majorana nanowire devices”. In: *Nat. Commun.* 10.1 (2019). DOI: 10.1038/s41467-019-13133-1.

[14] Prada, E. et al. “From Andreev to Majorana bound states in hybrid superconductor–semiconductor nanowires”. In: *Nature Reviews Physics* 2.10 (2020). DOI: 10.1038/s42254-020-0228-y.

[15] Fu, L. and Kane, C. L. “Superconducting Proximity Effect and Majorana Fermions at the Surface of a Topological Insulator”. In: *Phys. Rev. Lett.* 100 (9 2008). DOI: 10.1103/PhysRevLett.100.096407.

[16] Sau, J. D. et al. “Generic New Platform for Topological Quantum Computation Using Semiconductor Heterostructures”. In: *Phys. Rev. Lett.* 104 (4 2010). DOI: 10.1103/PhysRevLett.104.040502.

[17] Lutchyn, R. M., Sau, J. D., and Das Sarma, S. “Majorana Fermions and a Topological Phase Transition in Semiconductor-Superconductor Heterostructures”. In: *Phys. Rev. Lett.* 105 (7 2010). DOI: 10.1103/PhysRevLett.105.077001.

[18] Oreg, Y., Refael, G., and Oppen, F. von. “Helical Liquids and Majorana Bound States in Quantum Wires”. In: *Phys. Rev. Lett.* 105 (17 2010). DOI: 10.1103/PhysRevLett.105.177002.

[19] Sau, J. D. and Sarma, S. D. “Realizing a robust practical Majorana chain in a quantum-dot-superconductor linear array”. In: *Nat. Commun.* 3.1 (2012). DOI: 10.1038/ncomms1966.

[20] Liu, J. et al. “Zero-Bias Peaks in the Tunneling Conductance of Spin-Orbit-Coupled Superconducting Wires with and without Majorana End-States”. In: *Phys. Rev. Lett.* 109 (26 2012). DOI: 10.1103/PhysRevLett.109.267002.

[21] Mi, S. et al. “X-shaped and Y-shaped Andreev resonance profiles in a superconducting quantum dot”. en. In: *J. Exp. Theor. Phys.* 119.6 (2014). DOI: 10.1134/S1063776114120176.

[22] Pan, H. and Das Sarma, S. “Physical mechanisms for zero-bias conductance peaks in Majorana nanowires”. In: *Phys. Rev. Res.* 2 (1 2020). DOI: 10.1103/PhysRevResearch.2.013377.

[23] Liu, C.-X. et al. “Tunable Superconducting Coupling of Quantum Dots via Andreev Bound States in Semiconductor-Superconductor Nanowires”. In: *Phys. Rev. Lett.* 129 (26 2022). DOI: 10.1103/PhysRevLett.129.267701.

[24] Bordin, A. et al. “Tunable Crossed Andreev Reflection and Elastic Cotunneling in Hybrid Nanowires”. In: *Phys. Rev. X* 13 (3 2023). DOI: 10.1103/PhysRevX.13.031031.

[25] Leijnse, M. and Flensberg, K. “Parity qubits and poor man’s Majorana bound states in double quantum dots”. In: *Phys. Rev. B* 86 (13 2012). DOI: 10.1103/PhysRevB.86.134528.

[26] Dvir, T. et al. “Realization of a minimal Kitaev chain in coupled quantum dots”. In: *Nature* 614.7948 (2023). DOI: 10.1038/s41586-022-05585-1.

[27] ten Haaf, S. L. D. et al. “A two-site Kitaev chain in a two-dimensional electron gas”. In: *Nature* 630.8016 (2024). DOI: 10.1038/s41586-024-07434-9.

[28] Zatelli, F. et al. “Robust poor man’s Majorana zero modes using Yu-Shiba-Rusinov states”. In: *Nat. Commun.* 15.1 (2024). DOI: 10.1038/s41467-024-52066-2.

[29] Bordin, A. et al. “Crossed Andreev Reflection and Elastic Cotunneling in Three Quantum Dots Coupled by Superconductors”. In: *Phys. Rev. Lett.* 132 (5 2024). DOI: 10.1103/PhysRevLett.132.056602.

[30] Bordin, A. et al. “Enhanced Majorana stability in a three-site Kitaev chain”. en. In: *Nat. Nanotechnol.* 20.6 (2025). DOI: 10.1038/s41565-025-01894-4.

[31] Haaf, S. L. D. ten et al. “Observation of edge and bulk states in a three-site Kitaev chain”. en. In: *Nature* 641.8064 (2025). DOI: 10.1038/s41586-025-08892-5.

[32] Tsintzis, A., Souto, R. S., and Leijnse, M. “Creating and detecting poor man’s Majorana bound states in interacting quantum dots”. In: *Phys. Rev. B* 106 (20 2022). DOI: 10.1103/PhysRevB.106.L201404.

[33] Liu, C.-X. et al. “Enhancing the excitation gap of a quantum-dot-based Kitaev chain”. In: *Commun. Phys.* 7.1 (2024). DOI: 10.1038/s42005-024-01715-5.

[34] Souto, R. S. et al. “Probing Majorana localization in minimal Kitaev chains through a quantum dot”. In: *Phys. Rev. Res.* 5 (4 2023). DOI: 10.1103/PhysRevResearch.5.043182.

[35] Koch, R. et al. “Adversarial Hamiltonian learning of quantum dots in a minimal Kitaev chain”. In: *Phys. Rev. Appl.* 20 (4 2023). DOI: 10.1103/PhysRevApplied.20.044081.

[36] Pandey, B. et al. “Majorana zero modes in Y-shape interacting Kitaev wires”. In: *npj Quantum Materials* 8.1 (2023). DOI: 10.1038/s41535-023-00584-5.

[37] Bozkurt, A. M. et al. “Interaction-induced strong zero modes in short quantum dot chains with time-reversal symmetry”. en. In: *SciPost Physics* 18.6 (2025). DOI: 10.21468/SciPostPhys.18.6.206.

[38] Miles, S. et al. “Kitaev chain in an alternating quantum dot-Andreev bound state array”. In: *Phys. Rev. B* 110 (2 2024). DOI: 10.1103/PhysRevB.110.024520.

[39] Torres Luna, J. D. et al. “Flux-tunable Kitaev chain in a quantum dot array”. In: *SciPost Phys. Core* 7 (2024). DOI: 10.21468/SciPostPhysCore.7.3.065.

[40] Liu, C.-X. et al. “Scaling up a sign-ordered Kitaev chain without magnetic flux control”. In: *Phys. Rev. Res.* 7.1 (2025). DOI: 10.1103/PhysRevResearch.7.L012045.

[41] Driel, D. v. et al. “Cross-Platform Autonomous Control of Minimal Kitaev Chains”. In: (2024). DOI: 10.48550/arXiv.2405.04596.

[42] Liu, Z.-H., Zeng, C., and Xu, H. Q. “Coupling of quantum-dot states via elastic cotunneling and crossed Andreev reflection in a minimal Kitaev chain”. In: *Phys. Rev. B* 110 (11 2024). DOI: 10.1103/PhysRevB.110.115302.

[43] Ezawa, M. “Even-odd effect on robustness of Majorana edge states in short Kitaev chains”. In: *Phys. Rev. B* 109 (16 2024). DOI: 10.1103/PhysRevB.109.L161404.

[44] Samuelson, W., Svensson, V., and Leijnse, M. “Minimal quantum dot based Kitaev chain with only local superconducting proximity effect”. In: *Phys. Rev. B* 109 (3 2024). DOI: 10.1103/PhysRevB.109.035415.

[45] Benestad, J. et al. “Machine-learned tuning of artificial Kitaev chains from tunneling spectroscopy measurements”. In: *Phys. Rev. B* 110 (7 2024). DOI: 10.1103/PhysRevB.110.075402.

[46] Svensson, V. and Leijnse, M. “Quantum dot based Kitaev chains: Majorana quality measures and scaling with increasing chain length”. In: *Phys. Rev. B* 110 (15 2024). DOI: 10.1103/PhysRevB.110.155436.

[47] Souto, R. S. et al. “Majorana modes in quantum dots coupled via a floating superconducting island”. In: *Phys. Rev. B* 111.17 (2025). DOI: 10.1103/PhysRevB.111.174501.

[48] Pino, D. M., Souto, R. S., and Aguado, R. “Minimal Kitaev-transmon qubit based on double quantum dots”. In: *Phys. Rev. B* 109 (7 2024). DOI: 10.1103/PhysRevB.109.075101.

[49] Seoane Souto, R. and Aguado, R. “Subgap States in Semiconductor-Superconductor Devices for Quantum Technologies: Andreev Qubits and Minimal Majorana Chains”. In: *New Trends and Platforms for Quantum Technologies*. Springer Nature Switzerland, 2024. ISBN: 9783031556579. DOI: 10.1007/978-3-031-55657-9_3.

[50] Nitsch, M. et al. “Poor Man’s Majorana Tetron”. In: *PRX Quantum* 6.3 (2025). DOI: 10.1103/r75t-jv32.

[51] Luethi, M. et al. “From perfect to imperfect poor man’s Majoranas in minimal Kitaev chains”. In: *Phys. Rev. B* 110 (24 2024). DOI: 10.1103/PhysRevB.110.245412.

[52] Luethi, M. et al. “Fate of poor man’s Majoranas in the long Kitaev chain limit”. In: *Phys. Rev. B* 111.11 (2025). DOI: 10.1103/PhysRevB.111.115419.

[53] Gómez-León, Á., Schirò, M., and Dmytruk, O. "High-quality poor man's Majorana bound states from cavity embedding". In: (2024). DOI: 10.48550/arXiv.2407.12088.

[54] Pandey, B. et al. "Crystalline-symmetry-protected Majorana modes in coupled quantum dots". In: *Phys. Rev. Res.* 7.1 (2025). DOI: 10.1103/PhysRevResearch.7.L012022.

[55] Alvarado, M. et al. "Interplay between Majorana and Shiba states in a minimal Kitaev chain coupled to a superconductor". In: *Phys. Rev. B* 110.24 (2024). DOI: 10.1103/PhysRevB.110.245144.

[56] Liu, C.-X. et al. "Fusion protocol for Majorana modes in coupled quantum dots". In: *Phys. Rev. B* 108 (8 2023). DOI: 10.1103/PhysRevB.108.085437.

[57] Boross, P. and Pályi, A. "Braiding-based quantum control of a Majorana qubit built from quantum dots". In: *Phys. Rev. B* 109 (12 2024). DOI: 10.1103/PhysRevB.109.125410.

[58] Pandey, B., Okamoto, S., and Dagotto, E. "Nontrivial fusion of Majorana zero modes in interacting quantum-dot arrays". In: *Phys. Rev. Res.* 6 (3 2024). DOI: 10.1103/PhysRevResearch.6.033314.

[59] Tsintzis, A. et al. "Majorana Qubits and Non-Abelian Physics in Quantum Dot–Based Minimal Kitaev Chains". In: *PRX Quantum* 5 (1 2024). DOI: 10.1103/PRXQuantum.5.010323.

[60] Sau, J. D., Clarke, D. J., and Tewari, S. "Controlling non-Abelian statistics of Majorana fermions in semiconductor nanowires". In: *Phys. Rev. B* 84 (9 2011). DOI: 10.1103/PhysRevB.84.094505.

[61] Heck, B. van et al. "Coulomb-assisted braiding of Majorana fermions in a Josephson junction array". In: *New Journal of Physics* 14.3 (2012). DOI: 10.1088/1367-2630/14/3/035019.

[62] Karzig, T. et al. "Shortcuts to non-Abelian braiding". In: *Phys. Rev. B* 91 (20 2015). DOI: 10.1103/PhysRevB.91.201102.

[63] Hell, M. et al. "Time scales for Majorana manipulation using Coulomb blockade in gate-controlled superconducting nanowires". In: *Phys. Rev. B* 94 (3 2016). DOI: 10.1103/PhysRevB.94.035424.

[64] Bonderson, P., Freedman, M., and Nayak, C. "Measurement-Only Topological Quantum Computation". In: *Phys. Rev. Lett.* 101 (1 2008). DOI: 10.1103/PhysRevLett.101.010501.

[65] Plugge, S. et al. "Majorana box qubits". In: *New Journal of Physics* 19.1 (2017).

[66] Karzig, T. et al. "Scalable designs for quasiparticle-poisoning-protected topological quantum computation with Majorana zero modes". In: *Phys. Rev. B* 95 (23 2017). DOI: 10.1103/PhysRevB.95.235305.

[67] Alicea, J. et al. "Non-Abelian statistics and topological quantum information processing in 1D wire networks". en. In: *Nature Phys* 7.5 (2011). DOI: 10.1038/nphys1915.

[68] Liu, J. et al. “Minimal setup for non-Abelian braiding of Majorana zero modes”. In: *Science China Physics, Mechanics & Astronomy* 64.11 (2021). DOI: 10.1007/s11433-021-1773-3.

[69] Xu, L. et al. “Dynamics simulation of braiding two Majorana zero modes via a quantum dot”. In: *Phys. Rev. B* 108.11 (2023). DOI: 10.1103/PhysRevB.108.115411.

[70] Clarke, D. J., Sau, J. D., and Das Sarma, S. “Probability and braiding statistics in Majorana nanowires”. In: *Phys. Rev. B* 95 (15 2017). DOI: 10.1103/PhysRevB.95.155451.

[71] Hensgens, T. et al. “Quantum simulation of a Fermi–Hubbard model using a semiconductor quantum dot array”. In: *Nature* 548.7665 (2017). DOI: 10.1038/nature23022.

[72] Hsiao, T.-K. et al. “Exciton Transport in a Germanium Quantum Dot Ladder”. In: *Phys. Rev. X* 14 (1 2024). DOI: 10.1103/PhysRevX.14.011048.

[73] Riggelen, F. van et al. “A two-dimensional array of single-hole quantum dots”. In: *Applied Physics Letters* 118.4 (2021). DOI: 10.1063/5.0037330.

[74] Arute, F. et al. “Quantum supremacy using a programmable superconducting processor”. In: *Nature* 574.7779 (2019). DOI: 10.1038/s41586-019-1666-5.

[75] Pan, H., Sarma, S. D., and Liu, C.-X. “Rabi and Ramsey oscillations of a Majorana qubit in a quantum dot-superconductor array”. In: *arXiv:2407.16750* (2024).

[76] Knapp, C. et al. “The Nature and Correction of Diabatic Errors in Anyon Braiding”. In: *Phys. Rev. X* 6 (4 2016). DOI: 10.1103/PhysRevX.6.041003.

[77] Hu, X. and Das Sarma, S. “Charge-Fluctuation-Induced Dephasing of Exchange-Coupled Spin Qubits”. In: *Phys. Rev. Lett.* 96 (10 2006). DOI: 10.1103/PhysRevLett.96.100501.

[78] Petersson, K. D. et al. “Quantum Coherence in a One-Electron Semiconductor Charge Qubit”. In: *Phys. Rev. Lett.* 105 (24 2010). DOI: 10.1103/PhysRevLett.105.246804.

[79] Dial, O. E. et al. “Charge Noise Spectroscopy Using Coherent Exchange Oscillations in a Singlet-Triplet Qubit”. In: *Phys. Rev. Lett.* 110 (14 2013). DOI: 10.1103/PhysRevLett.110.146804.

[80] Scarlino, P. et al. “In situ Tuning of the Electric-Dipole Strength of a Double-Dot Charge Qubit: Charge-Noise Protection and Ultrastrong Coupling”. In: *Phys. Rev. X* 12 (3 2022). DOI: 10.1103/PhysRevX.12.031004.

[81] Connors, E. J. et al. “Charge-noise spectroscopy of Si/SiGe quantum dots via dynamically-decoupled exchange oscillations”. In: *Nature Communications* 13.1 (2022). DOI: 10.1038/s41467-022-28519-x.

[82] Throckmorton, R. E. and Das Sarma, S. “Crosstalk- and charge-noise-induced multiqubit decoherence in exchange-coupled quantum dot spin qubit arrays”. In: *Phys. Rev. B* 105 (24 2022). DOI: 10.1103/PhysRevB.105.245413.

[83] Burkard, G. et al. “Semiconductor spin qubits”. In: *Rev. Mod. Phys.* 95 (2 2023). DOI: 10.1103/RevModPhys.95.025003.

[84] Paladino, E. et al. “$1/f$ noise: Implications for solid-state quantum information”. In: *Rev. Mod. Phys.* 86 (2 2014). DOI: 10.1103/RevModPhys.86.361.

[85] Ithier, G. et al. “Decoherence in a superconducting quantum bit circuit”. In: *Phys. Rev. B* 72 (13 2005). DOI: 10.1103/PhysRevB.72.134519.

[86] Boross, P. and Pályi, A. “Dephasing of Majorana qubits due to quasistatic disorder”. In: *Phys. Rev. B* 105 (3 2022). DOI: 10.1103/PhysRevB.105.035413.

[87] Aghaee, M. et al. “Interferometric single-shot parity measurement in InAs–Al hybrid devices”. en. In: *Nature* 638.8051 (2025). DOI: 10.1038/s41586-024-08445-2.

[88] Miles, S. et al. *Braiding Majoranas in a linear quantum dot-superconductor array: Mitigating the errors from Coulomb repulsion and residual tunneling*. 2025. DOI: 10.5281/zenodo.14735329.

[89] Johansson, J. R., Nation, P. D., and Nori, F. “QuTiP: An open-source Python framework for the dynamics of open quantum systems”. In: *Computer physics communications* 183.8 (2012).

[90] Araya Day, I. et al. “Pymablock: An algorithm and a package for quasi-degenerate perturbation theory”. In: *SciPost Phys. Codebases* (2025). DOI: 10.21468/SciPostPhysCodeb.50.

CONCLUSION

In this thesis we have discussed methods, designs, and operation protocols relevant to the development of quantum dot based platforms for topological quantum computing.

We began by introducing Pymablock, a Python package that allows efficient computation of effective Hamiltonians. Calculating effective Hamiltonians is a standard task in the study of condensed matter systems. The most common method for their calculation is known by the name Schrieffer-Wolff perturbation theory. Automating this task allows to progress on projects more efficiently while enhancing reliability. The package has been utilized in the various projects related to Kitaev chains presented here, but also for studies on superconductivity in interacting systems [1], superconducting junctions [2, 3], and effective models of semiconducting wires [4].

Using these tools, we then demonstrated how the physics of Kitaev chains can be realized in chains of quantum dots featuring less constituents than the original proposals [5–7]. In regimes of limited Zeeman splitting, the excited Andreev bound state mediates an effective coupling equivalent to that of a single Andreev bound state coupled to two quantum dots. While the design allows to reduce the number of quantum dots, it highlights the challenges associated with next-nearest neighbor couplings upon scaling. Specfically, the previously exact zero energy crossing of a sweet spot is lifted regardless of the coupling strength between quantum dots. Similar next nearest neighbor couplings have later been discussed also for extended poor man's Majorana chains [8]. Despite the challenges, we foresee that our proposed design is well suited to demonstrate convergence to the topological limit in sufficiently long chains.

Next, we turned to a system of two quantum dots coupled via an Andreev bound state in the limit of zero magnetic field and strong on-site Coulomb repulsion. We showed that such a system hosts zero modes that can be associated with parafermions. To the best of our knowledge, this establishes the poor man's Majorana system as the simplest system to host parafermions that are robust against local detuning. Experimental demonstration of the nature of the zero modes however remains an important challenge. While experimental signatures of degeneracies have recently been observed [9], demonstrating the parafermionic nature of these modes is likely to remain experimentally prohibitive due to the stringent conditions required for their realization.

Finally, we have proposed a protocol to realize braiding in a system composed of two minimal Kitaev chains coupled via a normal quantum dot to verify the non-Abelian nature of the zero modes. Demonstrating the the non-Abelian nature of the zero modes is a necessary step to uniquely identify Majoranas. Additionally, the protocol realizes an elementary operation for the purpose of topological quantum computing. The main experimental challenge in realizing the proposal will be the noise in the system. While the realization of the protocol is a hard experimental task, avoiding the most impeding noise sources and reliable local parity read-out are the central challenges to overcome for

scalable quantum dot based platforms for topological quantum computing. We expect our protocol and system to provide valuable guidance in future experimental efforts.

REFERENCES

[1] Soldini, M. O., Fischer, M. H., and Neupert, T. "Charge-4*e* superconductivity in a Hubbard model". In: *Phys. Rev. B* 109 (21 2024). DOI: 10.1103/PhysRevB.109.214509.

[2] Bordin, A. et al. "Impact of Andreev Bound States within the Leads of a Quantum Dot Josephson Junction". In: *Phys. Rev. X* 15 (1 2025). DOI: 10.1103/PhysRevX.15.011046.

[3] Fatemi, V. et al. "Nonlinearity of transparent SNS weak links decreases sharply with length". In: *SciPost Phys.* 18 (2025). DOI: 10.21468/SciPostPhys.18.3.091.

[4] Miles, S. et al. "Effective Hamiltonians for Ge/Si core/shell nanowires from higher order perturbation theory". In: (2025). arXiv: 2511.11809 [cond-mat.mes-hall].

[5] Leijnse, M. and Flensberg, K. "Parity qubits and poor man's Majorana bound states in double quantum dots". In: *Phys. Rev. B* 86 (13 2012). DOI: 10.1103/PhysRevB.86.134528.

[6] Dvir, T. et al. "Realization of a minimal Kitaev chain in coupled quantum dots". en. In: *Nature* 614.7948 (2023). DOI: 10.1038/s41586-022-05585-1.

[7] ten Haaf, S. L. D. et al. "A two-site Kitaev chain in a two-dimensional electron gas". en. In: *Nature* 630.8016 (2024). DOI: 10.1038/s41586-024-07434-9.

[8] Torres Luna, J. D. et al. "Pareto-optimality of Majoranas in hybrid platforms". In: (2025). arXiv: 2510.07406 [cond-mat.mes-hall].

[9] ten Haaf, S. L. D. et al. "Probing ground-state degeneracies of a strongly interacting Fermi-Hubbard model with superconducting correlations". In: (2025). arXiv: 2512.13242 [cond-mat.mes-hall].

CURRICULUM VITÆ

Sebastian MILES

30.11.1996 Born in Soltau, Germany

EDUCATION

10.2015 - 09.2018 Bachelor of Science, Physics

Rheinisch-Westfälische Technische Hochschule, Aachen, Germany

Thesis: Application of the Matrix Numerov Method to Periodic or Singular Potentials in the 1D Schrödinger Equation
Supervisor: Prof. Dr. Fabian Hassler
Cosupervisor: Prof. Dr. David DiVincenzo

10.2018 - 09.2021 Master of Science, Physics

Rheinisch-Westfälische Technische Hochschule, Aachen, Germany

Thesis: Universal properties of boundary and interface charges in continuum models of one-dimensional insulators
Supervisor: Priv. Doz. Dr. Mikhail Pletyukhov
Cosupervisor: Prof. Dr. Herbert Schoeller

01.2022 - 03.2026 Doctoral studies, Condensed Matter Theory

Delft University of Technology, Delft, Netherlands

Thesis: Design and operation of degenerate quantum dot systems for topological quantum computing
Promotor: Prof. Dr. Michael Wimmer
Promotor: Dr. Anton R. Akhmerov

List of Publications

Journal publications and preprints

11. *Probing ground-state degeneracies of a strongly interacting Fermi-Hubbard model with superconducting correlations*
Sebastiaan L. D. ten Haaf, **Sebastian Miles**, Qingzhen Wang, A. Mert Bozkurt, Ivan Kulesh, Yining Zhang, Christian G. Prosko, Michael Wimmer, and Srijit Goswami
arXiv:2512.13242 [cond-mat.mes-hall]

10. *Effective Hamiltonians for Ge/Si core/shell nanowires from higher order perturbation theory*
Sebastian Miles, A. Mert Bozkurt, Daniel Varjas, and Michael Wimmer
arXiv:2511.11809 [cond-mat.mes-hall]

9. *Quantifying robustness and locality of Majorana bound states in interacting systems"*
William Samuelson, Juan Daniel Torres Luna, **Sebastian Miles**, A. Mert Bozkurt, Martin Leijnse, Michael Wimmer, and Viktor Svensson
arXiv:2510.20538 [cond-mat.mes-hall]

8. *Pareto-optimality of Majoranas in hybrid platforms*
Juan Daniel Torres Luna, **Sebastian Miles**, A. Mert Bozkurt, Chun-Xiao Liu, Antonio L. R. Manesco, Anton R. Akhmerov, and Michael Wimmer
arXiv:2510:07406 [cond-mat.mes-hall]

7. *Braiding Majoranas in a linear quantum dot-superconductor array: Mitigating the errors from Coulomb repulsion and residual tunneling*
Sebastian Miles, Francesco Zatelli, A. Mert Bozkurt, Michael Wimmer, and Chun-Xiao Liu
arXiv:2501.16056 [cond-mat.mes-hall]

6. *Pymablock: an algorithm and a package for quasi-degenerate perturbation theory*
Isidora Araya Day, **Sebastian Miles**, Hugo K. Kerstens, Daniel Varjas, and Anton R. Akhmerov
SciPost Phys. Codebases 50 (2025)

5. *Protocol for scaling up a sign-ordered Kitaev chain without magnetic flux control*
Chun-Xiao Liu, **Sebastian Miles**, Alberto Bordin, Sebastiaan L. D. ten Haaf, A. Mert Bozkurt, and Michael Wimmer
Phys. Rev. Research **7**, L012045 (2025)

4. *Interaction-induced strong zero modes in short quantum dot chains with time-reversal symmetry*
A. Mert Bozkurt, **Sebastian Miles**, Sebastiaan L. D. ten Haaf, Chun-Xiao Liu, Fabian Hassler, and Michael Wimmer
SciPost Phys. 18, 206 (2025)

3. *Kitaev chain in an alternating quantum dot-Andreev bound state array*
Sebastian Miles, David van Driel, Michael Wimmer, and Chun-Xiao Liu
Phys. Rev. B **110**, 024520 (2024)

2. *Fermionic quantum computation with Cooper pair splitters*
Kostas Vilkelis, Antonio Manesco, Juan Daniel Torres Luna, **Sebastian Miles**, Michael Wimmer, and Anton Akhmerov
SciPost Phys. 16, 135 (2024)

1. *Universal properties of boundary and interface charges in continuum models of one-dimensional insulators*
Sebastian Miles, Dante M. Kennes, Herbert Schoeller, and Mikhail Pletyukhov
Phys. Rev. B 104, 155409 (2021)

PATENTS

1. *Method of creating Majorana bound states in a quantum-dot chain*
Michael Wimmer, Chun-Xiao Liu, **Sebastian Miles**, David van Driel, Bart Roovers, and Sebastian L. D. ten Haaf
EP24761258 (originally NL2035759) filed 07.09.2023, received 13.03.2025
Patent pending.

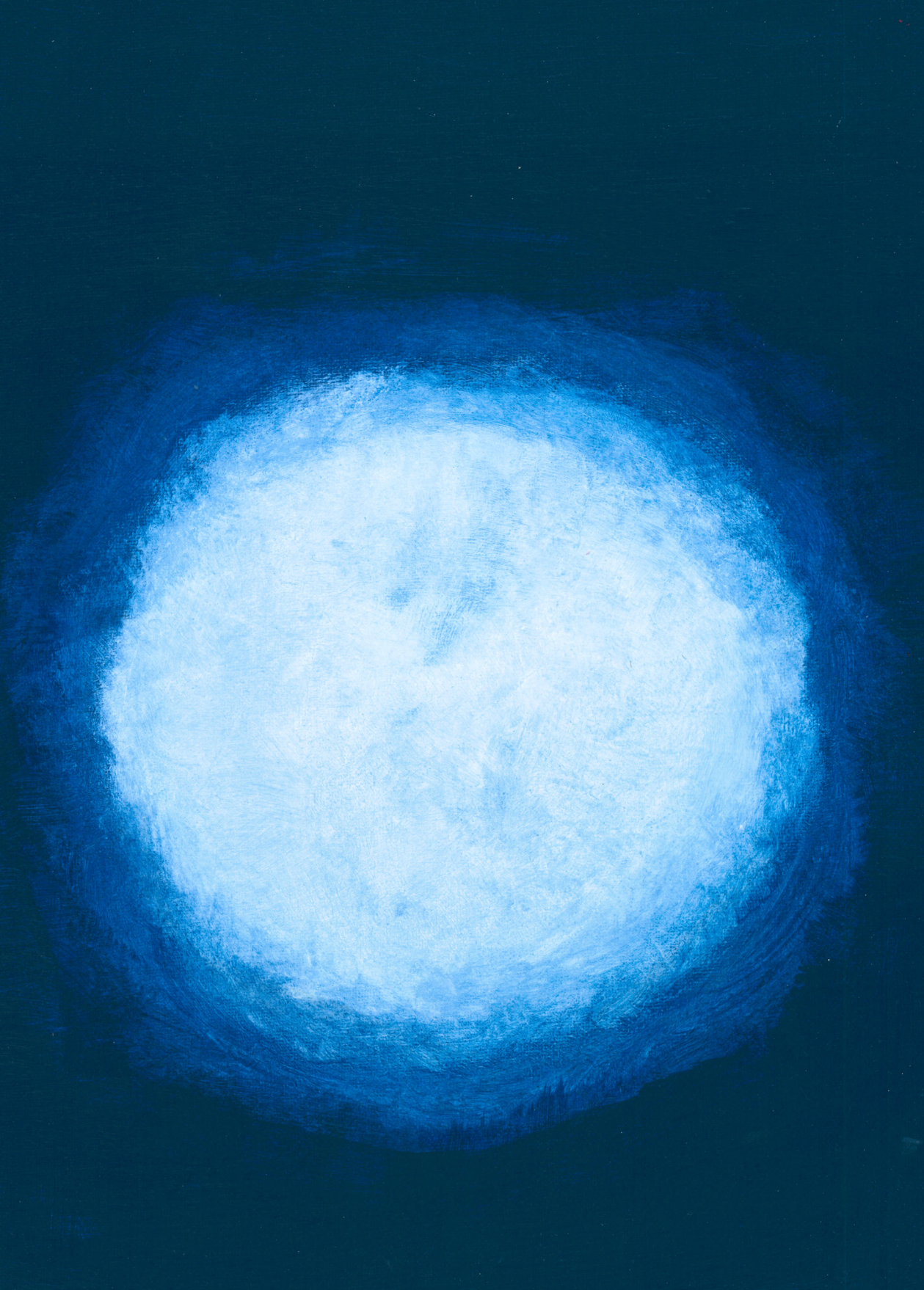

ISBN: 978-94-6518-250-6

No. 18